JPL Publication 91-30

Proceedings of the Third Airborne Synthetic Aperture Radar (AIRSAR) Workshop

May 23 and 24, 1991

Jakob J. van Zyl
Editor

August 1, 1991

NASA
National Aeronautics and
Space Administration

Jet Propulsion Laboratory
California Institute of Technology
Pasadena, California

JPL Publication 91-30

Proceedings of the Third Airborne Synthetic Aperture Radar (AIRSAR) Workshop

May 23 and 24, 1991

Jakob J. van Zyl
Editor

August 1, 1991

National Aeronautics and
Space Administration

Jet Propulsion Laboratory
California Institute of Technology
Pasadena, California

This publication was prepared by the Jet Propulsion Laboratory, California Institute of Technology, under a contract with the National Aeronautics and Space Administration.

FOREWORD

In the text and figure captions of some of the papers, reference is made to color slides; these 35-mm slides are located in a pocket at the end of the Proceedings. They are color versions of some of the referenced black-and-white figures within the Proceedings.

ABSTRACT

The third Airborne Synthetic Aperture Radar (AIRSAR) Workshop was held on May 23 and 24, 1991, at the Jet Propulsion Laboratory, Pasadena, California. Thirty oral presentations were made and 18 poster papers displayed during the workshop.

This publication contains papers from 25 of these presentations, which include analyses of AIRSAR operations and studies in SAR remote sensing, ecology, hydrology, soil science, geology, oceanography, volcanology, and SAR mapping and data handling. Results from these studies indicate the direction and emphases of future orbital radar-sensor missions that will be launched during the 1990s.

CONTENTS

N92-28014

Progress Towards SAR Based Ecosystem Analysis

K. Jon Ranson
NASA/GSFC
Greenbelt, MD

Guoqing Sun
Ressler Associates, Inc.
Laurel, MD

Abstract

This paper discusses recent progress towards a synthetic aperture radar based system for determining forest ecosystem attributes. Our SAR data processing and analysis sequence, from calibration through classification, is described. In addition, the usefulness of SAR image data for identifying ecosystem classes is discussed.

I. Introduction

Changes in forest ecosystems in response to natural and anthropogenic influences and the resulting feedbacks to climate are of major concern to scientists studying global change. In order to address the significance of change one must know the current state of the ecosystem under study in terms of species composition, carbon storage and biophysical functioning. Multifrequency and multipolarization synthetic aperture radar (SAR) systems present a significant tool to terrestrial ecologists engaged in global change research. For example, the ability of synthetic aperture radar to acquire image data independent of cloud cover and solar irradiance conditions is an important advantage for forest ecosystem studies, especially in northern latitudes. In our work we are vitally interested in utilizing SAR to determine ecosystem state (species composition), total biomass (carbon storage) and forest canopy functioning as revealed by productivity and presence of stress. In this paper we describe progress towards exploiting the unique capabilities of SAR image data for determining ecosystem state which is required for identification of ecosystem change and initialization of forest ecosystem models.

Several investigations have discussed identifying or mapping vegetation and land cover units from radar images. These include mapping forest units using multiple incidence angle images [1], geologic mapping and vegetation discrimination from multipolarization parameters, i.e. HH, VV, and HV images [2]. Recent research on the capability of polarimetric SAR data in vegetation classification [3,4] demonstrated that classification methods (maximum-likelihood, minimum distance) can be extended to classify polarimetric data and increase the classification accuracy. van Zyl [5] compared the polarization properties of each pixel in an image to that of simple classes of scattering such as even number of reflections, odd number of reflections, and diffuse scattering to distinguish between different scattering behaviors by the use of both the amplitude and phase information of polarimetric SAR data. In addition the rich information of polarimetric data is being exploited to design new image features (including texture) for vegetation discrimination [6].

The emphasis of this work is on the mapping of ecosystem classes using airborne multi-frequency, multi-date polarimetric SAR data. To use airborne SAR requires a series of processing steps including calibration, angle correction, filtering, enhancement, registration and finally, classification. Each step of this process is discussed, as well as, the results of our initial efforts to classify a northern forest for ecosystem analysis.

II. Study Site

Our study site, International Paper's Northern Experiment Forest, is located near Howland Maine (45^{o} 12'N, 68^{o} 08'W) consists of small plantations, multi-generation clearings, as well as large natural forest stands. Because of distinct management programs, useful historical background on specific areas is available. The natural stands in this boreal-northern hardwood transitional forest consist of aspen-birch, hemlock-spruce-fir, and hemlock-hardwood mixtures. Topographically, the region varies from flat to gently rolling, with a maximum elevation change of less than 68 m. Due to the region's glacial history, soil drainage classes within a small area may vary widely, from well drained to poorly drained. Consequently, an elaborate patchwork of forest communities has developed, supporting exceptional local species diversity. Additionally, almost 450 ha of the central NEF consists of bogs and other wetlands. Generally, the soils throughout the forest are glacial tills, acid in reaction, with low fertility and high organic composition. The climate is chiefly cold, humid, and continental and the region exhibits a snowpack of up to 2 m from December through March. This site is the focus of a NASA Multisensor Aircraft Campaign (MAC) for the Forest Ecosystem Dynamics project at GSFC (e.g., [7]).

The JPL DC-8 SAR was flown on 2 September 1989, 30 March 1990, 15 July 1990, and 17 July 1990 with P-, L-, and C-band frequencies at three image center incidence angles (25^o, 35^o, 45^o) while looking north over the Howland Forest test area. By flying a “race track” trajectory, two southern looking Howland views were also obtained. Preceding the overflight, field personnel positioned an array of corner reflectors inside the Howland Forest for SAR image calibration. Images of four dates with incidence angle 35^o looking toward the north have been used for this study. The four dates provide images of the forest under widely different phenologic or moisture conditions. On September 1989 the forest was undergoing senescence with a relatively dry canopy and understory. During the March 1990 overflight the deciduous tree were leafless , the ground was frozen and there was snow beneath the trees, but not in the open areas. On July 15 the forest had maximum leaf development and dry soil surface conditions, however, on July 17, soil surfaces were wet following a 12mm rain the day before.

III. Methods

A. Calibration

All images were calibrated using the POLCAL program provided by JPL [8-11] with the following modifications:

1) Suitable background areas for corner reflectors (i.e., smooth with no vegetation) in our test site are much smaller than the 16 by 16 radar image cells utilized in POLCAL and usually are in non-rectangle shapes. The modified program allows user to flexibly specify the pixels belonging to corner reflector or its background so that the proper parameters for image calibration can be estimated.

2) For P-band calibration, the corner reflectors currently used are too small and in most cases the signal to background ratio is too low for reliable calibration. Since the backscattering from a slightly rough surface at HH and VV polarization are equal in phase and the relative backscattering can be estimated from the model for a slightly rough surface the pixels from an interstate highway (I-95) from all four images were selected for phase calibration, cross-talk removal and channel imbalance calibration. Absolute calibration was done by dividing the image value by the pixel area and then subtracting an additional 4.5 dB, the correlation gain estimated by JPL [12].

B. Incidence angle correction

A disadvantage of using aircraft SAR image for classification is its large range of incidence angles across the image, so even areas belonging to the same category will have different backscattering signatures if they have very different incidence angles. At present we are not very clear how the incidence angle will influence the Stokes matrix and those variables derived from it. The calibration therefore is not applied to the Stokes matrix, but for each of the derived variables used for classification. Normalization by total power, as used in [13], eliminates most of the effect of incidence angle as well as the information contained in power intensity. It will be difficult to discriminate between two targets with similar scattering mechanisms, but different backscattering power intensity, on the normalized images.

A traditional method for angle correction is to carefully choose areas of the same category (e. g. softwood forest stands) along the range, and calibrate the image so that these areas will have the same signatures. The images of all channels were calibrated individually due to the reason mentioned above. We selected a portion of each image line, calculated the mean and standard deviation of these pixels, and discarded pixels falling outside of plus and minus two standard deviations. The remaining pixels were used to estimate the mean values at each line. In most cases, a linear regression was used to estimate the calibration ratio for each line. Depending on the scatter pattern of estimated mean values, however, a polynomial fitting procedure may be necessary in some cases.

C. Image filtering

A simple filter based on spatial autocorrelation was used to reduce image speckle before classification. An image with spatial autocorrelation can be simulated by the following process [14]. Let the value of pixel k in the image be influenced by the values in other pixels in a linear manner, via

$$x_k = \rho \sum_i w_{k,i}\, x_i + u_k \qquad (1)$$

where w_k is a weight, u_k is an noise term from a Gaussian distribution and ρ is a constant determining the strength of autocorrelation between neighbor pixels. If matrix X represents an image, the matrix notation of Equation (1) will be:

$$X = \rho\, W X + U \qquad (2)$$

For the simplest case, we assume that the value of a pixel is influenced directly only by its four nearest neighbors. In this case, each line of matrix W will have only 4 elements with value 1, and all of the rest elements will be zero.

Solving for X, we get:

$$X = (I - \rho\, W)^{-1}\, U \qquad (3)$$

To adapt this idea to image filtering, we treat a radar image of homogeneous area as a noise image and and produce a smoothed image through the processing above. We select a window size, say 9 by 9 pixels, then the U in (3) will be a vector with 81 pixel values, while $(I-\rho W)^{-1}$ will be an 81 by 81 matrix. Because only the center image of the window was to be modified, we picked the center line of matrix $(I-\rho W)^{-1}$ as our filter. Rearranging this line to be a 9 by 9 matrix one can see that the value of its elements is inversely proportional to its distance from the center, and the sum of all elements is 1.0. A window size of 9 by 9 and $\rho = 0.25$ were used in this study. Table 1 shows the filtering effect by listing the means and standard deviations of several training sites before and after filtering. The average change of means is +8.6% with all sites having roughly the same positive shifts. The standard deviations were reduced to about 37%.

D. Maximization of class separability

We examined a number of techniques to determine a method for maximizing the spectral separation of our forest classes. A polarization filtering technique has been suggested by Dubois and van Zyl [15] for finding the optimal antenna polarization from which the separability of a pair of selected targets (classes) is maximized. If only a pair of targets is considered, an alternative method can be used to maximize the distance between the two targets. Since the information from polarimetric data is contained in the nine independent elements of the Stokes matrix, we simply calculate the means of the two targets and project the 9-dimensional Stokes matrix data onto the axis connecting the two mean points. The resulting image (optim1 in Table 2) should have the largest distance for the two targets. This method maximizes the distance $\mu_1-\mu_2$,but does not necessarilly have the best separability defined by: $|\mu_1-\mu_2| / (\sigma_1+\sigma_2)$, since the term $\sigma_1+\sigma_2$ may also be enlarged. If the multiple channel image is transformed to principal components and then projected to the direction with maximum distance between the two targets, the separabilities will be higher (optim2 in Table 2).

This study is designed to use multi-frequency and multidate SAR image for ecosystem unit classification. If all images at four dates with C, L, and P Bands were used, there will be 4*3*9=108 channels or variables, which is much too large to be handled. Thus, feature reduction and optimization have to be implemented before classification. Considering that our goal is to discriminate more than two targets, and that pairwise targets are not very easy to choose in a hierarchical classification strategy (i.e. forests and non-forests for the first step), we decided to use the principal component analysis to reduce channels and maximize the target separability. Because we are most interested in the variances existing in our selected targets, only those pixels from class training areas were used for this purpose.

E. Image Registration

The first step to registration of multidate images is to convert them into ground range images. To register SAR image at areas with rough terrain, sophisticated methods involving DEM data, and aircraft flight navigation data may needed. Since our research area is quite flat, and the flight direction and incidence angle of the four images were purposely kept as close as possible, the registration is relatively easy. It was found that using a linear interpolation and about 10 control points produced much better results compared to 3-order polynomial interpolation with 20 control points. The flight conditions apparently were quite stable and the distortion was linear.

F. Classification

The 11 training sites were selected based on a forest map compiled by International Paper in September 1979 and updated in March 1990. They are: 1) S2 - Softwood with medium volume; 2) S3 - Softwood with high volume; 3) HS2-PB - 50-75% hardwood (Poplar birch) with medium volume; 4) H1-PB - Hardwood (Poplar birch) with low volume; 5) Aspen - low volume; 6) Plantation - Young mixtures; 7) Oldcut - Small trees, bush and rugged surface; 8) Bog-B; 9) Bog-F, flowage; 10) Open - hayfield; and 11) Water bodies.

A supervised minimum distance classifier was used for this study. Five principal components as described in the next section were selected for each date and classified individually. With certain confidence on the results from 9/2/89 and 3/30/90 images, the 10 components from these two dates were combined together and classified again. Figure 1 shows the four individual classifications and Figure 2 is the classification using combined data from Summer 1989 and the following winter (March 1990).

Airphotos (both color and color-infrared), a forest stand map and some field measurements were used to evaluate the classification. There are sample areas for monitoring tree growth by International Paper, where tree measurements have been periodically conducted . Trees less than 5 inch dbh are not counted so these data do not actually reflect the total number of trees in the sample plots. However, we feel the plots do provide a representative sample of diverse areas within the study site. We located the center of these circular research plots and extracted 9 by 9 pixels to see if the classification results give a reasonable species composition in these areas.

IV. Results and discussion

The results of filtering the data shown in Table 1 indicate that the mean backscattering changed by 7.0 to 11.5% over the classes used in our analysis. The ratio of standard deviations reveals a large decrease in the pixel variance suggesting that the filtering method is useful for reducing the effects of speckle without a corresponding change in the mean backscatter. Similar results were obtained for C- and P-band data with respect to means and standard deviations of the forest classes.

Table 2 shows the separability between Spruce (S2) and other forest classes obtained from the average cross section ($\sigma^0_{av} = 0.25*(2*\sigma^0{}_{hv}+\sigma^0{}_{hh}+\sigma^0{}_{vv})$), polarization ratio ($p=\sigma^0{}_{hh}/\sigma^0{}_{vv}$), linear depolarization ratio ($LDR = 2*\sigma^0{}_{hv}/(\sigma^0{}_{hh}+\sigma^0{}_{vv})$), phase difference between HH and VV polarizations (α), Optim1, and Optim2. Improvements in separability for all classes were obtained by optimization using the Optim2 method which includes variance information through the use of principal components.

Table 3 shows the relative information content of each principal component and the relative contribution of each feature to each principal component. The results in Table 3 are calculated from the image data of September 2, 1989. As discussed by Cumming and van Zyl [16], the last several components mainly represent some spatially independent features, to which the noise is the greatest contributor. The majority of the variance is concentrated in the first two principal components. The effect of the middle group of components is class dependent and the experiments to evaluate the effect were not performed at this stage. Therefore, in our study the components containing a total of about 70% of variance were selected for classification. That is, the first principal component of C-band and the first two components of both L- and P- bands.

By qualitatively comparing the classification with the airphotos and forest maps, the results from 9/2/89 and 3/30/90 look encouraging in the sense that the patterns match without very obvious misclassification. The classification results from 7/15/90 and 7/17/90 show much more hardwood dominated areas, especially in the eastern part of the image. This is also apparent in the classified images as larger areas of darker tones on the left side of the July 1990 images shown in Figure 1. Although some hints have been found by comparing signatures from all four dates for some obviously misclassified areas, the causes are not yet clear, but may be related to canopy and/or surface moisture conditions. A comparison of the available ground data and classification results for these locations is summarized in Table 4 . Here the data has been combined to form two classes consisting of hardwood species (mainly aspen and birch) and softwood species (mainly spruce and hemlock). The results indicate confusion between hardwood and soft classes for any single date image data, with the 9/2/89 and 3/30/90 classfications showing better correspondence with ground truth information. Combining a winter and summer image to form a single image produced improvement in discrimination between the two classes of trees. Also of interest is the correspondence between the percentage of cords for a class (an estimate of bole volume) and the percentages classified as tree class. This suggests that the radar may be more sensitive to the amount and arrangement of biomass.

V. Summary and Conclusions

This paper has described our efforts to develop a system for utilizing airborne SAR data for our ecosystem studies. Necessary components include the capability calibrate, filter, register and classify the image data into useful ecosystem classes. Our results are mixed in this regard, with only a cursory assessment of classification accuracy. Optimization and spatial filtering did improve separability of classes significantly. Our current classification technique requires further evaluation to determine if there are more optimum combinations of principal components. The multi-date analysis revealed definite differences in the classification under different moisture conditions. For example, areas classified as openings or clear cuts in images acquired in September or March were identified as bogs in the July data. There was also a tendency for spruce and hemlock stands to be misclassified as deciduous stands in the July Images. Based on even greater misclassificatons of the image acquired following a rain (July 17) it is suggested that site moisture seriously affects classifications. We will investigate this further during our Summer'91 field experiments in Maine. In addition we plan more extensive analysis of classification accuracies by implementing a GIS database.

Species classification is required to initialize our forest ecosystem models so we will continue to investigate the capabilities of SAR. However, since forest classification is only one aspect of our interests in using SAR data over northern forests, we plan to develop our modeling capabilities to address questions related to forest biomass, forest structure and spatial patterns.

REFERENCES

[1] Cimino, J.,Brandani, A.,Casey, D.,Rabassa, J., and Wall, S. D. [1986], "Multiple incidence angle SIR-B experiment over Argentina: Mapping of forest units," *IEEE Transactions on Geoscience and Remote Sensing* **27**: 36-45.

[2] Evans, D. E.,Farr, T. G.,Ford, J. P.,Thompson, T. W., and Werner, C. L. [1986], "Multipolarization radar images for geologic mapping and vegetation discrimination," *IEEE Transactions on Geoscience and Remote Sensing* **24**: 246-257.

[3] Lim, H. H., Swartz, A. A., Yueh, H. A., Kong, J. A., Shin, R. T., and van Zyl, J. J., [1989], Classification of earth terrain using polarimetric synthetic aperture radar images, *Journal of Geophysical Research* ,**94**: 7049-7057.

[4] Subotic, N., Gorman, J., DeGraaf, S., Sheen, D., Kasischke, E., and Beverstock, D., [1990], Classification of forested terrain using multifrequency, polarimetric SAR data, *Proceedings of IGARSS '90* 3: 2401.

[5] van Zyl, J. J. [1989], "Unsupervised classification of scattering behavior using radar polarimetric data," *IEEE Transactions on Geoscience and Remote Sensing* **27**: 36-45.

[6] Ott, J. S., Kasischke, E. S., French, N. H., Gross, M. F., and Klemas, V., [1990], Preliminary evaluation of a multi-channel SAR data set for a mid-Atlantic coastal Marsh, *Proceedings of IGARSS '90* 1: 453-456.

[7] Ranson, K. J. and Smith, J. A. [1990], “Airborne SAR experiment for forest ecosystems research - Maine 1989 Experiment,” *IGARSS'90*, The University of Maryland, College Park, Maryland, 861-864.

[8] Zebker, H. A. and Lou, Y. [1990], “Phase calibration of imaging radar polarimeter Stokes matrix,” *IEEE Transactions on Geoscience and Remote Sensing* **28**: 246-252.

[9] Freeman, A.,Shen, Y., and Werner, C. L. [1990], “Polarimetric SAR calibrations experiment using active radar calibrators,” *IEEE Transactions on Geoscience and Remote Sensing* **28**: 224-240.

[10] van Zyl, J. J. [1990], “Calibration of polarimetric radar images using only image parameters and trihedral corner reflector responses,” *IEEE Transactions on Geoscience and Remote Sensing* **28**: 337-348.

[11] van Zyl, J. J.,Burnette, C. F.,Zebker, H. A.,Freeman, A., and Holt, J. [1990], "POLCAL User's Manual," **JPL D-7715**, JPL, August 1990.

[12] van Zyl, J. J. and Freeman, A. [1990], "Jet Propulsion Laboratory interoffice memorandum," **3343-90-65**, JPL, September 7, 1990.

[13] Ulaby, F., and Elachi, C., [1990], *Radar Polarimetry for Geoscience Applications*, Artech House, Norwood, MA.

[14] Cliff, A. D. and Ord, J. K. [1981], *Spatial Processes: Models and Applications,* London, Pion.

[15] Dubois, P. C. and Zyl, J. J. v. [1989], “Polarization filtering of SAR data,” *IGARSS'89*, Vancouver, Canada, 1816-1819.

[16] Cumming, I. G. and Zyl, J. J. v. [1989], “Feature utility in polarimetric radar image classification,” *IGARSS'89*, Vancouver, Canada, 1841-1846.

Acknowledgements

Funding for this research was provided by NASA Headquarters Terrestrial Ecology and Biogeochemical Cycles Branch and the SIR-C Project. Thanks to NASA/AMES and NASA/JPLfor providing the SAR data overflights and processing. We gratefully acknowledge the cooperation of International Paper for the use of the Northern Experiment Forest and the able field assistance provided by Prof. Mike Goltz and Staff at the Univ. of Maine.

Table 1. Mean and standard deviations of class training sets before (Mean, SD) and after (Mean$_F$,SD$_F$) filtering. Percent difference (Dmean) and ratio of standard deviations are also shown. Results shown are from L-band,HH polarization data for 9/2/89 image.

Class	s2	s3	H1-PB	HS2-PB	Aspen	Plantation	Bog-B	Open	Avg.
Mean	-8.20	-7.10	-7.35	-8.18	-8.24	-9.11	-7.21	-10.87	
SD	2.96	2.86	2.89	2.63	2.87	2.71	2.96	2.59	
Mean$_F$	-7.58	-6.45	-6.59	-7.53	-7.55	-8.44	-6.38	-10.11	
SD$_F$	1.34	1.06	1.09	0.86	1.33	0.97	0.88	0.79	
Dmean ,%	7.6	9.2	10.3	7.9	8.4	7.4	11.5	7.0	(8.6)
SD$_F$/SD	0.47	0.37	0.38	0.33	0.46	0.36	0.30	0.31	(0.37)

Table 2. Separabilities between S2 and other classes derived from various data transformations.

Class	S3	Aspen	H1-PB	HS2-PB	Plant.-tation	Open	Bog-B	Bog-F
σ^0_{av}	0.11	0.52	1.85	0.15	0.39	1.07	1.44	0.73
p	0.13	0.29	0.85	0.23	0.20	0.21	0.48	0.31
LDR	0.07	0.05	1.07	0.04	0.11	0.13	0.97	0.80
α	0.05	0.05	0.13	0.06	0.14	0.26	0.03	0.05
Optim1	0.29	0.55	1.56	0.30	0.36	0.91	1.19	0.77
optim2	0.66	2.04	6.58	0.83	1.39	3.79	5.39	2.67

Table 4a. Field data for forest inventory plots from Northern Experiment Forest. Sw = softwood species, Hw = hardwood species.

Site	#of Trees	% Classified as:		Volume	% Classified as:	
	total	%Sw	%Hw	total cords	%Sw	%Hw
310	20	100	0	6.4	100	0
312	5	80	20	0.8	59	41
313	22	91	9	6.4	89	11
314	52	77	23	26.8	78	22
315	76	91	9	53.3	97	3
316	36	81	19	21.6	82	18
318	37	89	11	20.4	94	6

Table 4b. Classification results for individual date analysis and a combination of summer and winter (89s+90w) data. Sw = softwood species, Hw = hardwood species.

	Classified Image Date									
	9/2/89		3/30/90		89s+90w		7/15/90		7/17/9	
Site	%Sw	%Hw	%Sw	%Hw	%Sw	%Hw	%SW	%Hw	%Sw	%Hw
310	33	67	100	0	76	24	38	62	14	86
312	70	30	60	40	57	43	25	75	26	74
313	79	21	75	25	83	17	29	71	46	54
314	100	0	87	13	98	2	79	21	70	30
315	75	25	70	30	74	26	72	28	58	42
316	88	12	71	29	87	13	90	10	89	11
318	73	27	41	59	69	31	17	83	57	43

Table 3. Percentage of variance contained in each principal component and the contribution of each Stokes matrix variable to the total.

	Percent	HH*HH*	VV*VV*	HV*HV*	R(HH*VV*)	I(HH*VV*)	R(HH*HV*)	I(HH*HV*)	R(HV*VV*)	I(HV*VV*)
C-BAND										
PC1	70.0	-0.82	-0.02	0.02	0.00	-0.42	0.00	0.00	-0.40	0.02
PC2	7.04	-0.02	0.86	-0.37	0.02	0.07	-0.05	0.21	-0.09	-0.25
PC3	6.38	-0.01	-0.23	0.28	-0.01	0.07	0.03	0.44	-0.08	-0.81
PC4	4.91	-0.01	-0.43	-0.87	0.03	-0.10	-0.07	0.09	0.09	-0.15
PC5	4.31	0.01	-0.07	0.03	-0.06	0.08	-0.03	0.85	-0.07	0.50
PC6	3.63	0.01	0.13	0.11	-0.02	-0.68	0.00	0.15	0.69	-0.04
PC7	1.9	0.00	-0.02	0.06	0.97	-0.01	-0.25	0.05	0.01	0.02
PC8	1.82	0.00	-0.01	0.08	-0.25	0.01	-0.96	-0.04	-0.01	-0.03
PC9	0.0									
L-BAND										
PC1	61.32	-0.81	-0.08	0.03	0.00	-0.40	0.01	-0.05	-0.42	0.03
PC2	8.58	-0.05	0.66	-0.21	0.06	0.40	-0.09	-0.07	-0.45	-0.36
PC3	6.59	-0.03	0.21	0.66	-0.18	-0.05	0.07	0.65	0.02	-0.24
PC4	6.27	-0.01	0.23	-0.13	-0.14	0.18	-0.03	0.36	-0.19	0.84
PC5	5.66	0.02	-0.65	-0.24	-0.02	0.40	-0.07	0.41	-0.38	-0.21
PC6	5.40	-0.06	0.18	-0.60	0.02	-0.39	-0.29	0.47	0.33	-0.18
PC7	3.31	-0.01	0.06	-0.29	-0.16	-0.04	0.93	0.10	0.03	-0.08
PC8	2.89	0.00	0.02	0.08	0.96	0.00	0.17	0.20	-0.01	0.09
PC9	0.0									
P-BAND										
PC1	56.76	-0.80	-0.14	0.01	0.01	-0.45	-0.01	0.00	-0.35	0.12
PC2	10.92	-0.15	0.43	0.03	0.05	0.35	-0.02	-0.06	-0.50	-0.65
PC3	8.76	-0.03	0.70	0.03	-0.03	0.14	-0.06	-0.09	0.17	0.67
PC4	6.47	-0.04	0.46	-0.12	0.18	-0.44	0.13	-0.57	0.41	-0.18
PC5	5.65	-0.01	0.07	-0.82	0.26	-0.07	-0.35	0.36	0.06	-0.07
PC6	5.38	0.03	-0.30	-0.28	0.38	0.34	0.07	-0.62	-0.31	0.29
PC7	3.15	0.00	-0.04	0.02	-0.49	0.00	-0.79	-0.37	0.00	0.00
PC8	2.91	0.02	-0.01	0.49	0.72	-0.05	-0.48	0.10	0.07	-0.01
PC9	0.00									

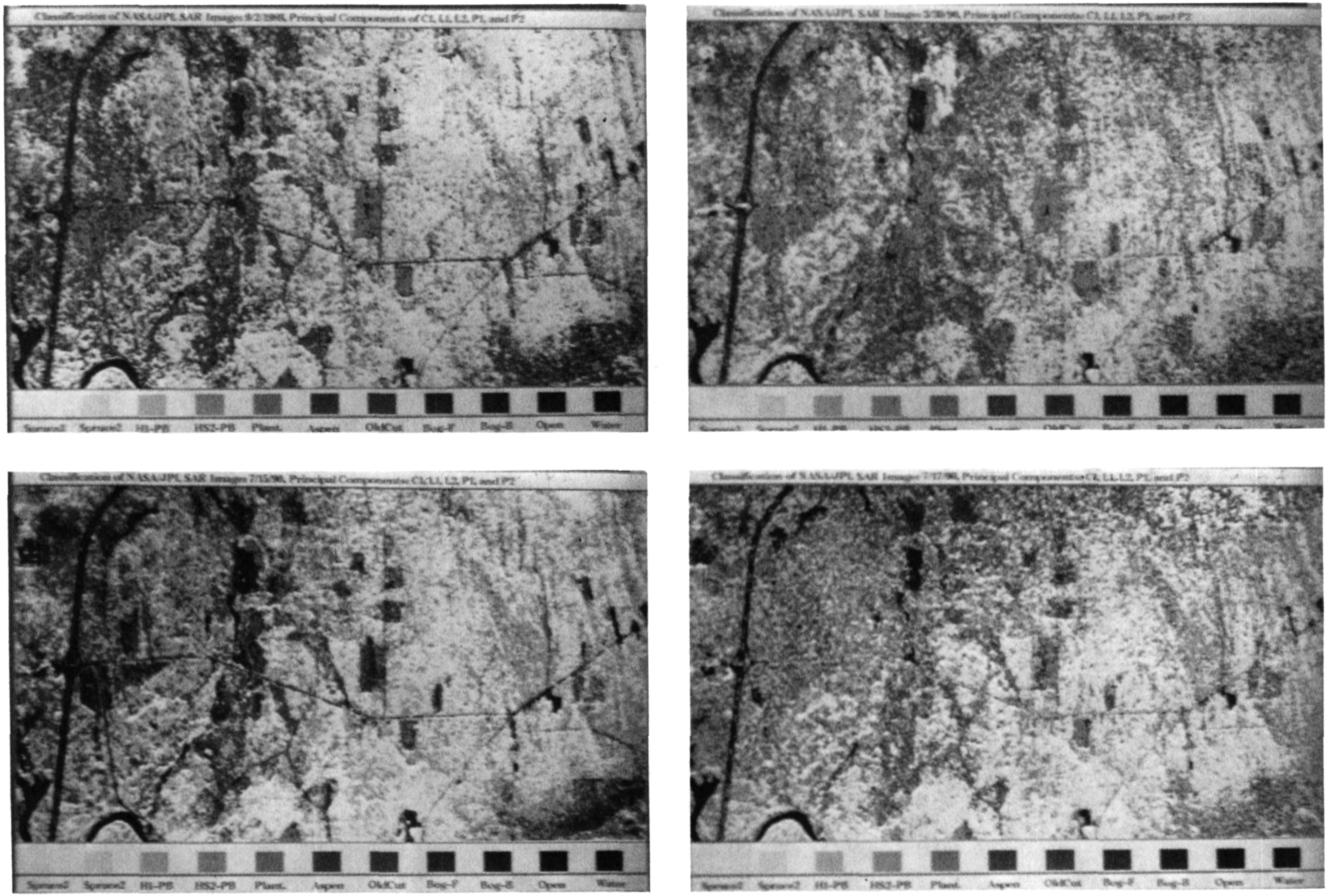

Figure 1. Classification of SAR images acquired at different times of the year: September 2, 1989 (upper left); March 30, 1990 (upper right); July 15, 1990 (lower left); and July 17, 1990 (lower right).

N92-28015

THE RELATIONSHIP BETWEEN ABOVEGROUND BIOMASS AND RADAR BACKSCATTER AS OBSERVED ON AIRBORNE SAR IMAGERY

Eric S. Kasischke
Laura L. Bourgeau-Chavez

Environmental Research Institute of Michigan
Ann Arbor, Michigan USA

Norman L. Christensen, Jr.
Duke University
Durham, North Carolina USA

M. Craig Dobson
The University of Michigan
Ann Arbor, Michigan USA

ABSTRACT

The initial results of an experiment to examine the dependence of radar image intensity on total aboveground biomass in a southern U.S. pine forest ecosystem are presented. Two sets of data are discussed. First, we examine two L-band (VV-polarization) data sets which were collected 5 years apart. These data sets clearly illustrate the change in backscatter resulting from the growth of a young pine stand. Second, we examine the dependence between radar backscatter and biomass as a function of radar frequency using data from the JPL AIRSAR and ERIM/NADC P-3 SAR Systems. These results show that there is a positive correlation between aboveground biomass and radar backscatter and at C, L and P-bands, but very little correlation at C-band. The biomass level for which this positive correlation holds decreases as radar frequency increases. This positive correlation is stronger at HH and HV polarizations than VV polarization at L- and P-bands, but strongest at VV polarization for C-band.

I. INTRODUCTION

NASA's Earth Observing System (EOS) is spurring a new series of research programs to continue the development of techniques to examine terrestrial ecosystems using remotely sensed data. Several EOS sensors represent technologies heretofore unavailable to the ecological community. Specifically, the information available from the High Resolution Imaging Spectrometer (HIRIS) and the Synthetic Aperture Radar (SAR) offer significant new opportunities for plant community and ecosystem analysis [1]. However, in utilization of these new sensors, scientists must not only be able to relate the remotely sensed signature to a specific biophysical property of a plant canopy, they must also develop new hierarchical techniques to utilize the remotely derived parameters in ecosystem models [2].

In this paper, we will focus our attention on the additional capabilities provided by multifrequency SAR systems. A detailed review of a wide number of potential uses for SAR in terrestrial ecosystem analysis is presented in refs [1,3]. In this paper, we specifically address the relationship between aboveground biomass in pine forests and radar image intensity.

There have been several studies performed which have demonstrated a significant correlation between radar image intensity and forest characteristics such as tree height, diameter and overall biomass level [4-7]. These studies preceded the development of several theoretically based models which predict radar scattering based upon the distribution of biomass characteristics within a tree canopy [8-10].

The development of these theoretical models has corresponded to the availability of a new class of airborne, multifrequency, polarimetric SARs such as those produced by JPL (the DC-8 C, L and P-band SAR) and ERIM (the P-3 X, C and L-band SAR). These new SARs have allowed for the planning and development of experiments specifically designed to investigate the causes of radar scattering from terrestrial ecosystems, which in turn are intended to develop the understanding needed for prediction of specific forest ecosystem parameters using SAR data. In this paper we will describe one such experiment and present some initial results from this investigation.

II. THE DUKE FOREST RADAR EXPERIMENT

In April of 1984, the CCRS/ERIM CV-580 SAR System collected a limited amount of multifrequency SAR data over the Duke University Forest, located west of Durham, NC (36 ° 00' N Latitude, 79 ° 00' W Longitude). A limited analysis of this data set revealed that there were correlations between biomass characteristics of the forest stands (e.g., height, diameter, stem density) and radar image intensity [5]. This abbreviated analysis led to a broader, long-term series of experiments to understand the relationship between biomass in loblolly pine forests and microwave scattering. While the ultimate goal of these experiments is to develop algorithms to estimate aboveground biomass in southern pines, in an inner-connected fashion these experiments are addressing a wide range of issues which need to be resolved before a set of generalized algorithms can be developed. Thus, theoretical modeling of microwave interactions with the pine forest canopies and development of techniques to provide SAR-derived inputs into forest ecosystem process models are both an important aspect of this experiment.

The Duke University Forest test site is being used to support experiments for ERS-1, SIR-C/X-SAR, and the EOS SAR Facility Instrument Team, in addition to the basic research being performed for NASA Headquarters. In support of all these experiments, a considerable amount of data are being collected and analyzed. These include:

AIRBORNE SAR DATA - In addition to the X, C and L-band data sets collected in 1984, three additional airborne SAR data sets have been collected. On 28 February 1989, an X, C and L-band, polarimetric data set was collected by the P-3 SAR System. This system also collected a data set on 31 August 1989. On 2 and 3 September, a C, L and P-band, polarimetric SAR data set was collected by the NASA DC-8 SAR System. In order to provide calibration for the SAR data, trihedral corner reflectors and active radar calibrators were deployed during each SAR overflight.

HELICOPTER SCATTEROMETER DATA - In order to develop a better understanding of the principal microwave scattering mechanisms from the loblolly pine forests, an X, C and L-band, multipolarization scatterometer data set was collected over a selected set of stands on 30 and 31 July and 1 August 1989.

DIELECTRIC MEASUREMENTS - Previous experiments have clearly shown that variations in the moisture properties of the tree boles and canopies and litter/soil layer play an important role in microwave scattering from forest canopies [11,12]. Thus, a series of dielectric measurements at X, C and L-bands were collected. These measurements include seasonal measurements of the dielectric constants of the following canopy constituents: trunk xylem, trunk phloem, soil layer, humus layer and litter layer. In addition, a set of diurnal measurements of the trunk phloem layer were also collected.

STAND GEOMETRY - Within the entire Duke University Forest, some 100 stands of loblolly pine, mixed pine/deciduous, and mixed deciduous have been sampled to determine overall species composition and structure of the forest canopy. The age of these stands ranges from 2 years to > 100 years. The aboveground biomass range of these stands is from 0.1 kg/m^2 to >50 kg/m^2. For stands with an average diameter at basal height (dbh) greater than 10 cm, the species composition and structure were sampled in ten 100 m^2 circular plots. These plots were located in a stratified random fashion to ensure complete spatial coverage within each stand. Within each plot, each tree was identified and classified into 5 cm dbh classes. The average height to the top and bottom of the canopy was estimated using a clinometer. For stands with an average diameter of less than 10 cm, a point-quarter sampling methodology was used. Ten center points were randomly located along a 100 m transect, and four quadrants defined by each major compass heading (i.e., north, south, east and west). Samples of distance to the tree from the center point, tree height, basal diameter, and height to the first branch were then obtained for the nearest stem greater than 1 m in height in each quadrant. To determine branch biomass and geometry, several techniques were utilized. For trees less than 10 m in height, several individual trees were felled, the number of total branches and whorls counted, the distances between whorls measured, angles and lengths of a subsample of branches measured, and wet and dry weights of the tree trunk, branches and needles obtained. Thus, a biomass profile of an average tree can be reconstructed, as well as total biomass per tree estimated. For larger trees, a combination of direct and indirect techniques were utilized. First, photographs of individual trees were taken in order to determine the relationship between dbh and number of branches, and branching angles. The total biomass of the various crown components for the larger trees were estimated using allometric equations developed for loblolly pines (Burkhart et al, 1972; Kinerson et al., 1974; Peet and Christensen, 1987).

III. COMPARISON OF 1984 AND 1989 L-BAND SAR DATA

In Figure 1, we present two L-band (VV-polarization) SAR images collected in the spring of 1984 and 1989. Also presented is a ground-truth map of five major sites of interest within the scene: (1) a grass field; (2-3) two stands which were cut and planted with loblolly pines in 1981; (4) one stand which was cut and planted with loblolly pines in 1983; and (5) a mature loblolly pine stand, 40 years in age. The bright points in the grass field are trihedral corner reflectors used to calibrate the images.

Included in Figure 1 are surface images of one of the pine stands planted in 1981. The pictures show the same general area, and illustrate the growth typical of loblolly pines during their establishment phase. While the density of the trees remained fairly constant over the 5 years between SAR images, the basal diameter increased from 1 to 8 cm, the height increased from 1 to 5 m, and the biomass increased from 0.2 kg/m^2 to 3 kg/m^2.

The SAR estimated radar scattering coefficient (σ^o) values for the bare field were -16.3 dB in the 1984 image and the -15.2 dB in the 1989 image. The characteristics of the field had changed somewhat between the two dates. First, the soil moisture was higher in 1984 due to rain the previous day. Thus, one would expect a slightly higher radar signature in 1984 due to moisture variations. However, the herbaceous vegetation present on the field was much higher in 1989 than in 1984, which may have resulted in a higher radar signature for the 1989 image. Based on these two factors, it is not unreasonable to expect the intensity from these two dates to be approximately equal. The 1.1 dB difference between the dates is very close to the absolute calibration accuracy for these data sets, which is estimated to be 1.5 dB.

The loblolly pine stand planted in 1981 and illustrated in Figure 1 had a σ^o value of -13.4 dB in the 1984 image and -8.7 dB in the 1989 image. Thus, the 3.8 kg/m^2 increase in biomass between dates resulted in a 3.6 to 4.7 dB increase in radar image intensity (the former figure results from comparing the intensity of the pine fields versus the grass field on the two dates, while the latter comes from a direct comparison of the scattering coefficients between the two dates). Finally, Figure 1 presents a plot of the relationship between aboveground biomass and σ^o for a composite of the two data sets.

IV. ANALYSIS OF 1989 C, L and P-BAND SAR DATA

The results in this paper will focus on average radar scattering coefficient (σ^o) signatures extracted from 4-look JPL AIRSAR data set collected on 2 September 1989. These signatures were generated for 58 different loblolly pine stands within the Durham Division of the Duke Forest. Each signature represents an average of a minimum of 100 samples from the digital SAR image. Average radar image intensity values were converted to scattering coefficients by multiplying by calibration coefficients provided by A. Freeman of JPL.

The manner in which biomass changes in the study test stands is extremely critical in understanding how imaging radars can be used to study these characteristics. There are three principal tree characteristics which describe total aboveground biomass in loblolly pine forests: (1) overstory density; (2) diameter; and (3) height. Figure 2 presents the relationship of these three factors to biomass, plotted as a function of seven different stand age classes. The first age class (0 to 10 years) represents the establishment phase of the loblolly pine forest, when a dense canopy of pine seedlings establish themselves in open fields [15]. Note, the tree density is highest at this time, but the overall biomass is low because of the small diameter and height of the individual trees. After this establishment phase, loblolly pines undergo a thinning phase, where the overall density of trees decreases due to individual tree mortality as a result of competition. This thinning phase can last for 40 to 90 years, depending upon initial stocking density and local site conditions. However, it is during the first 10 years of this stage that the most significant increments occur with respect to tree characteristics and aboveground biomass levels. Note in Figure 2 that between the 0 to 10 and 10 to 20 year age classes there is dramatic decrease in tree density, but significant increases in tree height and diameter, resulting in the biomass increase. As the pine stands continue to age, there is a continuing decrease in the number of overstory pine trees, and increase in the average diameter. However, after ~40 to 50 years, tree height growth stabilizes. The net result is that average aboveground biomass begins to stabilize after ~40 years, with some stands experiencing a decrease in biomass and others an increase depending on tree mortality rates. This variation is clearly evident in the range of biomass levels found in the test stands older than 40 years in our study.

Figure 3 presents a plot of radar scattering coefficients as a function of aboveground biomass levels for the three radar frequencies. For the P and L-band data, we can see a general increase in σ^o associated with biomass increases for levels less than 20 kg/m^2, but any trends at C-band are very difficult to discern.

The evidence presented in the comparison of the 1984 and 1989 data set (Figure 1) suggests that imaging radars are sensitive to changes in biomass during the successional sequence. This observation was used to assist in the analysis of the data sets. Our data sets were constrained in the following fashion. Tree diameter is the one tree factor which consistently increases with age. When only those stands whose average diameter was less than 30 cm were considered, a positive correlation between σ^o and biomass for the P-band data sets was found (see Figure 3). When only those stands whose average diameter was less than 20 cm were considered, a positive correlation between σ^o and biomass for the L-band data sets was found (see Figure 4). Finally, when only those stands whose average diameter was less than 20 cm and whose biomass was less than 10 kg/m^2 were considered, positive correlations were found between σ^o in the C-VV channel and biomass.

V. DISCUSSION

Analysis of the imaging radar data sets collected over the Duke University Forest has shown that there is a clear relationship between aboveground biomass and σ^o for loblolly pine stands. The data show that as radar frequency decreases, the biomass level for which this relationship holds increases. These relationships are not valid, however, over all stand conditions as expressed in average tree density, diameter and height. The relationships only hold true for specific diameter classes at L- and P-bands (dbh < 20 cm at L-band and dbh <30 cm at P-band). Only the C-VV data showed sensitivity to changes in biomass, and only where dbh < 10 cm, and biomass < 10 kg/m^2.

While to some these conditions may seem to be restricting the use of SAR for monitoring biomass in forest ecosystems, we view the results to be highly encouraging, and of great help to determine when and where SAR systems are best utilized. There are large areas of forested landscapes which are routinely subjected to disturbance. A few examples are natural fire in boreal forests, logging in the Pacific Northwest region of the U.S. and Canada, and land clearing in the tropics. The successional regrowth of forests on these disturbed landscapes represent areas to which imaging radars could provide valuable information for ecosystem process models.

VI. ACKNOWLEDGEMENTS

The authors are very grateful to Dr. J. Way for her efforts in arranging the DC-8 AIRSAR overflights of the Duke University Forest. These overflights were in support of an EOS Simultaneity Experiment, and support was provided by NASA Grant Nos. NAGW-1101 to the University of Michigan and ERIM, and NAGW-1866 to Duke University. Funding to support the analysis of the data were provided by grants from NASA's Terrestrial Ecosystems Program, under the direction of Drs. D. Wickland and A. Janetos. These grants include Grants No. NASW-4360 to ERIM, NAGW-1339 to Duke University and NAGW-1367 to the University of Michigan. This research was also supported under the SIR-C program under grants, under the direction of Dr. M. Baltuck. These included Grants No. NAS7-918 under subcontracts from JPL to ERIM and Duke University.

REFERENCES

[1] Ustin, S.L., C.A. Wessman, B. Curtiss, E.S. Kasischke, J.B. Way and N. Vanderbilt. 1991. Opportunities for parameterization of ecosystem models using the Eos imaging spectrometer and synthetic aperture radar. **Ecology** (in press).

[2] Kasischke, E.S. and N. L. Christensen, Jr. 1990. Connecting forest ecosystem and microwave backscatter models. **Int. J. Remote Sens., 11.** pp. 1277-1298.

[3] Kasischke, E.S., J.B. Way, N.L. Christensen, M.C. Dobson and F.T. Ulaby. 1990. Ecosystem monitoring with the Eos SAR, **Proc. 10th IGARSS Symposium.** IEEE 90CH2825-8. College Park, MD. pp. 2297-2301.

[4] Riom, J. and T. Le Toan. 1981. Relations entre des types de forêts de pins maritimes et la rétrodiffusion radar en bande-L. **Digest of ISP, Spectral Signatures of Objects in Remote Sensing.** Avignon, France.

[5] Kasischke, E.S. and R.W. Larson, Calibrated X- and L-band Scattering Coefficients from a Southern U.S. Forest. 1986. **Proc. IGARSS' 86 Symposium.** Zurich, Switzerland. pp. 895-900.

[6] Wu, S-T. 1987. Potential Application of Multipolarization SAR for Pine-Plantation Biomass Estimation. **IEEE Trans. Geosci. Remote Sens., GE-25.** pp. 403-409.

[7] Hussin, Y.A., R.M Reich, and R.M. Hoffer. 1991. Estimating Slash Pine Biomass Using Radar Backscatter. **IEEE Trans. Geosci. Remote Sens., GE-29.** pp. 427-431.

[8] Richards, J.A., G-Q. Sun and D.S. Simonett. 1987. L-band Radar Backscatter Modeling of Forest Stands. **IEEE Trans. Geosci. Remote Sens., 25.** pp. 487-498.

[9] Sun, G-Q. and D.S. Simonett. 1988. Simulation of L-band HH Microwave Backscattering from Coniferous Forest Stands: A Comparison with SIR-B Data. **Photogrammetric Eng. and Remote Sensing, 54.** pp. 1195-1201.

[10] Ulaby, F.T., K. McDonald, K. Sarabandi, M. Whitt and M.C. Dobson. 1990. Michigan Microwave Canopy Scattering Model (MIMICS). **International Journal of Remote Sensing, 11.** pp. 1233-1253.

[11] Way, J.B., J. Paris, E. Kasischke, C. Slaughter, L. Viereck, N. Christensen, M.C. Dobson, F.T. Ulaby, J. Richards, A. Milne, A. Sieber, F.J. Ahern, D. Simonett, R. Hoffer, M. Imhoff, and J. Weber. 1990. The Effect of Changing Environmental Conditions on Microwave Signatures of Forest Ecosystems. **Int. J. Remote Sensing, 11.** pp. 1119-1144.

[12] MacDonald, K.C., M.C. Dobson, and F.T. Ulaby. 1990. Using MIMICS to Model L-band Multiangle and Multitemporal Backscatter from a Walnut Orchard. **IEEE Trans. Geosci. Remote Sens., GE-28.** pp. 477-491.

[13] Burkhart, H.F., R.C. Parker, and R.G. Oderwald. 1972. Yields for Natural Stands of Loblolly Pine. **U.S.F.W.S. Publication FWS-2-72.** 13 pp.

[14] Kinerson, R.S., K.O. Higginbotham and R.C. Chapman. 1974. The Dynamics of Foliage Distribution within a Forest Canopy. **J. Appl. Ecol., 11.** pp. 347-353.

[15] Peet, R.K. and N.L. Christensen. 1987. Competition and Tree Death. **Bioscience, 37.** pp. 586-599.

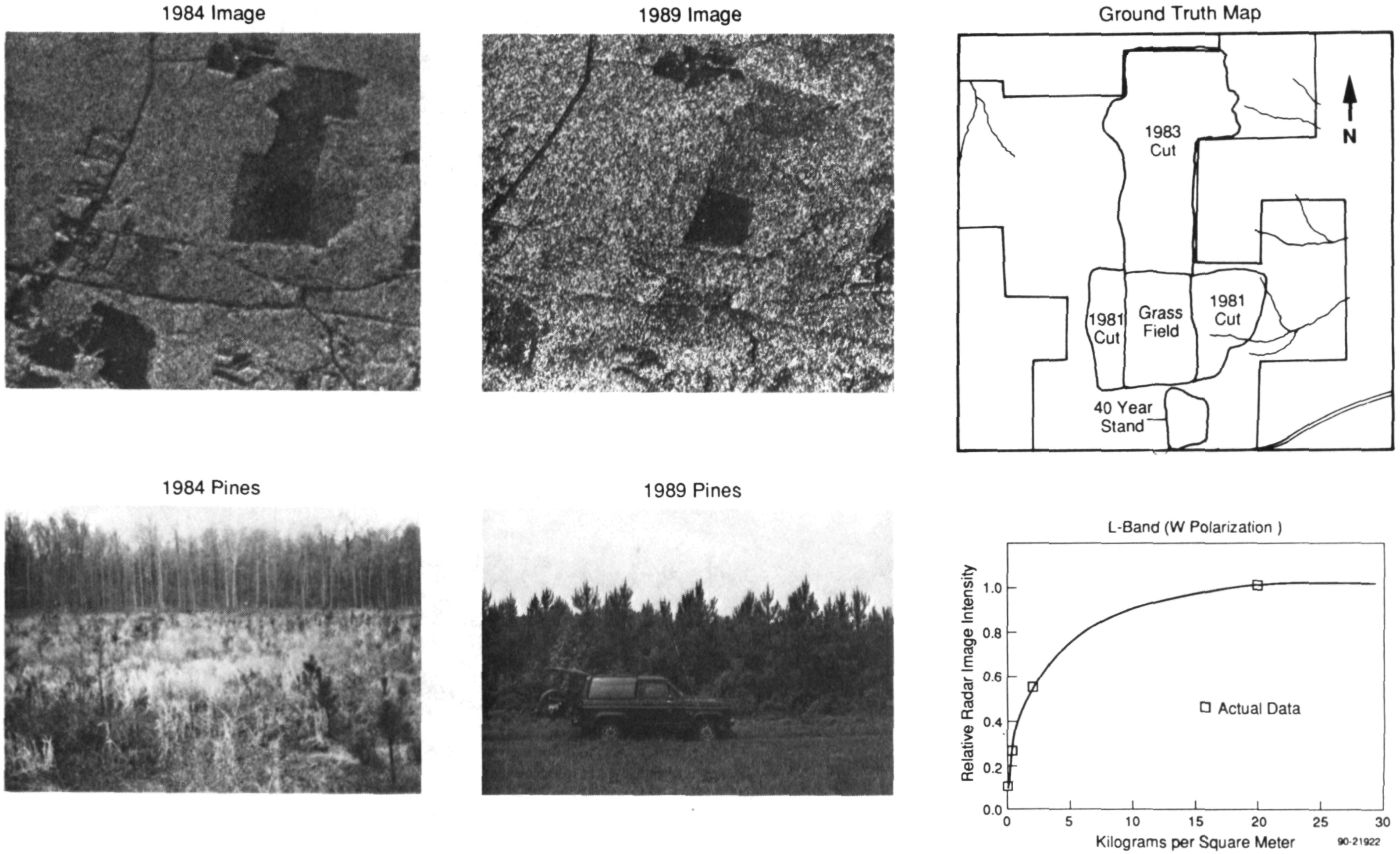

Figure 1. L-band SAR Images of an Immature Loblolly Pine Stand, Collected in 1984 and 1989 Illustrating Change in Image Intensity Associated with Tree Growth

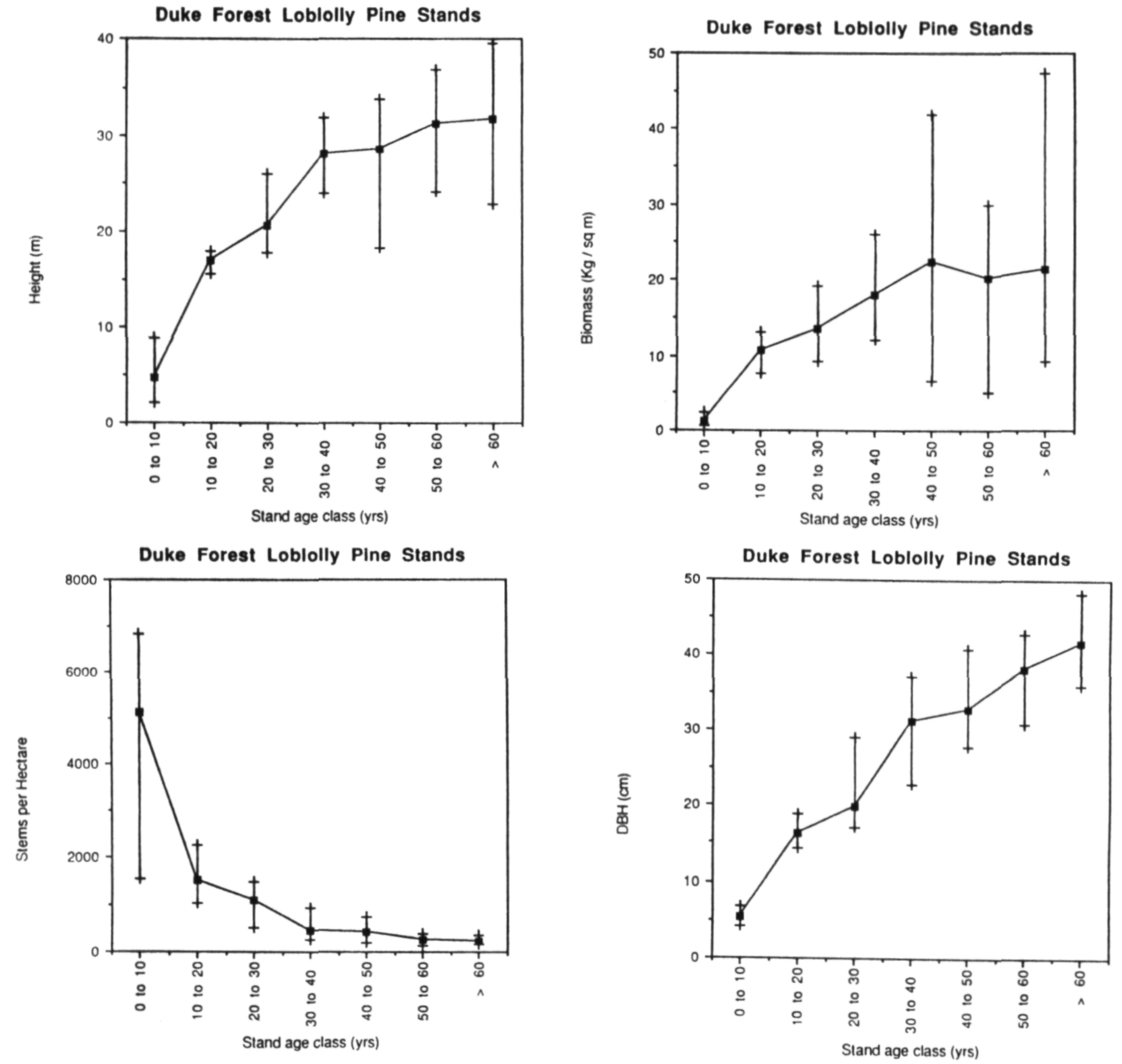

Figure 2. **Variation in Tree Density, Diameter, Height and Biomass as Function of Stand Age for the Loblolly Pine Test Sites Used in this Study**

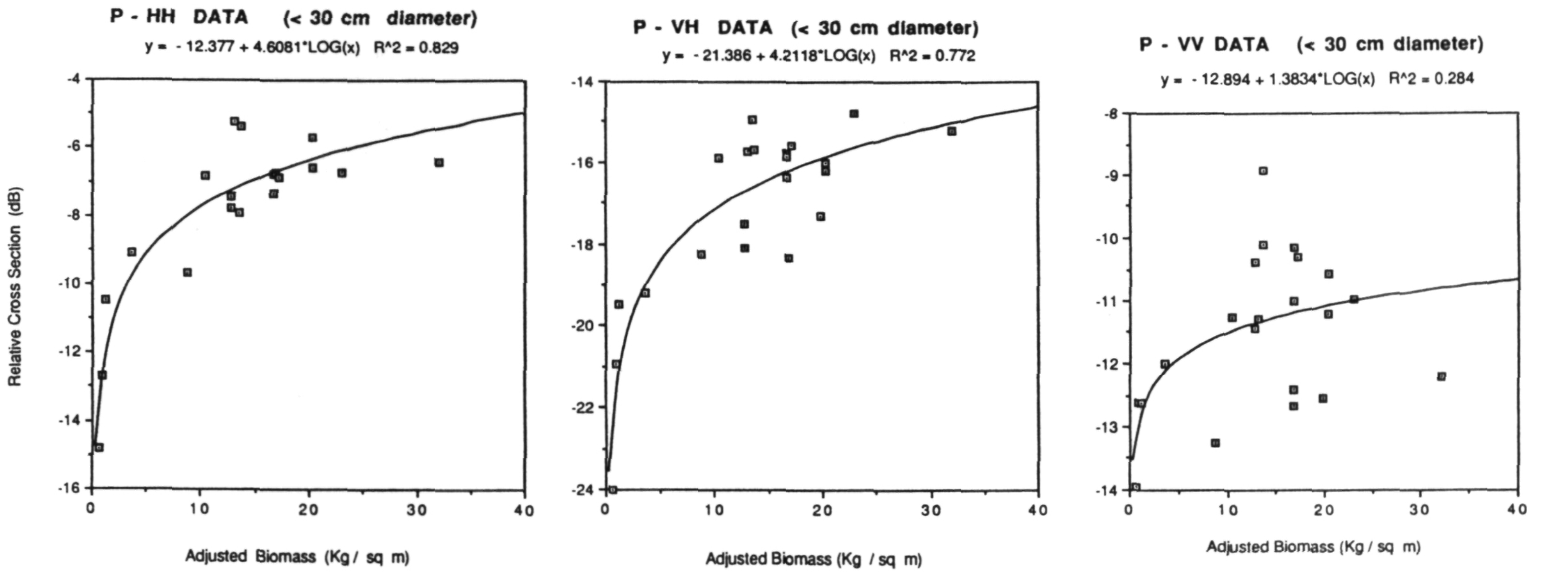

Figure 3. The Relationship Between P-band σ^o and Aboveground Biomass for Stands with an Average Diameter Less than 30 cm

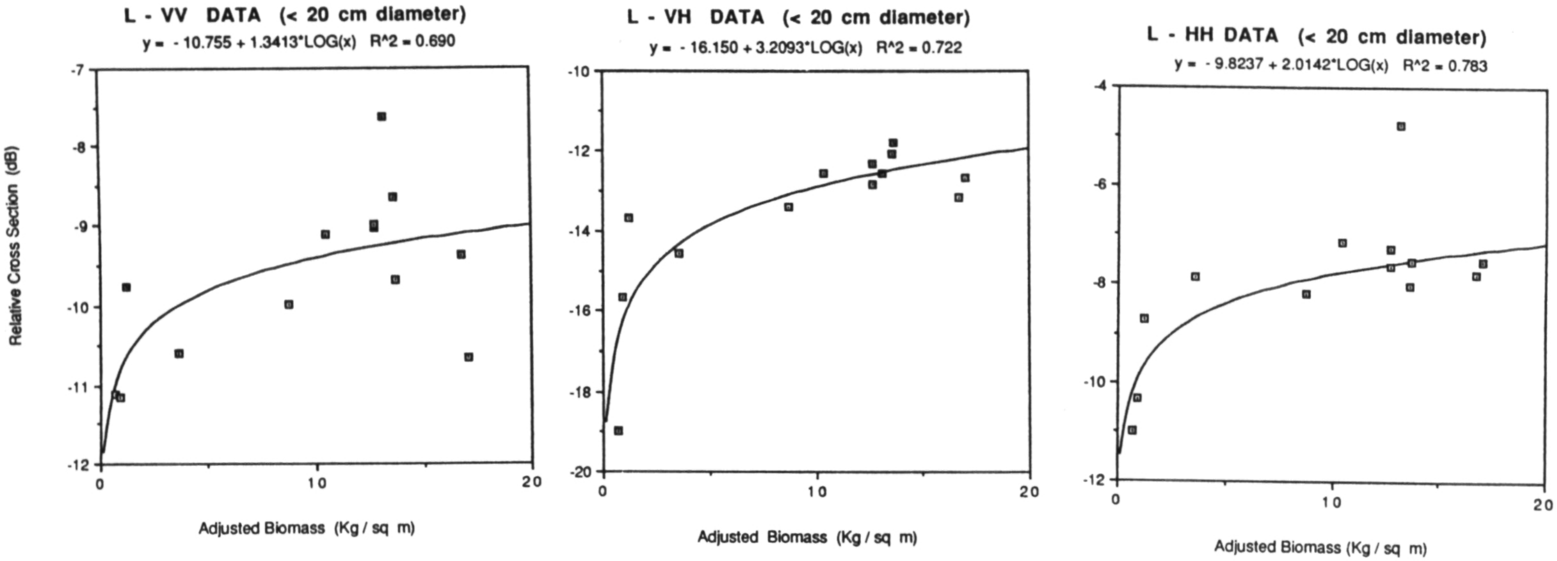

Figure 4. The Relationship Between L-band σ^o and Aboveground Biomass for Stands with an Average Diameter Less than 20 cm

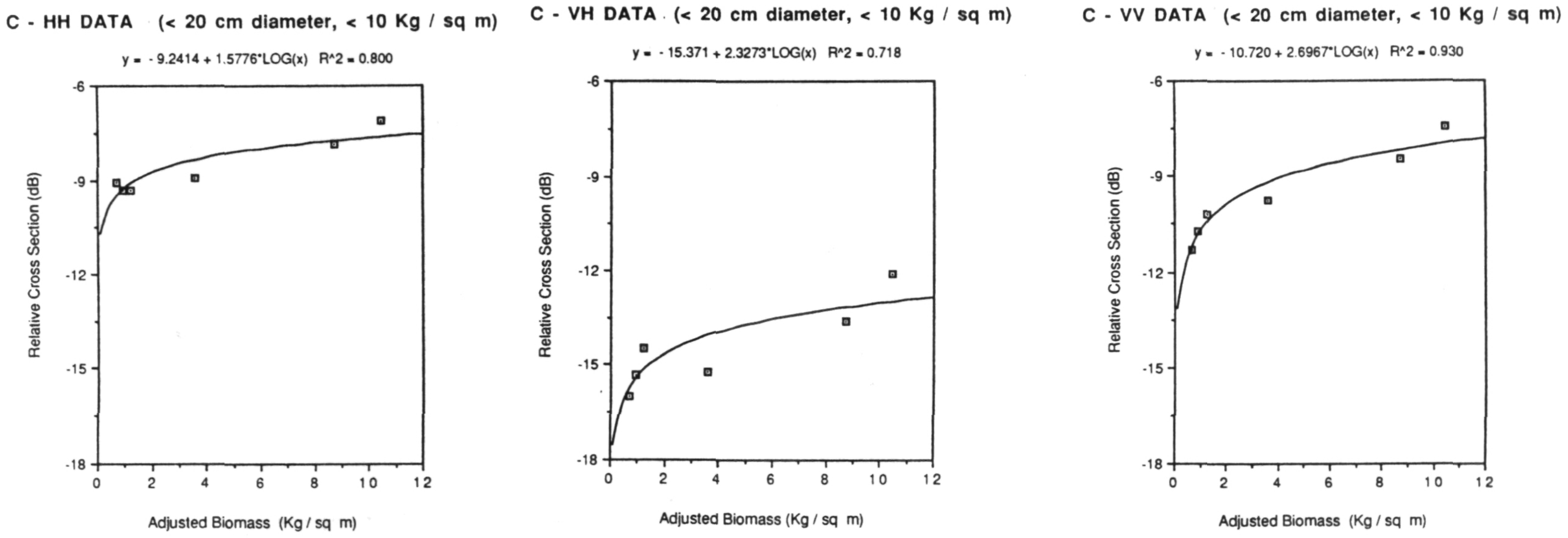

Figure 5. The Relationship Between C-band σ^o and Aboveground Biomass for Stands with an Average Diameter Less than 20 cm and Aboveground Biomass Less than 10 kg/m^2

N92-28016

ANALYSIS OF POLARIMETRIC SAR SIGNATURES OF VEGETATED AREAS

Nancy H.F. French
Laura L. Bourgeau-Chavez
Eric S. Kasischke
Daniel R. Sheen

Environmental Research Institute of Michigan
Ann Arbor, Michigan USA

ABSTRACT

Several techniques to quantitatively analyze the information in the polarimetric signature are discussed, including: (1) a shape (texture) parameter, (2) fractional polarization; (3) the phase difference signature; and (4) the correlation coefficient. These techniques are applied to airborne SAR imagery collected over several different vegetation communities, including a mangrove swamp, a mixed-age loblolly pine forest, and a flooded bald cypress forest.

I. INTRODUCTION

Much attention has been devoted to deriving and analyzing signatures generated by combining the information present in the four linearly-polarized channels collected by many imaging radar systems. Within the geoscience community, this analysis has primarily focused on interpretation of three-dimensional plots generated using the scattering or Stokes matrix (Figure 1) [1-4] or classification of information present in phase-difference images (Figure 2). In order to fully utilize the information present in polarimetric radar data, techniques to quantitatively analyze these data must be derived. In this paper we discuss several different analysis tools, and present results of their application to airborne SAR data collected over vegetated regions.

II. POLARIMETRIC SIGNATURES

The technique of deriving a synthetic polarimetric signature from imaging radar data was introduced by Zebker [1] and van Zyl [2] in 1987. The three-dimensional polarimetric signature plot in Figure 1 is a graphic representation of the Stokes matrix computed from the full scattering matrix, **S**, where

$$\mathbf{S} = \begin{bmatrix} S_{hh} & S_{vh} \\ S_{hv} & S_{vv} \end{bmatrix}, \tag{1}$$

Each element of the scattering matrix is the complex backscatter value from a given polarization channel and is measured from a fully-calibrated SAR image. The Stokes matrix is computed directly from the scattering matrix and consequently contains all information about the scattering characteristics of a point for all transmit and receive polarization combinations. Knowledge of the Stokes matrix for each scatterer in a SAR scene allows computation of both intensity and phase of the backscattered energy at any transmit and receive polarization combination. The polarimetric signature plot generated from the Stokes matrix shows the normalized radar cross section, σ^o , of the measured scatterer at all combinations of ϵ , the ellipticity angle, and τ , the orientation angle or tilt of the polarization ellipse [1]. Generally the polarization signature plots represent either the co-polarized case, with the transmit and receive antennas oriented the same way, or the cross-polarized case, with the antennas oriented at a 90 ° angle to each other.

Even without quantitative evaluation of the Stokes matrix, the polarization signatures of two regions can be visually compared for similarities and differences. For example, the polarization signatures in Figure 1 show that the response from black mangroves (top) is different from the response from red mangroves (bottom).

The polarization signature, or more specifically the Stokes matrix, can also be analyzed mathematically to extract both intensity and phase information of the measured scatterer at any polarization desired. The measurements for our study of vegetation signatures have been divided into two categories, intensity and phase, and are described in the following sections.

III. INTENSITY SIGNATURES

Several different measurements derived from the intensity of an area of interest in the radar scene can be calculated from the Stokes matrix. These include: (1) the radar cross section of the area for a specific linear polarization, σ^o ; (2) the minimum radar cross section for all polarization combinations, σ^o_{min} ; (3) the maximum radar cross section for all polarization combinations, σ^o_{max} ; (4) the fractional polarization, FP, which is an indication of the amount of unpolarized return from the scattering scene; and (5) the shape parameter, α , which gives information on the texture of the area. In this paper, we discuss σ^o, FP, and α .

III.A. Radar Cross Section, σ^o

The radar cross section represents the mean intensity of the backscatter from an area in an image. The intensity of each pixel in a region is measured directly from the calibrated complex image with each polarization channel measured independently. The mean intensity of the region is computed to obtain the radar cross section of the region.

III.B. Fractional Polarization (FP)

Fractional Polarization (FP) is an indicator of change in polarization which occurs between the transmitted and received microwave energy within a SAR scene, and is a means to quantitatively compare the like and cross-polarized channels. It is computed after [7] as

$$FP = \frac{\sigma^o_{max} - \sigma^o_{min}}{\sigma^o_{max} + \sigma^o_{min}} . \qquad (2)$$

When no depolarization occurs, $\sigma^o_{min} = 0$, and FP = 1. When maximum depolarization occurs, $\sigma^o_{min} \rightarrow \sigma^o_{max}$, and FP $\rightarrow 0$.

For comparison purposes, an additional fractional polarization was calculated (FP_1) based on the linear channels of the SAR, with σ^o_{max} equal to the larger value of the HH and VV channel, and σ^o_{min} equal to either the HV or VH channel.

III.C. Shape parameter, α

The shape parameter is a measurement of the variation in the radar cross section within a clutter type, and provides a quantitative measure of the texture of the area of interest. Shape parameters describe the statistical distribution of the intensity values within the scene, and a variety have been derived [5]. In this study, we used a shape parameter, α, based on the K-distribution [6], which can be computed for each linearly-polarized channel as:

$$\alpha = \frac{m^2}{\text{var}}, \tag{3}$$

where m is the mean radar cross section and var is the variance of the mean. When $\alpha = 1$, the variance is equal to the mean intensity squared, which is the case when there is no variation in intensity other than ideal, Rayleigh distributed speckle. With more texture in the scene, the variance increases compared to the mean, and α decreases.

IV. PHASE SIGNATURES

Two different phase signatures were analyzed: the polarization phase difference, $\Delta\Theta$, and the correlation coefficient, ρ.

IV.A. Polarization Phase Difference Signature, $\Delta\Theta$

The polarization phase difference, $\Delta\Theta$, is computed by finding the difference in phase between the HH-polarized and VV-polarized signals [8]

$$\Delta\Theta = \Theta_{hh} - \Theta_{vv}, \tag{4}$$

where Θ is computed from the complex σ^o value of a pixel measured from a calibrated SAR image. Phase differences are usually expressed in degrees ranging from -180° to +180°. It is important to note that the relative phase difference between the two polarization cases is being computed, not the absolute phase of the backscatter.

The difference between the phases of the HH and VV images provide insight into the primary scattering mechanisms of the target of interest. Single bounce and odd bounce scatterers produce no phase differences, but double bounce scatterers, such as dihedral reflectors, create a phase difference of 180°. Thus, classification techniques have been developed which use the phase difference information to discern the primary scattering mechanisms of a target [9].

Figures 2 and 3 present images which were generated using color to represent the HH-VV phase difference. The brightness of the images represents the intensity of the HH polarization. In these images, 0° phase is indicated by blue, and +180° and -180° by red. Figure 2 is a C-band image of a region which contains mangrove stands. The pink-colored stands in this image represent areas where flooding has occured, and have an average phase shift of 50° to 80°. Figure 3 consists of C- and L-band data collected over a flooded bald cypress forest. The red (flooded) areas in these images have an average phase shift of -120° to -150°.

Distribution plots, as illustrated in Figure 4, have typically been used to quantitatively examine the phase differences of an area [8]. Phase distibutions with a distinct peak at the mean are significant, while those whose distributions are more evenly spread out have no significant phase shift. The standard deviation of the mean phase has been used by some investigators to estimate the significance of the phase difference [7,8]. However, the standard deviation of the phase difference does not always characterize this significance. This is illustrated in Figure 4, where a comparison can be made between a signature with a strong peak (region 4) and a standard deviation of 91.5, and a signature lacking a distinct peak (region G) but having a smaller standard deviation of 44.7. As discussed in the next section, the correlation coefficient, ρ, seems to represent a better means for assessing the significance of a phase shift.

IV.B Correlation Coefficient, ρ

The correlation coefficient, ρ, is computed by:

$$\rho = \frac{<S_{hh}S_{vv}^{*}>}{(<S_{hh}S_{hh}^{*}><S_{vv}S_{vv}^{*}>)^{1/2}} , \qquad (5)$$

where <x> refers to the expected value of a variable, x, the * denotes the complex conjugate, and S_{vv} and S_{hh} are the complex backscatter values at VV and HH polarizations, respectively. If S_{hh} and S_{vv} are independent with zero mean, $\rho = 0$. If $S_{hh} = cS_{vv}$, where c is a constant, then $\rho = 1$. So, when $\rho = 0$, S_{hh} and S_{vv} are uncorrelated; when $\rho = 1$, S_{hh} and S_{vv} are perfectly correlated.

The strength of the correlation between the HH and VV channels is a good indicator of the significance of the phase shift. The plots in Figure 4 clearly show that as ρ increases, the peak around the average phase shift becomes more distinct. By comparing both the discreteness of the peak around the mean and ρ to the appearance of the area on a color phase shift image, we have concluded that phase shifts with a $\rho > .13$ are significant.

V. DATA SETS

The data sets used in this analysis were collected by the P-3 SAR System [10]. Data from two areas have been selected for analysis: (1) an area which contains mangrove vegetation, located on Boca Chica Key, Florida, which was imaged in September of 1989; and (2) an area containing mixed-age stands of loblolly pine and a flooded bald cypress stand, located near Durham, North Carolina, which was imaged in February and August of 1989. Calibrated trihedral corner reflectors were present in each scene. The SAR signal histories recorded by the P-3 SAR System were digitally processed into imagery, and calibrated utilizing the corner reflectors and standard techniques [11].

For the Florida study site, data were examined for the C and L-band channels. Signatures were generated using a minimum of 100 pixels for two different black mangrove stands and two red mangrove stands, including one mature stand and one stand that had been cut, whose shoots were only 30 to 60 cm tall. In coastal Florida waters, red mangrove grows in tidally inundated sites, while black mangrove grows in higher sites that only flood during extremely high tides. During the SAR overflights, only the red mangrove stands contained standing water at the base of the canopy.

For the North Carolina study site, data were examined for the X, C and L-band channels of the SAR. Signatures were generated using a minumum of 100 pixels for the cypress stand, for three different loblolly pine stands (ages 5, 15 and 55 years), a mixed oak/loblolly pine stand, and a mixed hardwood/oak stand. All stands were imaged at approximately the same incidence angle ($42^\circ \pm 2^\circ$) on each date.

V. RESULTS

Table 1 summarizes the statistics generated for the Florida mangrove test sites. While it is not possible to delve deeply into all possible observations in this paper, we will make a few. First, with respect to σ^o measurements, it appears that L-band is more suitable for discriminating the various mangrove stands than C-band, with the exception of the C-VV channel. For these stands, the fractional polarization signature does appear to have potential as an additional discriminator. It appears that the signature based on using only the linearly polarized signature (FP_1) works equally as well (if not better) than the signature based on the Stokes matrix data. Using the shape parameter, it appears that the L-band data contains more image texture than the C-band data, especially the L-HH channel. At C-band, all the phase difference signatures were felt to be significant, while at L-band only the black mangrove stands have a significant phase shift. It is felt that the phase shifts seen in the red and cut mangrove stands are the result of an enhancement of the ground-trunk, two-bounce scattering within the scene.

Table 2 summarizes the polarimetric statistics generated for the North Carolina forest stands. Another paper in this proceedings [12] discusses the information content of radar backscatter with respect to changes in loblolly pine biomass. We would like to make the following additional observations. The flooded bald cypress stands were clearly distinguishable for all radar frequencies for the winter data set, but only distinguishable on the L-band imagery for the summer data set. With the fractional polarization measurement, significant variations were noted in the X-band (winter), and L-band (winter and summer) data sets. L-band data seem to exhibit the most pronounced depolarization in the intensity images. At X and C-bands, there does appear to be some textural information in the intensity signatures which warrants further study. Finally, all the phase shift signatures appear to be significant for the North Carolina forest stands, based upon the correlation coefficient. At all frequencies, the flooded bald cypress stand resulted in a dramatically different phase signature than the other stands in the winter data set, again due to the enhancement of the ground-trunk scattering at the forest floor. This enhanced scattering is present in the summer data set at L-band. Another observation which can be made at X- and C-bands is that a distinct phase shift occurs between the winter and summer data sets. Because in-scene corner reflectors were used to provide the calibration, it is extremely unlikely that these shifts are due to calibration errors. The potential source of these phase shifts are: (1) the presence of leaves or increased needle biomass in the summer; (2) the higher moisture content of the soil layer in the winter; or (3) the presence of moisture in the canopy overstory due to precipitation on the day of the overflights in the winter.

VI. DISCUSSION

In this study, several techniques to quantify the information present in polarimetric SAR signatures were explored. The use of a fractional polarization measure (FP) on data derived from the Stokes matrix does not appear to provide more information than the same measure derived from the linearly-polarized signatures. There does appear to be significant information present in the textural measure (α) used in this analysis.

The correlation coefficient, ρ, is a potential means to measure the significance of the phase shift, $\Delta\ \Theta$, estimated from the polarimetric data. Significant phase shifts were found for several different vegetation classes at all three radar frequencies investigated (X, C, and L-bands). In some cases, the phase shifts observed at higher radar frequencies were more significant than those observed at lower frequencies for the same test site. The higher radar frequencies (X and C-bands) seemed to be exhibiting a variation in $\Delta\ \Theta$ related to some temporal variation in the vegetation canopy, something which has not been observed previously.

The results presented in this paper represent the initial observations of a longer-term study. This study's objectives are to address three basic questions: (1) WHAT polarimetric signatures are present in SAR imagery collected over vegetated areas? (2) WHY are these signatures present? and (3) HOW do we use this information in ecosystem process studies? The results of this study have demonstrated there are definitely unique signatures within the polarimetric SAR data collected over vegetated sites. There is still considerable research to be conducted on the questions of why we are seeing these signatures and how they are used in ecosystem process models.

VII. ACKNOWLEDGEMENTS

The research presented in this paper was supported by the National Aeronautical and Space Administration (NASA) through a variety of research grants, including NASW-4360 with NASA Headquarters, NAS7-918 via Contract No. 958448 with the Jet Propulsion Laboratory, and NASA-30747 with the Goddard Space Flight Center

VIII. REFERENCES

[1] Zebker, H. A., J. J. van Zyl, and D. N. Held. 1987. Imaging Radar Polarimetry From Wave Synthesis. **J. Geophys. Res. 92:B1.** pp. 683-701.

[2] van Zyl, J. J., H. A. Zebker, and C. Elachi. 1987. Imaging Radar Polarization Signatures: Theory and Observation. **Radio Science. 22:4**. pp. 529-543.

[3] Evans, D. L., T. G. Farr, J. J. van Zyl, H. A. Zebker. 1988. Radar Polarimetry: Analysis Tools and Applications. IEEE Trans. Geosci. Rem. Sen. **26:6**. pp. 774-789.

[4] Ulaby, F.T. and C. Elachi, 1990, **Radar Polarimetry for Geoscience Applications,** Artech House, Inc, Norwood, MA. 364. p.

[5] Kasischke, E.S., A.L. Maffett and R.W. Larson. 1987. Statistical Modeling of Speckle Distributions on Airborne SAR Imagery. **Proc. 1987 Inter. Geosci. Remote Sens. Symp.** Ann Arbor, MI. pp. 1357-1362.

[6] Sheen, D.R., E.S. Kasischke, L.P. Johnston and N.H.F. French, SAR-Derived Polarimetric Scattering Properties of Terrestrial Ecosystems. 1990. **Proc. 10th IGARSS Symposium.** IEEE 90CH2825-8. College Park, MD. pp. 1675-1678.

[7] Kwok, R. J. Way, E. Rignot, A. Freeman, and J. Holt. 1990. Polarization Signatures of Frozen and Thawed Forests of Varying Biomass. **Proc. IGARSS '90 Symposium.** pp. 337-340.

[8] Ulaby, F. T., D. Held, M. C. Dobson, K. C. McDonald, and T. B. A. Senior. 1987. Relating Polarization Phase Difference of SAR Signals to Scene Properties. **IEEE Trans. Geosci. Rem. Sen. GE-25:1**. pp. 83-92.

[9] van Zyl, J.J. 1989. Unsupervised Classification of Scattering Behavior Using Radar Polarimetry Data. **IEEE Trans. Geosci. Rem. Sen. GE-26.** pp. 36-45.

[10] Sullivan, R., A. Nichols, R. Rawson, C. Haney, F. Darreff, and J. Schanne, Jr. 1988. Polarimetric X/L/C-band SAR. **Proc. 1988 IEEE Radar Conf.** Ann Arbor, MI.

[11] Sheen, D.R., A. Freeman and E.S. Kasischke. 1989. Phase Calibration of Polarimetric Radar Images, **IEEE Trans. Geosci. Remote Sens., 27.** pp. 719-731.

[12] Kasischke, E.S., L.L. Bourgeau-Chavez, N.L. Christensen, Jr., and M.C. Dobson. 1991. Estimation of Aboveground Biomass Using Multiparameter SAR Data. **1991 JPL Airborne Remote Sensing Workshop (these proceedings).**

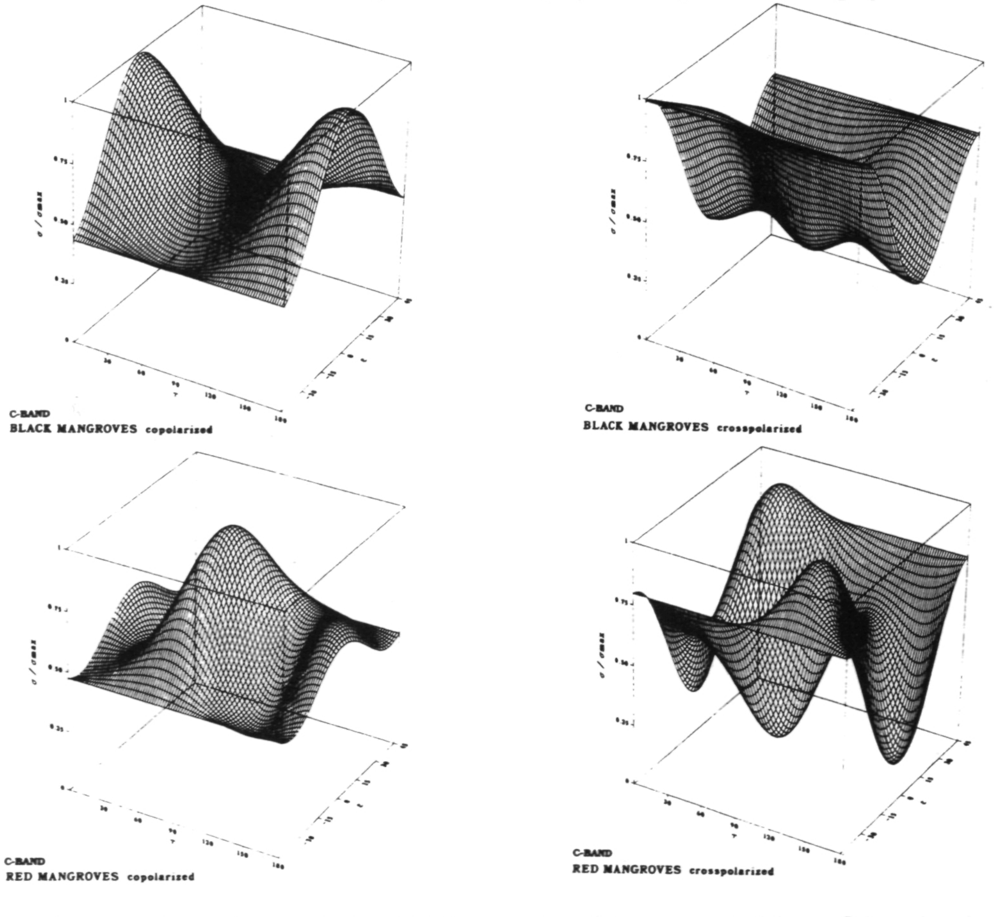

Figure 1. Like and co-polarized Stokes matrix plots generated from C-band polarimetric SAR images of red and black mangrove stands.

TABLE 1. SUMMARY OF POLARIMETRIC SIGNATURE STATISTICS FOR MANGROVE VEGETATION

VEGETATION TYPE	Mean RCS (dB) ($\sigma°$) HH	HV	VV	FP	FP_1	Shape Parameter (α) HH	HV	VV	ρ	$\Delta\Theta$
C-BAND										
Black mangrove 1	-8.9	-16.2	-11.2	.70	.69	.80	.82	.83	.42	-15.9
Black mangrove 2	-9.2	-15.5	-9.7	.64	.62	.80	.87	.94	.36	-11.4
Cut mangrove	-10.4	-14.2	-9.0	.64	.54	.77	.75	.77	.16	54.3
Red mangrove	-8.4	-16.6	-6.9	.88	.81	.90	.86	1.00	.31	80.0
L-BAND										
Black mangrove 1	-16.6	-16.3	-12.4	.67	.42	.79	.77	.84	.42	-15.4
Black mangrove 2	-13.8	-14.2	-10.7	.59	.38	.83	.74	.81	.23	-25.0
Cut mangrove	-19.0	-21.6	-16.3	.58	.54	.60	.74	.83	.03	32.6
Red mangrove	-16.1	-20.7	-13.2	.72	.70	.53	.46	.52	.06	103.4

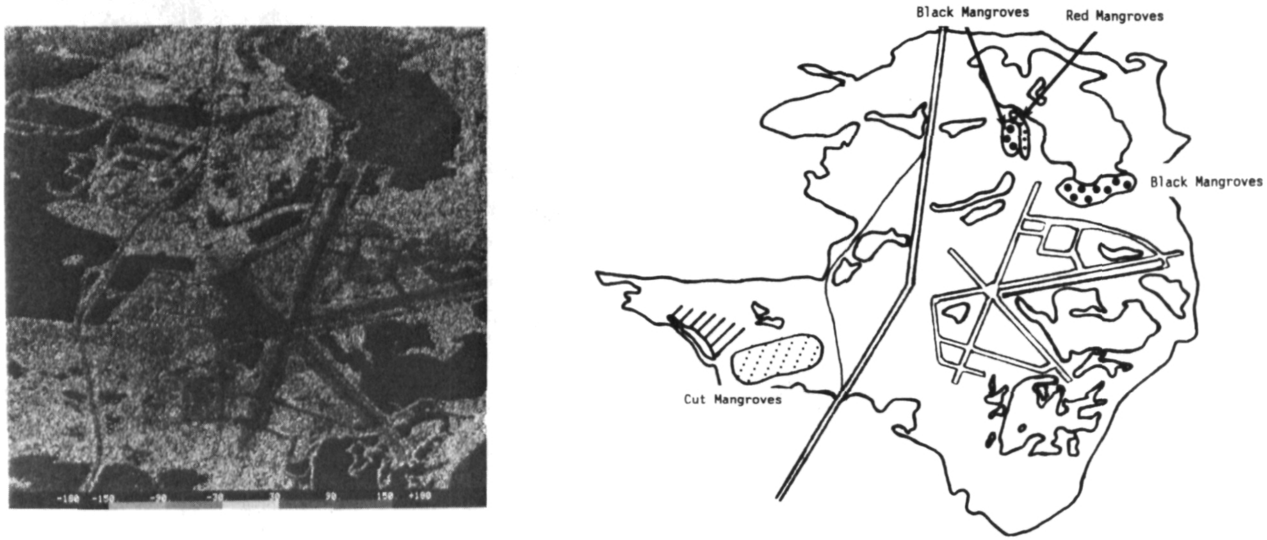

Figure 2. Example of a C-band SAR phase difference image of mangrove stands on Boca Chica Key, Florida: (a) black and white rendition of image (see slide no. 1); (b) map of location of stands used in this study.

ORIGINAL PAGE
BLACK AND WHITE PHOTOGRAPH

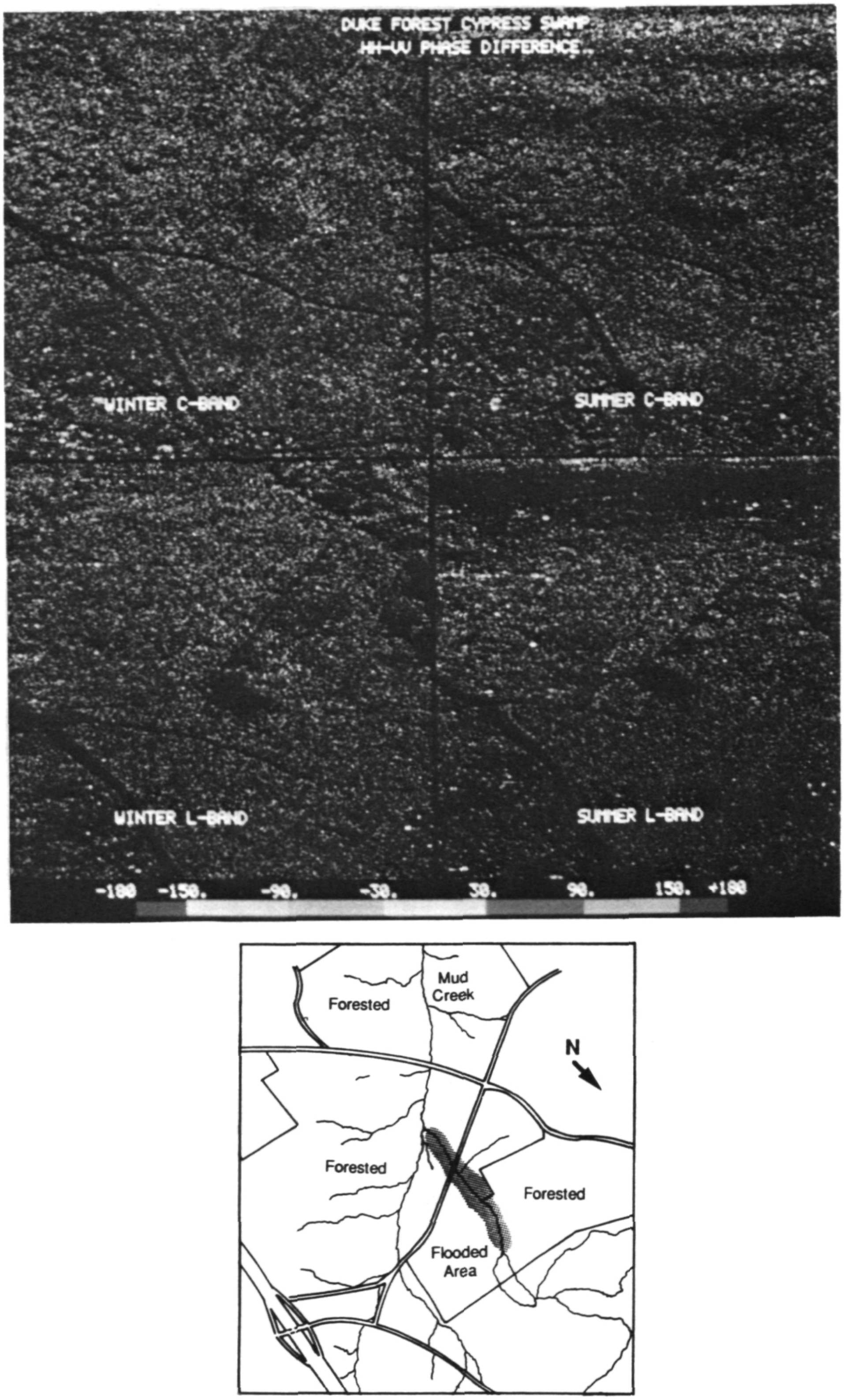

Figure 3. Examples of C and L-band SAR phase difference images of flooded bald cypress stands in North Carolina: (a) black and white rendition of image (see slide no. 2); (b) map of location of stands used in this study.

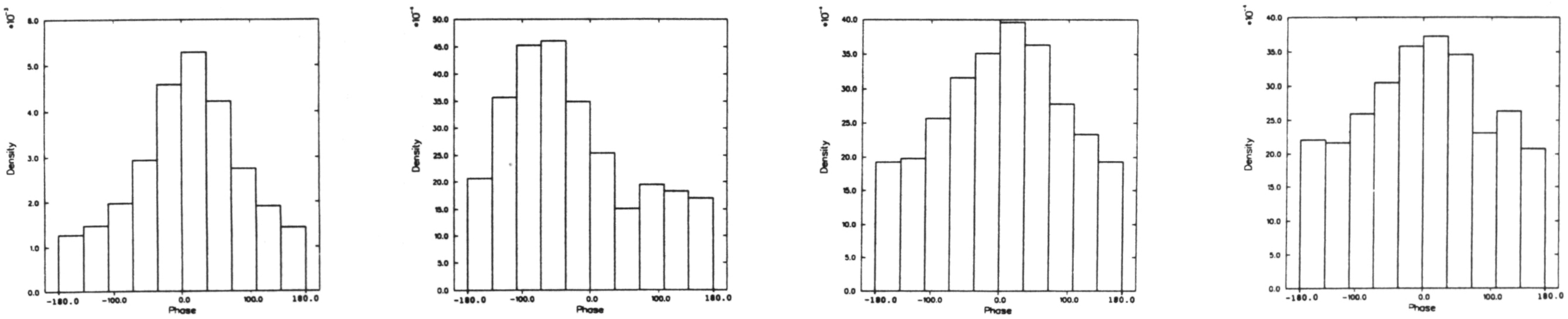

Region A
Mean: 15.3 ρ = 0.42
Std. dev.: 80.5

Region B
Mean: -68.9 ρ = 0.31
Std. dev.: 66.7

Region C
Mean: 11.7 ρ = 0.22
Std. dev.: 91.5

Region D
Mean: 6.0 ρ = 0.18
Std. dev.: 94.7

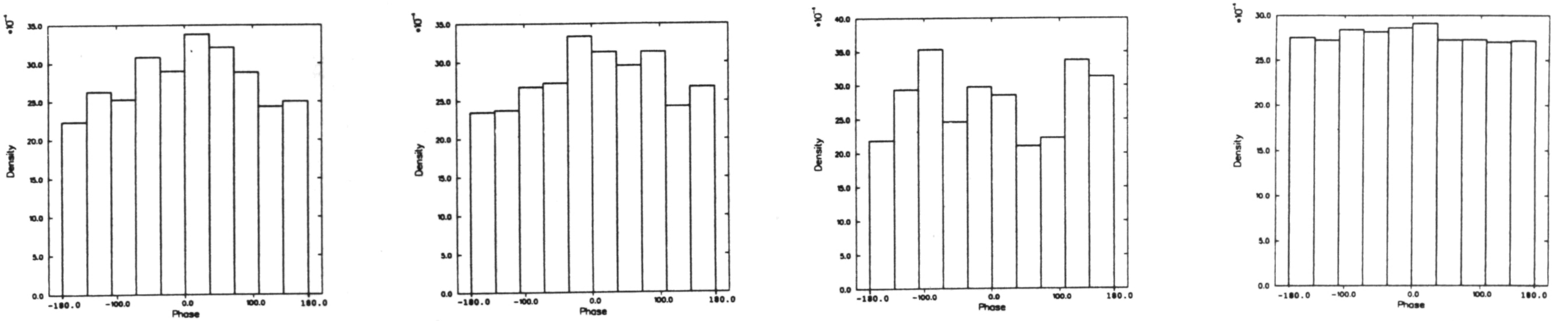

Region E
Mean: 14.1 ρ = 0.16
Std. dev.: 97.5

Region F
Mean: 23.4 ρ = 0.09
Std. dev.: 97.0

Region G
Mean: -113.9 ρ = 0.06
Std. dev.: 44.7

Region H
Mean: -26.4 ρ = 0.03
Std. dev.: 99.6

Figure 4. Histogram plots of SAR phase differences illustrating variation in strength of phase shift based on the standard deviation and correlation coefficient.

TABLE 2. SUMMARY OF POLARIMETRIC STATISTICS FOR NORTH CAROLINA FOREST TEST SITES

VEGETATION TYPE*	Mean RCS (dB) ($\sigma°$)			FP	FP1	Shape parameter (α)			ρ	$\Delta\Theta$
	HH	HV	VV			HH	HV	VV		
X-BAND WINTER										
LL5	-9.0	-13.6	-10.2	.55	.49	.70	.82	.74	.25	3.5
LL15	-9.1	-14.7	-11.3	.64	.57	.94	.89	.94	.31	-18.6
LL55	-7.0	-15.4	-9.2	.76	.75	.72	.78	.68	.29	-12.7
LL-OAK	-4.9	-14.1	-7.5	.79	.79	.83	.84	.79	.36	-17.2
OAK	-5.8	-13.3	-7.3	.71	.70	.83	.83	.65	.36	-3.7
BC	-2.7	-13.8	-7.1	.87	.86	.59	.98	.56	.14	-122.0
X-BAND SUMMER										
LL5	-12.4	-21.8	-18.6	.81	.79	.70	.79	.77	.35	-19.1
LL15	-13.4	-21.7	-18.5	.75	.74	.85	.93	.95	.24	7.3
LL55	-10.2	-17.5	-13.5	.70	.69	.65	.73	.49	.33	2.8
LL-OAK	-9.1	-17.5	-11.7	.77	.75	.55	.64	.62	.52	0.2
OAK	-9.2	-17.3	-13.6	.78	.73	.91	.77	.75	.54	16.5
BC	-8.6	-19.7	-21.2	.89	.86	.84	.69	.77	.29	-29.6
C-BAND WINTER										
LL5	-7.6	-16.6	-8.4	.78	.78	.73	.79	.82	.27	-48.6
LL15	-9.1	-17.8	-8.9	.79	.77	.95	1.00	1.00	.28	-39.5
LL55	-10.0	-18.8	-10.0	.78	.77	.69	.73	.80	.21	-26.1
LL-OAK	-7.9	-17.8	-7.4	.84	.83	.87	.90	.91	.32	-23.9
OAK	-7.0	-17.0	-8.0	.83	.82	1.00	.92	.73	.33	-45.0
BC	-5.4	-14.8	-5.4	.82	.79	1.00	1.00	.74	.13	-127.3
C-BAND SUMMER										
LL5	-13.8	-21.2	-11.6	.81	.80	.73	.62	.71	.38	-9.5
LL15	-15.8	-22.2	-12.7	.81	.80	.88	.90	.97	.25	-1.1
LL55	-13.2	-20.7	-10.7	.83	.82	.56	.75	.36	.35	-5.1
LL-OAK	-12.7	-20.5	-9.8	.85	.84	.70	.79	.72	.48	-1.0
OAK	-13.5	-20.8	-10.1	.86	.84	.89	.82	1.00	.52	7.5
BC	-7.4	-16.8	-9.2	.83	.79	.87	1.00	.78	.27	33.9

*KEY: LL5 - 5 yr old loblolly pine, LL15 - 15 yr old loblolly pine, LL55 - 55 yr old loblolly pine, LL-OAK - mixed loblolly pine/oak, OAK - mixed oak/hardwood, BC - flooded bald cypress.

TABLE 2. SUMMARY OF POLARIMETRIC STATISTICS FOR NORTH CAROLINA FOREST TEST SITES (concluded)

VEGETATION TYPE*	Mean RCS (dB) ($\sigma°$)			FP	FP1	Shape parameter (α)			ρ	ΔΘ
	HH	HV	VV			HH	HV	VV		
L-BAND WINTER										
LL5	-9.5	-15.3	-11.1	.59	.58	.95	1.00	1.00	.18	-10.4
LL15	-10.0	-14.1	-10.1	.45	.44	.99	1.00	1.00	.18	-2.3
LL55	-10.0	-15.8	-12.0	.60	.58	.88	.85	.96	.12	-34.4
LL-OAK	-8.7	-14.5	-10.2	.60	.58	.92	.94	.92	.20	-34.9
OAK	-7.9	-13.2	-9.6	.59	.54	.89	.90	.97	.12	-30.3
BC	-4.4	-13.0	-4.8	.82	.76	.99	.97	.77	.42	-149.0
L-BAND SUMMER										
LL5	-9.1	-16.1	-12.9	.67	.67	.86	.83	.80	.20	-17.4
LL15	-9.5	-14.8	-12.2	.57	.54	1.00	.90	.96	.13	-6.3
LL55	-9.8	-16.3	-12.8	.64	.63	.78	.79	.78	.12	-68.4
LL-OAK	-11.9	-17.7	-13.7	.59	.58	.74	.83	.84	.16	-13.7
OAK	-10.6	-15.6	-13.0	.56	.52	1.00	.83	.92	.23	-31.3
BC	-4.8	-12.6	-5.8	.84	.72	.74	1.00	.88	.61	-151.0

*KEY: LL5 - 5 yr old loblolly pine, LL15 - 15 yr old loblolly pine, LL55 - 55 yr old loblolly pine, LL-OAK - mixed loblolly pine/oak, OAK - mixed oak/hardwood, BC - flooded bald cypress.

N92-28017

Relating the Temporal Change Observed by AIRSAR to Surface and Canopy Properties of Mixed Conifer and Hardwood Forests of Northern Michigan

M. Craig Dobson, Kyle McDonald
and Fawwaz T. Ulaby
University of Michigan
Ann Arbor, Michigan

Terry Sharik
School of Forestry,
Michigan Technological University
Houghton, Michigan

Abstract

The mixed hardwood and conifer forests of northern Michigan were overflown by a 3-frequency airborne imaging radar in April and July, 1990. A set of 10 km x 10 km test sites near the University of Michigan Biological Station at Douglas Lake and within the Hiawatha National Forest in the upper peninsula of Michigan contained training stands representing the various forest species typic of forest communities across the ecotone between the coniferous boreal forest and mid-latitude hardwood and coniferous forests. The polarimetric radar data were externally calibrated to allow interdate comparisons. The April flight was prior to bud-break of deciduous species; and patchy snowcover was present. The July flights occurred during and 2 days after heavy rain showers, and provide a unique opportunity to examine the differences in radar backscatter attributable to intercepted precipitation. Analyses show that there are significant changes in backscattering between biophysically dissimilar forest stands on any given date and also between dates for a given forest stand. These differences in backscattering can be related to moisture properties of the forest floor and the overlying canopy and also to the quantity and organizational structure of the aboveground biomass.

1 INTRODUCTION

In preparation for the ERS-1 and SIR-C missions, a series of airborne SAR experiments have been conducted utilizing the Jet Propulsion Laboratory (P-, L- and C- band) AIRSAR. A test area in northern Michigan lies across the ecotone between the boreal forest and the mixed, northern hardwood and coniferous forest communities. Specific test sites, each approximately 10 km by 10 km in size, are located across the ecotone along a north/south axis as shown in Figure 1. While each test site contains a diverse assemblage of forest types with a relative species mix related to position across the ecotone and local conditions, many species are represented at all test sites.

These sites were overflown by the AIRSAR during the early spring (April 1, 1990) and mid-summer (July 8 and 10, 1990). The central site is located in the vicinity of the University of Michigan Biological Station at Douglas Lake. During the spring overflight, the conditions on the ground at UMBS included partial snowcover (mostly beneath the conifers) over frozen soil and with no leaves on the deciduous trees. The two summer overflights are characterized by full foliation of the tree canopy and the herbaceous groundcover layers. The two summer dates are differentiated by rainfall. The July 8 flight occurred 30 minutes after the cessation of heavy rain showers. The July 10 flight observed the same area after two days of drying.

The AIRSAR flight tracks are nearly identical for each flight so that interdate comparisons are not corrupted by incidence angle effects. Each SAR scene is externally calibrated using arrays of external point targets. The amplitudes and relative phase differences are extracted from the coregistered SAR imagery for a representative subsample of forest stands and other terrain conditions. These values are compared between stands for a given flight and between flights for specific forest stands.

Such comparisons of calibrated backscatter are useful in defining the capability of orbital SAR for (1) differentiating various forest communities, (2) estimating physical and biophysical properties of the scene (i.e., ground surface properties, aboveground woody biomass, foliar biomass, etc.), and (3) monitoring changes in such conditions related to the effects of seasonal phenologic development, weather patterns, anthropogenic impacts, and pestilence.

2 EXPERIMENT DESCRIPTION

The area surrounding the University of Michigan Biological Station (UMBS) at Douglas Lake contains a wide variety of forest communities ranging from conifer bogs and hardwood swamps to upland northern hardwood, aspen and pine forests. At UMBS, many individual stands have been studied over the last 70 years as this area has undergone reforestation subsequent to extensive harvest and repeated fires at the end of the last century.

For this study, the range of forest communities was used to stratify a sample population containing (1) northern hardwood forests of red maple (Acer rubrum), sugar maple (Acer saccharum), american beech (Fagus grandifolia) and northern red oak (Quercus rubra), (2) bigtooth aspen (Populus grandidentata) stands some of which are in transition to red oak, northern hardwoods or pine, (3) relatively pure pine forests of jack pine (Pinus banksiana), red pine (Pinus resinosa) or eastern white pine (Pinus strobus), (4) hardwood swamps of red maple, bigtooth aspen, trembling aspen (Populus tremuloides), paper birch (Betula papyrifera) and black ash (Fraxinus americana), and (5) conifer bogs of northern white cedar (Thuja occidentalis), eastern hemlock (Tsuga canadensis), trembling aspen, balsam fir (Abies balsamea), black spruce (Picea mariana), and white spruce (Picea glauca). For each forest community, several test stands were selected to represent the naturally occurring range of site conditions and age/size classes.

Training stands of each community were inventoried over a 1-ha area to evaluate homogeneity with respect to soils, topography, and vegetation composition and structure. Randomly selected positions along randomly selected transects were used to locate all sample points and plots. These were surveyed and marked for use during all overflights. A series of nested circular or square plots were used to provide a 10% sample of the upper strata, canopy trees (>5m height) and middle strata trees (1-5m height) and a 0.3% sample of the lower strata of vegetation (<1m height). Inventories were made of relatively static stand properties such as tree heights, diameters and density by specie.

During each overflight, additional measurements were made for leaf area, biomass, percent cover, litter depth and moisture, soil density and moisture, and snow properties (depth, % cover and wetness). In addition, in situ measurements were made of the L- and C-band dielectric properties of the mineral soil, tree trunks and foliage. For example, the dielectric properties of roughly 120 trees were measured at each site in conjunction with each AIRSAR flight date. Temperature and precipitation histories were locally recorded at UMBS and at the Emmet County Airport at Pellston, MI.

This rather extensive series of ancillary data provides the basis for interpretation of radar backscatter data extracted from SAR imagery and for use as inputs into the MIMICS radar scattering model [1].

3 SAR DATA AND SCENE CONDITIONS

Airborne, polarimetric SAR data was obtained by the JPL AIRSAR at P-, L- and C- bands on 3 dates in 1990: April 1, July 8 and July 10. On each date, the test area was overflown from various look directions to investigate the effects of azimuth view angle on radar backscatter. The same flight lines were used on each date, and the resulting imagery shows minimal (<3°) variance in local angle of incidence between dates for a given forest stand. An array of both active and passive calibration targets located at the Emmet County Airport were used to provide external calibration for all 3 SAR frequencies using the compressed 4-look Stokes matrix data[2]. The AIRSAR calibration accuracy is estimated to be within 1 dB in amplitude and 10 degrees in relative phase.

The locations of all forest stands and other representative features of interest are mapped into a geographic information system (GIS) as illustrated by Figure 2. These other features consist of water bodies (lakes), concrete (airport runways), gramineous surfaces (grasses and sedges), brush (alder) and forest clearcuts. The GIS containing scene locations was warped to each calibrated slant-range SAR image using a low-order polynomial fit to ground control points. Hence, no resampling of the Stokes matrix data was required. The coregistered GIS is used to segment the SAR images and extract the backscatter data for the training stands and conditions. The calibrated data is log transformed to dB and samples of the resultant total power images are shown in Figures 3 and 4 for April 1 and July 10, respectively. In Figures 3 and 4, the color assignments of red, green and blue are for P-, L- and C-bands, respectively.

Scatter plots of mean backscatter (HH vs. HV) from training stands of each scene category are given for each date and frequency in Figures 5 to 7. Each sample is the average of between 56 to 600 pixels.

On April 1, the lakes were covered with snow and ice. The mineral soil at all sites was frozen to a depth of at least 15 cm. Scattered snowcover was present where ever there was sufficient shadowing from coniferous trees. Snow cover ranged from 100% with an average depth of 25 cm in the conifer bogs to 0% in the aspen and hardwood stands. Pine stands typically had patchy snowcover (<15%) with an average depth <8 cm. The measured snow wetness ranged between 4-5% by volume over the period of the overflight with temperatures of 0.2°C and 8.0°C for the snow and air, respectively. The xylem sap was flowing in all tree species. The buds had not broken on any deciduous species.

On July 8, passage of a cold front brought heavy rain showers. The AIRSAR data was obtained within 1/2 hour of a break in the showers. No additional rainfall was recorded on July 9 or 10. There was standing water in the hardwood swamps for both days. Soil moisture for the organic soils of the conifer bogs averaged >45% (by volume) on both days. For the mineral soils beneath upland stands, average volumetric soil moistures decreased by 2% to 10% over the 2 day period. The organic litter layer covering the humus and mineral soil was generally saturated on July 8 and had dried somewhat by July 10 to typical values of 55%, 65% and 85% for aspen, jack pine and red pine stands, respectively. The dielectric properties of the trees were observed to be similar for both dates, but can vary considerably between specie and as a function of local site conditions.

4 DIFFERENTIATION OF SCENE CATEGORIES

It is clear from Figures 5 to 7 that average σ^0 at any frequency (P-, L- or C-bands) and linear polarization can be easily used to discriminate between nonvegetated surfaces (such as ice, water and concrete) and all vegetated areas particularly at the longer wavelengths. Furthermore, this separability is enhanced by the fact that $\sigma^0_{HH}/\sigma^0_{HV}$ is greatest for these relatively smooth, nonvegetated surfaces. Soils covered by short grasses and sedges (<20 cm) are shown to be most similar to nonvegetated surfaces with respect to σ^0 and especially at longer wavelengths.

To first approximation, $\sigma^0_{f,p}$ is also found to be proportional to aboveground biomass within the vegetated areas. It is of interest to note that this relationship saturates, and does so at biomass levels which scale to wavelength. This is evident in Figures 5 to 7 where the dynamic range of σ^0_{HH} from vegetated areas is shown to decrease from 25 dB at P-band to 18 dB at C-band, and the dynamic range of forested areas is shown to be 11 dB, 6 dB and 5 dB for P-, L- and C-bands, respectively. σ^0_{HH} at P-band is especially sensitive to aboveground biomass in the tree boles (trunks). σ^0_{HH} for 10 year old aspen saplings (basal area = 7.5 m^2/ha) is 10 dB to 12 dB less than that for mature aspen stands (basal area = 40 m^2/ha).

The clustering of mean σ^0 (HH and HV polarizations) over a 3-4 dB range for mature forest stands does not impose a serious impediment to differentiating forest communities and age, size and class, except at C-band. This is because $\sigma^0_{HH}/\sigma^0_{VV}$ relationships are found to be distinctive for the various forest communities at P- and L-bands (Figure 8). $\sigma^0_{HH}/\sigma^0_{VV}$ is found to be particularly effective in discrimination of conifers, even those in the understory of deciduous stands. In addition, areas of brush (primarily alder) and stands of young aspen saplings yield a highly distinctive VV polarized return due to coupling with the arrays of verically oriented trunks and branches especially at P-band. σ^0_{VV} can be as much as 6 dB greater than σ^0_{HH} for these conditions.

Relative phase difference $\Delta\phi_f = \phi_{HH} - \phi_{VV}$ is also useful in differentiating forest communities. $\Delta\phi_f$ is sensitive the orientation, height, density and dielectric properties of the constituent elements of the vegetation canopy. At P- and L-band, $\Delta\phi_f$ is found to be dominated by ground-trunk specular scattering mechanisms. At C-band, $\Delta\phi_f$ is dominated by scattering within the crown layer of branches and foliage. Histograms of $\Delta\phi_f$ distributions for a stand of 10 year old aspen samplings and a mature aspen stand are shown in Figures 9 and 10 at P- and L-bands respectively.

5 EFFECTS OF SEASON AND PHENOLOGIC CHANGE

The effects of season and phenologic development of vegetation are best demonstrated through a comparison of the SAR data obtained on April 1 and July 10. For the surface layer, thawing of the upper soil layer increases the reflection coefficient at this boundary. The generally thin and patchy snow cover present on April 1 should have negligible effect on backscatter at *P*- and *L*-bands; and those effects which may be present at *C*-band are obscured by the attenuation and scattering of the heavy forest cover associated with the presence of snow on April 1.

Phenologic change of vegetation over this period results in two factors: an increase in foliar and stem biomass in the crown region and changes in vegetation dielectric properties. Both of these factors are specie dependent and also vary somewhat depending upon site conditions. For pine stands (jack pine and red pine), midsummer conditions lead to an average decrease in $\sigma^0_{f,p}$ of 1-2 dB at *P*- and *L*-bands and an increase of 1 dB at *C*-band. These changes in $\sigma^0_{f,p}$ are consistent with the hypothesis that the changes in the crown layer are enhancing attenuation at the longer wavelengths while scattering in the crown dominates at *C*-band (l = 6 cm). For deciduous species, foliation and associated dielectric changes in the trunks and branches leads to a decrease in σ^0 at all frequencies. This decrease is greater for *P*-band (2 to 4 dB) and least for *C*-band (0 to 2 dB). These changes cannot be explained only on the basis of attenuation and scattering differences in the crown since these trees also exhibit significant changes in bole dielectric properties over this time period.

6 EFFECTS OF INTERCEPTED PRECIPITATION

The rain showers associated with the SAR overflights on July 8 provide a unique opportunity to examine the impact of intercepted rainfall on radar backscatter from forests. Incident rainfall is intercepted by foliage and branches and is retained for a period of time as droplets or thin films. The quantity of intercepted water suspended in the canopy is proportional to crown biomass and is also dependent upon leaf and branch size, shape and orientation. Rainfall also increases the volumenteric moisture content of the soil surface and the overlying organic litter layer.

For areas with short graminoid vegetation covers (grasses and sedges), the rainfall on July 8 is found to increase σ^0 by 1.5 dB, 5.5 dB and 4 dB for like-polarized backscatter at *P*-, *L*- and *C*-bands, respectively. This is expected for what is essentially surface scattering at the ground. However, as biomass is increased (i.e., shrubs and forest), the increase in σ^0 noted for grasses is reduced at all frequencies. While increased moisture at the surface increases reflection at this boundary, this is largely masked by enhanced extinction in the wet crown layer. Consequently, backscatter from mature forests on July 8 is typically greater than that on July 10 by 0 dB, 1 to 2 dB and 2 to 3 dB at *P*-, *L*- and *C*-bands, respectively. It is interesting that the effect of rainfall on backscatter from forest vegetation is negligible at *P*-band.

7 CONCLUSIONS

Radar backscatter from terrain can clearly be used to differentiate between bare surfaces and various categories of vegetation cover (i.e., grasses, shrubs and forest). The amplitude is found to be roughly proportional to aboveground biomass, particularly at longer wavelengths. This effect saturates at relatively low levels of foliar biomass at *C*- band. Differentiation between forest communities is certainly possible, especially if polarization and relative phase information is available. Seasonal changes in vegetation related to foliar growth have demonstrable effects on frequency and polarization dependent scattering and attenuation by the crown layer. These effects are also dependent upon tree specie and local site conditions. Seasonal change in backscatter related to phenologic development is most pronounced for deciduous species. Increased foliar and branch biomass contributes to greater extinction by the crown layer. This results in a general decrease in backscatter for the foliated midsummer conditions. Rainfall intercepted by forest cover causes an increase in σ^0 (except at *P*-band). This increase is less than that observed from both bare surfaces and graminoid vegetation covers. Consequently, such events should be readily detectable at *L*- and *C*-bands using change detection approaches in SAR image analysis.

ACKNOWLEDGMENTS

This research is supported by the National Aeronautics and Space Administration under grants NAGW-1362 and JPL-C-958437-NASA Prime.

REFERENCES

[1] Ulaby, F. T., K. Sarabandi, K. McDonald, M. Whitt, and M. C. Dobson, "Michigan Microwave Canopy Scattering Model (MIMICS)," International Journal of Remote Sensing, Vol. 11, No. 7, pp. 1223-1253, July, 1990.

[2] F.T. Ulaby and C. Elachi, editors, Radar Polarimetry for Geoscience Applications, Dedham, MA: Artech House, Inc., 1990.

Figure 1 - Michigan forest test sites

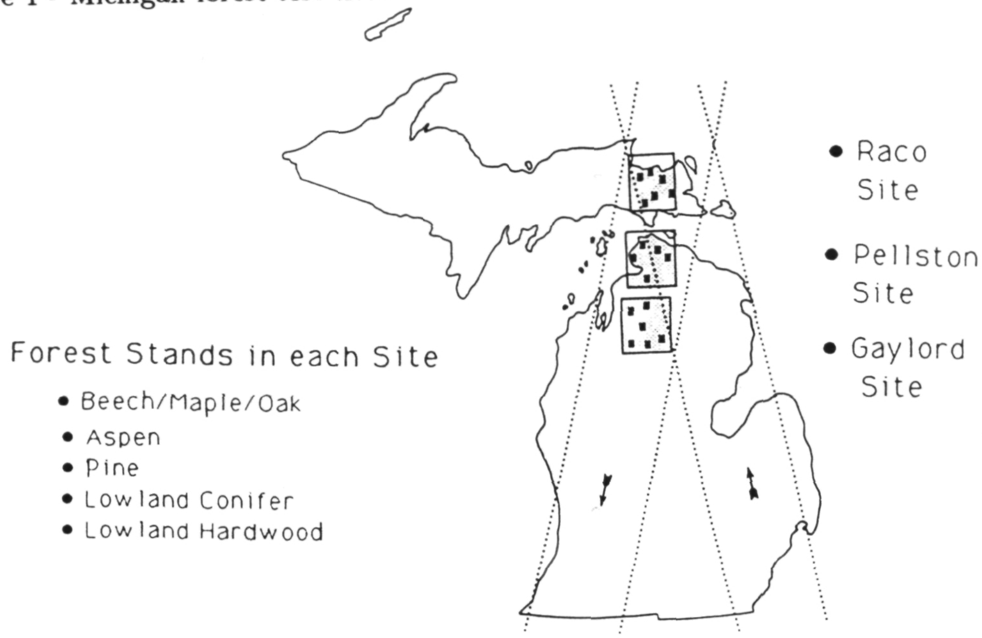

Figure 2 - Elements of geographical information system

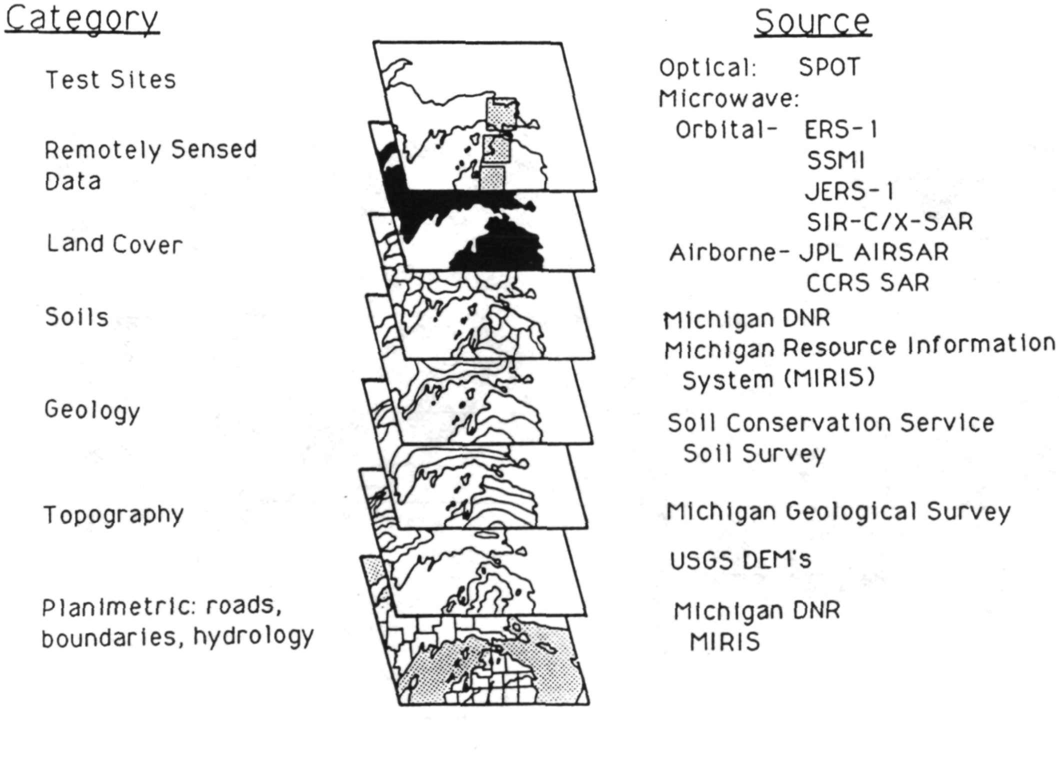

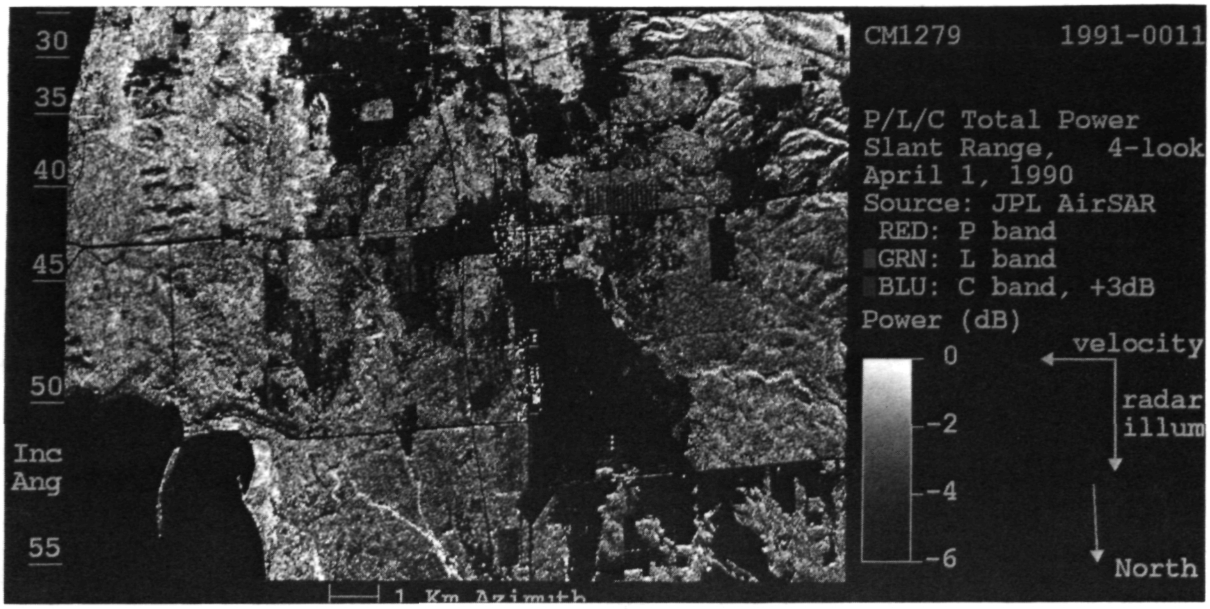

Figure 3 – AIRSAR total power image for April 1, 1990 (see slide no. 3).

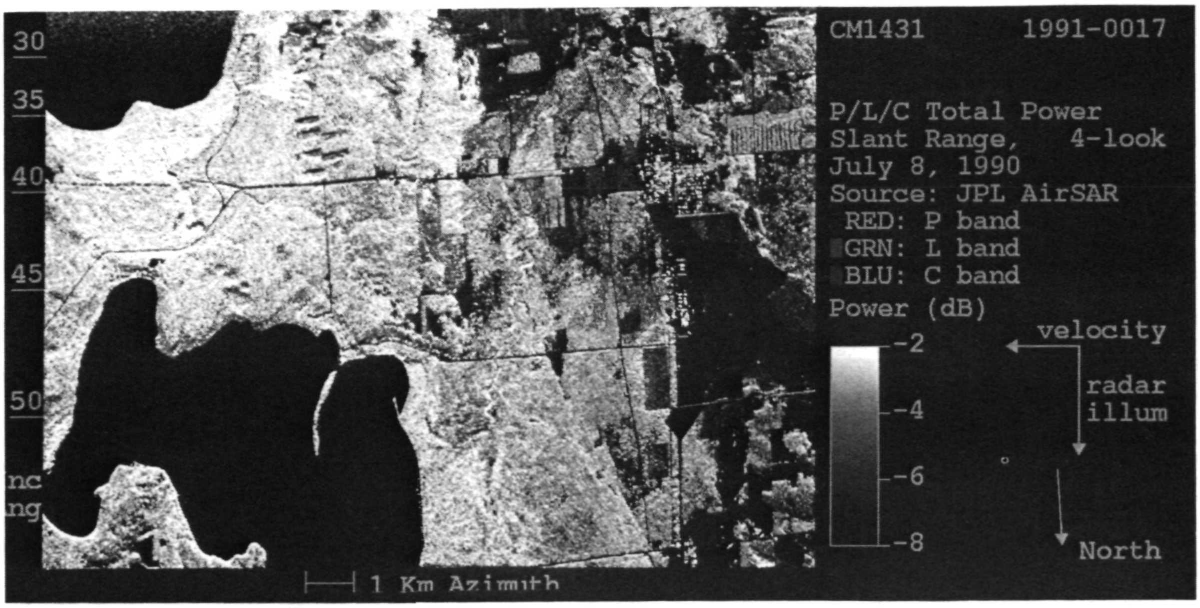

Figure 4 – AIRSAR total power image for July 8, 1990 (see slide no. 4).

Figure 5 - Average backscatter for HH and HV polarizations on April 1, 1990.

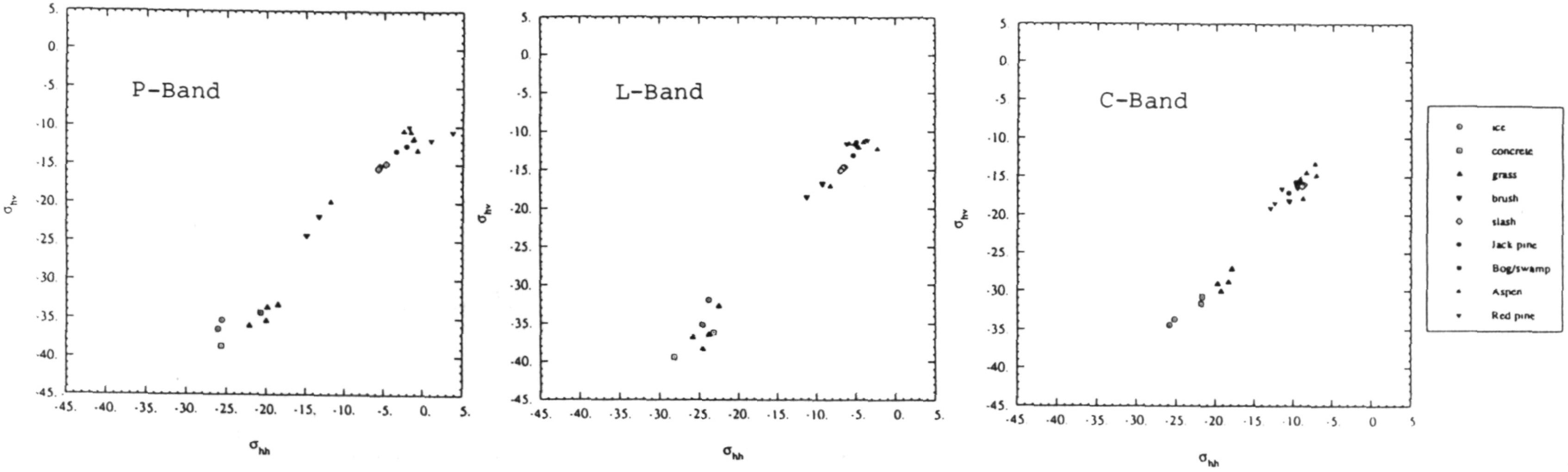

Figure 6 - Average backscatter for HH and HV polarizations on July 10, 1990.

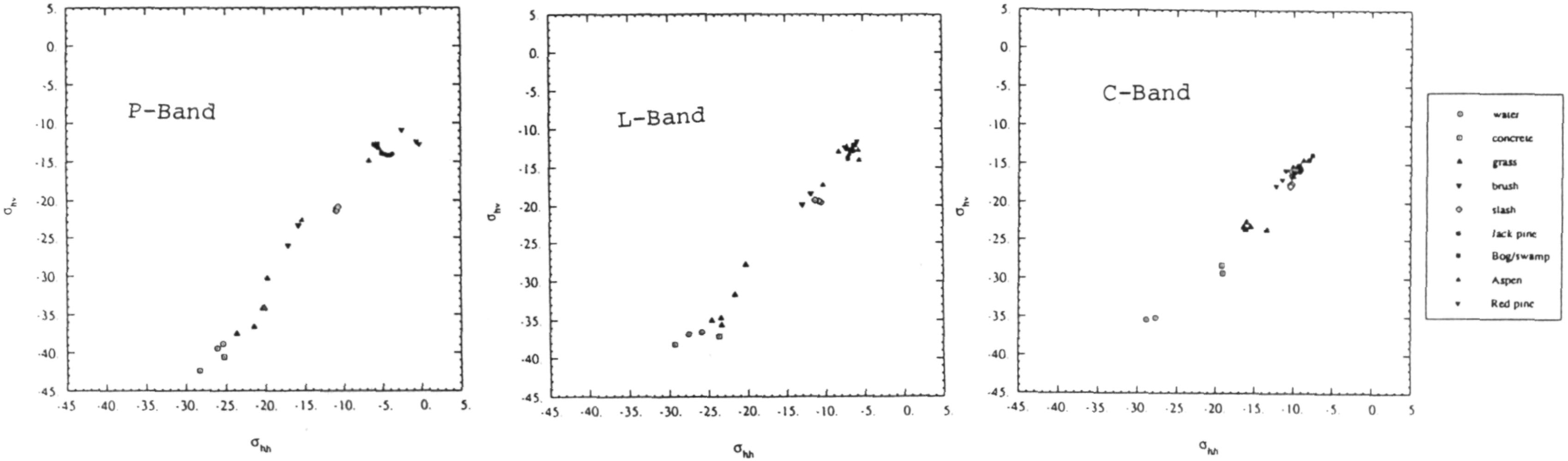

Figure 7 - Average backscatter for HH and HV polarizations on July 8, 1990.

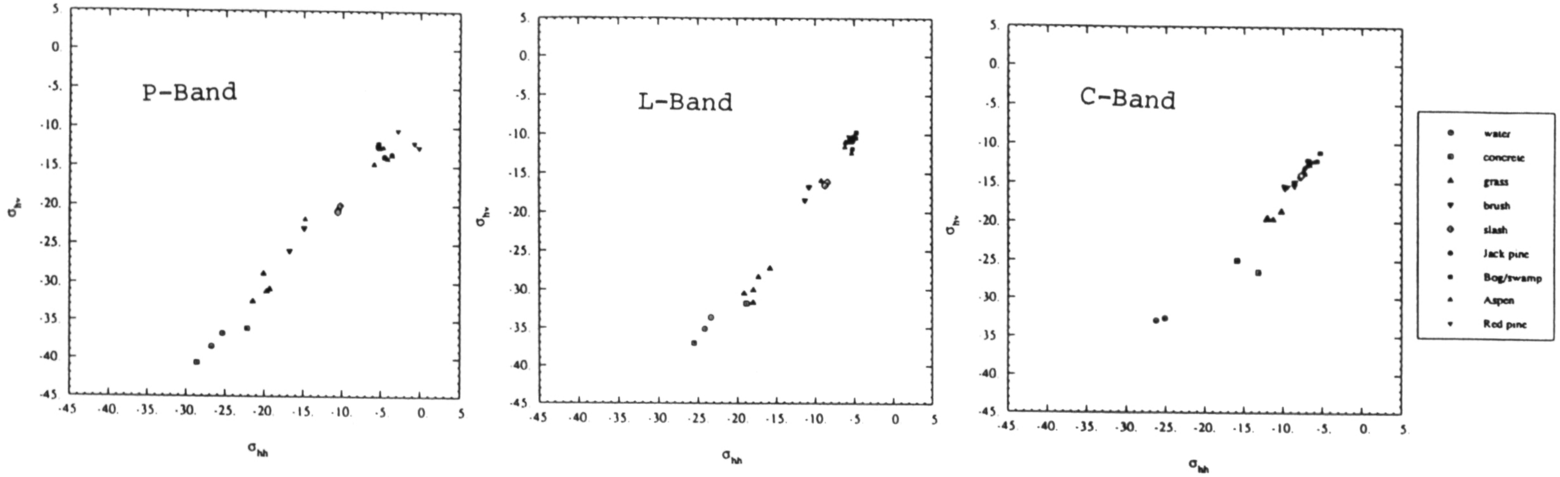

Figure 8 - Average backscatter for HH and HV polarizations on April 1, 1990.

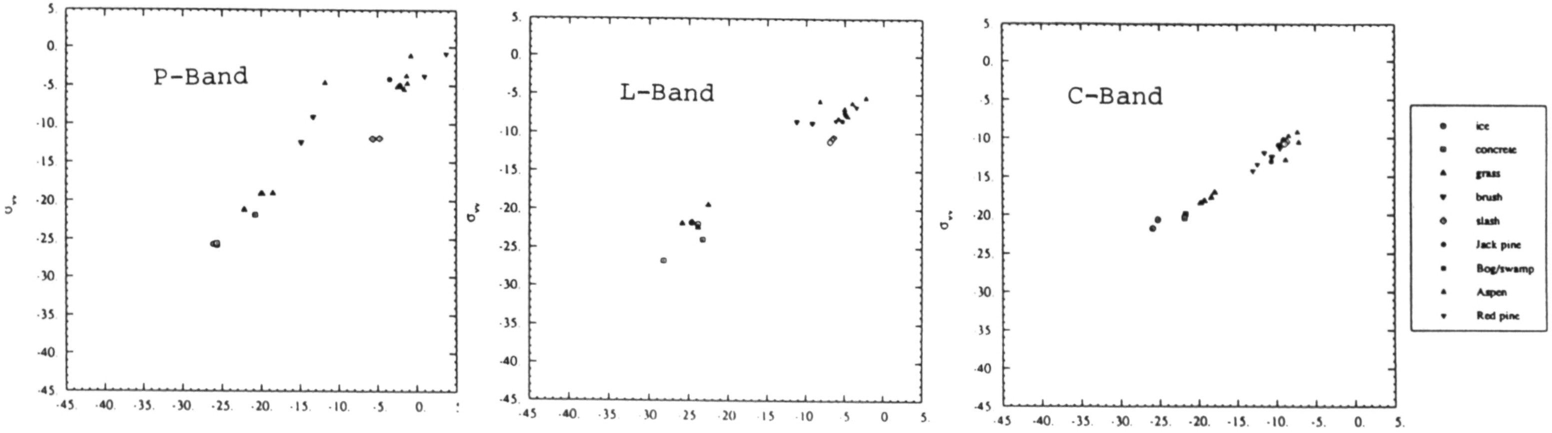

Figure 9 - Histograms of $\Delta\phi$ for a stand of 10-year old aspen saplings on July 10, 1990.

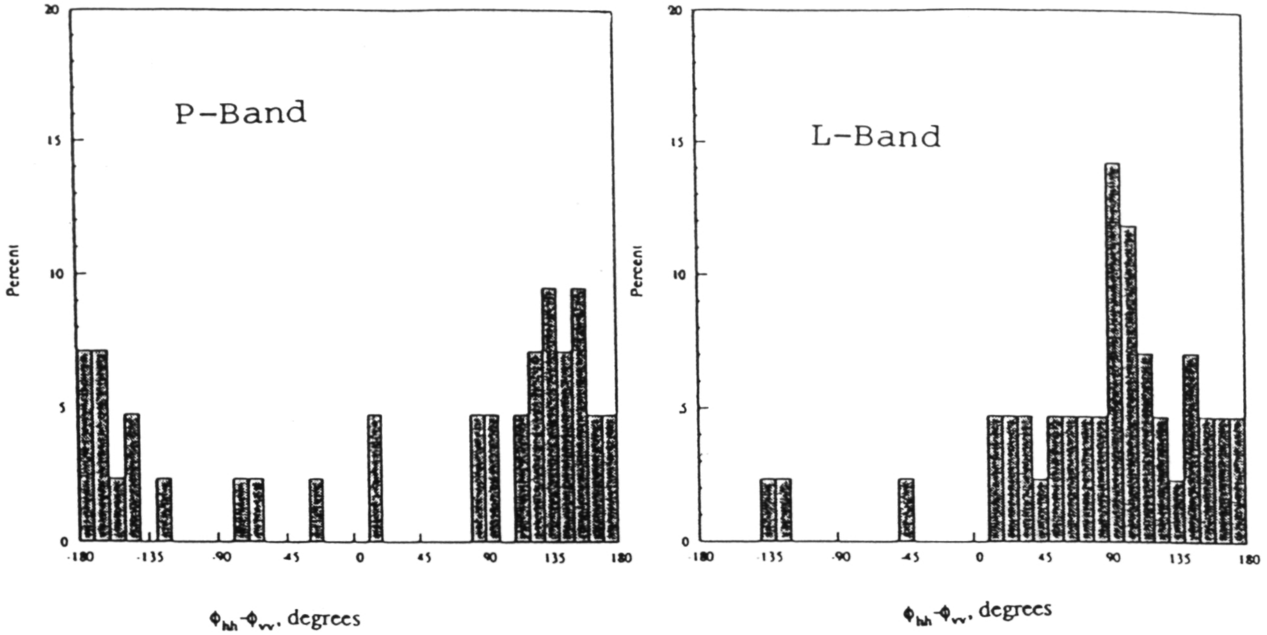

Figure 10 - Histograms of $\Delta\phi$ for a stand of mature aspens on July 10, 1990.

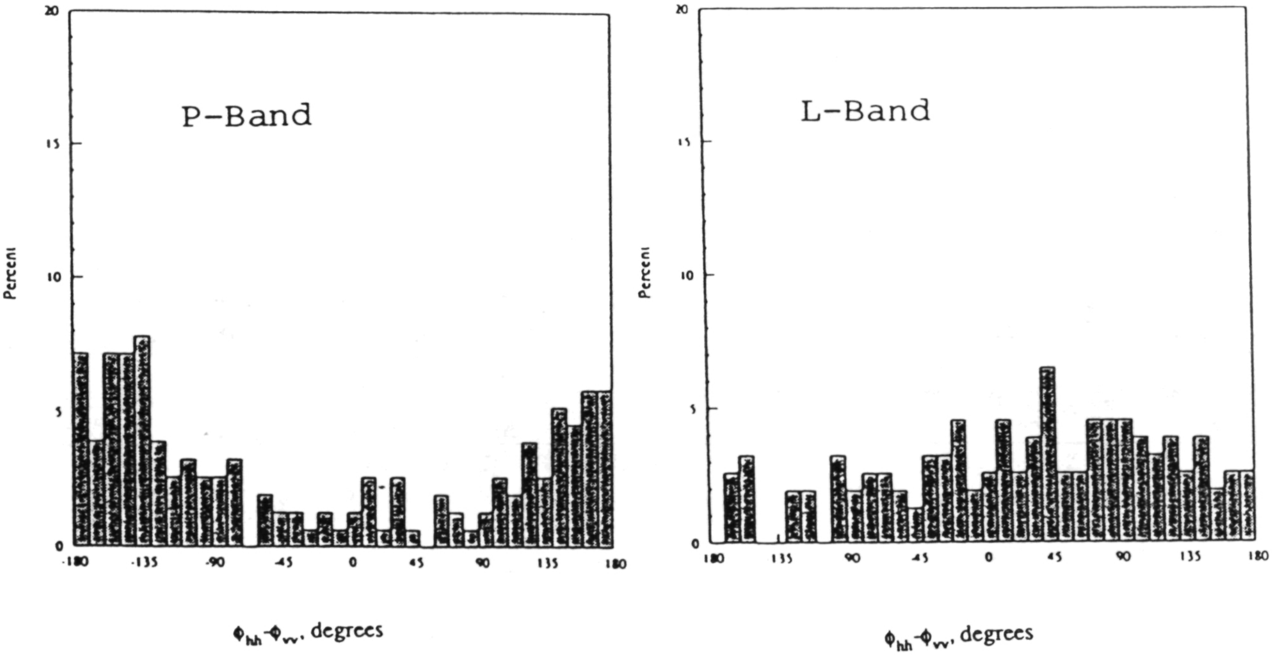

N92-28018

Multi-frequency and polarimetric radar backscatter signatures for discrimination between agricultural crops at the Flevoland experimental test site.

A. Freeman, J. Villasenor and J. D. Klein

Jet Propulsion Laboratory
California Institute of Technology
Pasadena, CA 91109

Abstract

We describe the calibration and analysis of multi-frequency, multi-polarization radar backscatter signatures over an agricultural test site in the Netherlands. The calibration procedure involved two stages: in the first stage, polarimetric and radiometric calibrations (ignoring noise) were carried out using square-base trihedral corner reflector signatures and some properties of the clutter background. In the second stage, a novel algorithm was used to estimate the noise level in the polarimetric data channels by using the measured signature of an idealized rough surface with Bragg Scattering (the ocean in this case). This estimated noise level was then used to correct the measured backscatter signatures from the agricultural fields.

We examine the significance of several key parameters extracted from the calibrated and noise-corrected backscatter signatures. The significance is assessed in terms of the ability to uniquely separate among classes from thirteen different backscatter types selected from the test site data, including eleven different crops, one forest and one ocean area. Using the parameters with the highest separation for a given class, we use a hierarchical algorithm to classify the entire image. We find that many classes, including ocean, forest, potato, and beet, can be identified with high reliability, while the classes for which no single parameter exhibits sufficient separation have higher rates of misclassification. We expect that modified decision criteria involving simultaneous consideration of several parameters increase performance for these classes.

I. Calibration of the DC-8 SAR data

To calibrate the NASA/JPL DC-8 SAR [1] data, we used the algorithms described in [2] and [3]. Both of these algorithms utilize the reciprocity between HV and VH backscatter from natural targets (i.e., $S_{HV} = S_{VH}$) and the lack of correlation between like- and cross-polarized backscatter for many natural scenes (e.g., $<S_{HV}S_{HH}^*> = 0$) to estimate the channel balance between the two cross-polarized returns and the system cross-talk or leakage. Both the scattering matrix and Stokes matrix data formats were calibrated and archived at JPL, although the analysis presented in this report only applies to the Stokes matrix data for the Flevoland site. The signatures from a trihedral corner reflector (or a set of trihedral corner reflectors) are used to balance the amplitude and phase between the HH and VV measurements, and to absolutely calibrate the data, so that it is in units of normalized radar cross-section, σ^o (m^2/m^2). In the case of the Flevoland data, we used square-base trihedrals instead of triangular-base trihedrals, but this did not cause any special problems in calibration, except in the field deployment, since the elevation boresite angles for the two types of trihedral are different. The residual calibration uncertainties (as estimated from the trihedral signatures) are presented in Table 1. In Figure 1, we present an example of a calibrated C-Band HV polarized image extracted from the Flevoland data set.

II. Noise-equivalent $\sigma°$ estimation from ocean backscatter data

The calibration procedures described in [2] and [3] do not correct for radiometric errors or relative phase errors introduced by additive noise, which may be due to thermal noise in the SAR system or quantization errors. What is needed is a way of quantifying the noise level in each of the polarization channels for each frequency, so that it can be corrected for. This information is not currently supplied with the NASA/JPL DC-8 SAR data. In what follows, we present an approach for estimating the noise level from polarimetric backscatter measurements extracted from an idealized rough surface with Bragg scattering, in this case the patch of ocean on the right-hand side of the Flevoland scene (see Figure 1).

Consider the scattering matrix measurement,

$$\mathbf{M} = Ae^{j\phi}\begin{pmatrix} 1 & \delta_1 \\ \delta_2 & f_1 \end{pmatrix}\begin{pmatrix} S_{HH} & S_{VH} \\ S_{HV} & S_{VV} \end{pmatrix}\begin{pmatrix} 1 & \delta_4 \\ \delta_3 & f_2 \end{pmatrix} + \begin{pmatrix} n_{HH} & n_{VH} \\ n_{HV} & n_{VV} \end{pmatrix}$$

$$= \mathbf{R}^t\mathbf{S}\mathbf{T} + \mathbf{N} \qquad (1)$$

where **R** and **T** are matrices representing the receive and transmit characteristics of the polarimetric radar, **S** is the actual scattering matrix of the target of interest, and **N** is a matrix representing the noise in each polarization channel. We characterize the (complex) noise terms as having two-dimensional, zero-mean, Gaussian distributions, with the following properties:

$$\begin{aligned}&\langle n_{jk}\rangle = 0\\ &\langle n_{jk}n_{jk}^{*}\rangle = \sigma_{jk}^{n}\\ &\langle n_{jk}n_{lm}^{*}\rangle = 0 \text{ , for } j \neq l \text{ or } k \neq m.\\ &\langle n_{jk}S_{lm}^{*}\rangle = 0 \text{ , for any } j, k, l, m.\end{aligned} \qquad (2)$$

where σ_{jk}^{n} is the noise power (or noise-equivalent sigma-zero) in the polarization channel jk. We assume that the noise terms are uncorrelated with each other and with the scattering matrix (signal) terms.

After polarimetric calibration using either of the methods described in [2] and [3], the relative amplitude and phase between channels should be balanced such that $f_1 = f_2 = 1$ (which is 0dB). In addition, the level of the cross-talk terms (the δ's in (2)) should be fairly small. We will assume, for simplicity, that the cross-talk terms after calibration are dominated by the residual contribution from the passive antenna, so that $\delta_1=\delta_3$ and $\delta_2=\delta_4$.

Now consider the scattering matrix model for Bragg scattering from an idealized rough surface, such as the ocean [5], which is:

$$S = \begin{pmatrix} a & 0 \\ 0 & b \end{pmatrix} \begin{array}{l}\text{with a,b real, } b>a>0\\ \text{and } \langle ab^{*}\rangle = ab\end{array} \qquad (3)$$

i.e., a scattering matrix with zero cross-polarized return, HH and VV returns which are completely correlated and zero phase difference between the HH and VV returns. The ratio a/b and the absolute backscatter level are dependent on the surface roughness (i.e., the sea-state in this case) but need not be known a priori.

Substituting (4) into (2), and making the assumptions described above, we obtain:

$$M = Ae^{j\phi}\begin{pmatrix} a + b\delta_1^2, & a\delta_2 + b\delta_1 \\ a\delta_2 + b\delta_1\ , & a\delta_2^2 + b \end{pmatrix} + \begin{pmatrix} n_{HH} & n_{VH} \\ n_{HV} & n_{VV} \end{pmatrix} \qquad (4)$$

In what follows, we shall ignore the absolute amplitude A and phase ϕ in the signal term. After "symmetrization" of the HV and VH measurements to yield one average cross-polarized measurement, which is the first step in the formation of the Stokes matrix data format, we obtain [4]:

$$M' = \begin{pmatrix} a + b\delta_1^2 \\ a\delta_2 + b\delta_1 \\ a\delta_2^2 + b \end{pmatrix} + \begin{pmatrix} n_{HH} \\ (n_{HV} + n_{HV})/2 \\ n_{VV} \end{pmatrix} \tag{5}$$

where M' is shown in vector form. In what follows, we will drop the dash notation for the vector representation. The next step in converting from scattering matrix data to Stokes matrix data format is to form the six possible cross-products between the M_{HH}, M_{HV} and M_{VV} measurements, which is followed by an average over four adjacent measurements (pixels) in the along-track direction. Then various linear combinations of the real and imaginary parts of the cross-products give the ten Stokes matrix terms [6]. It is possible to completely recover the cross-products from the Stokes matrix terms, so in what follows we will only consider the cross-products.

Assuming that the individual noise terms are uncorrelated, and that the backscatter and noise terms are uncorrelated, we can estimate the expected values for each of the cross-products generated from equation (5), i.e.,

$$\langle M_{HH}M_{HH}^{*}\rangle = \left(a + b\delta_1^2\right)\left(a + b\delta_1^2\right)^{*} + \sigma_{HH}^{n} \tag{6a}$$

$$\langle M_{HV}M_{HV}^{*}\rangle = \left(a\delta_2 + b\delta_1\right)\left(a\delta_2 + b\delta_1\right)^{*} + \left(\sigma_{HV}^{n} + \sigma_{VH}^{n}\right)/4 \tag{6b}$$

$$\langle M_{VV}M_{VV}^{*}\rangle = \left(a\delta_2^2 + b\right)\left(a\delta_2^2 + b\right)^{*} + \sigma_{VV}^{n} \tag{6c}$$

$$\langle M_{HH}M_{VV}^{*}\rangle = \left(a + b\delta_1^2\right)\left(a\delta_2^2 + b\right)^{*} \tag{6d}$$

$$\langle M_{HH}M_{HV}^{*}\rangle = \left(a + b\delta_1^2\right)\left(a\delta_2 + b\delta_1\right)^{*} \tag{6e}$$

$$\langle M_{HV}M_{VV}^{*}\rangle = \left(a\delta_2 + b\delta_1\right)\left(a\delta_2^2 + b\right)^{*} \tag{6f}$$

Equations (6a) - (6f) constitute six equations in just six unknowns, counting the noise power in the $|M_{HV}|^2$ measurement, $\left(\sigma_{HV}^{n}+\sigma_{VH}^{n}\right)/4$, as a single unknown. Note that, as pointed out in [7], if all the noise levels on the input polarization channels are roughly equal, then the noise level in the "symmetrized" $|M_{HV}|^2$ measurement will be 3dB lower than the noise-levels in the like-polarized backscatter intensity measurements.

Solving (6a)-(6f) for the noise power terms, we obtain:

$$\sigma_{HH}^{n} = \langle M_{HH}M_{HH}^{*}\rangle - \frac{\langle M_{HH}M_{VV}^{*}\rangle\langle M_{HH}M_{HV}^{*}\rangle^{*}}{\langle M_{HV}M_{VV}^{*}\rangle} \tag{7}$$

$$(\sigma^n_{HV}+\sigma^n_{VH})/4 = \langle M_{HV}M^*_{HV}\rangle - \frac{\langle M_{HH}M^*_{HV}\rangle\langle M_{HV}M^*_{VV}\rangle^*}{\langle M_{HH}M^*_{VV}\rangle} \tag{8}$$

and

$$\sigma^n_{VV} = \langle M_{VV}M^*_{VV}\rangle - \frac{\langle M_{HH}M^*_{VV}\rangle\langle M_{HV}M^*_{VV}\rangle^*}{\langle M_{HH}M^*_{HV}\rangle} \tag{9}$$

Unfortunately, the above estimates for σ^n_{HH} and σ^n_{VV} were not found to be very robust. The problem lies in the fact that the correlations between the like- and cross-polarized returns, $\langle M_{HH}M^*_{HV}\rangle$ and $\langle M_{HV}M^*_{VV}\rangle$, are often very small numbers after calibration, since they depend predominantly on the level of the cross-talk terms, δ_1 and δ_2 (see equations (6e) and (6f)). Thus, a small error in one of these terms can lead to a large error in the ratio of the two. This can, in turn, lead to negative estimates for the noise power in the HH and VV channels. The noise power estimate for the HV channel is less sensitive to this problem, since it involves a product of the two terms, which tends to be very small.

A number of possible solutions were tried, with various simplifications, to attempt to reach a robust estimate for the noise powers. The common feature of these solutions was that they employed a ratio of the two like-to cross-polarization terms. Eventually, to avoid using such a ratio, the problem was simplified as follows: First, we assume that $\delta_1 = \delta_2 = \delta$ and that $\sigma^n_{HH} = \sigma^n_{VV}$. Next, we neglect terms in δ^2 or $|\delta|^2$, except in equation (6b), where they could be significant. Finally, we take the modulus of the equations (6d)-(6f), to give:

$$\langle M_{HH}M^*_{HH}\rangle \cong a^2 + \sigma^n_{HH} \tag{10a}$$

$$\langle M_{HV}M^*_{HV}\rangle \cong (a^2 + b^2 + 2ab)|\delta^2| + (\sigma^n_{HV} + \sigma^n_{VH})/4 \tag{10b}$$

$$\langle M_{VV}M^*_{VV}\rangle \cong b^2 + \sigma^n_{HH} \tag{10c}$$

$$|\langle M_{HH}M^*_{VV}\rangle| \cong ab \tag{10d}$$

$$|\langle M_{HH}M^*_{HV}\rangle| \cong (a^2 + ab)|\delta| \tag{10e}$$

$$|\langle M_{HH}M^*_{VV}\rangle| \cong (b^2 + ab)|\delta| \tag{10f}$$

We solve these equations by first constructing a quadratic in b^2. Subtracting eq. (10c) from eq. (10a):

$$\langle M_{HH}M^*_{HH}\rangle - \langle M_{VV}M^*_{VV}\rangle = a^2 - b^2 \tag{11}$$

But, from eq. (10d):

$$a^2 = |\langle M^1_{HH}M^{1*}_{VV}\rangle|^2 / b^2 \tag{12}$$

Therefore,

$$b^4 + b^2\left(\langle M_{HH}M_{HH}^*\rangle - \langle M_{VV}M_{VV}^*\rangle\right) - \left|\langle M_{HH}M_{VV}^*\rangle\right|^2 = 0 \tag{13}$$

which is straightforward to solve for b^2 (which must be positive). Next, we solve for the noise power in the HV measurement, $\overline{\sigma}_{HV}^n$ $\left[\equiv(\sigma_{HV}^n + \sigma_{VH}^n)/4\right]$, via:

$$\overline{\sigma}_{HV}^n = \langle M_{HV}M_{HV}^*\rangle - \frac{\left|\langle M_{HV}M_{VV}^*\rangle\right|\left(\left|\langle M_{HH}M_{HV}^*\rangle\right| + \left|\langle M_{HV}M_{VV}^*\rangle\right|\right)}{\left(b^2 + \left|\langle M_{HH}M_{VV}^*\rangle\right|\right)} \tag{14}$$

It is then a simple matter to solve for a^2, σ_{HH}^n and $|\delta|$ from equations (10)-(12).

In Table 2, we present results from application of the above algorithm to the data corresponding to the patch of sea in the right-hand edge of the Flevoland image. [Note that from Figure 1 it can be seen that the C-Band HV image of this patch of ocean is fairly uniform, suggesting that the noise is indeed the major contributor to the HV measurement in this case.] Results are shown in the table for the noise-equivalent $\sigma°$ in the HH and HV measurements as well as the level of the cross-talk after calibration, $|\delta|^2$.

III. Backscatter signatures

Let us now return to the scattering matrix measurement for an arbitrary (but reciprocal, i.e., $S_{HV} = S_{VH}$) scattering matrix given in equation (1). After symmetrization and formation of the six cross-products, ignoring terms of order δ^2 where possible, and again assuming that $f_1 = f_2 = 1$, $\delta_1 = \delta_3$ and $\delta_2 = \delta_4$, that the like- and cross-polarized backscatter terms are uncorrelated, and that the different noise and backscatter terms are uncorrelated, we have:

$$\langle M_{HH}M_{HH}^*\rangle \cong |S_{HH}|^2 + \sigma_{HH}^n \tag{15a}$$

$$\langle M_{HV}M_{HV}^*\rangle \cong |S_{HV}|^2 + \sigma_{HV}^n \tag{15b}$$

$$\langle M_{VV}M_{VV}^*\rangle \cong |S_{VV}|^2 + \sigma_{VV}^n \tag{15c}$$

$$\langle M_{HH}M_{VV}^*\rangle = \langle S_{HH}S_{VV}^*\rangle \tag{15d}$$

$$\langle M_{HH}\ M_{HV}^*\rangle = \delta_2^*|S_{HH}|^2 + \delta_1^*\langle S_{HH}S_{VV}^*\rangle + 2\delta_2^*|S_{HV}|^2 \tag{15e}$$

$$\langle M_{HV} M_{VV}^{*} \rangle = \delta_1 |S_{VV}|^2 + \delta_2^{*} \langle S_{HH} S_{VV}^{*} \rangle + 2\delta_2 |S_{HV}|^2 \qquad (15f)$$

Note that equations (15e) and (15f) do not contain any information about the backscatter properties, which cannot be gleaned from equations (15a)-(15d), provided the noise powers are known. Equations (15e) and (15f) could be used instead to estimate the residual cross-talk after the calibration procedure has been carried out, in an identical fashion to [2], except that we can take noise into account by subtracting the appropriate noise terms from the HH, HV and VV measurements.

Equations (15a) to (15d) contain the basic pieces of information regarding the polarimetric scattering behavior of the target of interest. After noise subtraction, these are $|S_{HH}|^2$, $|S_{HV}|^2$, $|S_{VV}|^2$ and $\langle S_{HH} S_{VV}^{*} \rangle$. Many other parameters, including backscatter ratios, the Stokes matrix parameters, texture measures, pedestal heights, coefficient of variation, etc., can be derived from these basic measurements and their statistics.

Figure 2 shows a ground data map for the Flevoland site, which was collected around the time of the X-Band SLAR and DC-8 SAR overflights. The map is not complete, and may even be wrong in some instances, e.g., where farmers harvested their crops between the ground flight data collection and the overflight dates. From the figure, we have identified thirteen different backscatter types (classes), given in Table 3. There are eleven different types of agricultural fields in the data set, as well as one forest and one ocean data cell. In selecting the sites, we tried to choose the largest possible areas for each class and to reduce the spread of incidence angles across the data set (the smallest is 37° and the largest is 48°). For each of the thirteen sites, we extracted the first- and second-order statistics of the cross-products shown above, correcting the mean HH, HV and VV powers for the noise in each, estimated from the ocean data cell.

IV. Supervised classification

Using the corrected data for each of the thirteen classes, we formed a set of 21 parameters consisting of the HH, VV, and HV sigma-zeroes, HH/VV and HV/HH amplitude ratios, HH/VV phase difference, and HH/VV correlation coefficient magnitude for each of the three bands. We then produced a series of plots displaying the parameters as a function of site number (ie., target class) and band as shown in Figure 3. The particular order in which the classes are presented is of no importance; what we seek for each class is a parameter allowing it to be readily distinguished from all the others. Differences were considered significant if they exceeded the radiometric calibration uncertainty for the parameter. In the example of Figure 3, we found that the ocean (site 1), flax (site 9), and possibly forest (site 2) were easily identified by means of their HV backscatter. Examination of similar plots for the other parameters resulted in a list of the parameters most likely to allow identification of a given class (Table 4). While classes such as ocean and forest are easily identified using any one of a number of parameters, several including winter wheat and red beet cannot be distinguished at all when only one parameter is used.

With the thirteen selected sites serving as training areas, we then performed supervised classification of the entire image using decision criteria derived from

Table 4. This hierarchical classification scheme was found to be superior to linear discriminant analysis, which forces targets of all classes to be identified using the same subset of the 21 total parameters. Hierarchical classification uses a very small but changing (as a function of target type) set of parameters, allowing each class to be identified using the parameter(s) best suited to that class. We sought to minimize the error rate by first seeking classes which can be identified with great reliability. For example, if an area has an HV sigma-zero of under -35 dB, it is classified as water. If not, it is tested against the expected backscatter for flax, then forest, and so on. Areas which fail to meet tests for any of the classes are simply left unclassified.

Quantitative evaluation of the classification error rates was compounded by several factors. First, ground truth data are available for only a portion of the image. Second, as mentioned earlier, its accuracy is suspect, and some of the apparent misclassifications may be due to errors in the ground truth data. A field which is classified as a mixture of stem beans and forest has certainly been misclassified, but a field marked as "winter wheat" in the ground truth data, but in which 100% of the pixels are classified as bare soil may well have been harvested before the overflights. We found that classes such as water and forest, as well as certain crops (among them potatoes, peas, and beets) were correctly classified at rates of over 90%, while winter wheat and red beet are the hardest to classify.

Figure 4 shows a classifcation map of the entire image, with classes identified by the color key to the right of the image. For each 2-pixel by 2-pixel area of the image, we used backscatter parameters averaged over a 5-pixel by 5-pixel region as input to the hierarchical decision algorithm described above. By comparing this image with the ground truth data, we found that rectangular regions with few or no color variations are, in general, agricultural fields which have been correctly classified, while misclassification is evidenced by a mottled mixture of two or more colors. Classification errors due to the averaging process can also be seen along some field boundaries. The ocean (blue area in upper right) and forest (green, in lower right adjacent to the shoreline) are classified with very few errors. Potatoes (yellow in Figure 4, red in Figure 2) are also clearly identified.

V. Future Work

Identifying the decision criteria to use in classification is currently a rather tedious process which must be repeated each time a new set of classes is desired. An efficient, automated procedure for criteria selection would allow us to easily test the techniques described in this report on a number of different images. We did in fact develop some algorithms to calculate the usefulness of various parameters in distinguishing between classes, but these algorithms do not actually suggest decision criteria. Other possible areas of investigation include quantitative evaluation of classification error rates with and without the noise subtraction, and the sensitivity of error rates to changes in look angle.

References:

[1] Held, D.N, et. al., The NASA/JPL Multifrequency, Multipolarization Airborn SAR System, Proc. IGARSS'88, Edinburgh, Scotland, Ref. ESA SP-284, August 1988.

[2] van Zyl, J. J., Calibration of Polarimetric Radar Images Using Only Image Parameters and Trihedral Corner Reflector Responses, IEEE Trans. on Geoscience and Remote Sensing, Vol. GE-28, No. 3, pp. 337-348, May 1990.

[3] Klein, J. D., Calibration of Complex Quadpolarization SAR Images Using Backscatter Correlations, submitted to IEEE Trans. on Aerospace and Elec. Sys., 1989.

[4] Freeman, A., van Zyl, J. J., Kein, J. D., Zebker, H. A., and Shen, Y., Calibration of Stokes and Scattering Matrix Format Polarimetric SAR Data, submitted to IEEE Trans. Geoscience and Remote Sensing, January 1991.

[5] Zebker, H. A, van Zyl, J. J. and Held, D. N., Imaging Radar Polarimetry From Wave Synthesis, Journal of Geophysical Research, vol. 92, no. B1, January 1987, pp. 683-701.

[6] Dubois, P. C., and Norikane, L., Data Volume Reduction for Imaging Radar Polarimetry, Proc. IGARSS '87, Michigan, USA, 1987.

[7] Raney, R. K., A Free 3dB in Cross-Polarized SAR Data, Proc. IGARSS '87, Michigan, USA, pp. 565-569, 1987.

Acknowledgement:

Part of the research described in this paper was carried out by the Jet Propulsion Laboratory, California Institute of Technology, under a contract with the National Aeronautics and Space Administration. The authors would like to thank all those who took part in the summer 1989 campaign over Flevoland, particularly P. Hoogeboom and Jos Groot of FEL-TNO, and the crew of the DC-8 SAR, as well as those involved in collecting ground truth at the site and in deploying the radar calibration equipment.

Table 1: Estimated calibration performance (after calibration) from trihedral signatures

	L	C	P
Relative Radiometric error (across swath)	±1.7dB	±1.4dB	±1.7dB
Channel amplitude imbalance HH/VV	±2.1dB	±1.7dB	±1.2dB
Channel phase imbalance HH/VV	±4.3°	±8.0°	±12.6°
Cross-talk	<-25dB	<-26dB	<-19dB

Table 2: Noise equivalent σ^o and cross-talk estimates from ocean data.

	L-Band	C-Band	P-Band
σ^n_{HH}	-33.9dB	-32.2dB	-30.8dB
σ^n_{HV}	-40.9dB	-38.2dB	-34.8dB
$\lvert\delta\rvert^2$	-33.6dB	-30.9dB	-27.3dB

NOTE: $\sigma^n_{HH} = \sigma^n_{VV}$ in the model used.

Table 3: Backscatter types identified in the Flevoland image

Site #	Ground truth
1	Water
2	Forest
3	Stem Beans
4	Potatoes
5	Lucerne
6	Winter Wheat
7	Peas
8	Beet
9	Flax
10	Bare Soil
11	Red Beet
12	Grass
13	Summer Barley

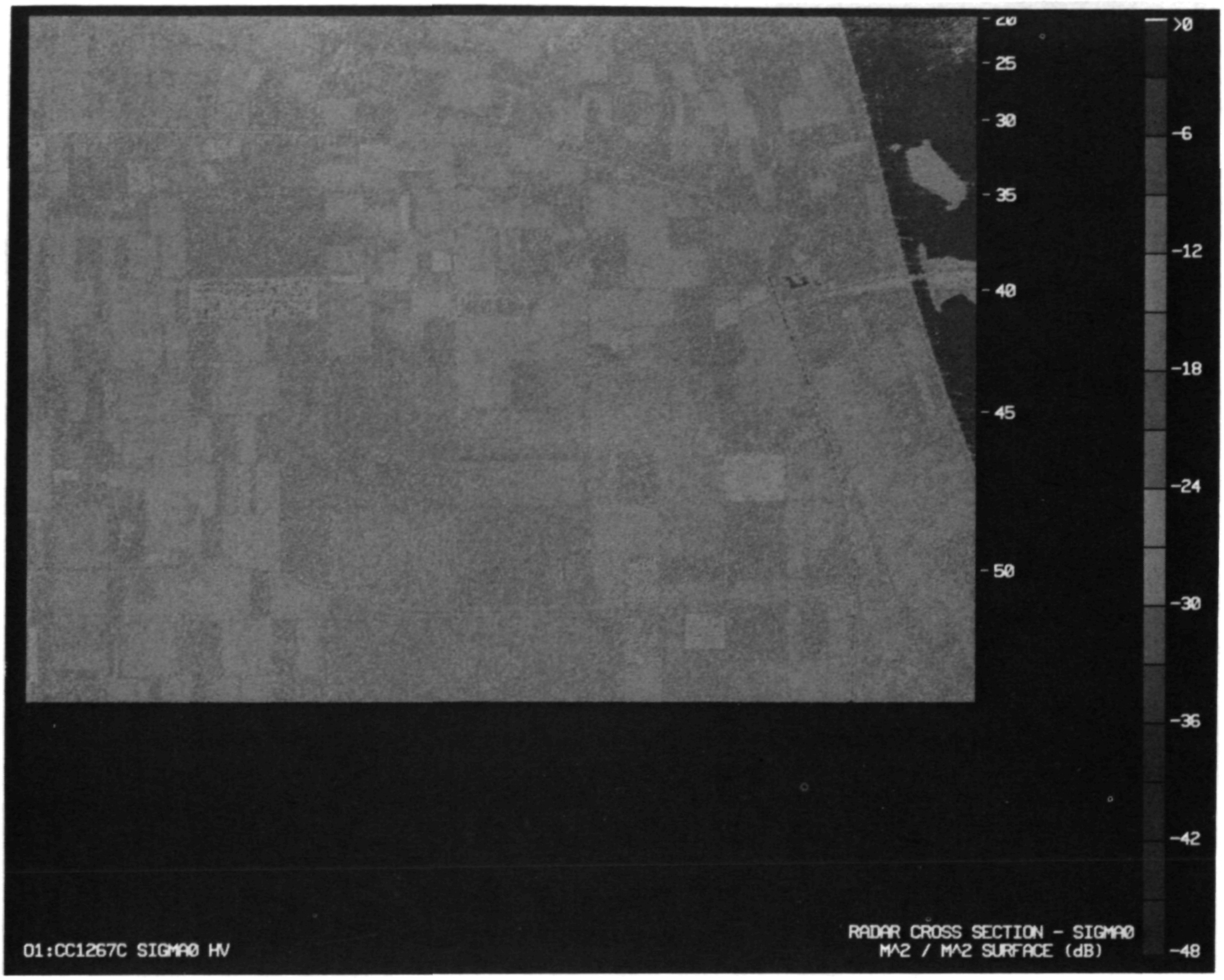

Figure 1. Calibrated C-band HV-polarized image of the Flevoland scene (see color slide no. 5).

Table 4: Parameters for unique separation between classes amongst the thirteen selected Flevoland data cells. Results are based on analysis of the separation between classes for each individual parameter (not combinations of parameters).

Parameters	1 Ocean	2 Forest	3 Stem beans	4 Po-tatoes	5 Lu-cerne	6 Wntr Wheat	7 Peas	8 Beet	9 Flax	10 Bare Soil	11 Red Beat	12 Grass	13 Smr. Barle
L-Band σ^o_{HH}	X												
L-Band σ^o_{HV}									X				
L-Band σ^o_{VV}													
C-Band σ^o_{HH}	X								X				
C-Band σ^o_{HV}									X			X	
C-Band σ^o_{VV}	X												
P-Band σ^o_{HH}		X											X
P-Band σ^o_{HV}		X											
P-Band σ^o_{VV}		X											X
L-Band HH/VV	X												
L-Band HV/HH		X											
C-Band HH/VV	X											X	X
C-Band HV/HH	X								X				
P-Band HH/VV	X			X			X						
P-Band HV/HH	X									X			
L-Band ϕ_{HHVV^*}		X	X										
C-Band ϕ_{HHVV^*}													
P-Band ϕ_{HHVV^*}		X	X					X					
L-Band $(1-\rho)$			X				X			X			
C-Band $(1-\rho)$	X								X				
P-Band $(1-\rho)$				X								X	

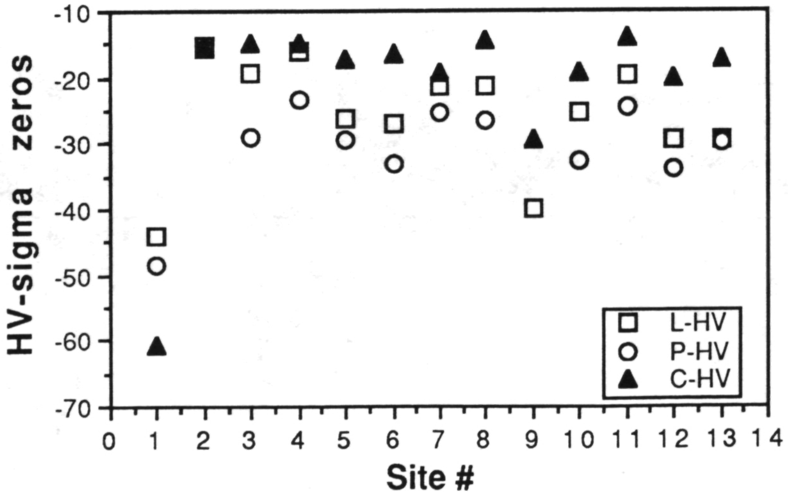

Figure 3: HV sigma-zeros for the 13 selected sites

Figure 2: Ground map for the Flevoland site for early August, 1989

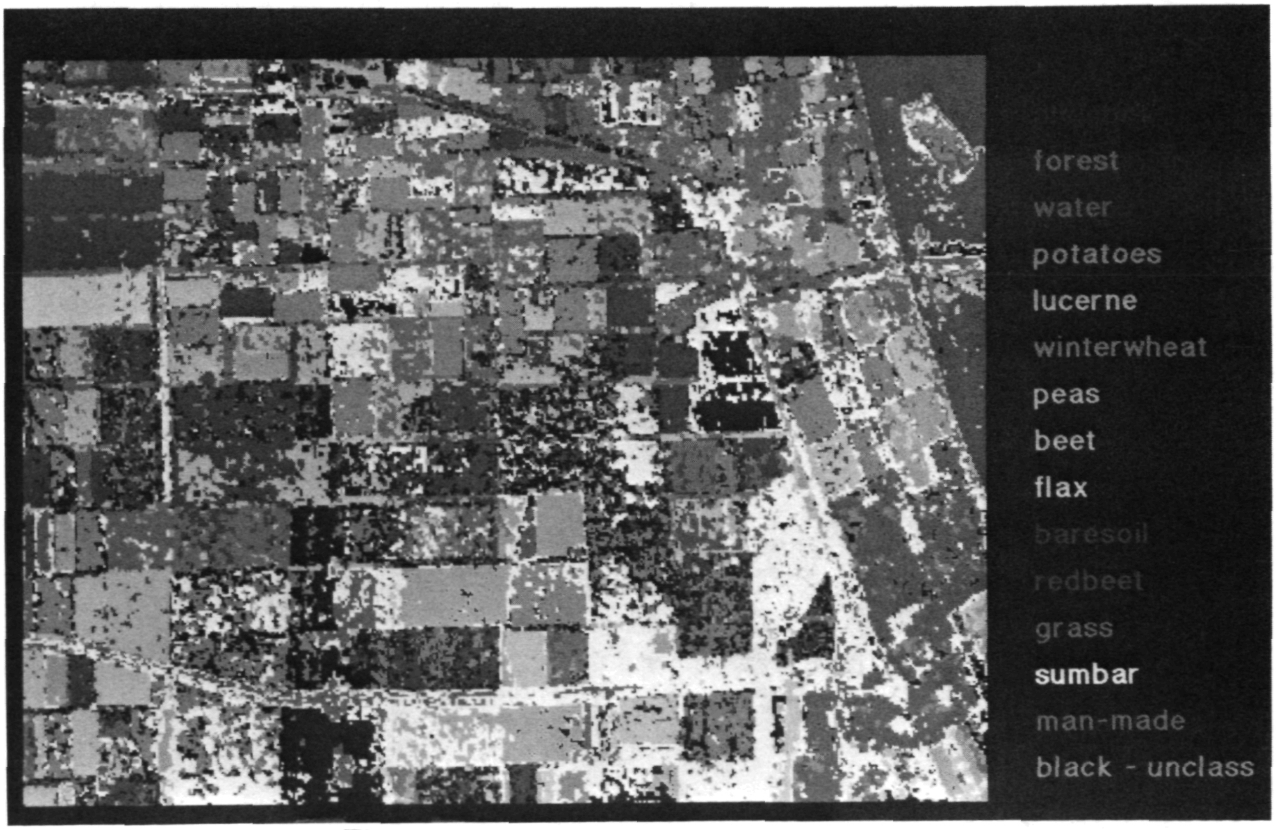

Figure 4: Classified image

N92-28019

MULTI-POLARIZATION C-BAND SAR FOR SOIL MOISTURE ESTIMATION

R.J. Brown
Canada Centre for Remote Sensing
Ottawa, Ontario, Canada

B. Brisco
Intera Kenting
Nepean, Ontario, Canada

ABSTRACT

Previous studies of synthetic aperture radar (SAR) imagery have shown qualitative relationships between radar backscatter and soil moisture. However, to be able to use these data in operational programs it will be necessary to establish quantitatively how the radar return is related to soil moisture and the effects of surface roughness, soil type, and vegetation cover and growth stage, as a function of frequency and polarization. To this end, a multi-year experiment began in 1990 as a cooperative venture amongst the Canada Centre for Remote Sensing, the Ontario Centre for Remote Sensing, the Land Resource Research Centre (Agriculture Canada), and the Universities of Guelph, Sherbrooke, Laval, and Waterloo.

During 1990, SAR imagery was acquired during two periods (May and July) to correspond to times of minimal and substantial vegetation cover. SAR data were acquired on three days in May and on four days in July to cover different soil moisture conditions. This unique comprehensive data set will be used to investigate the relationships between soil moisture and radar backscatter. This paper describes the experiment and data collected as well as providing a preliminary qualitative interpretation of the relationship between soil moisture and image tone.

INTRODUCTION

The determination of soil moisture is one of the important economic application areas (vegetation condition assessment) of synthetic aperture radar (SAR) which has good potential for success (Schmugge et al., 1980; Dobson and Ulaby, 1986) . Starting with the launch of the European Space Agency (ESA) European Remote Sensing Satellite (ERS-1) in 1991, there will be a multitude of SAR sensors in space during the 1990s including the Japanese Earth Resources Satellite (JERS-1) (1992), Shuttle Imaging Radar (SIR-C) (1993,94,95), Radarsat (1994), ESA ERS-2 (1994) and an Earth Observation System (EOS) SAR (1999). In order to effectively use these data operationally it is necessary to establish a quantitative relationship between the radar backscatter and soil moisture which is valid over the wide range of SAR parameters. To address this problem a multi-year experiment was begun in 1990 called OXSOME (**OX**ford County **SO**il **M**oisture **E**xperiment) with the following objectives:

1) To evaluate the capabilities of multi-date, multi-parameter SAR to estimate near surface soil moisture in an agricultural environment for a variety of soils and crops early in the season (post emergence stage) and mid-season (peak growth stage).
2) To develop a robust model relating radar backscatter to soil moisture taking into account surface roughness, crop type, soil texture and other factors which affect this relationship.
3) To evaluate the effects of free canopy water on crop separability information as a function of frequency and polarization.

This latter objective was included to investigate the all-weather capabilities of SAR for crop discrimination.

This experiment was a cooperative venture amongst the Canada Centre for Remote Sensing (CCRS), the Land Resource Research Centre (LRRC) (Agriculture Canada), the Ontario Centre for Remote Sensing (OCRS), and the Universities of Guelph, Laval, Sherbrooke, and Waterloo. In any field experiment, it is difficult, but imperative, to collect a statistically valid data set which correctly characterizes the ground. In this experiment, this was accomplished with great success, by pooling the efforts and resources of 30 persons to generate about 20,000 soil moisture observations as well as an extensive ancillary data set.

Remotely sensed data were collected in May and July under a variety of soil moisture conditions and supported by an extensive ground data set. These ground data included soil moisture (Portable Dielectric Probe (PDP), Time Domain Reflectometry (TDR) and soil bulk density samples), soil surface roughness, crop type and condition information, plant moisture, anomaly investigation, and meteorological information. In addition, corner reflectors and active radar calibrators (ARC) were deployed so that relative and absolute calibration of the SAR data could be carried out.

SITE DESCRIPTION

The study site is located in southern Ontario just south of the town of Norwich. The detailed study site, which is approximately 3 by 6 km, is comprised of three major soil types (Proud et al., 1990) and the fields that were sampled represented an array of different crop types on this variety of soils. Oxford County has been previously used for remote sensing studies and thus a geographic information system database exists for the site.

AIRBORNE DATA

The CCRS airborne SAR (Livingstone et al., 1987, 1988) was used to acquire C- and X-band data at four polarizations (VV, VH, HH and HV) in three modes; nadir, narrow and wide with various resolutions and incidence angles. Table 1 provides a summary of the system parameters of the CCRS SAR for these operating modes. These data were acquired three times in May and four times in July, 1990 just after significant rains. The flights were scheduled to follow the drying of the soil with the additional flight on July 14 used to acquire data while it was raining to address crop discrimination under wet plant and soil conditions. In summary the dates of acquisition and site conditions were as follows:

(a) May 22 and July 10 - Soil conditions were very wet, standing surface water was evident on the majority of the fields. However, the soil dried somewhat throughout the day (day 1);
(b) May 23 and July 12 - Soil conditions were less saturated with water. Almost all the surface water had dried. The soil had dried out mainly in the 1 - 2 cm surface range (day 2);
(c) May 25 and July 13 - Soil conditions were considerably drier, with the surface dry from the surface to 5 - 7 cm (day 3); and
(d) July 14 - The flight took place during a light rain event (about 1 cm of precipitation).

Infrared air photographs were acquired by the Ontario Centre for Remote Sensing on May 22 and on July 19 to coincide with the radar overflights. Ground information was acquired on and between the flight days with priorities established according to the dynamics of the target. Quick Look imagery on silver halide paper from the Real Time Processor in the CCRS aircraft was used for in-situ anomaly assessment. During the experiment these Quick Look images were taken back into the field within a day of data acquisition to determine the cause of anomalous tones on the images (anomaly assessment).

Three ARCs and three corner reflectors were deployed on separate bare soil plots on each of the flights in May and July (in July one was deployed near a sewage pond so that the recirculation signal would propagate over the water) to insure a low backscatter background for each of the calibration devices. During the flight while it was raining (July 14), the ARCs were covered with plastic to protect them from the precipitation. A detailed description of the ARC architecture and operating characteristics can be found in Brunfeldt and Ulaby, (1984) and the use of these devices for calibration of the CCRS SAR is described in Hawkins et al., (1989), Ulander et al., (1990), and Daleman et al., (1990).

The SAR soil moisture experiment plan required both relative and absolute calibration to meet the study objectives. Relative calibration establishes a relationship between the sensor output and a reference source. Hence, relative calibration establishes measurement consistency. Absolute calibration establishes a relationship between the sensor output and a physical quantity (such as a radar cross section of a point target). Hence, absolute calibration provides measurements which are independent of the specific system and directly represent a quantitative and predictable measure of a ground target property.

GROUND DATA

SOIL MOISTURE MEASUREMENTS

Twenty-one fields were extensively sampled to determine soil moisture on the May and July flight days using the following instruments/techniques:

(a) portable dielectric probes (PDP);
(b) time domain reflectometry instruments (TDR);
(c) soil sampling (bulk density samples) and sample weighting to extract volumetric soil moisture, bulk density, organic matter, and soil grain size distribution.

The main characteristics of these three instruments/techniques are fully described in: Brunfeldt (1987); Topp et al. (1980), and Cihlar et al. (1987), respectively. The fields were sampled along three transects (Figure 1). There were three "tie points" along the central transect where all three techniques/instruments were used to collect data to establish correlations between the different measuring techniques.

The PDPs measure the complex dielectric over a small depth (approximately 1 cm), consequently a depth profile of dielectric constant of the soil can be obtained. This profile can then be converted into a volumetric soil moisture profile using algorithms developed at CCRS (Brisco et al., 1991). The OXSOME experiment used four PDP's (two C-bands, one L-band, and one P band). Disks of known dielectric value were used to calibrate the PDP instruments after each flight period. Seven soil dielectric measurements were made at each 2 cm depth intervals from 0-10 cm at sites 1, 3, and 5 of transect 2 (Figure 1).

The TDR instrument (furnished by LRRC) provides a quick, reliable, and non-destructive average measurement of the soil dielectric values over a depth determined by the length of the probe. This average soil dielectric value can be converted into average volumetric soil moisture content using the relationship established by Topp et al. (1980). Accuracies achieved with TDR compare favourably to those obtained using gravimetric techniques. The TDRs were used to make measurements of 0-5, 0-10, and occasionally 0-15 cm layers at sites 1, 3, and 5 on all three transects (Figure 1). Three measurements were made at each depth range.

The bulk density sample technique is the most widely used method to determine soil moisture mainly because of its simplicity. The sample is obtained by vertically pressing a tube of known volume into the soil. The excessive soil at both ends of the tube is then removed to produce smooth/level planes, and the soil is then placed into an airtight bag. Samples were double bagged to prevent water loss and sent to a portable computerized weighing station within hours of extraction. The samples are then oven-dried and were weighed again at LRRC. Six bulk density samples were obtained per site, three at the 0-5 cm layer and three at the 5-10 cm layer. The bulk density samples were taken from all sites on transect 2 and from sites 2 and 4 on transects 1 and 3 (Figure 1). Samples were also saved for further soil analysis which included organic matter content and particle size distribution. The methodology used to acquire samples on the rain flight (July 14) was different due to limited resources and poor field conditions (it rained heavily for the first hour and lightly the second hour). TDR, PDP, and one bulk density sample were obtained at site 1 on each of the transects.

SURFACE ROUGHNESS

The surface roughness measurements were taken on May 24 and 25 and on July 11 using the Surface Roughness Meter model SRM-100 (Brisco et al., 1989; Paterson et al., 1990). This instrument is a two-component system designed to measure the roughness along 50 cm lengths on the ground using a photogrammetric technique. The field component of the system is based upon a 35 mm camera which photographs the target from a height of about a meter. Illumination is provided by a xenon flash which projects a rectangular bar of light onto the target. The camera is mounted at an acute angle to the axis of the projector, and thus the image contains information about the profile of the surface along the two edges of the bar.

The laboratory component of the system is an micro-computer interfaced to a solid-state video camera. The images of the light bars on the 35 mm negatives film are digitized and the subsequent analysis of the images provides full (x:y:z) profiles of each edge of the projected bar of light, RMS heights, and correlation lengths. The SRM-100 system was calibrated by using a photograph of a flat surface as an image positioning point. In addition to this flat-surface calibration process, three additional artificial surfaces, (rough, medium and fine), were measured to further compare the SRM-100 method of measuring with other surface roughness instruments. The results of the roughness calibration indicate accuracies of ≈ 1 mm in RMS and 5 mm for correlation length (Winebrenner et al., 1991).

For this experiment a roughness measurement consisted of six separate photographs, three perpendicular and three parallel to the row direction. In May, the roughness of five of the 21 detailed fields was measured at sites 1, 3, and 5 on all three transects. Also roughness measurements were obtained for many bare and semi-bare fields that appeared to have different roughnesses in the general study site. For the July sortie, roughness measurements were taken on four of the original May fields and on one extra field (bean field). These were taken on transects 1 and 3 at sites 1, 2 and 3.

VEGETATION SAMPLING

Vegetation biomass samples were obtained from all fields where soil moisture measurements were acquired, if sufficient plant cover existed. This was done once during the May and once during the July flight period. One sample was cut with a knife at the soil surface from sites 1, 3 and 5 on all three transect lines. The grain, pasture, alfalfa, and bean samples were cut from a twenty-five cm square. The corn plants were sampled as whole plants, and the number of plants per meter row was recorded. Biomass samples were placed in two plastic bags to prevent moisture loss, weighed within two hours of extraction, then dried at 70 degrees C, and weighed again to obtain the dry weight.

Biomass sampling was also conducted during the rainfall on July 14. Wet canopy biomass samples were acquired from site 1 on all three transect lines (Figure 1). The general methodology was the same as the dry canopy biomass methodology, but the samples were bagged in a way that attempted to capture all the canopy water. This was done by placing the plant material in the bag before cutting it away from the ground.

The following general ground information was also collected on each field within the study site using procedures described in King and Mack, (1984): vegetation/crop type, plant maturity, percentage of cover, plant condition, weed infestation, canopy height, row direction and spacing, photographs of each field, and general comments.

METEROLOGICAL DATA

Three farmers within the study site recorded temperature and precipitation measurements from May 1 to July 31. In addition, a Campbell Scientific portable weather station was set up on the site. The weather station recorded hourly information on the temperature, humidity, wind speed, and precipitation. Further weather data and storm radar information were also obtained from Environment Canada. Another 15 rain gauges were set up prior to the July 14 wet SAR flight. These rain gauges were placed at three different locations within the fields (i.e. between plants along a row, between rows, and in an adjacent bare field). The data obtained from the rain gauges will qualitatively aid in determining how much water actually reached the soil surface and how it is distributed within the canopy. During the rain-day acquisition about 10 mm of rain fell, within the first hour of the two hour event followed by light rain in the second hour.

QUALITATIVE INTERPRETATION

At the time of this writing the ground data have been checked for quality control and put into digital format for subsequent analysis. The qualitative evaluation of these data indicate the excellent nature of this data set and the wide range of soil moisture and surface roughness conditions prevalent during the experimental period. For example the data in Table 2 summarizes the roughness statistics from 65 fields measured in May. The data represent a large range of conditions from quite smooth (RMS=2.53 mm) to quite rough (RMS=33.7 mm). The May gravimetric soil moisture data for a "sandy" versus a "clay" field are given in Table 3. The sandy field is considerably drier on day 1 (May 22) with about a 10 % decrease in soil water content when compared to the clay field. This difference is only about 4 % by day 3 (May 25). These results are also supported by the PDP data shown in Figures 2 and 3. Here the progressive drying of the soil profile and increasing depth of the wetting front is apparent. The convergence of soil moisture content for the sandy and clay fields over the experiment period is also supported in these figures. The qualitative interpretation of the ground data was very promising, as these results show, and excellent quantitative results are expected.

This is supported by an image interpretation of a three-band colour composite shown in Figure 4. This image is a combination of C-VV (red), C-HV (green), and C-HH (blue) narrow swath data from May 22 and clearly demonstrates several aspects of the data set. First of all, notice that the field marked A on Figure 4, which is alfalfa, has a lower backscatter than the bare fields in all polarizations and thus are very dark on the colour composite. Thus the vegetation appears to be attenuating the radar backscatter and thus severely limiting the information content on soil moisture content. Secondly, notice the range of backscatter in the bare fields indicating different polarization response from the bare soil. Roughness, row direction and soil water content could all play a role in determining these differences, which will be investigated in later analyses. Also note the area marked B in Figures 4 and 5 where there is a marked change in backscatter due to the soil change from a sandy soil to a heavier textured clay soil. This soil type change is very evident on the SAR false colour image and shows up clearly in the aerial photography (Figure 5) as well. These relationships will be studied in detail once the data is calibrated, which is the next step in the overall analysis plan.

SUMMARY

This paper is intended to give an overview of the airborne and ground data set which was acquired during OXSOME 1990. There will be a considerable number of scientific publications on the results of the analysis which will appear in the open literature in the next couple of years.

ACKNOWLEDGEMENTS

The authors would like to acknowledge the splendid cooperation of the farmers within the test area who gave us permission to carry out ground information acquisition on their land. Also, we would like to acknowledge the efforts of all the persons who contributed to the ground data acquisition, the flying of the aircraft and data acquisition, and the laboratory crews who weighed and documented all of the soil samples.

REFERENCES

Brisco, B., R.J. Brown, J. Cihlar, and R.S.W. Brancker, 1989, "A Field Instrument for Surface Roughness Measurement", International Geoscience Remote Sensing Symposium / 12th Canadian Symposium on Remote Sensing, Vancouver, B.C., July 10-14, pp. 1177-1180.

Brisco, B., T.J. Pultz, R.J. Brown, G.C. Topp, M.A. Harris, and W.D. Zebchuk, 1991, "Soil Moisture Estimation with Portable Dielectric Probes and TDR Techniques", submitted to Water Resources Research.

Brunfeldt, D.R., 1987, "Theory and Design of a Field - Portable Dielectric Measurement System", International Geoscience and Remote Sensing Symposium Digest, IEEE Cat. No. 87CH2434-9, Vol. 1, pp. 559-563.

Brunfeldt, D.R., and F.T. Ulaby, 1984, "Active Reflector for Radar Calibration", IEEE Trans. Geoscience and Remote Sensing, Vol. GE-22, No. 2, pp. 165-169.

Cihlar, J., M.C. Dobson, T. Schmugge, P. Hoogeboom, A.R.P. Janse, F. Baret, G. Guyot, T. Le Toan, P. Pampaloni, 1987, "Review Article - Procedures for the Description of Agricultural Crops and Soils in Optical and Microwave Remote Sensing Studies", International Journal of Remote Sensing, Vol. 8(3), pp. 427-439.

Daleman, P.S., R.K. Hawkins, T.I. Lukowski, 1990, "Experience with Active Radar Calibrators for Airborne SAR", International Geoscience and Remote Sensing Symposium, Washington, D.C., May 22-25, pp. 795-798.

Dobson, M.C. and F.T. Ulaby, 1986, "Active Microwave Soil Moisture Research", IEEE Trans. Geoscience Remote Sensing, Vol. GE-24, pp. 23-36.

Hawkins, R.K., T.I. Lukowski, A.L. Gray, and C.E. Livingstone, 1989, "Calibration for Airborne SAR", International Geoscience and Remote Sensing Symposium / 12th Canadian Symposium on Remote Sensing, Vancouver, B.C., July 10-14, pp. 238-242.

King, G.J., and A.R. Mack, 1984, "A Manual for Recording Significant Agricultural Ground Information in Remote Sensing Programs", Draft #3E, Agriculture Canada, Ottawa.

Livingstone, C.E., A.L. Gray, R.K. Hawkins, R.B. Olsen, J.G. Halbertsma, and R.A. Deane, 1987, "CCRS C-band Airborne Radar System: Description and Test Results", Eleventh Canadian Symposium on Remote Sensing, Waterloo, Ontario, June 22-25, pp. 503-515.

Livingstone, C.E., A.L. Gray, R.K. Hawkins, and R.B. Olsen, 1988, "CCRS C/X- Airborne Synthetic Aperture Radar: An R and D Tool for the ERS-1 Time Frame", Proceedings of the 1988 IEEE National Radar Conference, April 20-21, The University of Michigan, Ann Arbor, Michigan, pp. 15-21.

Paterson, J.S., B. Brisco, S. Argus, and G. Jones, 1990, "In-Situ Measurements of Micro-Scale Surface Roughness of Sea Ice", Arctic, in press.

Proud, B., R. Protz, and B. Brisco, 1990, "Temporal Changes in Radar Backscatter of Crop Canopies due to Soil Effects", Canadian Journal of Remote Sensing, Vol. 16(3), pp. 30-36.

Schmugge, T.J., T.J. Jackson, and H.L. Mckim, 1980, "Survey of Methods for Soil Moisture Determination ", Water Resources Res., Vol. 16(6), pp. 961-970.

Topp, G.C., J.L. Davis, and A.P. Annan, 1980, "Electromagnetic Determination of Soil Water Content: Measurements in Coaxial Transmission Lines". Water Resources, Vol. 16(3), pp. 574-582.

Topp, G.C., 1987, "The Application of Time-Domain Reflectometry (TDR) to Soil Water Content Measurement", International Conference on Measurement of Soil and Plant Water Status, Logan, Utah, U.S.A. Vol. 1, pp. 85-93.

Ulander, L.M.H., R.K. Hawkins, C.E. Livingstone, and T.I. Lukowski, 1990, "Absolute Radiometric Calibration of the CCRS SAR", submitted to International Journal of Remote Sensing.

Winnebrenner, D., B. Brisco, C. Garrity, R. Ramseier, M. Romkens, A. Fung, and R. Brown, 1991, "A Comparison of Methods for In Situ Measurement of Sea Ice Surface Roughness", to be submitted to IEEE Geoscience and Remote Sensing.

Table 1

CCRS C/X SAR System Parameters

	Mode Nadir	Narrow Swath	Wide Swath
Resolution (m)	6x6	6x6	range-20 azimuth-10
Swath Width (km)	22	18	63
Incidence Angle (°)	0-74	45-76	45-85

Table 2

Summary of Roughness Statistics for Bare Fields in May

Number of Fields	RMS Height (mm)		Correlation Length (mm)	
	Min	Max	Min	Max
65	2.53	33.70	7.0	52.0

Table 3

Summary of 0.5 cm Gravimetric Soil Moisture (gm/cm^3) Content for May.

Date	Sand	Clay
May 22	21.7 ± 4.8	31.1 ± 1.1
May 23	20.7 ± 4.9	28.7 ± 2.1
May 25	18.8 ± 4.5	22.5 ± 1.7

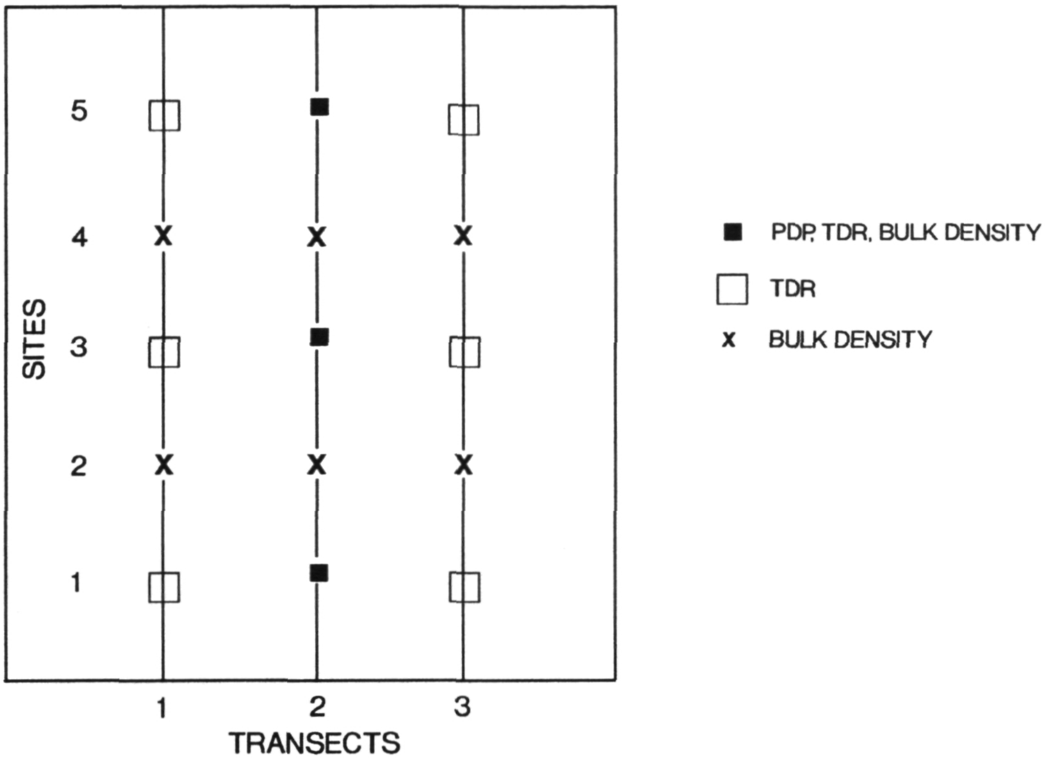

Figure 1. Soil moisture sampling scheme (32 metres spacing between sites).

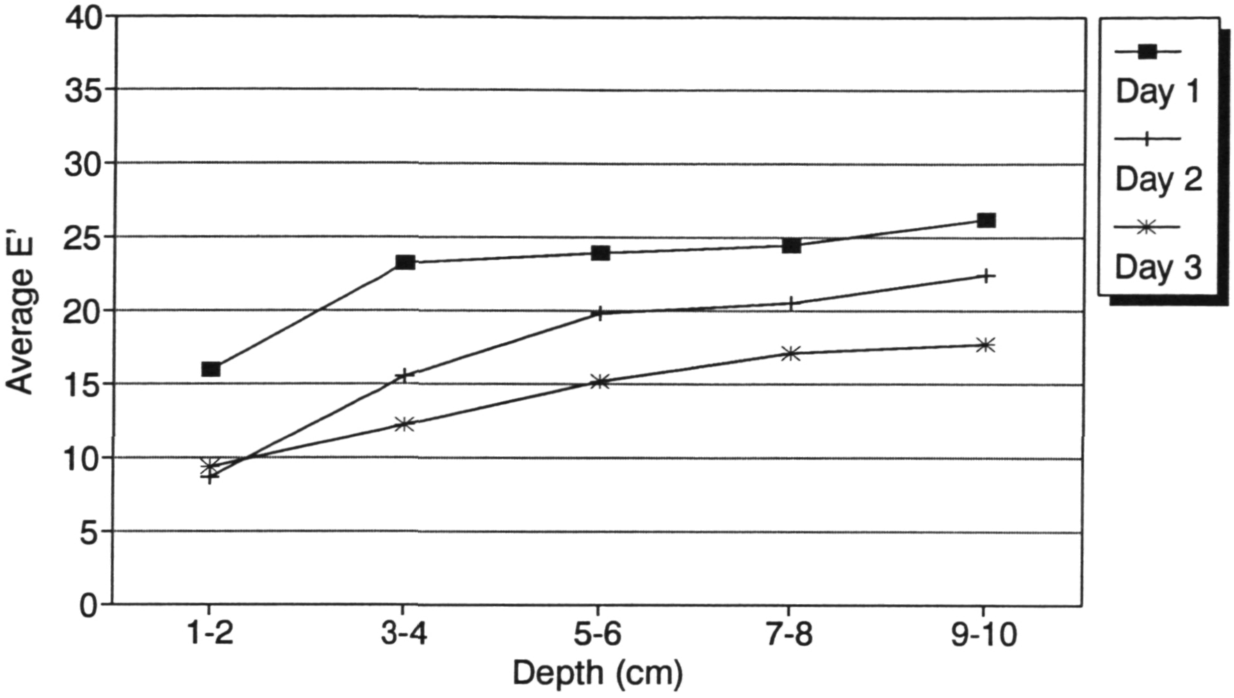

Figure 2. The dielectric constant verses depth of a sandy field for the three flights in May.

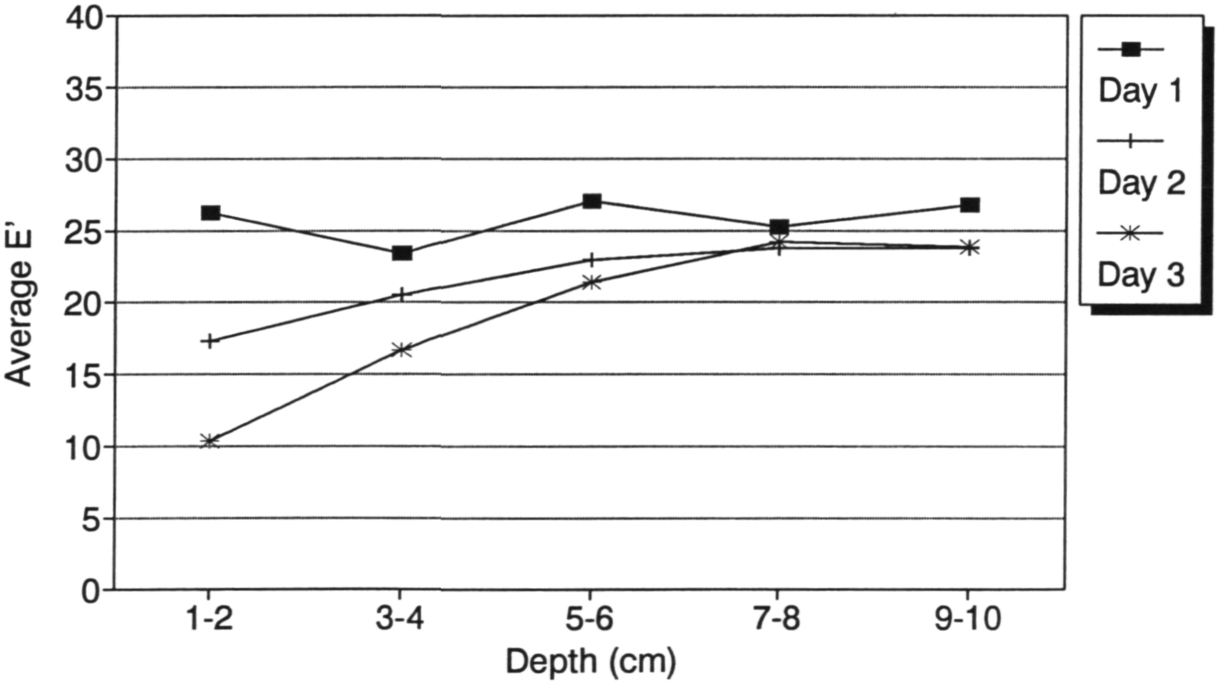

Figure 3. The dielectric constant verses depth of a clay field for the three flights in May.

Figure 4 False colour SAR composite of C-W, C-HV, and C-HH narrow swath data from May 22 **(see slide no. 6).**

Figure 5 A colour infra-red photograph of the study area showing the change from clay to sandy soil **(see slide no. 7).**

N92-28020

SOIL MOISTURE MEASUREMENTS FROM AIRBORNE SAR

Jiancheng Shi, Joao V. Soares
and Laura Hess
CRSEO
University of California,
Santa Barbara

Edwin T. Engman
NASA/GSFC
Hydrological Sciences Branch

Jakob J. van Zyl
Jet Propulsion Laboratory
California Institute of
Technology

Abstract — This paper reports preliminary results of algorithm development and testing for soil moisture retrieval at high incidence angles. Based on first-order surface backscattering models, a physically based algorithm for retrieval of soil moisture has been developed and evaluated using NASA/JPL aircraft SAR data. It shows that the co-polarization ratio is sensitive to soil moisture change but not to surface roughness at high incidence angles. This algorithm performed well at L-band and should be useful for repetitive, large-area soil moisture monitoring, without requiring surface roughness measurements. This study suggests that incidence angles greater than 40° are optimal for such monitoring.

Keywords: soil moisture, dielectric function, radar models.

I. INTRODUCTION

Estimates of soil moisture are of great importance in numerous environmental studies, including hydrology, meteorology, and agriculture. In spite of its importance, soil moisture information is not widely used in resource monitoring or prediction because it is difficult and costly to obtain on a routine basis over large areas [1]. Ground-level, aircraft, and satellite measurements of radar backscattering from agricultural fields [2, 3] aircraft altitudes [4], and at satellite altitude [5] indicate that the backscattering coefficient is sensitive to soil moisture up to 5 or 10 cm below the surface, and that the optimal radar parameters for estimating soil moisture are C-band, incidence angles of 5 to 20 degrees, and HH polarization.

Because radar backscatter is affected by surface roughness and vegetation, as well as by soil moisture, any practical application of radar must be able to account for all three of these target features. Thus, if one were interested in monitoring soil moisture over a mixed area, the effects of surface roughness and plant canopy would have to be subtracted from the measurements of radar backscatter in order to isolate soil moisture effects. At small incidence angles, surface roughness effects on the received radar signature are minimized. Results of other investigators have shown considerable variability in the relationship between soil moisture and radar backscattering for different sites, and a large range in suggested optimal incidence angles for soil moisture monitoring. This variability suggests that many algorithms are site-specific, and that a need exists for portable algorithms that do not require fitting to specific site conditions. Furthermore, algorithms that are limited to small incidence angles narrow the spatial application of airborne imaging radar to the near range of the swath. Because SAR measurements generally range from 15° to 55° in incidence angle, algorithms to retrieve soil moisture at a wider range of angles are needed. The main objective of this study is to develop and evaluate an algorithm to estimate bare soil moisture using far-range SAR data. The problems of minimizing surface roughness effects and the performance of some commonly available models using a large data set are addressed.

II. DESCRIPTION OF EXPERIMENT

An experiment was conducted in September 1989 with the NASA/JPL airborne imaging radar polarimeter in an agricultural area near Fresno, California. The experiment consisted of two flights six days apart (Sept. 8 and 14). An L-band three-polarization (VV-red, HH-green, and HV-blue) image of the study site is shown in Figure 1. At the time of the study, most of the fields were either bare or covered with mature cotton plants. Crops in the remaining fields included alfalfa, corn, lettuce, vineyards, and orchards.

Ground measurements of soil moisture and surface roughness were taken on both flight dates in eight of the bare fields. Soil samples were obtained for three depths: 0 to 5 cm, 5 to 10 cm, and 10 to 15 cm, and soil moisture was determined gravimetrically. The volumetric soil moisture for the sampled dry fields varied between 3 and 9 percent, corresponding to real dielectric constants of 3 to 5.5 for C- and L-bands. Some of the measured fields were too small to obtain an adequate number of radar pixels for algorithm testing. In addition, the measured fields all fell within the near range of the radar swath; because the focus of this analysis is the far range, dielectric constants for other bare dry fields in the far range of the swath were assumed to range from 3 to 5.5 also. This assumption is felt to be valid because the fields are flat and essentially uniform in soil texture. None of them had been irrigated for at least several weeks; under conditions of high temperatures, low humidity, and no rainfall, the fields approach a fairly constant and homogeneous surface moisture condition until winter rains or irrigation begins.

Surface roughness was estimated using photographs of a gridded panel, oriented both parallel and perpendicular to rows in furrowed fields. Photographs were digitized, and the correlation length and standard deviation of the surface height were determined. For the flat fields, the standard deviation of the surface height was within 1 cm, and the correlation distance varied from 3 to 19 cm, depending on the starting point. The condition of stationarity was not observed, so that extrapolation from field measurements to the pixel level could not be done.

Five corner reflectors were deployed during the two flights. The measured elements of the Stokes matrix were fully calibrated using the algorithms developed by van Zyl and others [6], which include phase, cross-talk, channel imbalance, and absolute calibration.

III. PHYSICAL BASIS OF ALGORITHMS

The interaction between electromagnetic waves and bare soil can be approximately described as a surface scattering problem. The scattering of electromagnetic waves by rough surfaces has been studied for many years, but no exact closed-form solutions have been obtained. Numerical techniques can be used to compute the exact solution, but in general these techniques are computationally prohibitive and are used only in evaluating the accuracy and range of validity of approximate models [7]. When dealing with practical applications, simpler approximate models are often used. Although valid only within a limited range of rough surface parameters, these models can still be used quite effectively in many situations. Three types of surface scattering model are generally used in soil backscattering simulation, depending on surface roughness conditions.

- The small perturbation method assumes that variations in surface height are small relative to the wavelength and that the surface slope is small.
- The physical optics model (the Kirchhoff model under the scalar approximation) is given by the sum of the coherent part σ_{cp}, noncoherent part σ_{np}, and the term due to surface slope σ_{sp}. The approximation is valid when the radius of curvature is large and the rms surface slope is small relative to the wavelength.
- The geometrical optics model (the Kirchhoff model under the stationary-phase approximation) is generally valid when both the average radius of curvature and the vertical roughness are large relative to the wavelength.

Detailed explanations and validity conditions for these models can be found in [8]. The correlation function for a rough surface may be Gaussian or exponential in form, depending on the surface roughness characteristics.

Since surface scattering is a function of reflectivity and surface roughness, all three surface backscattering models can be represented as a product of dielectric and surface roughness functions:

$$\sigma^{pp}(f,\theta_i) = D(f,pp,\theta_i) \times S(f,\theta_i,s,l) \tag{1}$$

where *pp* indicates polarization, *f* is frequency, and θ_i is incidence angle.

For the small perturbation model, the dielectric functions can be expressed as a function of frequency, polarization, surface dielectric properties, and incidence angle, as follows:

$$D(hh,\theta_i) = |\alpha_{hh}(\theta_i)|^2 = \left| \frac{\varepsilon_r - 1}{(\cos\theta_i + \sqrt{\varepsilon_r - \sin^2\theta_i})^2} \right|^2 \tag{2}$$

and

$$D(vv,\theta_i) = |\alpha_{vv}(\theta_i)|^2 = \left| \frac{(\varepsilon_r - 1)\,(\varepsilon_r\,(1 + \sin^2\theta_i) - \sin^2\theta_i)}{(\varepsilon_r \cos\theta_i + \sqrt{\varepsilon_r - \sin^2\theta_i})^2} \right|^2 \tag{3}$$

where ε_r is the relative dielectric constant. The surface roughness function at given frequency f and incidence angle θ_i is given by:

$$S(f,\theta_i,W) = 8k^4 \cos^4\theta_i\, W(2k\sin\theta_i) \tag{4}$$

It is characterized by a function of frequency, incidence angle, and the surface roughness spectrum W.

Similarly, for the physical optics model, the coherent part of the backscatter signal can be ignored at incidence angles that are not near normal; when we consider the backscatter from the noncoherent term only [9], the dielectric functions are given as:

$$D(f,pp,\theta_i) = |R_{pp}(\theta_i)|^2 \tag{5}$$

where

$$R_{vv}(\theta_i) = \frac{(\varepsilon_r - 1)\,(\varepsilon_r \cos^2\theta_i - \sin^2\theta_i)}{(\varepsilon_r \cos\theta_i + \sqrt{\varepsilon_r - \sin^2\theta_i})^2} \tag{6}$$

and R_{hh} is same as α_{hh} in the equation (2). And

$$D(f,pp,\theta_i) = |R_{pp}(\theta_i)|^2\,(1 + \sin^2\theta_i) + Re\,[R_{pp}(\theta_i)\,R^*_{pp\,1}(\theta_i)]\,\sin 2\theta_i \tag{7}$$

$$R_{hh\,1}(\theta_i) = -\,\frac{2\sin\theta_i\, R_{hh}(\theta_i)}{\cos\theta_i + \sqrt{\varepsilon_r - \sin^2\theta_i}} \tag{8}$$

where

$$R_{vv\,1}(\theta_i) = \frac{\sin\theta_i\,[R_{vv}(\theta_i)\,(\varepsilon_r + 1) - \varepsilon_i + 1]}{\varepsilon_r \cos\theta_i + \sqrt{\varepsilon_r - \sin^2\theta_i}} \tag{9}$$

when we consider the backscattering from both the noncoherent term and that due to slope [10]. Assuming a Gaussian correlation form, the surface roughness function for the physical optics model is given by

$$S(f,\theta_i,s,l) = (kl)^2 \exp(-K_0) \sum_{n=1}^{\infty} \frac{(K_0)^n}{n\,n!}\, exp\,(-\frac{(kl\sin\theta_i)^2}{n}) \tag{10}$$

where $K_0 = 4k^2 s^2 \cos^2(\theta_i)$, k is the wave number in free space, s is the standard deviation of surface height, and l is the surface horizontal correlation length.

For both the small perturbation and physical optics models, the dielectric functions are a function of incidence angle, frequency, polarization, and dielectric properties of the surface. They are independent of both the surface roughness correlation function form and the roughness parameters. The surface roughness functions are a function of frequency, incidence angle, the surface roughness correlation form, and its roughness parameters. They are independent of polarization.

For the geometrical optics model, the dielectric and surface roughness functions are given by

$$D(f) = |R_{hh}(0)|^2 = |R_{vv}(0)|^2 = \frac{\sqrt{\varepsilon_r} - 1}{\sqrt{\varepsilon_r} + 1} \tag{11}$$

and

$$S(\theta_i) = \frac{1}{2m^2 \cos^4(\theta)} \, exp\,(-\frac{\tan^2(\theta)}{2m^2}) \tag{12}$$

which indicate that for this model the dielectric function depends only on the dielectric properties of the surface at a given frequency. It is independent of polarization and incidence angle. The surface roughness function is characterized by a function of incident angle and mean random surface slope. It is independent of both polarization and frequency.

If surface backscattering is modeled by either the small perturbation or the physical optics model, the measured ratio

$$\frac{\sigma^h(f,\theta_i)}{\sigma^v(f,\theta_i)} = \frac{D(f,hh,\theta_i)}{D(f,vv,\theta_i)} \tag{13}$$

is expected to be independent of the surface roughness function. Because single surface scattering mechanics indicates that the relative phase difference between HH and VV polarizations approaches zero, the imaginary part of the dielectric function is very small. Therefore, we can either use the magnitude of the dielectric constant to replace the complex dielectric constant or express the dielectric function as a function of incidence angle θ_i and refractive angle θ_t at a given frequency and polarization through Snell's law [11]. For instance, the dielectric function ratio between HH and VV polarizations for the small perturbation model can be written as

$$\frac{\sigma^h(f,\theta_i)}{\sigma^v(f,\theta_i)} = \frac{\cos^4(\theta_i - \theta_t)}{\sin^2\theta_i + \cos^2\theta_t} \tag{14}$$

so that the refractive angle is the only unknown value in this ratio and can be easily solved for. After solving for the refractive angle, the magnitude of the dielectric constant can be obtained through Snell's law, as can soil moisture.

If the geometrical optics model is used, the ratio of co-polarization signals does not provide any information about surface dielectric properties and roughness conditions because both dielectric and surface roughness functions are the same for the co-polarization signals.

Figure 2 shows the ratio of the HH and VV dielectric functions for the small-perturbation model. It shows that the dielectric function ratio is sensitive to soil moisture change at higher incidence angles but not at near-nadir angles. At a given dielectric constant, the value of the ratio decreases for the small-perturbation model, with incidence angle increasing, but it increases for the physical optics model. With increasing incidence angle, the sensitivity of the dielectric function ratio to surface dielectric constant and soil moisture increases, especially at soil moistures less than 30 percent by volume. Sensitivity decreases as soil moisture increases, and is essentially the same for L-band and C-band. This indicates that neither frequency has an advantage when using the co-polarization ratio if surface roughness conditions are within the valid range for both bands.

IV. RESULTS AND DISCUSSION

To develop an algorithm for monitoring soil moisture over large areas, we need to select scattering models from the observed signals for different surface roughness conditions on a pixel-by-pixel basis. Since the surface roughness function $S(f,\theta,s,l)$ is independent of polarization, the ratio of co-polarization signals not only is independent of the surface roughness function but also indicates which surface backscattering model should be applied.

- For the small-perturbation model, σ^h / σ^v is always less than one except at near-normal incidence.
- For the physical optics model, the ratio is greater than one because σ_h is greater than σ_v, except at near-normal incidence.
- For the geometrical optics model, the ratio is always equal to one.

Therefore, the surface roughness condition and the choice of scattering model can be automatically determined for each image pixel by using the ratio of the co-polarization signals.

In addition to selecting a scattering model, we need to consider both the problem of speckle and the limitation that the algorithms can only be applied to single surface-scattering problems because they are based on first-order solutions. To overcome these problems, we first apply the scattering-based classification algorithms developed by Van Zyl [12] and only use those pixels that are classified as single reflections. Secondly, we determine the physical ranges of the co-polarization dielectric function ratio for the models by testing two extreme cases of possible soil moisture conditions, as shown in Figure 3. We then select those pixel values that are in the physical ranges and apply the inversion algorithms for dielectric constant retrieval. Since some pixels are either out of the physical ranges or do not show single-reflection scattering, some pixels with missing values are expected. After the algorithm is applied, a median filter is used to remove unexpected values and a linear interpolation is applied to fill in pixels with missing values.

Figures 4 and 5 show a SAR image of the study area (L-band, HH polarization) and an image of the inversion-derived dielectric constant, respectively. The image brightnesses are proportional to the backscattering coefficient and the magnitude of the dielectric constant. The bare dry fields are displayed in dark tones in both images. At higher incidence angles, the dry bare fields are clearly distinguishable from the vegetation-covered fields because of greatly increased volume scattering from the vegetation layer. At lower incidence angles (<30°), bare fields cannot reliably be distinguished from vegetated fields because the backscattering coefficients are not very sensitive to the volume scattering from the vegetation layer. Table 1 shows the inversion results for test fields. The algorithm-derived dielectric constant range of 1.96 to 4.5 agrees well with the ground estimate of 3 to 5.5 for those bare dry fields. As marked, there are two bare fields on both images, one has rough surface at an incidence angle 43.5° with lower backscattering coefficients and the other has relative rough surface at 47.3° with higher backscattering coefficients. The only explanation is that the second field has greater soil moisture. The soil moisture difference of these two fields and the wet lettuce fields are all clearly measured as shown in the dielectric constant image (Figure 5).

Since the algorithm only accounts for surface scattering, the volume-scattering contribution or even a small error introduced by the calibration or signal noise can result in a mis-estimation of the surface dielectric constant. This confirms that the co-polarization ratio is sensitive to the surface dielectric constant or soil moisture only at higher incidence angles, as discussed earlier in this section. Because the interactions between radar signals and corn or cotton fields involve less multi-scattering phenomena at L-band than at higher frequencies, they still show the characteristics of single reflections. Therefore, the algorithm still considers those fields within the valid conditions. Since neither the volume scattering by vegetation nor the interactions between the surface and vegetation cover are included in this algorithm, an overestimation of the dielectric constant for those vegetation-covered fields is also shown in Figure 4.

Because of the difficulty of extrapolating the surface roughness correlation function from point measurements to the pixel scale, attention was focused on the dielectric function in this study. These dry bare fields had not been irrigated for at least several weeks and they are flat and uniform in soil texture. There is thus little chance for moisture movement other than vertical, and a spatial uniformity of soil moisture between dry bare fields can be assumed. The standard deviation of the rms surface height is from 0.6 cm to 0.8 cm for the dry bare fields from the ground measurements. This indicates that the small perturbation and physical optics models should be applied to the L-band and C-band data, respectively.

The inversion results for the C-band data do not agree with the field measurements. Applying the physical optics algorithm when it includes both a noncoherent term and that due to slope, only a few pixels in the image data set are within the physical range. On the other hand, a great number of pixels fall into the physical range when the algorithm includes only the noncoherent term. When comparing the inversion results from L-band and C-band data, C-band results were two to four times greater than those obtained from L-band for the same pixel. Since there is little difference in the dielectric constants at L-band and C-band for dry bare soils, there appears to be a problem with the application of the physical optics model for this application; this problem requires further study. Possible reasons for the algorithm's failure to estimate the surface dielectric constant or the soil moisture at C-band might be that more multiple scattering is involved at C-band and that the surface roughness parameters might not be within the validity condition range for the physical optics model. Engman and Wang (1987) also found that the small perturbation model matched SIR-B data best of the three surface backscatter models, based on intensive field measurements. Since our algorithm is based only on surface backscatter models, the good agreement of the inversion results at L-band also indicated that the small perturbation model performs better.

V. CONCLUSIONS

This study shows preliminary results on developing and testing algorithms for soil moisture retrieval at high incidence angles. Two surface backscattering models and the ratio of the co-polarization signals were evaluated for their ability to measure soil moisture. The small perturbation model and its ratio of the co-polarization signals gave better results for bare fields without periodic row structures. The relative roughness of the fields was not great enough to evaluate the geometrical optics model.

The co-polarization ratio shows good potential for measuring soil moisture for both bare and some short vegetation-covered fields, such as onion and lettuce, at high incidence angles. This ratio is sensitive to soil moisture change--especially when soil moisture is less than 30 percent by volume--but not to surface roughness at high incidence angles. The inversion algorithm performs well at L-band and should prove useful for routine and large-area soil moisture monitoring. This study also suggests that the optimal incidence angle range for this application is above 40°.

REFERENCES

[1] J. R. Wang, E. T. Engman, J. C. Shiue, M. Rusek, and C. Steinmeier, ''The SIR-B observations of microwave backscatter dependence on soil moisture, surface roughness, and vegetation covers,'' *IEEE Trans. on Geosci. and Remote Sensing*, vol. GE-24, no. 4, pp. 510-516, 1986.

[2] F. T. Ulaby, P. P. Batlivala, and M. C. Dobson, ''Microwave backscatter dependence on surface roughness, soil moisture, and soil texture: Part I - bare soil,'' *IEEE Trans. on Geosci. Electron.*, vol. GE-16, pp. 286-295, 1978.

[3] F. T. Ulaby and P. P. Batlivala, ''Optimum radar parameters for mapping soil moisture,'' *IEEE Trans. on Geosci. Electron.*, vol. GE-14, no. 2, pp. 81-93, 1976.

[4] F. T. Ulaby, G. A. Bradley, and M. C. Dobson, ''Microwave backscatter dependence on surface roughness, soil moisture, and soil texture: Part II - vegetation-covered soil ,'' *IEEE Trans. on Geosci. Electron.*, vol. GE-17, no. 2, pp. 34-40, 1979.

[5] E. T. Engman and J. R. Wang, ''Evaluating roughness models of radar backscatter,'' *IEEE Trans. Geosci. Remote Sens.*, vol. GE-25, no. 6, pp. 709-713, 1987.

[6] J. J. van Zyl, ''Calibration of polarimetric radar images using only image parameters and trihedral corner reflector responses,'' *IEEE Trans. on Geosci. and Remote Sensing*, vol. 28, no. 3, pp. 337-348, 1990.

[7] M. F. Chen and A. K. Fung, ''A Numerical Study of the Regions of Validity of the Kirchhoff and Small-Perturbation Rough Surface Scattering Models,'' *Radio Science*, vol. 23, no. 2, pp. 163-170, 1988.

[8] F. T. Ulaby, R. K. Moore, and A. K. Fung, *Microwave Remote Sensing: Active and Passive, 3, From Theory to Applications*, pp. 1065-2162, Dedham, MA: Artech House, 1986.

[9] L. Tsang, J. A. Kong, and R. T. Shin, *Theory of Microwave Remote Sensing*, New York: Wiley, 1985.

[10] F. T. Ulaby, K. Sarabandi, K. C. McDonal, M. W. Whitt, and M. C. Dobson, *Michigan microwave canopy scattering model (MIMICS)*, Report No. 022486-T-1: The Univ. Mich. Radiation Laboratory, 1988.

[11] J. Shi, J. Dozier, and R. E. Davis, "Simulation of snow-depth estimation from multi-frequency radar," *Proceedings IGARSS '90*, pp. 1129-1132, 1990.

[12] J. J. van Zyl, "Unsupervised classification of scattering behavior using radar polarimetry data," *IEEE Trans. on Geosci. and Remote Sensing*, vol. 27, no. 1, pp. 36-45, 1989.

Table 1. Algorithm-derived dielectric constants for test fields

Bare Fields

fields #	1	2	3	4	5
mean dc	3.31	7.15	3.21	6.64	7.39
incidence angle	49.3°	45.2°	38.4°	24.4°	24.8°

Bare Dry Fields

fields #	1	2	3	4
mean dc	3.05	3.52	6.01	6.42
incidence angle	43.3°	38.9°	27.8°	32.3°

Bare Fields with Rough Surface

field type	rough	rough	relative rough	relative rough
mean dc	6.43	3.09	7.80	3.48
incidence angle	21.9°	43.5°	47.3°	39.1°

Short Vegetation Covered Fields

field type	Onions 1	Onions 2	Lettuce 1	Lettuce 2	Lettuce 3	Lettuce 4
mean dc	4.11	3.49	7.87	5.17	5.55	7.95
incidence angle	44.8°	39.3°	42.3°	43.3°	43.1°	44.0°

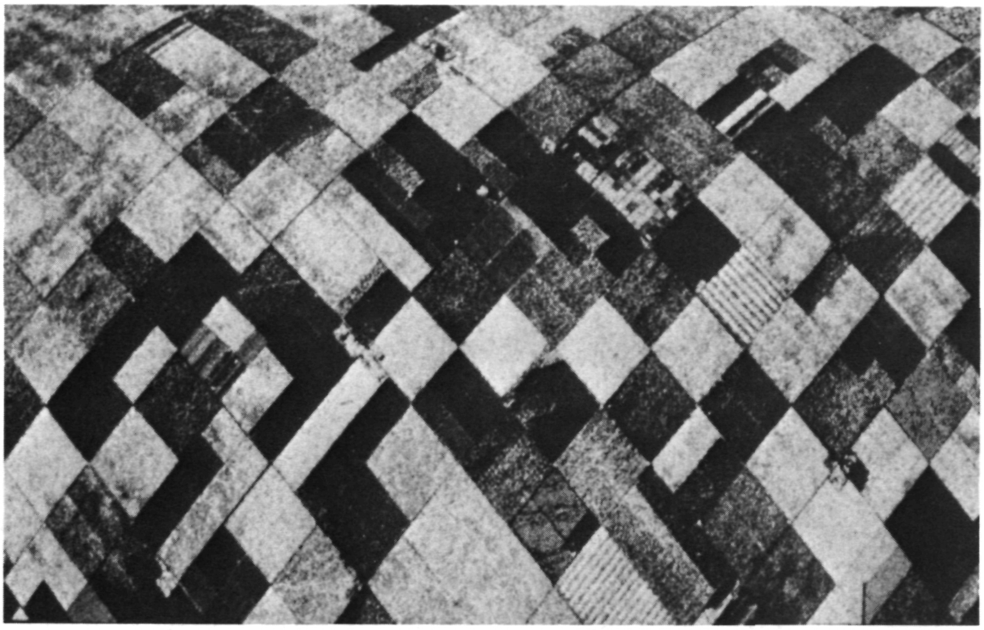

Figure 1. L-Band Multipolarization Image (see color slide no. 8).

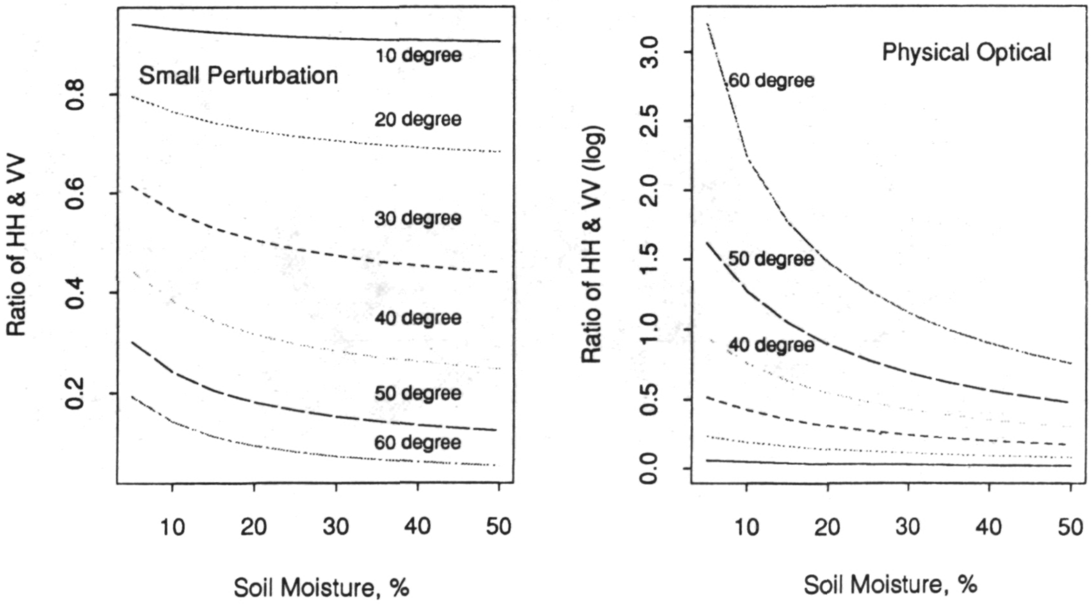

Figure 2. C-Band Ratio of Dielectric Functions vs. Soil Moisture

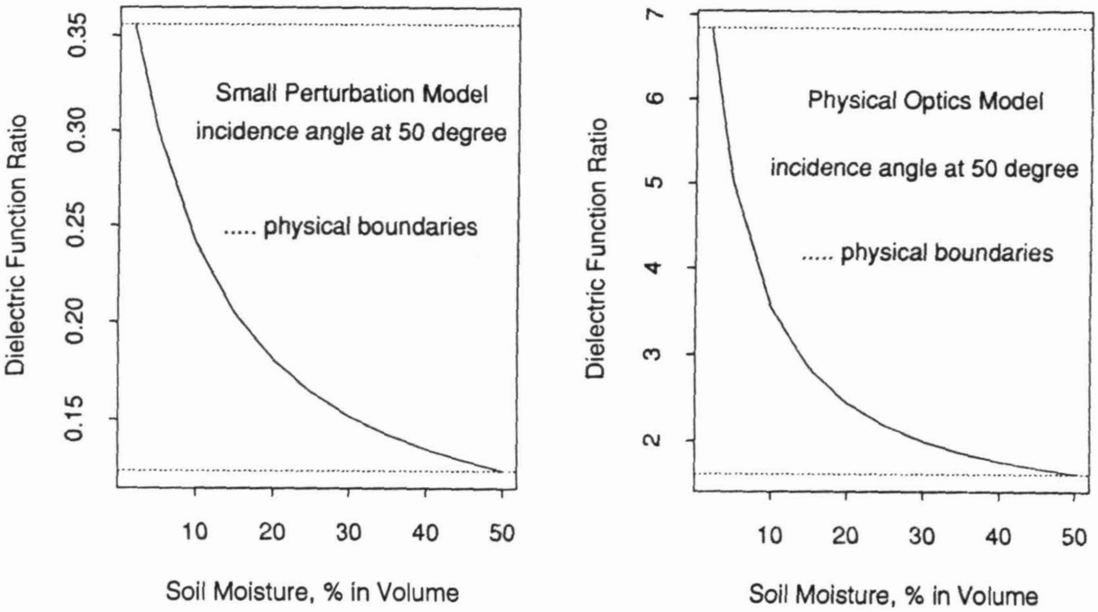

Figure 3. Physical Boundaries of Dielectric Functions

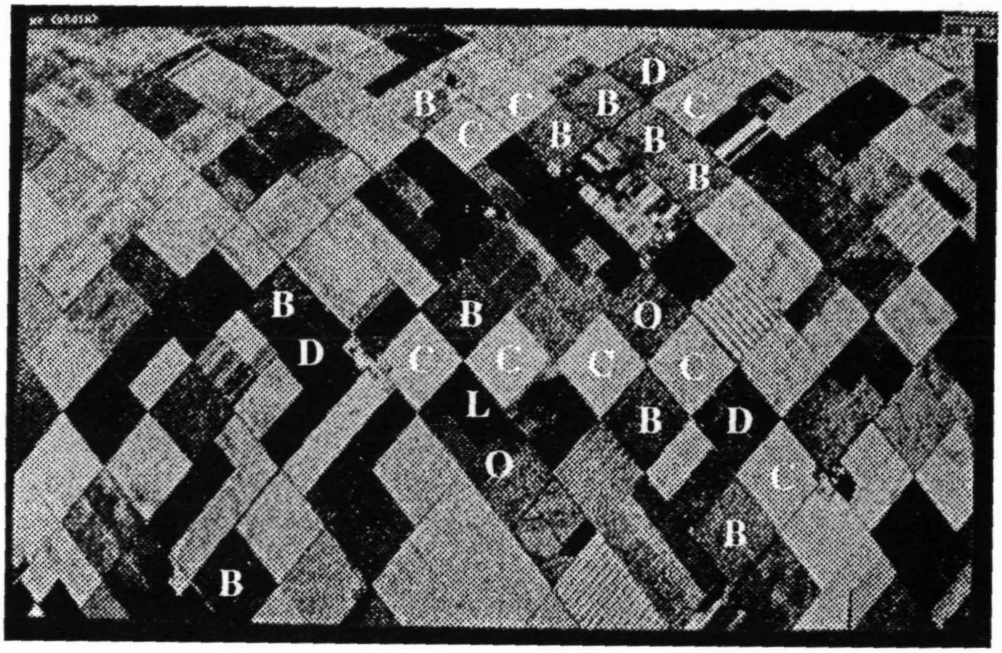

B - bare fields **C** - cotton fields **D** - dry, bare fields
L - lettuce fields **O** - onion fields

Figure 4. L-band HH-polarization Image, Showing The Different Types of Fields

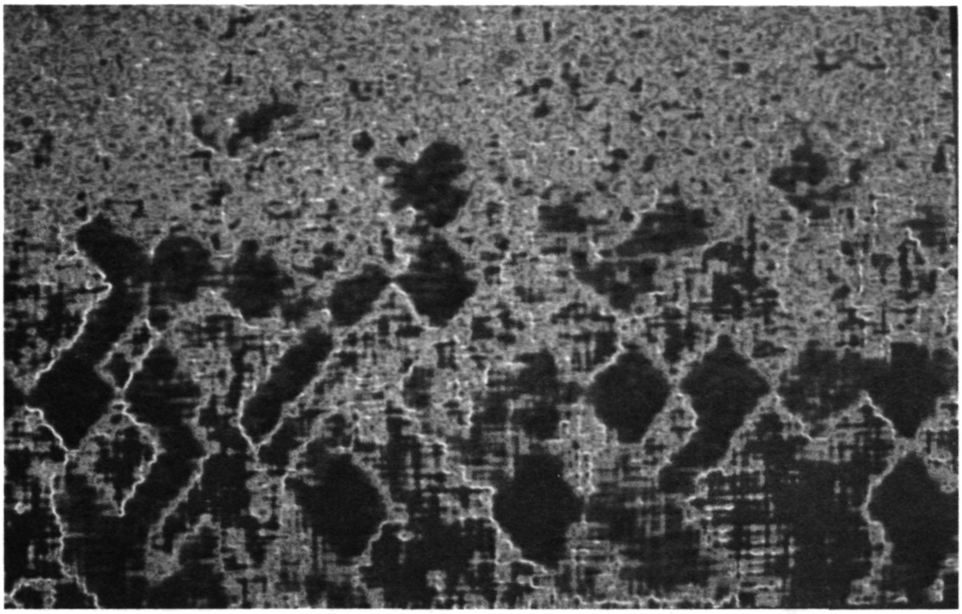

Figure 5. Dielectric Constant Image (see color slide no. 9).

N92-28021

SNOW AND GLACIER MAPPING WITH POLARIMETRIC SAR

Jiancheng Shi and Jeff Dozier
CRSEO
UC Santa Barbara
CA 93106 USA

Helmut Rott
Institute of Meteorology & Geophysics
University of Innsbruck
Innrain 52, A-6020 Innsbruck/Austria

Robert E. Davis
CRREL
U.S. Army Corps Engineers
Hanover NH 03755 USA

Abstract. The objective of this study was to examine the capability of mapping snow and glaciers in alpine regions using SAR imagery when topographic information is not available. The topographic effects on the received power for a resolution cell can be explained by the change in illuminated area and incidence angle in a slant-range representation of SAR imagery. The specific polarization signatures and phase difference between HH and VV components are relatively independent of the illuminated area, and the incidence angle has only a small effect on these parameters. They provide a suitable measurement data set for snow and glacier mapping in a high-relief area. The results show that the C-band images of the enhancement factor, the phase difference between HH and VV scattering components, and the normalized cross product of VV scattering elements provide the capability to discriminate among snow with different wetnesses, glaciers, and rocky regions.

Keywords: topographic effect, snow, glacier, classification.

I. INTRODUCTION

For climatological and hydrological investigations, the areas of snow cover and glacial ice cover are important parameters. For instance, the snow line on glaciers is an important quantity for hydrological applications and mass balance studies. Visible and near-infrared sensors have been used extensively to measure these quantities, but are hampered by cloud cover, which can be pervasive in some regions. In particular, snow cover must be measured on a timely basis to be useful for operational hydrology, and the opportunities for obtaining suitable data from these sensors can be infrequent. Microwave remote sensing is a methodology that is less influenced by cloud conditions, depending on frequency. Active microwave sensors are capable of discriminating between snow and bare ground, and have a spatial resolution compatible with the topographic variation in alpine regions.

In attempting to use SAR data to map snow and glaciers over remote and inaccessible areas, we are faced with two major problems:

- Compensation must be made for the effects of rugged terrain.
- Snow and glaciers must be distinguished from other surface covers.

Previously, mapping snow with conventional SAR imagery of alpine regions has been done by comparing a geocoded SAR image with a simulated image [1]. This method requires compatible topographic information in the form of a digital elevation model (DEM), which is used both to geocode the SAR image and to generate the simulated image. Although it is possible that digital elevation data may be used to simulate the topographic effects on a SAR image, precise registration of the elevation data with the SAR data, and accurate estimation of illuminated pixel area in a high relief region are often impossible because of the poor quality of most digital elevation data. Moreover, topographic information in the form of DEMs is not available for many of the world's alpine regions. Therefore, a general technique to map snow and glaciers should avoid requiring detailed topographic information. This is our objective of the study, to develop a method to map snow and glaciers in rugged terrain, which does not require topographic information.

Through evaluation of the characteristics of the polarization response of snow and glacier covered area, two fundmental questions are addressed in this study for snow and glacier mapping:

- How can we minimize the effects of rugged terrain when topographic information is not available?
- What are advantages and disadvantages of a polarimetric SAR vs. conventional SAR?

II. EXPERIMENT DESCRIPTIONS

On August 18, 1989, the central part of the Otztal test site was surveyed by the polarimetric AIRSAR, which operates at the three frequencies 440 MHz (P-band), 1.25 GHz (L-band), and 5.3 GHz (C-band). The flight altitude determined from the geocoded corner reflectors was about 8,330 meters, which is about 5,500 meters above the mean terrain altitude of the study site. The processed SAR scene covers about 12 km x 10 km. The data were processed at JPL and made available in the 4-looks compressed-data format with 12.1 m azimuth resolution and 6.662 m slant range resolution. Polarimetric and radiometric calibration, based on external targets, was necessary for quantitative signature studies. For calibration purposes and as geometric reference points trihedral corner reflectors with leg lengths between 0.65 m and 1.8 m were deployed on the glaciers. Because our objective is to evaluate the capability of mapping snow and glacier in alpine regions without requiring topography information, only the overall scene calibration, which uses the corner reflectors information and assume the flat surface for the study area, was performed. This SAR data is not absolutely calibrated since the antenna patterns are not removed correctly. Removing the antenna patterns requires the topographic information (DEM) and the parameters of the aircraft SAR looking geometry.

The test site includes narrow valleys, which become wider and are covered by glaciers at elevations about 2,500 to 2,800 meters. The overall test site altitude ranges from 1,800 to 3,700 meters above sea level. The firn areas of Gepatschferner (glacier area 17.7 km^2) and the Kesselwandferner (4.2 km^2) form a large plateau with comparatively gentle topography. Hintereisferner glacier has an area 9.1 km^2. At the time of the radar survey the snow cover was wet at all elevation zones. The liquid water content of the top snow layer was in the order of 5 to 6 percent by volume at elevations of 3,000 meter and decreased to 2 or 3 percent at the highest elevations. The snow densities and depths ranged from 492 to 580 $kg\ m^{-3}$ and from 45 to 114 cm respectively. The snow grain radius was 1.0 to 1.5 mm at the top snow layer and decreased to 0.5 to 1.0 mm along the snow vertical profile. The snow cover showed standard deviations of surface height in order of 1 to 2 cm, the correlation lengths were typically in the range 15 to 20 cm, with an overall variation between 10 to 25 cm. Before and during the SAR overflight, precipitation with locally heavy intensity fell all over the test site, up to elevations of about 3,300 m as rain, and above that as wet snow. In addition to the field measurements on dielectric and roughness properties of the main targets, the cloud-free satellite imagery of the test site was acquired by TM and SPOT seven days after the DC-8 overflight, which provides a great value for comparative and combined studies with the AIRSAR data. Figure 1 shows TM (band 2 - red, band 3 - green, and band 4 - blue) image of the study site. Snow with white, glacier with grey white to light yellow and rock with blue color can be clearly distinguished.

III. BASIC CONSIDERATIONS

In contrast to images from optical sensors, SAR images show a more complicated geometric mapping. SAR mapping is mainly an integration of backscattered signals having the same Doppler frequency as along-track measurements and the same distance as across-track measurements. The characteristic radar measurements are *range* - the distance from the sensor to an object point, and *time* - the position of the sensor along its flight path where the data are collected. They define the two-dimensional SAR image space.

Topographic effects on radar images can be considered as two aspects: (1) the effects on received radar power, which result from a great variation in illuminated area and incidence angle for a pixel resolution, and (2) the geometric distortions on image coordinates which are mainly dependent upon the distance between an imaged pixel and the sensor. The first aspect can be described as the variation of the received power from an inclined surface compared to the received power from a horizontal surface [2].

This variation is a function of the relative orientation of the surfaces with respect to the illuminating source and their position relative to the sensor.

The radar image geometry is characterized by foreshortening, layover and radar shadow; these effects depend on the combined effects of the topography, radar look geometry, and the orientation of the terrain features. Radar foreshortening is the shortening of a terrain slope on a radar image in all cases, except that slopes seen at grazing incidence angle are displayed as their correct ground length. In the case where the slope faces the radar, the illuminated area increases and the incidence angle decreases for a pixel resolution cell, so that the slope appears relatively brighter when compared to a flat surface. Radar layover is an extreme case of foreshortening that occurs when the angle of the facing slope is greater than the depression angle of the incident signal. Layover only occurs in an across-track line and appears much brighter than the surrounding regions. In the case of terrain sloping away from the radar, a decreasing illumination area and increasing incidence angle for the pixel resolution cell are expected so that the surface appears relatively darker when compared with a flat surface. Shadow regions, which appear as dark regions in the SAR image, are independent from the backscattering of the imaged terrain.

The effects of rugged terrain on the received power result from the change in illuminating area and incidence angle for a resolution cell so that the assumption of distributed targets is still valid. The total received power from a resolution cell is proportional to the radar cross section, and the rest of the factors in the radar equation are generally assumed constant. For distributed targets, the scattering cross section for the normalized electric field is given as

$$\sigma(\chi_r,\psi_r,\chi_t,\psi_t) = \frac{4\pi}{k^2} \begin{pmatrix} 1 \\ \cos 2\chi_r \cos 2\psi_r \\ \cos 2\chi_r \sin 2\psi_r \\ \sin 2\chi_r \end{pmatrix} \sum_{n=1}^{N} [\mathbf{M}^{(n)}] \begin{pmatrix} 1 \\ \cos 2\chi_t \cos 2\psi_t \\ \cos 2\chi_t \sin 2\psi_t \\ \sin 2\chi_t \end{pmatrix} \tag{1}$$

where $[\mathbf{M}^{(n)}]$ is the Stokes matrix of nth measurement, ψ is the polarization ellipse orientation angle, and χ is the ellipticity angle. The radar cross section is usually a function of polarization, frequency, viewing geometry, and illuminated area, in addition to factors such as the dielectric properties and geometric structure of the targets. To eliminate the dependence on illumination area, the backscattering coefficient σ^0 is usually presented in terms of a normalized radar cross section

$$\sigma^0 = \frac{\sigma}{A} \tag{2}$$

where A is illumination area.

A conventional single SAR imagery provides high resolution digital images but with only one fixed polarization state of the antenna. With only one intensity measurement per pixel, we thus have to rely mainly on the radiometric properties in order to distinguish snow and glacier covered area from other targets, such as bare ground or vegetated areas. For a flat area, both illumination area and incidence angle of a pixel can be reasonably estimated so that the backscattering coefficient can be obtained. In this case wet snow and bare ground can be distinguished from the difference between their dielectric and surface roughness properties. Since the radiometric quality of SAR images in an alpine region is dependent on flight and imaging parameters (e.g. flight altitude, radar elevation angle) and the topography of the imaged area, the representation of the target materials is likely to be inaccurate. This variation in radar backscatter that is unrelated to the surface cover type is particularly evident for high relief surfaces where a large variation of slope and aspect creates a great variation of local incidence angles and illuminated areas. For example, rock surfaces with greater incidence angle could have lower power return than that from snow or glacier covered areas with smaller incidence angle.

Rather than just measuring amplitude, an imaging radar polarimeter measures the amplitude and relative phase for every polarization state. These complex measurements lead to nine independent real elements of the Stokes matrix, which describes how the scattering mechanisms in each pixel transform the illuminating electromagnetic wave back to the receiving antenna. The *polarization feature* derived from the Stokes matrix, is the radar cross section as a function of the antenna polarization state and is useful in interpreting the scattering mechanisms within a resolution cell. The first element of the matrix is the total power or *span*. The nine cross products of the pixel scattering matrix can be obtained by the linear combinations from the *span* and the other Stokes matrix elements. In addition to the polarization signature, many other features describing the scattering mechanisms within a pixel can be derived from the Stokes matrix. These include: the pixel intensity synthesized from the polarization signature for fixed antenna polarization states [5], the polarization phase difference of the scattering matrix elements [6], the coefficient of variation [7], the enhancement factor [8], the scattering mechanism and the degree of polarization [9]. Thus polarimetric measurements provide much more information per pixel than a single fixed antenna SAR imager, and have been shown to be effective in classification of terrain [10]. These measurements have great opportunity to minimize the topographic effects on radar images.

IV. DATA SETS SELECTION AND CLASSIFICATION

Radar backscatter from a pixel consists of the superposition of a number of waves of a variety of polarizations. To examine the significance of the polarization signatures as applied of snow or glacier mapping, we show in Figure 2 a *coefficient of variation* image of the study area in which the brightness of a pixel is proportional to the coefficient of variation. The *coefficient of variation* is defined as the ratio of the minimum received power to the maximum received power [11]. Small coefficients of variation indicate that there are large differences between the minimum and maximum power received as the transmitted and received polarization are varied. This suggests that the scattering mechanisms across a pixel are relatively similar. Snow and glacier cover are realized as relatively uniform features in both their surface roughness distribution and the microstructure of their volume when compared with rock, soil and vegetation. The individual polarization signatures result from similar scattering mechanisms, so that the resulting received power will tend to exhibit large variation as a function of polarizations. Within a snow covered area, the high water content snow has the smaller coefficient of variation value than that of the low water content snow. This is caused by the significantly increased scattering term of the surface and volume interaction which mainly produces the unpolarized power, especially when snow-air interface is rough. The glacier region has a higher coefficient of variation value than that of the wet snow covered region because of more volume scattering involved. On the other hand, greater coefficients of variation from rock areas show that changing the polarization of the transmitter and receiver will not significantly affect the power received from these regions. This is because of multiscattering, or large variations of surface roughness, which result in several scattering mechanisms within the pixel resolution. Thus, the coefficients of variation show that a great advantage can be obtained by using the polarization synthesis technique in mapping a snow and glacier covered area.

The problem of finding the polarization of the receive and transmit antennas which maximizes the ratio of signal power scattered by one type of target to that scattered by another type of target have been addressed by several authors [12,13]. The selection of the optimum polarization to enhance the contrast between two types of scatterers is also known as a *polarization filter*. For a fixed transmitting polarization, the optimum contrast ratio is given by

$$CR_{\max}(\psi_t,\chi_t) = \frac{S_{01}S_{02} - \mathbf{s}_1\cdot\mathbf{s}_2}{S_{02}^2 - \mathbf{s}_2\cdot\mathbf{s}_2} + \sqrt{\left[\frac{S_{01}S_{02} - \mathbf{s}_1\cdot\mathbf{s}_2}{S_{02}^2 - \mathbf{s}_2\cdot\mathbf{s}_2}\right]^2 - \frac{S_{01}^2 - \mathbf{s}_1\cdot\mathbf{s}_1}{S_{02}^2 - \mathbf{s}_2\cdot\mathbf{s}_2}} \tag{3}$$

where

$$\begin{bmatrix} S_{01} \\ \mathbf{s}_1 \end{bmatrix} = \overline{\mathbf{M}}_1\overline{\mathbf{A}}(\psi_t,\chi_t) \tag{4}$$

$$\begin{bmatrix} S_{02} \\ \mathbf{s}_2 \end{bmatrix} = \overline{\mathbf{M}}_2 \overline{\mathbf{A}}(\psi_t,\chi_t) \tag{5}$$

where $\overline{\mathbf{A}}(\psi_t,\chi_t)$ and $\overline{\mathbf{A}}(\psi_r,\chi_r)$ are the normalized Stokes vectors. The optimum transmitting polarization can be found numerically from the above equation. Once the maximum contrast is found, the optimum receiving polarization can be found from

$$\mathbf{a}_r = \frac{\mathbf{s}(CR_{opt})}{\sqrt{\mathbf{s}(CR_{opt})\cdot\mathbf{s}(CR_{opt})}} \tag{6}$$

where

$$\mathbf{s}(CR_{opt}) = \mathbf{s}_1 - CR_{opt}\mathbf{s}_2 \tag{7}$$

To quantify the performance of the polarization filter, Dubois and van Zyl (1989) introduced an *enhancement factor,* which is a measure of how radar polarization alone provides discrimination between two classes of scatters, defined as

$$\text{Enhancement Factor} = \frac{\overline{\mathbf{A}}(\psi_r,\chi_r)\cdot\overline{\mathbf{M}}_1\overline{\mathbf{A}}(\psi_t,\chi_t)}{\overline{\mathbf{A}}(\psi_r,\chi_r)\cdot\overline{\mathbf{M}}_2\overline{\mathbf{A}}(\psi_t,\chi_t)}\,\frac{(M_{11})_2}{(M_{11})_1} \tag{8}$$

where M_{11} is the first element of Stokes matrix or total power. They also found the enhancement factor is independent of the incidence angle and size of training areas used.

In this study, five classes were chosen in the study area for classification testing:

Class 1 - the high water content snow (5 to 6 % in volume);
Class 2 - the low water content snow (2 to 3 % in volume);
Class 3 - Glacier ice;
Class 4 - Rock;
Class 5 - Moraine.

The representative Stokes matrix for each class is obtained by averaging the total number of pixels in the training sites. The selection of the training sites is based on both a TM data set, which provides the distribution of wet snow and glacier covered regions as well as rock regions, and the coefficient of variation image, which indicates the degree to which polarization filtering can be used to enhance the contrast between the classes. The training sites for the high and low water content snow regions were obtained from the field observations. The reason for choosing Class 5 (Table I.) is that these regions have similar coefficient-of-variation values with those from glacier and snow covered regions. This indicates the possibility that the contrast between those regions should be reduced when we are trying to enhance the contrast between other regions.

Using equations (3) to (8), the polarization filters for obtaining the maximum contrast between each pair of classes can be obtained. Table I. summarizes the parameters of polarization filtering and enhancement factors for each class pair. In Table I. class 2-1 means that the signature from class 2 is maximized and that from class 1 is minimized. The high water content snow covered area has the best contrast with all other classes. We also noticed that better contrast can be obtained by minimizing the signatures from the region that has a smaller coefficient of variation and maximizing that from the regions which have greater coefficients of variation. Figure 3 shows an enhancement factor image which was generated by using polarization filtering parameters for the enhanced contrast between the high and low water content snow covered regions. We can achieve a greater contrast of the specific polarization signatures up to 2.56 dB for these two classes.

In addition to these nine enhancement factor images (the image ratio of the synthesised polarization image to the total power image) for each class pair, the nine normalized cross products of the scattering matrix's elements also provide specific polarization feature measurements which are all independent of the intensity and are expected to be independent of the illuminating pixel area. Thus, twenty initial data sets, which include nine enhancement factor images, nine normalized cross products of the scattering matrix's elements and two phase difference images, were selected for classification. These measurements should provide the better data sets for snow or glacier mapping in alpine regions.

According to the concept of feature separation [14], a feature is said to provide good separation if the distance between the class mean values is large compared to the standard deviation for that feature. In order to determine the best data sets for classification, we have evaluated the separability of each element of the normalized scattering matrix and the enhancement factor images for different class pairs from the selected training sites. The separability between class k and l is defined by

$$S_{k,l} = \frac{|\mu_k - \mu_l|}{\sigma_k + \sigma_l} \tag{9}$$

where μ and σ are mean value and standard deviation of the feature for each class, respectively.

A problem common to many applications of classifiers in remote sensing is the limited applicability of training sets of data. The polarization signatures of the individual measurements may be not identical, so the parameters of the polarization filters obtained from the averages over the limited training fields may not perform as well on the whole image. There are the possibilities that the same surface cover might show different polarization signatures and that different surface covers might show similar polarization signatures for the given parameters of the filters. Therefore, it is necessary to evaluate the behavior of the polarization signature on the total performance in each class-pair discriminator. The slight differences in the separabilities also suggests that the data sets for classification can be minimized by 1) testing overall separabilities for each class pair and 2) evaluating the overall performance on the whole image. Based on assessment of these two factors, the twenty data sets for classification can be reduced to three data sets - the image of the normalized cross product of VV scattering matrix's element, the image of the phase difference of the HH and VV scattering elements, and the enhancement factor image to enhance the high and low water content snow covered regions. The normalized cross product of VV scattering matrix's element, as shown in Figure 4., has the best discrimination of snow and glacier covered areas from rock and moraine surfaces, but does not allow separation of the low water content snow and glacier covered area. The phase difference of the HH and VV scattering elements, as shown in Figure 5., provides the great contrast between the snow covered areas and glaciers, but can not distinguish the pair of the low and high water content snow areas and the pair of glacier and rock, moraine regions. The enhancement factor image as shown in Figure 3. provides the discrimination between the high and low water content snow covered areas but does not allow separation glacier and the high water content snow covered region. Using Bayes classifer, the classification was performed several times until the result did not change significantly. The probability of each class was obtained from the previous result in each run. In order to reduce the speckle and improve the classification performance, a spatial function represented by the average of the specific polarization features and the phase difference over a 5 x 5 window, was used. Figure 6 shows the classification result in which the low water content snow is shown as white color, the high water content snow as grey blue, glacier as blue, rock as orange brown, and moraine as brown. Compared with TM data, the result of the classification shows very good agreement for almost all snow and glacier regions except for a very small amount of rock being classified as glacier and glacier being classified as rock, possibly caused by the relative small separability of these two classes in the data sets for classification.

V. CONCLUSIONS

This paper reports our preliminary results on mapping snow and glaciers in alpine regions using SAR radar imagery when topographic information is not available. Mapping snow and glaciers in remote alpine regions by a conventional single polarization SAR imagery requires the topographic information in order to remove the topographic effects on the radiometric properties measured from SAR imagery. We show that the specific polarization signatures and the phase difference between HH and VV scattering elements from the C-band polarimetric SAR can be used effectively to map the different water content snow and glacier covered area without requiring any topographic information. In a recent study [15] on the E-SAR of DLR - C-/X-band SAR with HH polarization over the same test site, both C- and X-band has excellent discrimination of snow covered and snow free areas in the ice free part of the test site. The contrast between glacier ice and ice free surface is only slightly higher in X-band than that in C-band. But the contrast between snow and glacier ice at C-band is an average 9 dB, whereas the difference is only about 5 dB in the X-band. In addition to the lower contrast between the two surface types, larger variation in backscattering coefficients has been found. Thus, both studies indicate the optimal frequency is at C-band for snow and glacier mapping applications without regarding the intensity classifer - backscattering coefficients in a conventional SAR or the specific polarization signature classifer - a polarimetric SAR, to be used. To develop operational algorithms of mapping snow and glacier from polarimetric SAR, further study is still needed to evaluate the effect of the error, which is introduced by incorrect antenna pattern assumption, on the data sets.

ACKNOWLEDGMENT We wish to acknowledge with sincere gratitude the co-operation of the JPL Radar Imaging Group for supplying SAR data. The research is supported by the National Aeronautics and Space Administration under grant JPL/NASA 958473.

REFERENCES

[1] H. Rott, C. Mätzler, D. Strobl, S. Bruzzi, and K. B. Lenhart, "Study on SAR land applications for snow and glacier monitoring," Final Rep., European Space Agency Contr. No. 6618/85/F/FL(SC) Institut für Meterologie und Geophysik, Universität Innsbruck, 1988.

[2] B. Holben and C. Justice, "An examination of spectral band ratioing to reduce topographic effect on remotely sensed data," *Intl. J. Remote Sens.*, vol. 2, no. 2, pp. 115-133, 1981.

[3] Jakob J. van Zyl, Howard A. Zebker, and Charles Elachi, "Imaging radar polarization signatures: Theory and observation," *Radio Science*, vol. 22, no. 4, pp. 529-543, 1987.

[4] W. M. Boerner, B. Y. Foo, and H. J. Eom, "Interpretation of the polarimetric co-polarization term in radar images obtained with the JPL airborne L-band SAR system," *IEEE Trans. on Geosci. and Remote Sens.*, vol. GE-25, no. 1, pp. 77-81, 1987.

[5] H. A. Zebker, J. J. van Zyl, and D. N. Held, "Imaging radar polarimetry from wave synthesis," *J. Geophys. Res.*, vol. 92, no. B1, pp. 683-701, 1987.

[6] F. T. Ulaby, D. N. Held, M. C. Dobson, K. C. McDonald, and T. B. A. Senior, "Relating polarization phase difference of SAR signals to scene properties," *IEEE Trans. on Geosci. and Remote Sens.*, vol. GE-25, no. 1, pp. 77-81, 1987.

[7] D. L. Evans, T. G. Farr, J. J. van Zyl, and H. A. Zebker, "Radar polarimetry: Analysis tools and applications," *IEEE Trans. Geosci. Remote Sens.*, vol. 26, no. 6, pp. 774-789, 1988.

[8] P. C. Dubois and J. J. Van Zyl, "Polarization filtering of SAR data," *Proceedings IGARSS '89*, pp. 1816-1819, 1989.

[9] Jakob J. van Zyl, "Unsupervised classification of scattering behavior using radar polarimetry data," *IEEE Trans. on Geosci. and Remote Sens.*, vol. 27, no. 1, pp. 36-45, 1989.

[10] H. H. Lim, A. A. Swartz, H. A. Yueh, J. A. Kong, R. T. Shin, and J. J. van Zyl, "Classification of earth terrain using polarimetric Synthetic Aperture Radar images," *J. Geophys. Res.*, vol. 94, no. B6, pp. 7049-7057, 1989.

[11] Jakob J. van Zyl, Howard A. Zebker, and Charles Elachi, "Imaging radar polarization signatures: Theory and observation," *Radio Science*, vol. 22, no. 4, pp. 529-543, 1987.

[12] P. C. Dubois and J. J. Van Zyl, "Polarization filtering of SAR data," *Proceedings IGARSS '89*, pp. 1816-1819, 1989.

[13] A. A. Swartz, H. A. Yueh, J. A. Kong, L. M. Novak, and R. T. Shin, "Optimal polarizations for achieving maximum contrast in radar images," *J. Geophys. Res.*, vol. 93, no. B12, pp. 15252-15260, 1988.

[14] I. G. Cumming and J. J. Van Zyl, "Feature utility in polarimetric radar image classification," *Proceedings IGARSS '89*, pp. 1841-1846, 1989.

[15] H. Rott and R. E. Davis, "Multi-parameter airborne SAR experiments at an alpine test site," *IGARSS'91*.

TABLE I. Polarization filtering parameters and enhancement factors

Class pairs	Transmitter χ_t	Transmitter ψ_t	Receiver χ_r	Receiver ψ_r	Enhancement factor in dB
class 2-1	-12°	76°	4°	164°	2.56
class 3-1	-18°	70°	6°	154°	2.31
class 4-1	-4°	89°	-2°	177°	3.63
class 5-1	-6°	2°	0°	95°	3.90
class 3-2	25°	154°	-5°	88°	2.23
class 4-2	1°	95°	-1°	4°	1.52
class 5-2	-3°	1°	2°	96°	1.69
class 4-3	3°	95°	-6°	5°	1.90
class 5-3	-6°	128°	-19°	101°	1.35

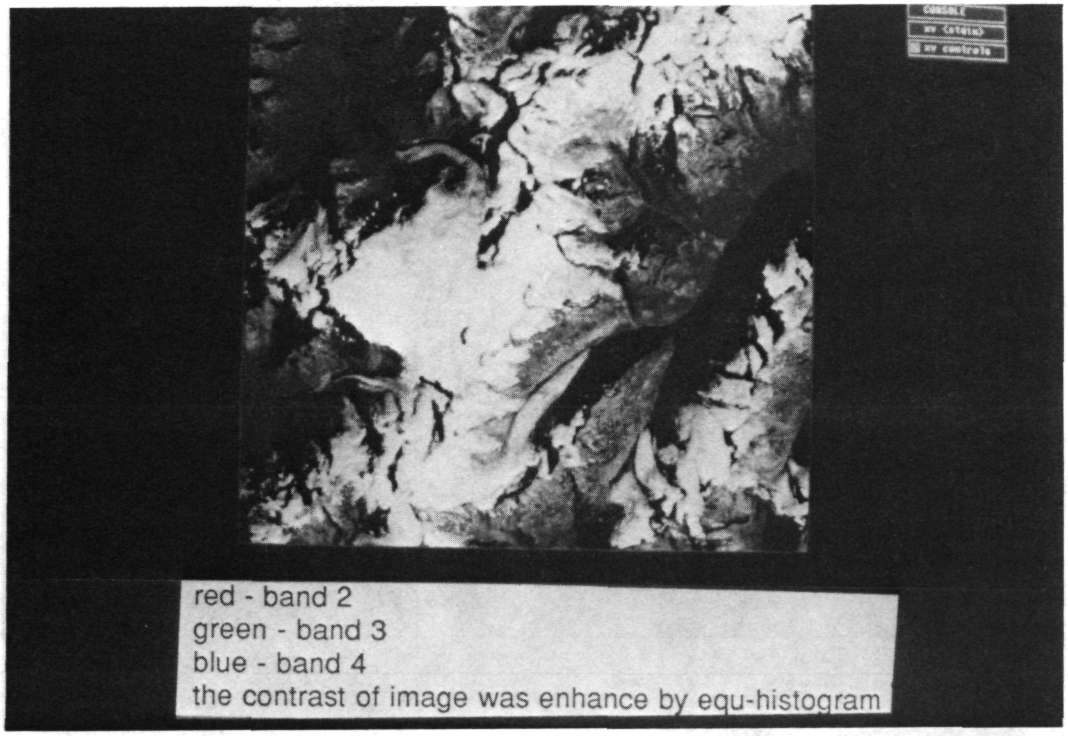

red - band 2
green - band 3
blue - band 4
the contrast of image was enhance by equ-histogram

Figure 1. **TM image of study area (see color slide no. 10)**

Figure 2. Coefficient variation image

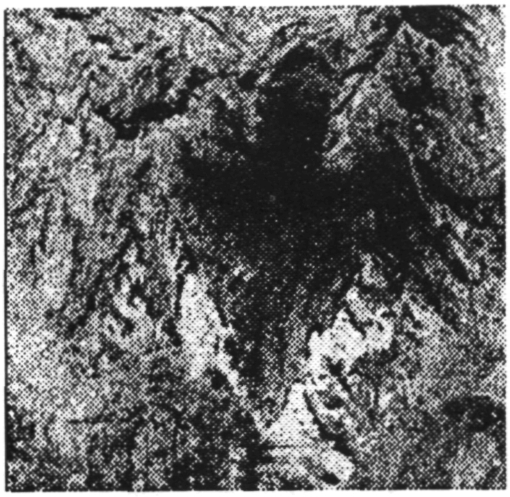

Figure 3. Enhancement factor image

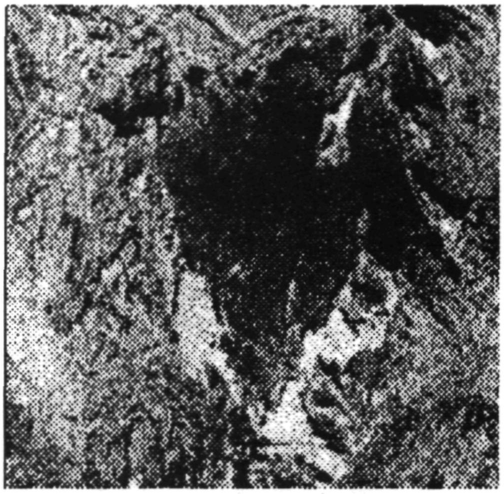

Figure 4. Normalized VV cross product

Figure 5. HH-VV phase difference image

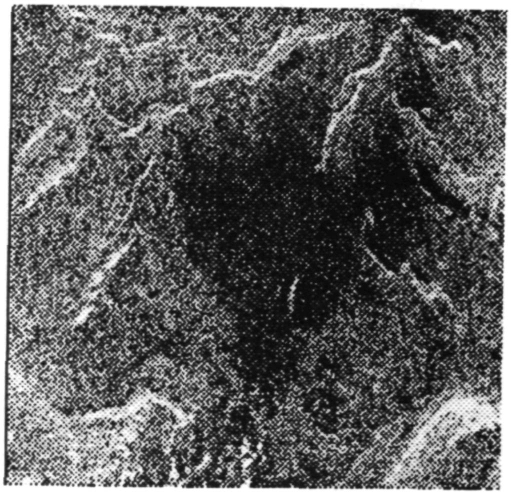

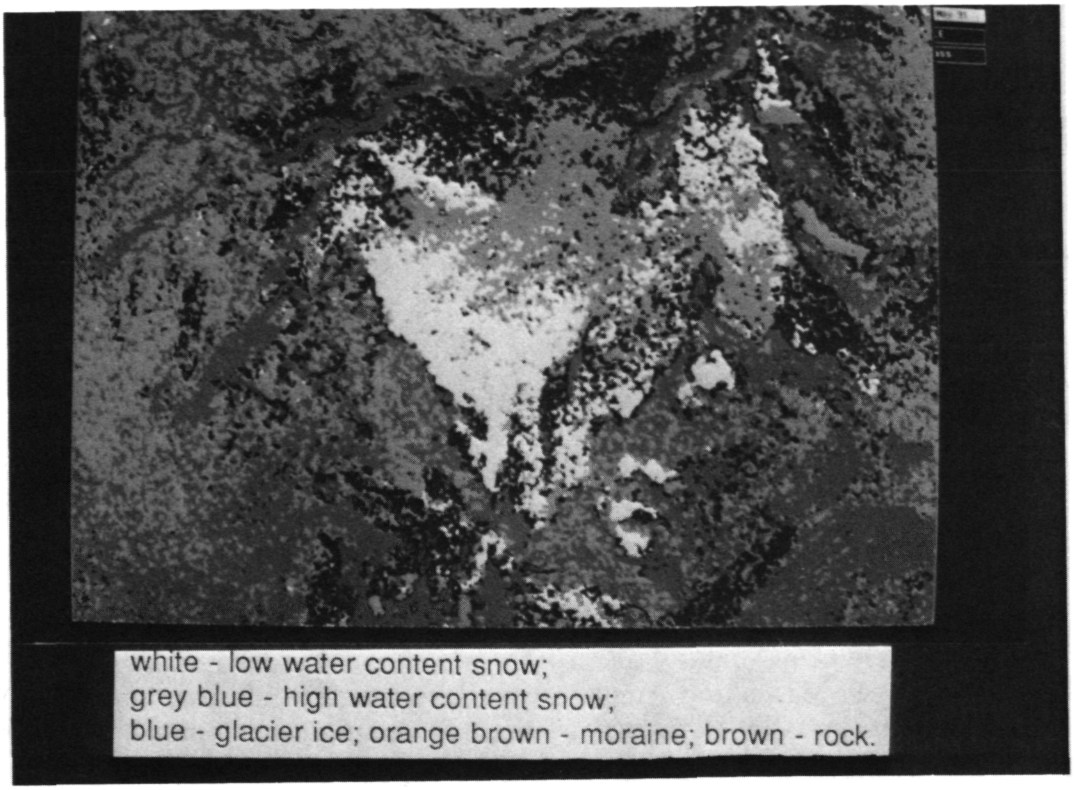

Figure 6. Snow and glacier map (see color slide no. 11)

N92-28022

MONSOON '90: PRELIMINARY SAR RESULTS

Jakob J. van Zyl, Pascale Dubois and Abel Guerra
Jet Propulsion Laboratory
California Institute of Technology
Pasadena, California

Abstract

Multifrequency polarimetric SAR images of the Walnut Gulch watershed near Tombstone, Arizona were acquired on March 28, 1990 and on August 1, 1990. Trihedral corner reflectors were deployed prior to both overflights to allow calibration of the two SAR data sets. During both overflights, gravimetric soil moisture and dielectric constant measurements were made. Detailed vegetation height, density and water content measurements were made as part of the Monsoon '90 experiment.

This report presents preliminary results based on analysis of the multitemporal polarimetric SAR data. Only the C-band data (5.7-cm wavelength) radar images show significant differences between March and August, with the strongest difference observed in the HV images. Based on the radar data analysis and the *in situ* measurements, we conclude that these differences are mainly due to changes in the vegetation and not due to the soil moisture changes.

I. Introduction

One of the most important variables in the energy balance is the amount of water available in the ground surface either for evapotranspiration or to be extracted from the ground by plants. In studying global circulation problems, however, knowledge of the available water at one point is not enough; the spatial variation of this quantity is as important as the point value [1].

The Monsoon '90 experiment took place during July and August 1990. The study site is the Walnut Gulch watershed just outside Tombstone, Arizona. One of the aims of this experiment was to investigate the possibility of using multiparameter SAR data to infer changes, both spatially and temporally, of soil moisture.

The radar part of the experiment involved acquiring polarimetric SAR images of the Walnut Gulch watershed on two different dates. The data were acquired using the NASA/JPL three-frequency polarimetric synthetic aperture radar system flown on a DC-8 aircraft operated by NASA's Ames Research Center. This report describes results inferred from a preliminary analysis of the SAR data.

II. Radar and *in situ* Measurements

The NASA/JPL airborne SAR system (AIRSAR) acquires fully polarimetric SAR data at three frequencies, P-band (68-cm wavelength), L-band (24-cm wavelength) and C-band

(5.7-cm wavelength) simultaneously [2]. As part of the Monsoon '90 experiment, SAR images of the Walnut Gulch watershed were acquired on March 28, 1990 (spring, dry season) and again on August 1, 1990 (summer, wet or "monsoon" season). Unfortunately, the flight in August occurred at the end of a dry period, with resulting soil moisture conditions comparable to those measured in March, compromising the original goals of the radar experiment. In fact, two hours after the radar data were acquired on August 1, a thunderstorm moved through the watershed. Due to tight scheduling of the DC-8 aircraft, however, it was not possible to refly the area. (Typical DC-8 schedules are made up months before the actual experiments. The Walnut Gulch flight in August formed part of a transcontinental flight that ended at Moffet Field in Mountain View, California even before the thunderstorm reached the watershed. Two days later the DC-8 departed Moffet Field for a week's deployment to Hawaii.) Even though soil moisture conditions for the March and August flights were very similar, significant differences in vegetation cover, especially in some parts of the watershed were observed, and the preliminary SAR data analysis seem to confirm that these differences were observed by at least some of the radar wavelengths.

Prior to the March and August radar overflights, trihedral corner reflectors were deployed in the watershed area. The signals from these corner reflectors are used to calibrate the radar images after standard SAR processing [3]. The software used to calibrate these images is the POLCAL program developed at the Jet Propulsion Laboratory [4]. After calibration, the radar images acquired in the spring were co-registered with those acquired in the summer using software developed at the Jet Propulsion Laboratory and described by Evans *et al.* [5]. Once the images are co-registered, one can quantitatively compare differences on a pixel-by-pixel basis. We shall describe the results in the next section.

During both radar overflights numerous dielectric constant measurements were made in the watershed. In the spring, dielectric constant measurements were made using a portable dielectric constant probe (PDP) similar to the one described by Jackson [6]. These measurements were made at P-band and L-band. We were unable to calibrate the C-band probe and therefore did not make any measurements at that frequency. The dielectric constant measurements were made at various random locations along roads inside the watershed as shown on the map in Figure 1. At one position, the Kendall watershed (marked as 1 on the map in Figure 1), we measured the dielectric constant as a function of position across a small watershed. At each place we made dielectric constant measurements, we also collected a soil sample (0-5 cm depth) in previously weighed cans. These cans with soil samples were subsequently weighed, dried in ovens at the Agriculture Research Service station in Tombstone, and then reweighed. This provided us with the gravimetric soil moisture during the overflight.

The measured real parts of the dielectric constant for the spring flight varied between 2.0 and 3.5 at L-band and between 2.3 and 4.0 at P-band. All values quoted were measured on the surface. The gravimetric soil moisture measured during the spring varied between 1% and 4% by weight. Figure 2 shows examples of the measured gravimetric soil moisture as a function of position along two transects across the Kendall watershed during the March overflight. Figure 3 shows examples of the L-band dielectric constant measurements for a similar transect. All dielectric constant values are averages of 5 measurements in an area about 1 square meter.

During the August overflight, the dielectric constant measurements were repeated. In addition to the PDP measurements, dielectric constants were also measured using a three-pronged probe and the time domain reflectometry (TDR) method [7]. The measured real parts of the dielectric constant for the August flights varied between 3.5 and 4.5 at P-band and between 2.3 and 3.5 at L-band. The gravimetric soil moisture was measured to vary between 2% and 8%. The TDR probe measurements of the dielectric constant varied between 2.0 and 5.1. Figures 4 and 5 show the measured real parts of the dielectric constant and the gravimetric soil moisture for a transect across the Kendall watershed in August.

We also performed a soil size distribution analysis of the soil samples collected along the transect across the Kendall watershed. Figure 6 shows the percentage of sand and gravel in the soil samples. As expected, there is a greater percentage of sand near the bottom of the wash than near the tops of the ridges.

We notice from Figures 4 and 5 that the PDP and TDR measurements of the real parts of the dielectric constant are quite different, and that the TDR measurements seem to be more correlated with the gravimetric soil moisture measurements than those made using the PDP. A possible explanation for this apparent discrepancy is the fact that the PDP measurements were made on the surface, whereas the TDR measurements represent the average dielectric constant of the top 15 cm (the length of the TDR probe) of the soil. The soil samples were collected for depths of roughly 3-10 cm. The PDP results seem to indicate that dielectric constants should not be measured at the surface, but that the top few centimeters of the soil should be scraped off before measurements are taken.

III. Radar Data Analysis and Results

Figure 7 (Slide 12) shows the radar images of part of the Walnut Gulch watershed for the March 28 flight and for the August 1 flight. These images are false-color composites in which the red color corresponds to the total P-band radar return, the green color to the total L-band return, and the blue color to the total C-band return. Note that there are few obvious differences between these images, the exception being the drainage area in the center of the images, which appears brighter in August than it did in March.

In order to investigate the differences between the images more quantitatively, we formed images that correspond to the ratio of the radar backscatter cross-section in the August image to that of the March image. This was done on a pixel-by-pixel basis using the co-registered polarimetric radar data sets. Figure 8 (or Slide 13) shows the C-band ratio image as a false-color composite where the red color corresponds to the ratio for the radar cross-sections measured using horizontally polarized transmitted waves and receiving the scattered waves with vertically polarized antennas, or the ratio of σ_{hv}. The green and blue colors correspond to the ratios of σ_{vv} and σ_{hh}, respectively. Because of a strong interference contamination of unknown source in the P-band and L-band data, the corresponding ratio images were omitted. The appearance of relief in Figure 8 is the result of imperfect registration of the two radar data sets, mainly due to the local topography. The C-band ratio image shows a strong increase in radar cross-section from March to August for a large area in the center of the image. The bright area of increase shows a pinkish tint, suggesting a larger increase in σ_{hv} than in σ_{hh} and σ_{vv}.

To investigate this increase in radar cross-section at C-band quantitatively, we studied a number of smaller areas (outlined and numbered in Figure 8) in more detail. The results are presented in Table 1. We compare σ_{hv}, σ_{hh} and σ_{vv}, as well as the correlation coefficient for the co-polarized channels, ρ. This correlation coefficient is defined as

$$\rho = \frac{\langle S_{hh}^{*} S_{vv} \rangle}{\sqrt{\langle S_{hh}^{*} S_{hh} \rangle \langle S_{vv}^{*} S_{vv} \rangle}} \tag{1}$$

and S_{hh} and S_{vv} are the co-polarized elements of the measured scattering matrix [8]. In (1), $\langle \cdot \rangle$ is the spatial average of $\cdot$. We marked the areas that show a noticeable increase between the March and the August flights by an asterisk (*).

Table 1 shows that σ_{hv} increased more than σ_{hh} and σ_{vv} from March to August. It also shows that, in general, the correlation coefficient is larger in the March data than in the August data. Furthermore, the difference between σ_{hh} and σ_{vv} is generally smaller in the August image than in the March image. We believe that these results can be attributed to an increase in vegetation rather than a significant change in either soil moisture or surface roughness. Apart from the supporting evidence in the *in situ* measurements, we believe that the following observations in the radar data support our interpretation:

(1) The changes are observed primarily at C-band and not at L-band and P-band. One would expect similar changes at L-band and P-band if the surface roughness or soil moisture changed significantly. The exception may be if the change in soil moisture is confined to a thin layer (thin compared to the L-band and P-band wavelengths). Our *in situ* measurements of soil moisture did not show this, however. (Even though we did not make soil moisture measurements as a function of depth, we believe that we would have noticed if only a thin layer at the top was moist. If anything, we observed the opposite, *i.e.*, that the top centimeter or so of the soil was drier than the rest.) Instead, we believe that the shorter wavelength C-band radar waves interact more strongly with the relatively short and sparse vegetation in the Walnut Gulch watershed, hence the greater increase in radar cross-section at C-band.

(2) The correlation coefficient is smaller for the August image than for the March one. This decrease in the correlation coefficient is due to an increase in randomness in the phase difference between S_{hh} and S_{vv}. Vegetated surfaces typically show a more random S_{hh} to S_{vv} phase difference - a fact that has been exploited to perform unsupervised classification of polarimetric SAR images [9]. An increase in soil moisture alone would not be expected to decrease the correlation coefficient, but the second-order small perturbation model [10] predicts a decrease in the correlation coefficient for an increase in roughness. (In [10] it is shown, both with observations and predictions using the second-order small perturbation model, that rougher surfaces exhibit higher "pedestals" in their polarization signatures. Generally, the higher the pedestal, the lower the correlation coefficient between the co-polarized channels.) If, however, the decrease in the correlation coefficient was caused by an increase in surface roughness, one would expect that the L-band and P-band images would show similar decreases in correlation coefficients and a corresponding increase in the radar cross-section from March to August - something that was not observed.

(3) The strongest increase in radar cross-section is observed in the cross-polarized return. The second-order small perturbation model predicts increases of the same order for σ_{hh} and σ_{hv} and a slightly larger relative increase in σ_{vv} for an increase in dielectric constant (or an increase in soil moisture). The same model predicts similar increases for all three cases for an increase in roughness. Simple models have shown that the

presence of a thin layer of vegetation, however, can show a marked increase in σ_{hv}, mostly due to the random orientation of the thin branches [11]. The shorter wavelength, we believe, interacts more strongly with the thin branches of the sparse vegetation of the Walnut Gulch watershed.

(4) Finally, the ratio of σ_{hh} to σ_{vv} is larger in the August C-band image than in the March one. According to the small perturbation model the ratio of σ_{hh} to σ_{vv} would *decrease* for an increase in soil moisture - an effect observed by us in other experiments to be described elsewhere. Thin layers of vegetation with branches preferentially oriented vertically would attenuate vertically polarized waves more than horizontally polarized ones. This effect is especially noticeable when the vegetation layer is thin and sparse enough so that the resulting scattering for the co-polarized return is still mostly from the underlying soil surface [11] and simple models predict that under the right conditions σ_{hh} can actually be larger than σ_{vv} - a fact observed in the August C-band image.

Figure 9 (Slide 14) illustrates the changes in vegetation cover between spring and summer. The left two pictures were taken during the spring deployment and the right two in the summer. The top scene was photographed next to Corner Reflector 3, in an area which shows slight changes in backscatter from spring to summer. The bottom scene corresponds to Target 3 which displays large changes in backscatter. In both cases, the vegetation is denser in the summer, but note that only the bottom scene has a higher backscatter. This may be due to the relative amounts of change in different types of vegetation (e.g., shrubs in the top scene and grass in the bottom scene) as well as the change in the amount of ground cover.

IV. Conclusion

We have presented results from a preliminary analysis of multitemporal polarimetric SAR data acquired over the Walnut Gulch watershed near Tombstone, Arizona. Even though comparable soil moisture conditions existed for the two different dates on which radar data were acquired, significant changes in radar backscatter cross-section were observed in the C-band images, but very little change in the L-band and P-band images. We have provided some arguments to show that the changes are observed primarily due to a change in the vegetation between the two dates on which radar data were acquired.

The Walnut Gulch data set demonstrates the usefulness of multifrequency polarimetric SAR imagery to explain temporal changes. Without either the multifrequency or the polarimetric nature of the data, we would not have been able to explain the results. Future work will concentrate on detailed analysis of the changes observed in order to investigate the feasibility of extracting quantitative information about the vegetation changes.

Acknowledgment

This work was performed at the Jet Propulsion Laboratory, California Institute of Technology, under contract with the National Aeronautics and Space Administration. Our special thanks to the staff of the Agricultural Research Service station in Tombstone, Arizona, for their help and the use of their facilities during the field campaigns. We would also like to thank J. Washburne and A. Chehbouni for their precious help in deploying the corner reflectors. Many thanks to M. Weltz for providing us with helpful information on the vegetation and geology of the Walnut Gulch Watershed. Finally, we would like to thank the team in the NASA/JPL AIRSAR program that acquired and processed the data used in this manuscript.

References

[1] Engman, E.T., Hydrological Research Before and After AGRISTARS, *IEEE Transactions on Geoscience and Remote Sensing,* **GE-24**, pp. 5–11, 1986.

[2] Held, D. N. *et al.,* The NASA/JPL Multifrequency, Multipolarization Airborne SAR System, *Proc. of IGARSS '88 Symposium,* 1988.

[3] van Zyl, J.J., "Calibration of Polarimetric Radar Images using only Image Parameters and Trihedral Corner Reflectors," *IEEE Transactions on Geoscience and Remote Sensing,* **GE-28**, pp. 337–348, 1990.

[4] van Zyl, J.J. *et al.* "POLCAL User's Manual," JPL Document Number D-7715, 1990 (JPL Internal Document).

[5] Evans, D.L., J.J. van Zyl and C.F. Burnette, "Incorporation of Polarimetric Radar Images into Multi-sensor Data Sets," *IEEE Transactions on Geoscience and Remote Sensing,* **GE-28**, pp. 932–939, 1990.

[6] Jackson, T.J.,"Laboratory Evaluation of a Field-portable Dielectric/Soil-Moisture Probe," *IEEE Transactions on Geoscience and Remote Sensing,* **GE-28**, pp. 241–246, 1990.

[7] Topps, G.,C., J. L. Davis, "Measurement of Soil Water Content using Time-domain Reflectometry (TDR): A Field Evaluation," *Soil Science Society Am. Journal,* **Vol-49**, pp. 19–24, 1985.

[8] Zebker, H.A., J.J. van Zyl and C. Elachi, "Polarimetric Radar System Design," Chapter 6 in *Radar Polarimetry for Geoscience Applications,* Ulaby and Elachi (Eds), Artech House, Norwood, MA, 1990.

[9] van Zyl, J.J., "Unsupervised Classification of Scattering Behavior using Radar Polarimetry Data," *IEEE Transactions on Geoscience and Remote Sensing,* **GE-27**, pp. 36–45, 1989.

[10] van Zyl, J.J., H.A. Zebker and C. Elachi, "Imaging Radar Polarization Signatures: Theory and Observations," *Radio Science,* **22**, pp. 529–543, July-August 1987.

[11] van Zyl, J.J. "On the Importance of Polarization in Radar Scattering Problems," Ph.D. Thesis, Caltech Antenna Laboratory Report No. 120, pp. 81–91, California Institute of Technology, Pasadena, CA 1985.

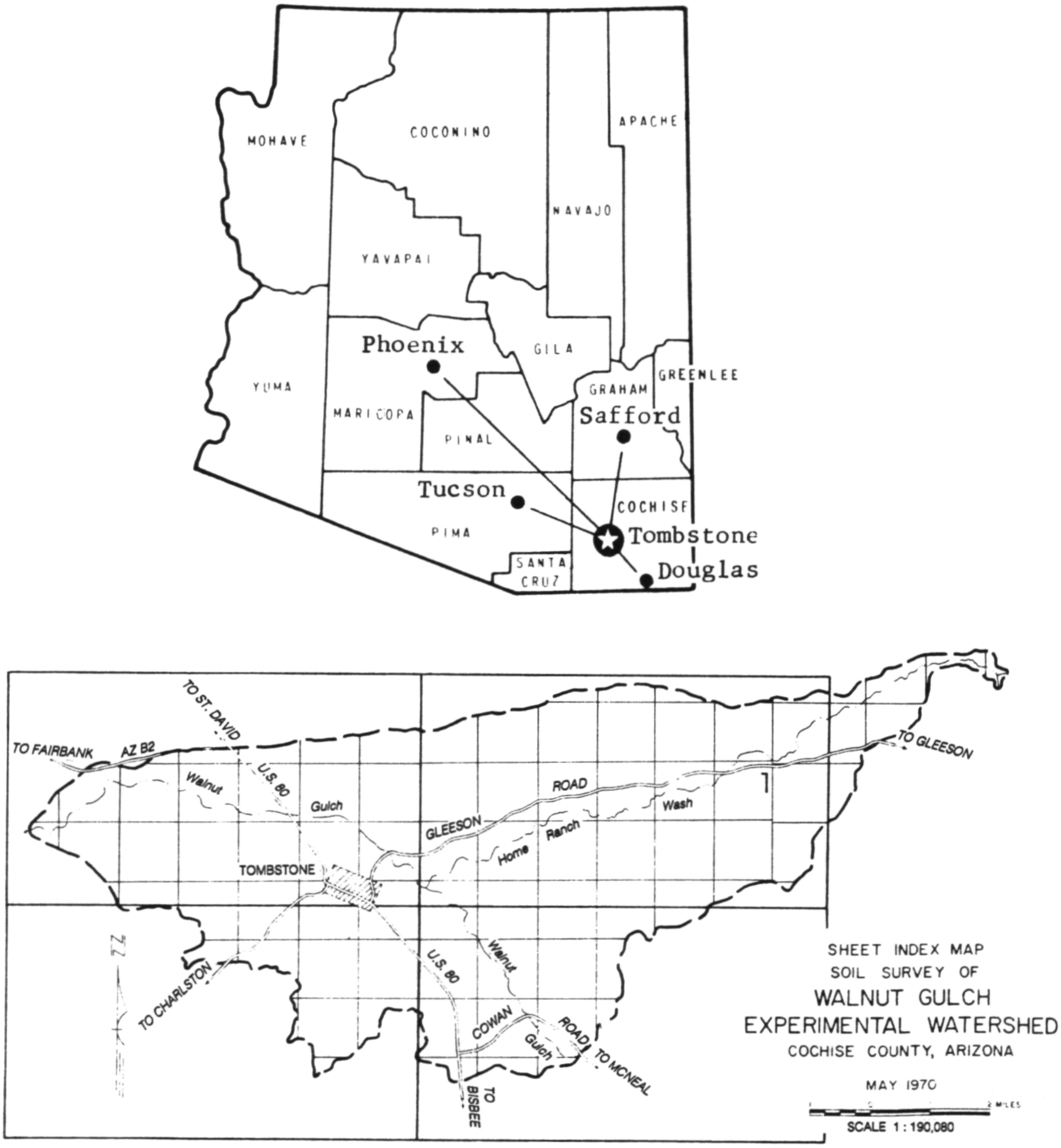

Figure 1: Map of the Walnut Gulch Watershed

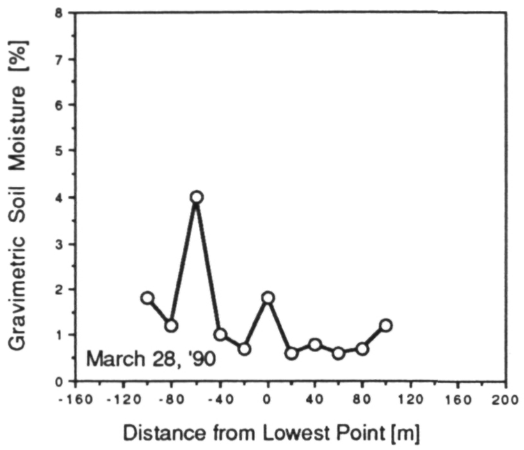

Figure 2: Soil Moisture Content along Transect

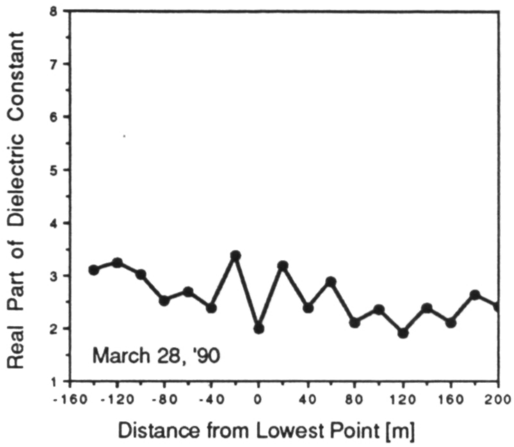

Figure 3: Real Part of Dielectric Constant along Transect

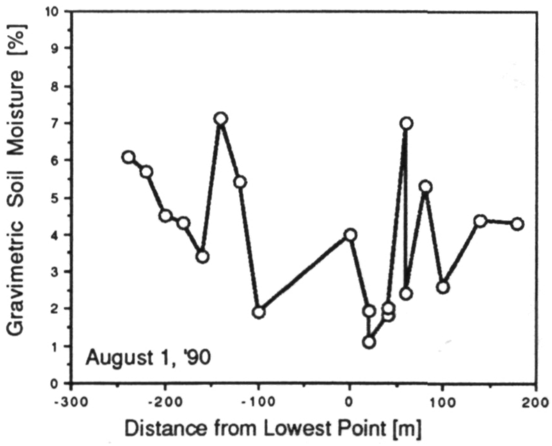

Figure 4 : Soil Moisture Content along Transect

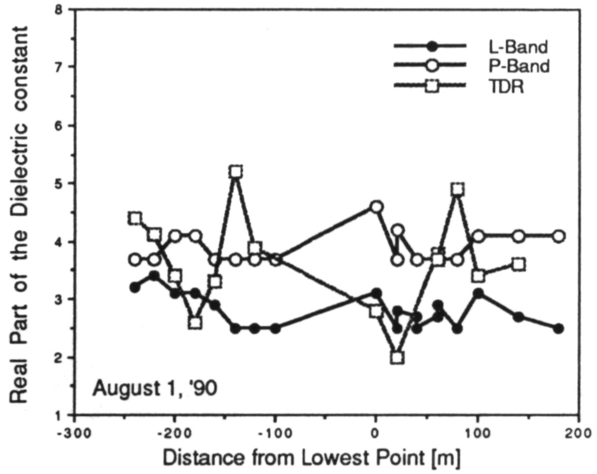

Figure 5 : Real Part of Dielectric Constant along Transect

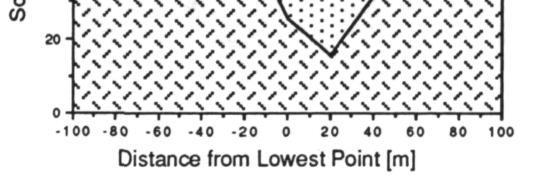

Figure 6 : Soil Composition along Transect

ORIGINAL PAGE
BLACK AND WHITE PHOTOGRAPH

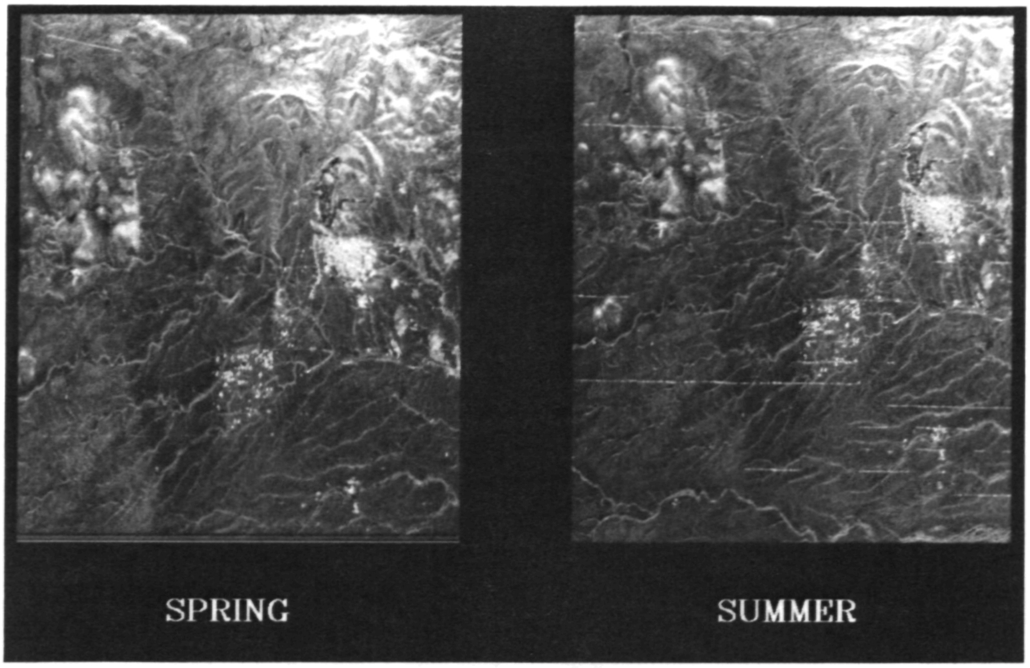

Figure 7 : Spring and Summer Images, Three-frequency overlay, P-Band (red), L-Band (green) and C-band (blue) (see Slide 12).

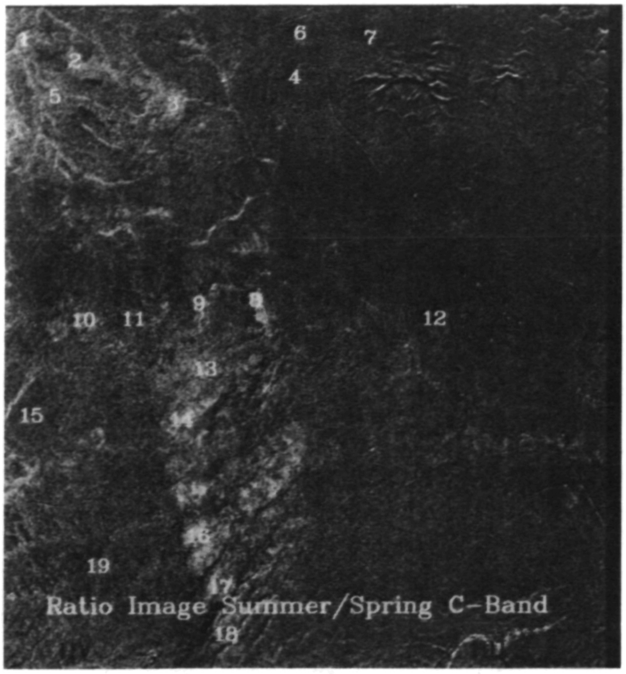

Figure 8 : Three-Polarization Overlay of the C-Band Ratio image (summer/spring), HV (red), VV (green) and HH (blue). Note the brighter area in the center. We have also marked the areas used for analysis (see Slide 13).

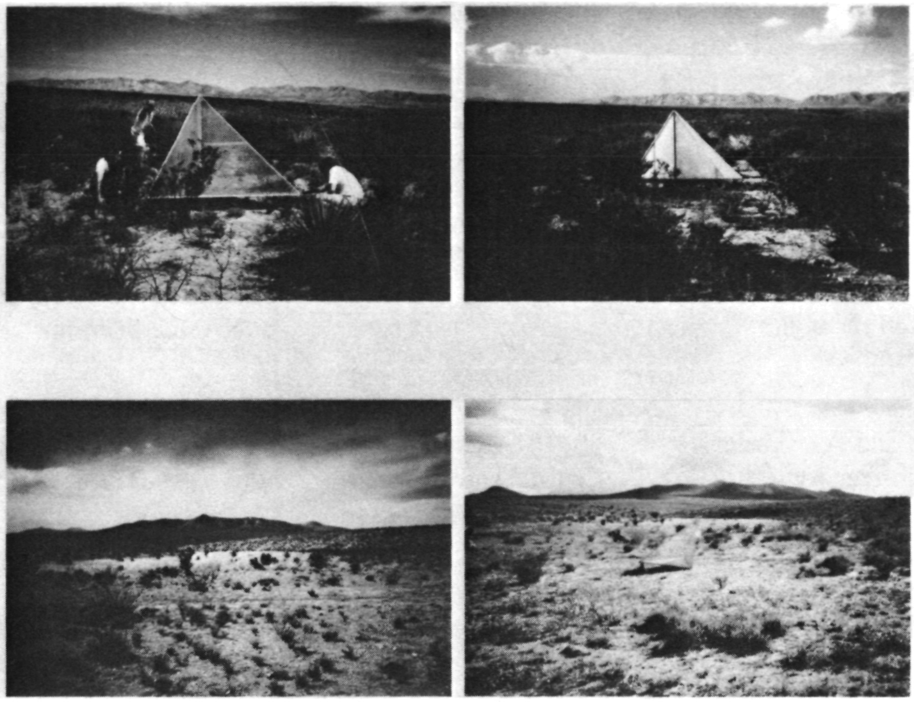

Figure 9 : The top scene corresponds to an area next to Corner Reflector 3, which displays only minor changes between the spring (left image) and summer (right image) in the backscatter coefficient. The bottom scene corresponds to target 3, which has large changes in backscatter coefficent. In both cases, the vegetation is greener in the summer **(see slide 14).**

Target Number	CC Sum	CC Sp	HH/VV Sum	HH/VV Sp	Ratio HH	Ratio VV	Ratio HV
1 *	0.49	0.55	1.72	-0.95	4.59	1.93	5.36
2 *	0.58	0.76	0.86	-0.51	2.77	1.4	4.82
3 *	0.55	0.59	0.6	-0.46	2.87	1.81	6.23
5 *	0.63	0.63	0.61	0.22	1.48	1.09	2.08
8 *	0.39	0.49	1.03	-0.95	5.04	3.06	6.16
9 *	0.42	0.38	0.62	-1.62	2.31	0.05	2.06
10 *	0.05	0.22	2.75	0.88	3.06	1.19	3.57
13 *	0.4	0.45	0	-0.85	4.26	3.42	5.7
14 *	0.41	0.41	0.18	-1.52	4.47	2.79	5.26
16 *	0.32	0.43	0.01	-1.17	4.91	3.74	5.67
17 *	0.36	0.48	0.75	-0.62	4.13	2.76	3.48
18 *	0.33	0.5	0.33	-0.68	2.19	1.18	2.41
4	0.62	0.57	-0.12	-0.6	0.09	-0.39	-0.55
6	0.61	0.58	0.99	-0.08	-0.31	-1.39	-1.97
7	0.63	0.53	1.31	0.18	0.19	-0.94	-1.6
11	0.46	0.48	0.14	-1.43	0.51	-1.06	0.03
12	0.37	0.39	0.38	-0.81	-0.38	-1.57	-1.09
15	0.46	0.4	-0.16	-1.22	0.18	-0.88	0.05
19	0.4	0.41	0.31	-0.91	0.65	-0.56	0.77
20	0.4	0.38	-0.73	-1.21	-0.17	-0.65	-0.2

Table 1 : Data analysis for the twenty selected targets. (CC) stands for correlation coefficient as in equation (1), (Sum) stands for summer, (Sp) stands for spring. (ratio) is the summer value divided by the spring value.

N92-28023

AIRSAR Observations of the Gulf Stream With Interpretation from Sea Truth and Modeling

G.R. Valenzuela, S.R. Chubb, G.O. Marmorino, C.L. Trump, J.S. Lee, A.L. Cooper,
F. Askari, W.C. Keller, J.A.C. Kaiser, R.P. Mied, and S.A. Mango
Naval Research Laboratory
Washington, DC

M. Kobrick and R.M. Goldstein
Jet Propulsion Laboratory,
Pasadena, CA

A.R. Ochadlick, K. Birney, and P.H. Cho
NADC, Warminster, PA

J.M. Morrison and A. Riordan
NC State University
Raleigh, NC

J.R. Bennett
ERIM, Ann Arbor, MI

E.W. Foley and R.J. Lai
DTRC, Bethesda, MD

P.M. Smith
NOARL, Stennis Space Center, MS

D. Sheres
University of So. MS, Stennis S.C., MS

R.C. Beal and T. Gerling
APL/Johns Hopkins University
Laurel, MD

Abstract: On July 20 the NASA JPL/DC-8 SAR participated in the 17-21 July 1990 NRL Gulf Stream (GS) experiment in preparation for SIR-C missions in '93, '94 and '96 for calibration purposes and to check modes and techniques for operation at our experimental site off the East Coast of the U.S. During this experiment, coordinated and near simultaneous measurements were performed from ship (R/V Cape Henlopen) and other aircraft (NADC/P-3 and NRL/P-3) to address scientific questions relating to the origin of "slick-like" features observed by Scully-Power, the refraction and modulation of waves by variable currents, the effect of current and thermal fronts on radar imagery signatures and the modification of Kelvin ship wakes by fronts. The JPL/DC-8 and NADC/P-3 SARs are fully polarimetric systems. Their composite frequency range varies between P- and X-band. In this paper we describe in detail the AIRSAR participation in the July 1990 GS experiment and present preliminary results of the ongoing analysis and interpretation of the radar imagery in the context of ground truth, other remote measurements and modeling efforts.

I. Introduction

Radar images of the ocean contain a variety of ocean features, ranging in size from the mesoscale (~100 km) to gravity waves (~100 m), as a result of the transmitted electromagnetic (e.m.) radiation being scattered back to the radar by the dynamical ocean surface (a time dependent boundary value problem) (Valenzuela, 1989). The coverage of synthetic aperture radar (SAR), but not the resolution, depends on altitude. Hence, space platforms image swaths of the ocean of the order of 100 km wide, while the lower altitude aircraft systems provide more moderate coverage of only tens of km wide.

Besides system constraints, impacting the imagery process are fundamental aspects in ocean hydrodynamics, e.m. scattering from the ocean, and signal processing. These are reviewed and discussed in Hasselmann et al. (1985). Most of these processes are well understood, but in many instances need to be quantified further, and are areas of active research today. Important questions to be answered are the strength of the signatures contained in radar imagery, and their dependence on radar and environmental parameters. Important parameters are: radar frequency, radar polarization, angle of incidence, azimuthal dependence, wind stress, atmospheric stability, state of development of wave field, current gradients and other forcing variables.

Although airborne SARs are more suited for local studies of processes, space systems are ultimately needed for operational purposes to address geophysical problems involving the earth environment, such as climate and global change. A number of space platforms containing SARs are forthcoming: ERS-1, JERS-1, SIR-C, ERS-2, RADARSAT, SIR-E(EOS), etc.

Here, we report on pre-mission measurements off Norfolk, VA relating to NASA's SIR-C launchings in '93, '94, and '96. We concentrate on JPL/DC-8 SAR data collected in the presence of extensive in situ measurements from R/V Cape Henlopen and other remote measurements from NADC/P-3 and NRL/P-3 aircraft during the 17-21 July 1990 GS experiment. Unfortunately, due to problems in scheduling and airspace clearances, both JPL and NADC SARs were not able to collect data on the same day as originally planned for comparison and cross calibration.

II. SAR Data

On 20 July the measurements in the GS experiment were concentrated on the North edge of the GS at 36° 43.12' N, 72° W where the thermal front was located. (See Valenzuela et al. (1991) for a detailed description of the operational plan for the experiment.) The JPL/DC-8 departed Langley, VA slightly before 0930 (EDT) and performed scheduled flight patterns for approximately 7 hours, collecting SAR data at P-, L-, and C-band in the standard mode and at L&C band in the interferometric mode (INSAR) (Goldstein et al., 1989) according to the flight plan developed by JPL in coordination with the participants in the GS experiment (Kobrick, 1990).

The coverage of the JPL/DC-8 is shown in Figure 1. Overall, 80 min 27 s of data were collected in the standard SAR mode and 36 min 58 s in the INSAR mode. The system parameters of JPL/DC-8 SAR are well known, so they will not be repeated here.

The JPL/DC-8 aircraft first flew a straight track over Chesapeake Light Tower (CLT) located at 36° 54' N, 75° 42' W) at 26,000 ft altitude using the INSAR mode to obtain data on the dynamics of ''slick-like'' features (Figure 2) over the continental shelf. The NADC/P-3 SAR (L,C&X band) already covered this region during the two previous days (Ochadlick et al., 1991). Figure 3 provides the flight tracks of NADC/P-3. The system parameters of NADC SAR are given in Ochadlick et al. (1989). Scully-Power (1986) observed similar features with photography from SIR-B, and Ochadlick et al. (1989), observed these ''slick-like'' features with SAR. One of the objectives of the GS experiment was to infer the origin of "slick-like" features, and the measurements in the GS experiment concentrated in this area on July 18 (see Valenzuela et al., 1991).

After the flight over CLT, the DC-8 performed a 45° STAR pattern over the North edge of the GS (Figure 4) with SAR mode, flying the legs of the STAR pattern in both directions to resolve the ambiguity in the direction of wave propagation on the radar imagery in later analysis. The STAR pattern was performed to obtain data on the azimuthal dependence of both the wave field and the radar signatures over the thermal front and current curvature region. Thereafter, the DC-8 made three incremental 60° passes with INSAR over the North edge of the GS to attempt to extract GS current features to provide an independent measurement of the GS current structure. One uncertainty in the INSAR measurements is the phase unwrapping of the INSAR data in cases where there is no stationary target in the image.

Immediately after the above patterns, the DC-8 flew from the North to the South edge of the GS and beyond with standard SAR mode to obtain information on the refraction and modulation of ocean waves by the GS current. Once beyond the South edge of the GS, INSAR mode was used in a 155° pass towards the center of an extremely energetic cold eddy that had formed at 34° 18' N, 71° 30' W to assess the potential of INSAR to detect cold eddies. (These produce weak signatures in standard SAR imagery because when water is colder than the air, the stable atmospheric conditions are conducive to reduced wind stress and the amplitude of Bragg resonant waves is smaller.)

After the pass over the cold eddy, the JPL/DC-8 descended to 17,000 ft to reduce the range-to-velocity ratio, appropriate for obtaining a more linear SAR transfer function and thus to reducing "velocity bunching" effects. At this lower altitude the DC-8 flew back from the South edge to the North edge in a straight track and then performed a Cross pattern on the North edge, using the standard SAR mode. Then the airplane ascended to 26,000 ft and flew back in a straight flight line over CLT with INSAR mode to obtain additional data on the "slick-like" features over the continental shelf.

III. Sea Truth

Throughout the GS experiment, extensive in situ measurements were performed from the R/V Cape Henlopen which are described in detail in Valenzuela et al. (1991). Here we provide a brief description of these measurements.

The GS experiment had two distinct phases of operation, on July 18 the ship measurements concentrated between Station 1 (37° N, 75° W) and CLT where the "slick-like" features are found. On July 19 and 20, the ship was stationed on the North edge of the GS (Station 2) where the effects of thermal and current fronts on the wave field, atmospheric boundary layer, and radar signatures were to be investigated.

The in situ measurements consisted of standard oceanographic and meteorological information (wind vector, air and water temperature, salinity, etc.) plus balloon soundings of the atmospheric boundary layer, subsurface stratification with CTD and XBT casts, ENDECO buoy for directional spectrum of waves (0.047-0.5 Hz) and SPAR buoy for short waves (~ 10 cm). In addition, the subsurface current field components were obtained with an Acoustic Doppler Current Profiler (ADCP), and Lagrangian drifters were deployed to measure near surface currents.

Also, in the bow of the ship were mounted a Ku-band scatterometer, two video cameras (narrow and wide coverage), and an infrared PRT-5 thermometer to obtain more information on the water surface. Surface tension was measured from a Zodiac (power boat) and an X-band Marine radar was used on the 18th to obtain directional information on the long waves. On July 18th, the wind was light (1-2 m/s) and the waves were 0.5 m in height. On July 19 there were showers, the winds were 2-3 m/s with gustiness, and the waves were 0.75 m. On July 20, the winds reached over 9 m/s from 230° and the waves were about 1 m.

IV. Preliminary Results

Twenty-seven one-minute frames of SAR and INSAR data were selected from the JPL Survey imagery for digital synthesizing by JPL. Three additional advanced requests were made: RCB requested one frame over the South edge of the GS (SS 360-1) (see Figure 1), MK requested one frame from the North edge of the GS (NS 135-1) (see Figure 4), and RMG requested one frame over CLT. To date JPL has digitally synthesized these advanced requests and 6 more from our general request list and for all these we have received the standard products: total power color image photos and the compressed Stokes matrix data (van Zyl and Burnette, 1990). As usual, the data have been system calibrated and other additional calibrations are possible with POLCAL (van Zyl, 1990) even without trihedral corner reflectors (Freeman et al., 1991). Of all the one-minute frames processed, two are for INSAR data and these presently are being phase unwrapped and airplane motion compensated by RMG.

At NRL we are concentrating on the analysis and interpretation of two images with strong linear features. One is over the South edge of the GS (Slide 15), and the other is near the North edge of the GS (Slide 16). The other imagery does not contain evidence of strong linear features and will be analyzed in relation to the directional properties of the wave field at the thermal front and current curvature region in the context of the extensive in situ measurements we have.

In Figure 5, a region of 512 x 512 pixels near the center of slide 15 has been recovered by NRL Digital Image Processing Laboratory (DIPL) from the compressed Stokes matrix data supplied by JPL and displayed as a function of frequency and polarization. The last three images are the SPAN (the total power) at P-, L- and C-band. It is clear from Figure 5, that the SAR signatures over the South edge of the GS looking to the West are strongest for P-, and L-band, and are weaker for C-band. However, the signatures are also polarization dependent.

To obtain more quantitative information on the strength of these signatures in SAR over the GS, in Figure 6 we have plotted the image intensity (averaged over 7 pixels in azimuth to reduce speckle; Lee, 1986) along a cut in range in Slides 15 and 16. The left column of curves corresponds to data for Slide 16, about 25 km inside the North edge of the GS with the radar looking towards 45°. We have separated the curves according to frequency and polarization (the line is in the range direction centered at 400 pixels from the left end of Slide 16). An arrow has been placed to indicate where the strong signature (4-6 dB) occurs at P-band, while for that angle of incidence the L-band plots show a large decrease in image intensity. Careful study of the imagery intensity should obtain signatures at other angles of incidence as well.

The image intensity curves on the right column of Figure 6 correspond to data of Slide 15. Here the center of the range line has been placed 544 pixels from the left of that slide. Also, again an arrow denotes a signal (2-3 dB) at L-band, but at P-band the signature is absent for that angle of incidence. Analysis of the image intensity curves reveals signatures at other angles of incidence. Figures 5 and 6 demonstrate the complex nature of SAR signatures over the GS, which are frequency and polarization dependent.

Modeling efforts are ongoing to explain and predict these SAR signatures. For this purpose, the Lyzenga and Bennett (1988) model, which contains a full-wave description of the wave field and relies on composite surface scattering for the radar backscatter, has been applied to a Gaussian approximation for the GS current profile (with a spread of 100 km) with a meander in the Stream function of form y-B tanh (Ax) (x is in the East and y in the North directions, with A,B suitable constants). For a wind speed of 9.6 m/s blowing from 231° the cross section map prediction for X-band (C-band is very similar) is shown in Figure 7. Two linear signatures of about 1 dB are evident in Figure 7, which seem to be related to both wind and current gradient. As the wind decreases, the signatures weaken and move away from the center of the jet and disappear for a wind speed less than 2.4, or if the wind direction is reversed. These preliminary modeling efforts are encouraging, but comparison with Figures 5 and 6 also indicates that higher resolution is needed in the modeling, and the profile of the GS current is much more complex with, perhaps, current filaments, intrusions and discontinuities modifying the Gaussian current profile.

Finally we present an objective map of the surface temperature field for July 20 (Figure 8) derived from NRL/P-3 data with an infrared PRT-5 thermometer on board. The 8 passes used are given in Figure 9. The synthesized temperature map is in agreement with in situ temperature measurements from R/V Cape Henlopen.

V. Conclusions

This report has presented preliminary results on the JPL/DC-8 SAR data collected July 20 during the Gulf Stream experiment. The results obtained demonstrate the complexity of the signatures in radar imagery over the GS. These signatures depend on radar frequency and polarization as well as on environmental parameters. To achieve a quantitative explanation and prediction of the strength of the signatures on SAR of the GS, a detailed description of the GS temperature and current structure are required. More of the extensive in situ measurements obtained from R/V Cape Henlopen will be assimilated into the numerical models, which will allow for more quantitative comparisons between predictions and SAR measurements. We also expect that additional calibration of the JPL/DC-8 SAR imagery will be required, in particular the phase and cross-talk calibrations by POLCAL.

Acknowledgments

The authors would like to thank the flight crews of JPL/DC-8, NADC/P-3 and NRL/P-3 for their skills in acquiring the remote sensing data. We would also like to thank the Radar Science group of JPL for data processing, Jakob van Zyl for expediting the delivery of the AIRSAR data, and Anthony Freeman for advice in calibration and furnishing the POLCAL software package. We also acknowledge a computational grant from the Pittsburgh Supercomputing Center.

References

Freeman, A., Y. Shen, J. van Zyl, and J.D. Klein, Calibration of NASA/JPL DC-8 SAR data, Proc. IGARSS '91, Espoo, Finland, 1991.

Goldstein, R.M., T.P. Barnett, and H.A. Zebkar, Remote sensing of ocean currents, Science, **246**, 1282-1285, 1989.

Hasselmann, K., R.K. Raney, W.J. Plant, W. Alpers, R.A. Shuchman, D.R. Lyzenga, C.L. Rufenach, and M.M. Tucker, Theory of synthetic aperture radar ocean imaging: a MARSEN view, J. Geophys. Res., **90**, 4659-4686, 1985.

Kobrick, M., AIRSAR Data Digest Summer 1990, Jet Propulsion Laboratory JPL D-8123, Pasadena, CA, December 1990. (JPL internal document.)

Lee, J.S., Speckle suppression and analysis for SAR images, Opt. Eng., **25**, 636-643, 1986.

Lyzenga, D.R. and J.R. Bennett, Full-spectrum modeling of synthetic aperture radar internal wave signatures, J. Geophys. Res., **93**, 12345-12354, 1988.

Ochadlick, A.R., K. Birney, P.C.A. Carreras, C. Haney, S. Krasznay, and S. Lyness, SAR measurements during SAXON by the NADC aircraft, Proc. IGARSS '89, 1934-1937, Vancouver, B.C., Canada, 1989.

Ochadlick, A.R., G.R. Valenzuela, K. Birney, P. Cho, J. Evans-Morgis, R.P. Mied, J.M. Morrison, and J. Yannone, Evolution of ocean surface features observed with SAR during the July 90 Gulf Stream experiment, Proc. IGARSS '91, Espoo, Finland, 1991.

Scully-Power, P., Navy Oceanographer Shuttle Observations, STSS 41-G, Mission Report, NUSC Tech. Doc. 7611, 26 March 1986.

Valenzuela, G.R., SAR Imaging of Ocean Waves in the Presence of Variable Currents, in "Radar Scattering of Modulated Wind Waves," G.J. Komen and W.A. Oost (eds.), Kluwer, 1989, pp. 141-153.

Valenzuela, G.R., R.P. Mied, A.R. Ochadlick, M. Kobrick, P.M. Smith, F. Askari, R.J. Lai, D. Sheres, J.M. Morrison, and R.C. Beal, The July 1990 Gulf Stream experiment, Proc. IGARSS '91, Espoo, Finland, 1991.

van Zyl, J.J., Calibration of Polarimetric Radar Images Using Only Image Parameters and Trihedral Corner Reflector Responses, IEEE Trans., GE-28, 337-348, 1990.

van Zyl, J.J. and C.F. Burnette, Data volume reduction for single-look polarimetric imaging radar data, submitted to IEEE Transactions on Geoscience and Remote Sensing, 1990.

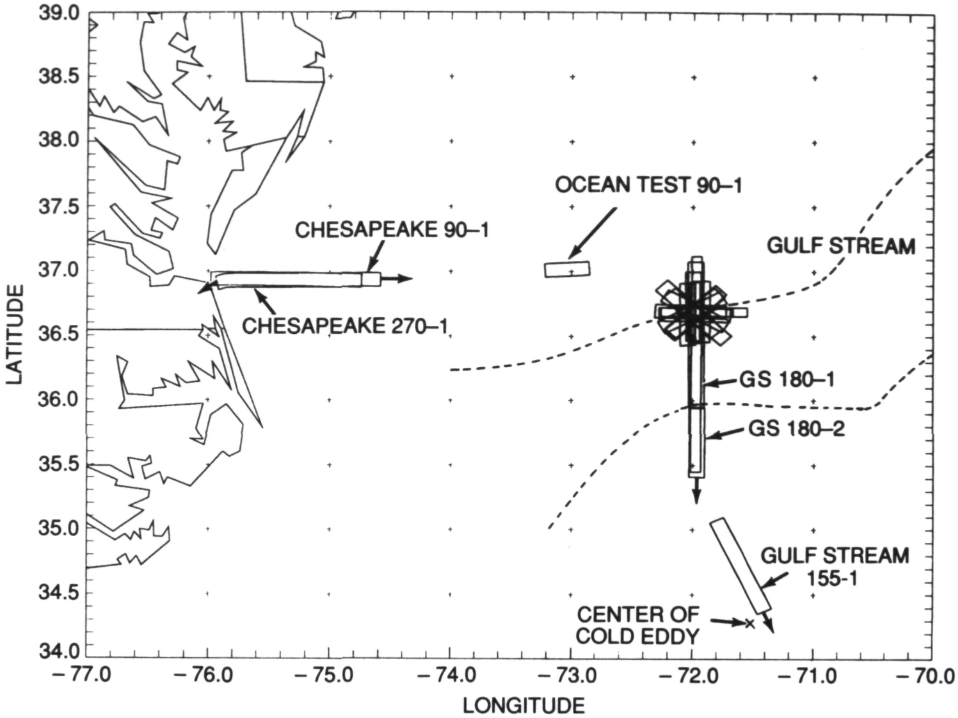

Figure 1. Summary of JPL/DC-8 SAR/INSAR coverage for 20 July 1990.

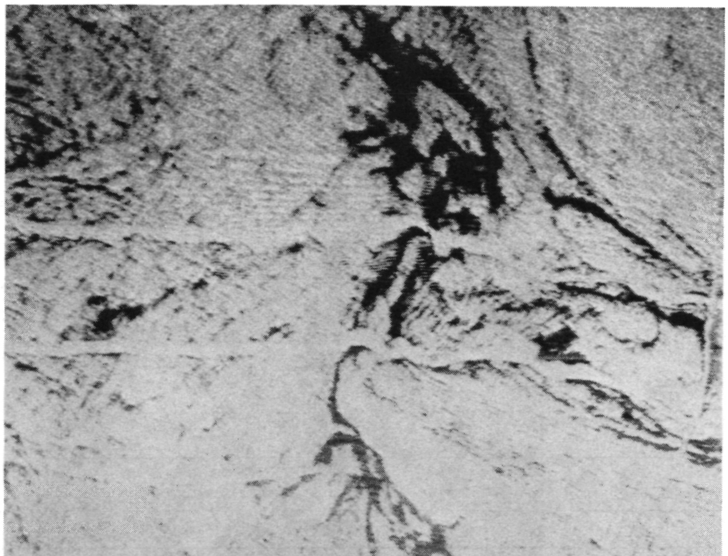

Figure 2. NADC digitally processed imagery (LVV) of a "slick-like" feature. Data from pass #7 of 18 July 1990; the vertical is in the range direction and is 13.4 km high.

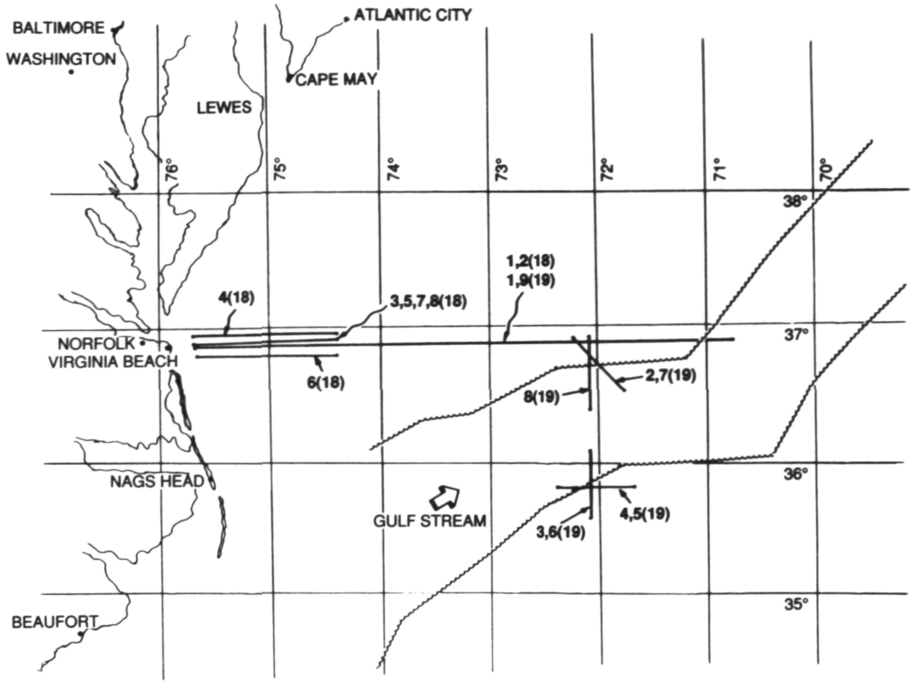

Figure 3. Flight tracks for NADC/P-3 airplane for 18 and 19 July 1990.

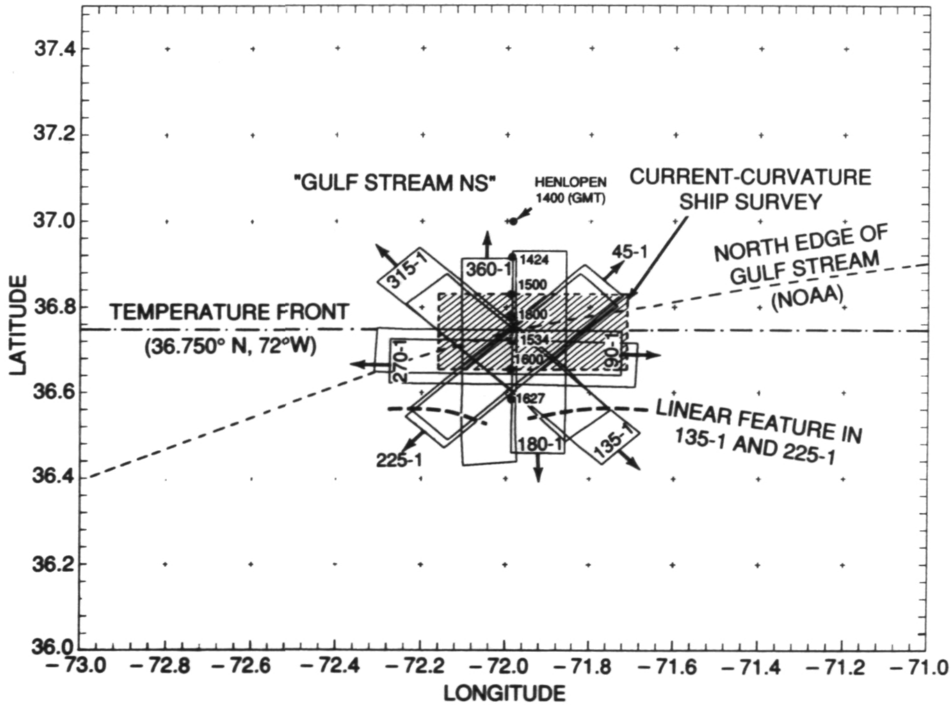

Figure 4. STAR pattern performed by JPL/DC-8 on the North edge of Gulf Stream.

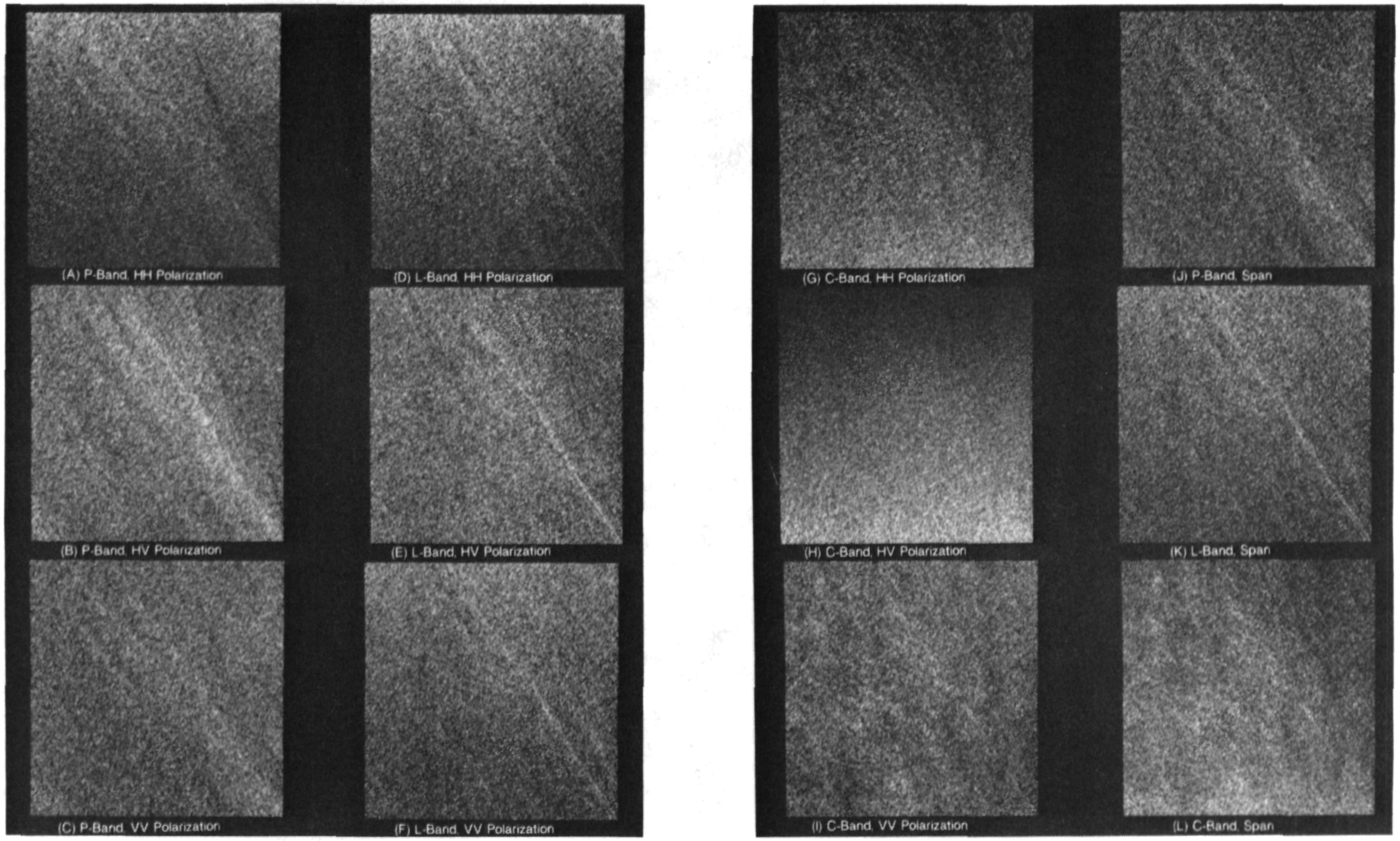

(A) P-Band, HH Polarization

(B) P-Band, HV Polarization

(C) P-Band, VV Polarization

(D) L-Band, HH Polarization

(E) L-Band, HV Polarization

(F) L-Band, VV Polarization

(G) C-Band, HH Polarization

(H) C-Band, HV Polarization

(I) C-Band, VV Polarization

(J) P-Band, Span

(K) L-Band, Span

(L) C-Band, Span

Figure 5. Section of SAR imagery (512 x 512 pixels) near the center of Slide 15 as a function of frequency and polarization.

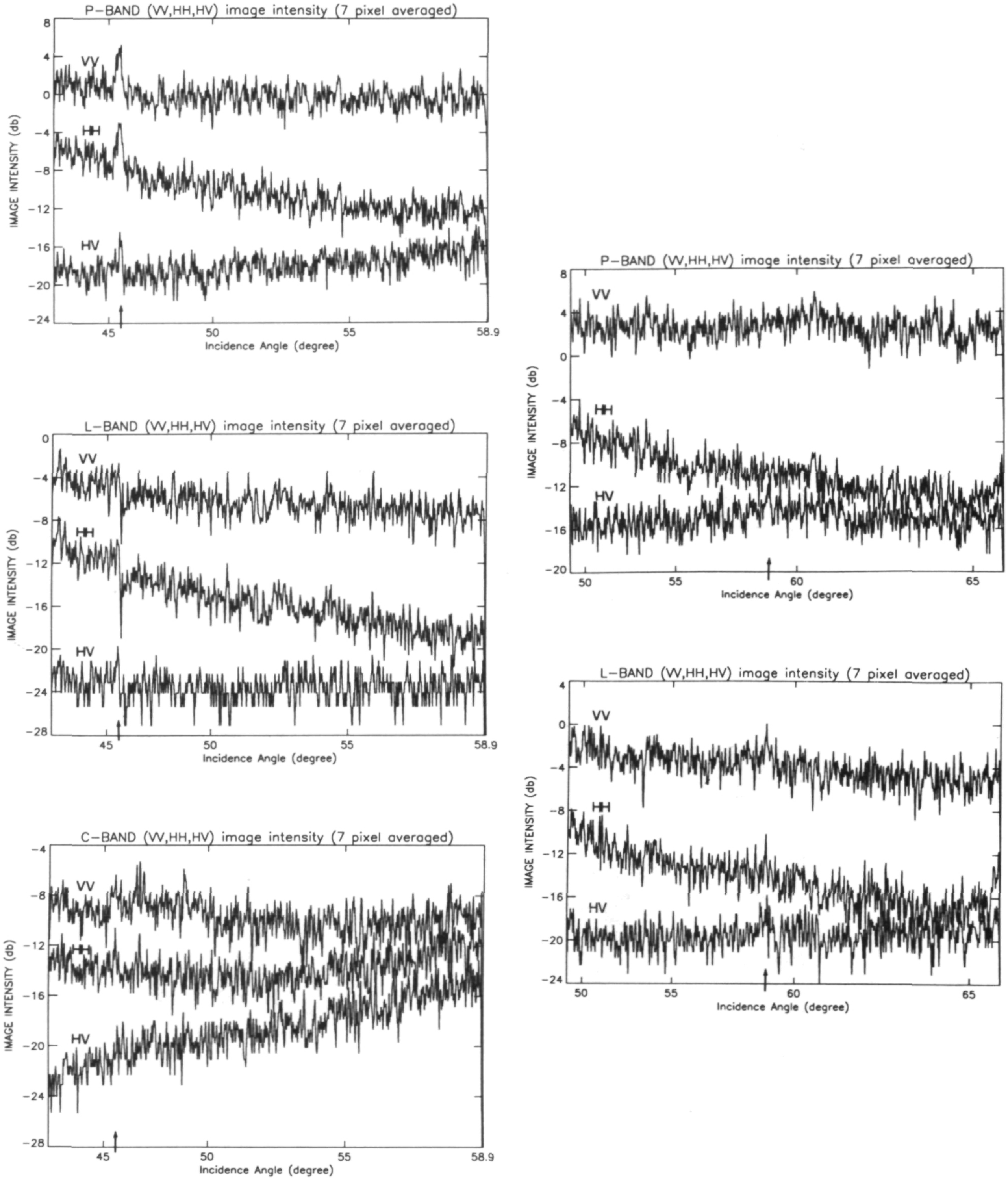

Figure 6. Image intensity variation as a function of frequency (P,L&C) and polarization (HH, HV & VV) along a line in range cut for Slides 15 and 16. The left curves correspond to Slide 16; the line transect is centered at 400 pixels from the left side of the slide. The right curves correspond to Slide 15; the line transect is centered at 544 pixels from the left side of the slide.

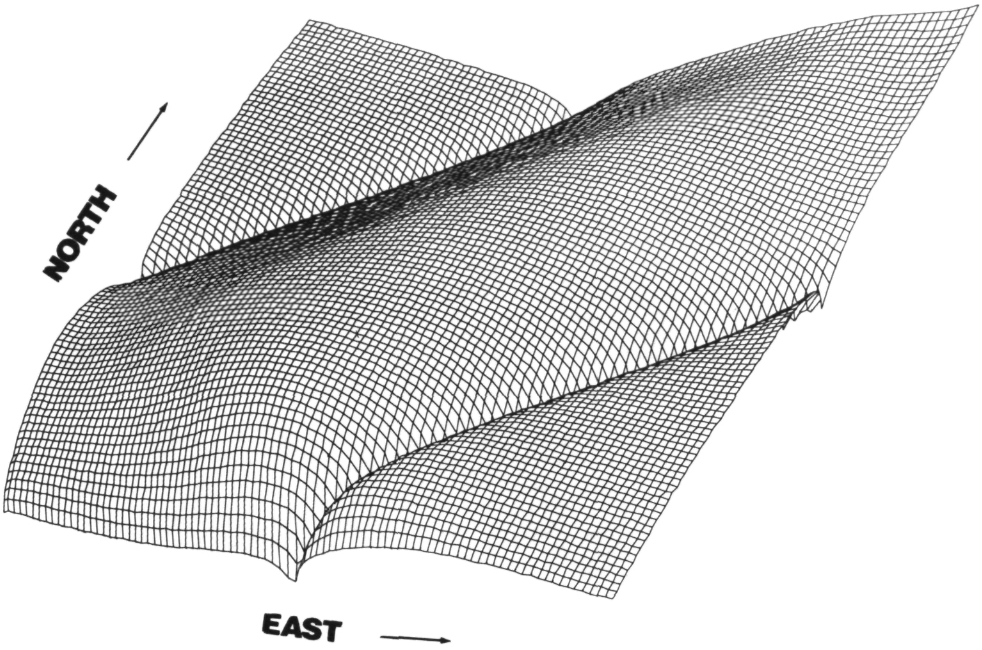

Figure 7. Simulated radar cross-section map (X-band) (the map for C-band is quite similar) for a region 76 x 76 km containing a meander of a Gaussian Gulf Stream current profile. Wind speed = 9.6 m/s from 231°; resolution 840 m, and for HH polarization.

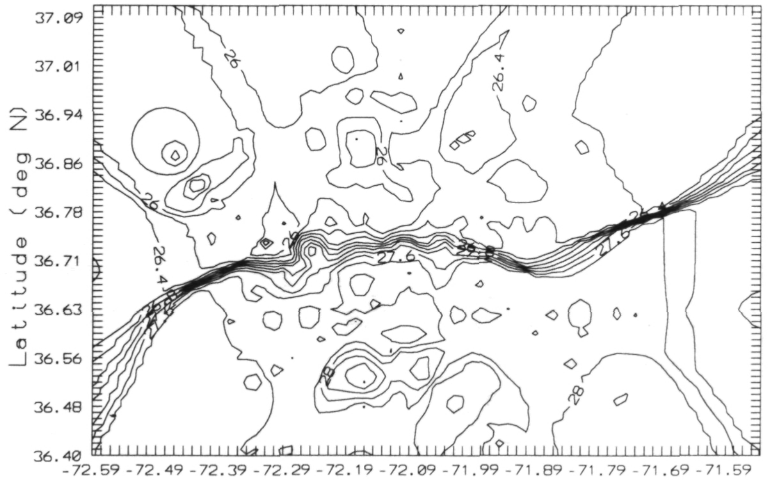

Figure 8. Objective surface temperature map derived from infrared PRT-5 thermometer data from NRL/P-3 aircraft, 20 July 1990. Contours are in °C.

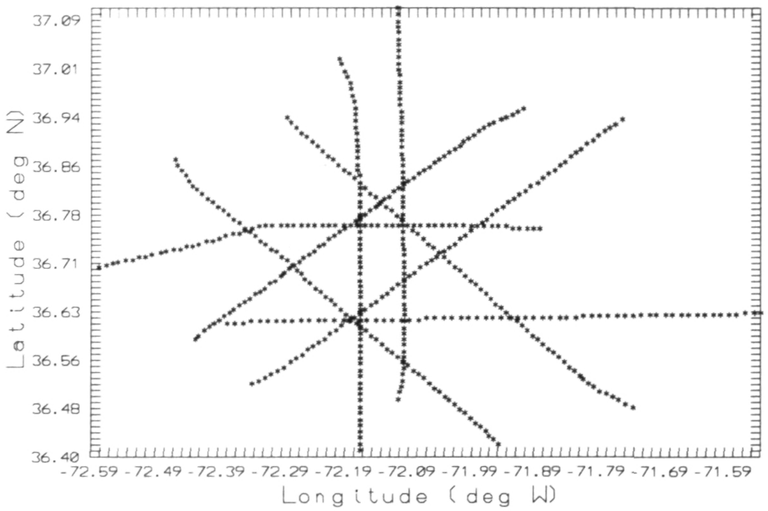

Figure 9. Flight tracks of NRL/P-3 for 20 July 1990 from which objective temperature map was derived.

Dual Frequency Along-Track Interferometry:
A Status Report

R. E. Carande, R. M. Goldstein, Y. Lou, T. Miller, K. Wheeler
Jet Propulsion Laboratory
California Institute of Technology
Pasadena, California

Abstract. In recent months, the JPL AIRSAR system has had a C-band Along-Track Interferometer installed. This, in addition to the L-band interferometer already operating in the system, makes it possible to simultaneously acquire two frequency interferometer data. Also, another upgrade involving the radar digital system allows each interferometer to be operated in such a way as to obtain two along-track interferometric baselines differing by a factor of 2 in length. An engineering checkout flight has demonstrated the ability to acquire and process both frequencies to high-resolution velocity maps of the ocean surface. The status of these interferometers and some initial data are presented in this paper.

1.0 Introduction

Successful imaging of the ocean surface to measure surface currents using the Along-Track Interferometric (ATI) technique was first reported by Goldstein and Zebker in 1987[1]. Since then, the Along-Track Interferometer has proven very useful in the study of the ocean from studying currents associated with the Gulf Stream[2], to currents generated behind moving ships[3]. Currently there is a great interest in using interferometric techniques for more accurately determining ocean wave spectra[4].

The current AIRSAR system has been acquiring L-band ATI data since 1988. This spring, two new antennas for a C-band Cross-Track Interferometer were added to the AIRSAR system for topographic mapping[5]. Care was taken in the placement of these antennas with respect to the current quad-pol C-band antenna, so that one of the new antennas, in conjunction with the existing antenna, would produce a useful C-band baseline in the along-track direction for ocean observations.

2.0 Antenna Geometry and Operations

Figure 1 shows the geometry of the JPL AIRSAR antenna systems. The L-band antennas are separated by a distance of 19.3 meters fore and aft along the fuselage of the DC-8. When the aircraft flies in a straight line with no pitch or yaw, the antenna translations are collinear. Any yaw or pitch produces a cross-track component. The along-track C-band system utilizes the standard quad-pol C-band antenna at the aft of the plane and the lower cross-track antenna just forward. As can be seen from the figure, there is a substantial cross-track component using this interferometer.

Both L-band and C-band interferometers are operated in such a way that two interferometric baselines for each frequency may be constructed. The operation is similar to the standard quad-pol method of interleaving H and V transmit events, with fore (F) and aft (A) replacing the two polarizations. Simultaneous multiple baselines will be useful in the study of the decorrelation process of the ocean surface.

Transmitting out of the aft antenna and receiving returns through both the aft and fore antennas will allow an interferometric baseline corresponding to half the antenna separation (D/2) to be achieved by combining the two complex images produced. This has been the standard ATI method used in the AIRSAR system. The same baseline is also achieved by transmitting out the fore antenna and receiving through both. By transmitting out both the fore and aft antennas (interleaving transmit events) and receiving through both, four complex images may be made: FF, FA, AF, and AA, where the letter pair corresponds to transmit and receive antenna combinations. Combining FF and AA will produce an interferometric baseline of the antenna separation D.

3.0 System Sensitivities

The principle behind Along-Track Interferometry is that two antennas view the same pixel at slightly different times. If nothing in the pixel changes, the phases associated with the complex images will be identical. However, if something in the pixel changes, the phases in the two images will be different. If the change is caused by a movement toward the aircraft of a distance less than half the radar wavelength, the phase difference will correspond directly to the speed of the movement.

Table 1 shows the ambiguous speeds for each frequency and baseline. The ambiguous speed is the speed that will cause a phase change of 2π to be observed between the images. Note that the ambiguous speeds for the half baseline of the L-band system and the full baseline of the C-band system are about equal. Also note that the ambiguous speeds are greater than twice the corresponding Bragg wave velocities at an incidence angle of 45 degrees.

The velocity resolution obtainable using the JPL ATI has not been measured as of yet. However, strong coherence down to 1/32 of the ambiguous velocity has been observed. The accuracies of the measurements are strongly dependent on the quality of the motion compensation applied to the data and the signal-to-noise ratio associated with each image.

4.0 Engineering Data

The first engineering flight to test out the new interferometric systems (both along and cross-track) occurred on May 13, 1991. To date, this is the only data available from the new systems. To test the along-track systems, a flight path of heading 156° along the coast of California was chosen. The imaged area included the San Francisco Bay outlet to the Pacific Ocean. This is a favorite target area for AIRSAR ATI tests as there are usually strong currents associated with tidal flow present, as well as wave fields interacting with this current and the shore.

Figures 2 and 3 show the interferometric images produced using the following baselines: LAA/LAF and CAA/CFF. The SAR processing involved processing each of the antenna data to 16 complex single-look images, applying motion compensation to the individual looks, interfering the looks and multilooking to obtain the results presented. Images are registered by applying measured range and azimuth delays during processing. The motion compensation includes removing the range phase gradient associated with the cross-track baseline (which must be known accurately) and the along-track attitude drift of the aircraft. The multilook process is carried out by adding the complex vectors of each look coherently to obtain multilook pixel phases, and incoherently to obtain multilook pixel powers. The images shown in figure 2 have color proportional to 16-look phase difference, or velocity, and intensity corresponding to the 4th root of the 16-look power.

Notice the strong phase contouring on the land in the C-band ATI image. This is due to the considerable cross-track C-band antenna displacement built into the system. (This cross-track interferometer is not sensitive enough to be affected by the ocean waves present; therefore ocean "topography" is not a contributing factor to the phase changes seen on the ocean surface in this image.) The much milder elevation contouring at L-band is due to the nonzero attitude of the aircraft during the data acquisition. The 4.5-degree yaw produced a cross-track component between the L-band antenna at the front of the aircraft and the one at the rear.

5.0 Conclusion

Based on the initial engineering checkout flight of the L- and C-band along-track interferometers installed in the JPL AIRSAR system, both are working and producing ocean image data that exhibit strong complex correlation. Waves can clearly be seen in the phase-difference images in addition to the amplitude image. It appears that the data acquired in this dual-frequency mode will be scientifically useful. Software development for the removal of the aircraft motion and phase distortions associated with any cross-track interferometer components, possibly using redundant baseline information, will continue. The dual-frequency ATI system described will be used this summer for imaging the wakes behind surface ships, in addition to several other experiments.

6.0 Acknowledgment

The work described in this report was carried out at the Jet Propulsion Laboratory of the California Institute of Technology, under a contract with the National Aeronautics and Space Administration.

---

[1] R.M. Goldstein and H.A. Zebker, "Interferometric Radar Measurements of Ocean Surface Currents," *Nature*, Vol. 328, 20 August 1987.

[2] G. Valenzuela, *et al.*, "AIRSAR observations of the Gulf Stream with Interpretation from Sea Truth and Modeling," In these proceedings.

[3] R. Carande, "Observations of Internal Waves Generated by Ships at Loch Linnhe Using the L-Band Along-Track Interferometer," JPL Interoffice Memorandum, Jet Propulsion Laboratory, Pasadena, California, 1991.

[4] D.R. Lyzenga, J.R. Bennet, "Estimation of Ocean Wave Spectra Using Two-Antenna SAR Systems," *IEEE Trans. Geosci. Remote Sensing. vol. 29, no. 3, May 1991.*

[5] H. Zebker, E. Rodriguez, J. Martin, J. van Zyl, "Cross-Track Interferometry: A Status Report," In these proceedings.

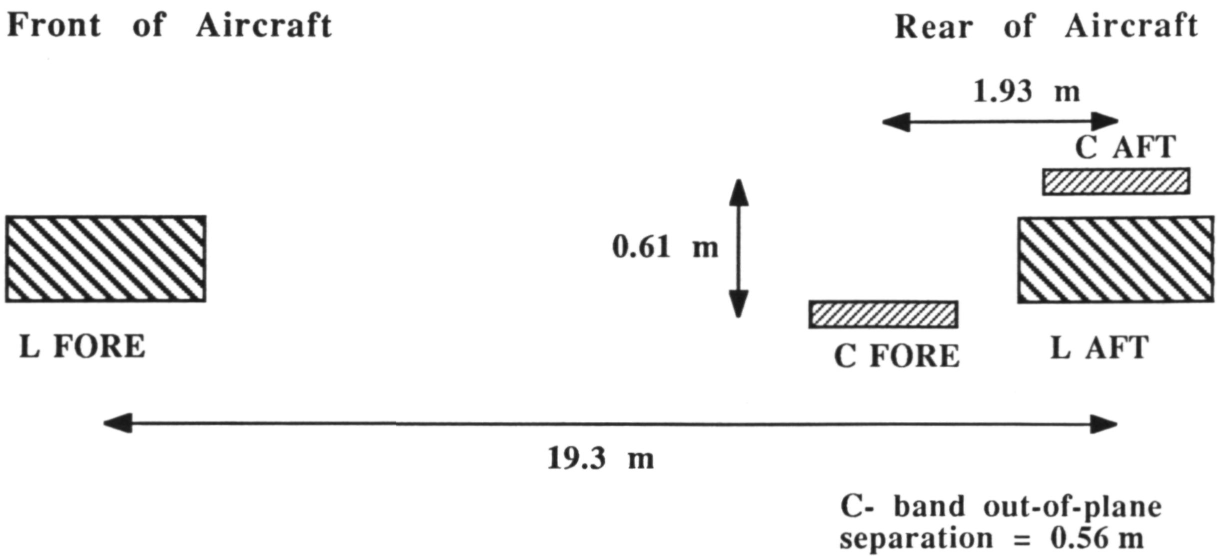

Figure 1: Geometry of the L- and C-band Along-Track Interferometer antennas installed on the DC-8 fuselage. The nominal velocity of the DC-8 aircraft during data acquisition is about 210 m/s, leading to full baseline image delays of 92 ms and 9.2 ms for L- and C-bands respectively

	BASELINE D	BASELINE D/2	RADIAL BRAGG WAVE SPEED (45 DEG INC.)
L-BAND	1.2 m/s	2.5 m/s	0.36 m/s
C-BAND	3.1 m/s	6.3 m/s	0.16 m/s

Table 1: Ambiguous velocities for the L- and C-band inteferometers at both the full baseline (D) and the half baseline (D/2). The radial component of the Bragg wave velocities at an incidence angle of 45 degrees is also shown.

ORIGINAL PAGE
BLACK AND WHITE PHOTOGRAPH

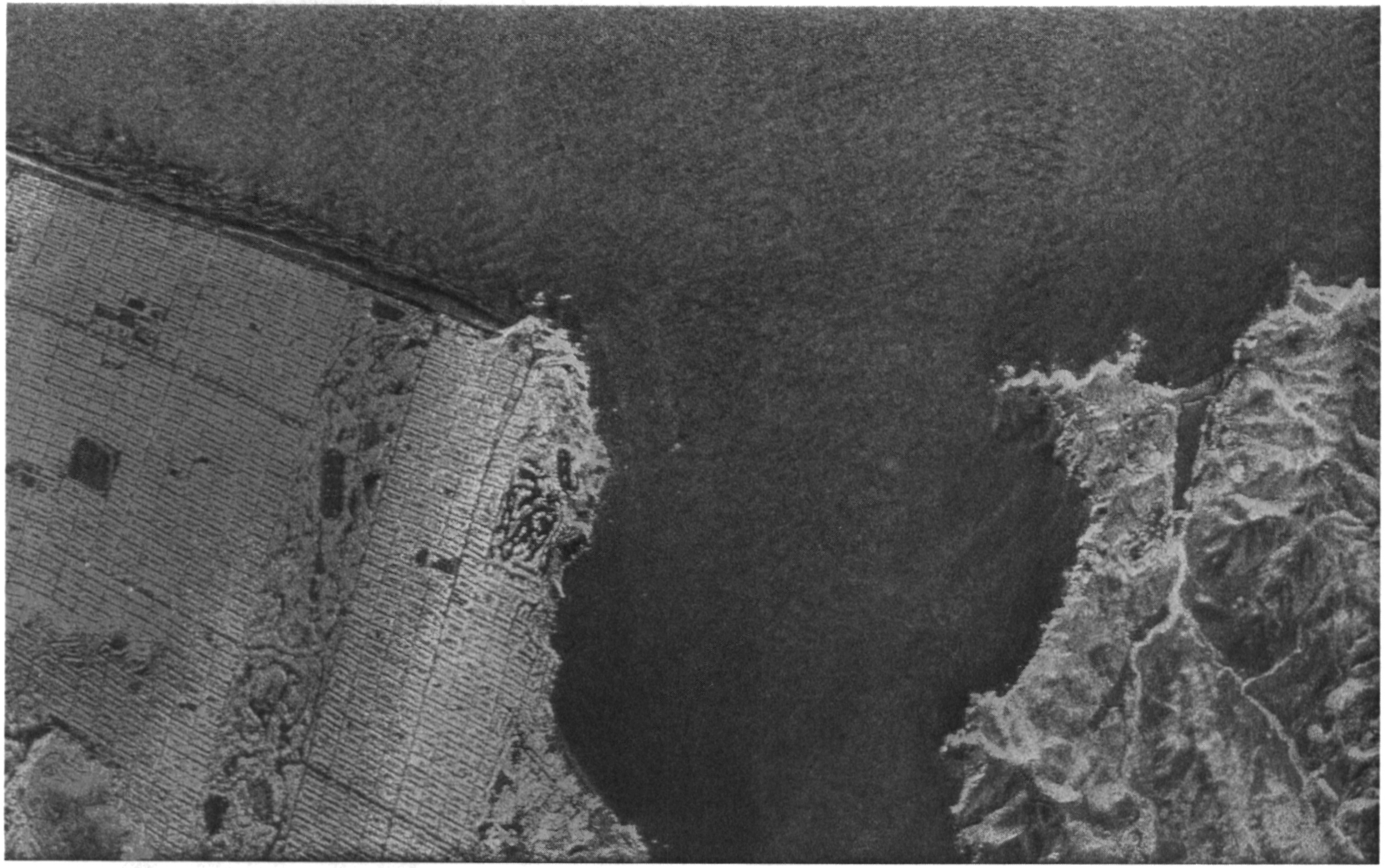

Figure 2. 16 - look L-band Along-Track Interferometer image produced from images formed by transmitting out the aft antenna and receiving through both the fore and aft antennas. The scene is of the outlet of the San Francisco Bay to the Pacific Ocean. North is to the right. The aircraft flight is from north to south (right to left) and above the image (looking east). The image is coded such that the pixel color represents phase change between the fore and aft images, while pixel intensity is proportional to the fourth root of the 16-look power detected. (See color slide no. 17.)

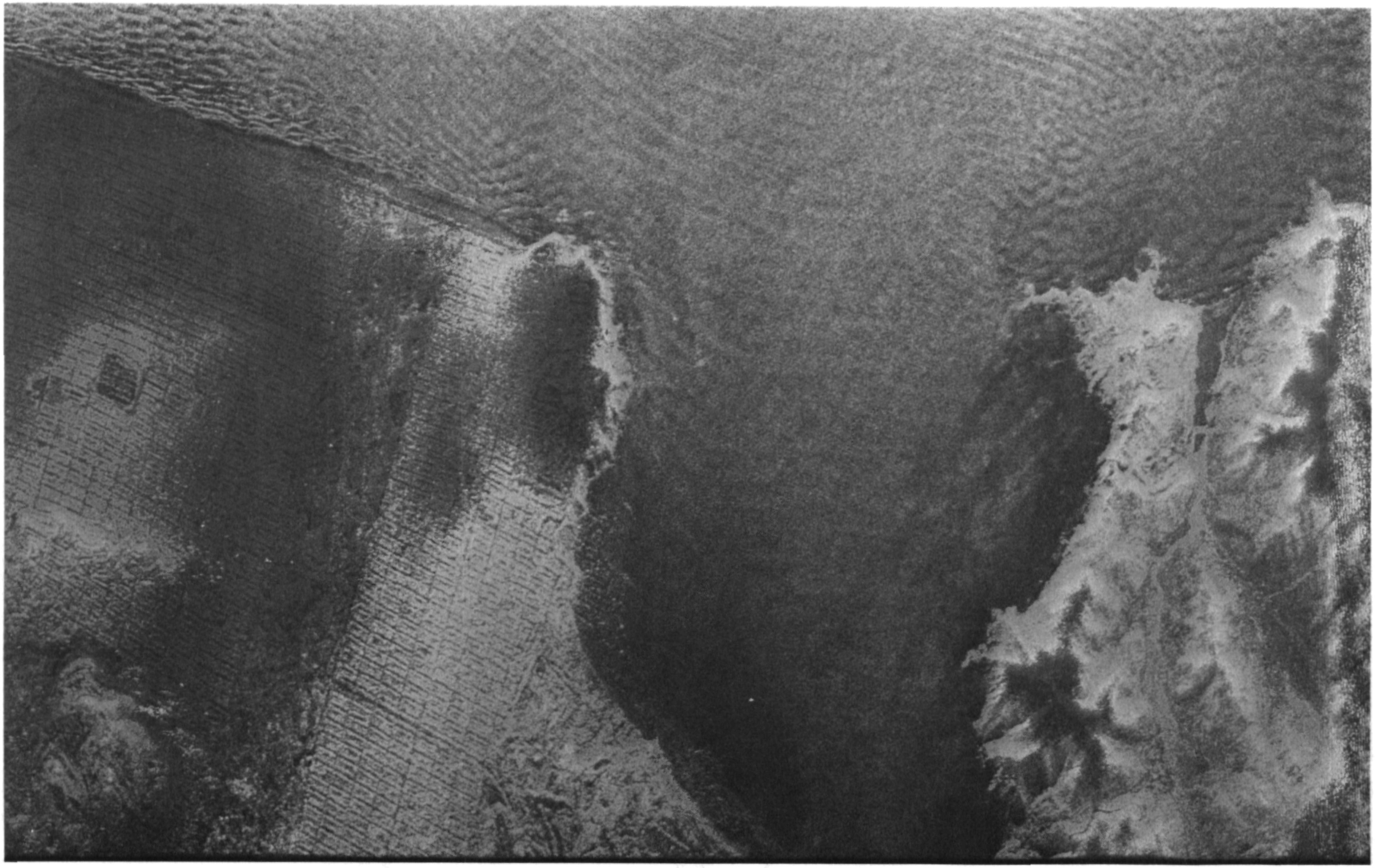

Figure 3. 16-look C-band Along-Track Interferometer image produced from Fore/Fore and Aft/Aft complex images. This data was acquired simultaneously with the L-band data shown in figure 2.

(See color slide no. 18.)

N92-28025

Polarization Signatures for Abandoned Agricultural Fields in the Manix Basin Area of the Mojave Desert

Terrill W. Ray
Division of Geological and Planetary Sciences
California Institute of Technology
Pasadena, California

Tom G. Farr and Jakob J. van Zyl
Jet Propulsion Laboratory
California Institute of Technology
Pasadena, California

Abstract. Polarimetric signatures from abandoned circular alfalfa fields in the Manix Basin area of the Mojave desert show systematic changes with length of abandonment. The obliteration of circular planting rows by surface processes could account for the disappearance of bright "spokes", which seem to be reflection patterns from remnants of the planting rows, with increasing length of abandonment. An observed shift in the location of the maximum L-band co-polarization return away from VV, as well as an increase in surface roughness, both occurring with increasing age of abandonment, seems to be attributable to the formation of wind ripples on the relatively vegetationless fields. A Late Pleistocene/Holocene sand bar deposit, which can be identified in the radar images, is probably responsible for the failure of three fields to match the age sequence patterns in roughness and peak shift.

I. Introduction:

The Manix Basin Area is located in the Mojave Desert between Yermo and Afton Canyon along I-15 (figure 1). This area consisted of a series of lakes beginning in the late Pleistocene, about 350,000 years ago. A great diversity of flora and fauna was supported by Lake Manix as is evident from the variety of fossils which have been recovered [1]. The area is dotted with fields which have been used for raising alfalfa, typically using central-pivot, pressure-driven irrigation systems which rely on groundwater. Many fields have been abandoned, including all of those north of I-15, primarily, according to residents of the area, because of the extremely high cost of electricity needed for pumping the water. Figure 2a is a sketch index map showing the locations of the fields used in this study and the locations of pertinent background areas, and table 1 gives a summary of data about these fields including the year of abandonment.

On June 28, 1990, JPL AIRSAR in standard configuration was flown over the study area. The frame containing the group of fields used in this study was processed and calibrated using trihedral corner reflector data [2] from a flight in a different area a few days later. The south edge of the image is towards the top with the aircraft flight line parallel to the south edge of the image. Incidence angles range from 25^{o} near the south edge to 60^{o} near the north edge. Figures 2b, c and d are the total power images for the C- (5.6 cm), L- (24 cm) and P-band (68 cm) respectively; slide 19 is a color composite of these images with blue, green and red representing C-, L- and P-band respectively.

II. Analysis:

A. General Overview: There are several active fields in the southern area of the image which show very strong responses in the C- and L-band. It is also observed that the active fields have very pronounced bright spokes in both the L- and P-band images. Close examination of the active field shaped like Pac-man reveals that the currently used circular area is centered in a darker square area which probably represents the original field before the circular system was installed.

The abandoned fields are darker than the desert background in the C- and L-bands. A few of the abandoned fields show bright spokes in the L- and P-bands which are considerably less impressive than those on active fields. All of the abandoned fields (except field 3) have one bright line extending from the center of the field to its edge; these lines are the radial overhead pipes of the irrigation systems, and they can be seen in some of the active fields as well. The bright rings around fields 3, 4 and 5 are the result of a combination of fences, trees and roads. There is some corruption of the P-band data at the north of the image by an off-image, horizontally polarized radar, and there are some minor bands of interference in the L-band data as well.

Slide 20 is a composite color image of L-band polarization with HH polarization as red, VV polarization as green and VH polarization as blue. A striking feature of this image is the area in the north central and northeastern part of the image which has a reddish cast indicating a strong response in the HH polarization. Fields 3, 4, 5 and 8 all lie in this region, while the other fields are located in background desert areas which exhibit the more typical VV response of rough surface scattering [3,4]. More is said about this region in part E below.

B. Spokes: The bright spokes evident on the active fields and some of the abandoned fields are caused by the circular planting furrows plowed in these fields. Bright spots are caused by the radar beam striking a face of the berm between the rows and being reflected back as single-bounce specular reflections, a phenomenon that has been observed in the past. Figure 3a, taken on the most recently abandoned field, clearly shows that wild desert plants which are growing on this field are arranged in concentric circles around the center of the field. Wind berms are formed by the clusters of plants forming a set of broken concentric circles. Field 2 shows this same phenomenon to a much lesser extent. The oldest field exhibiting a spoke is field 4 which exhibits a spoke in its northwestern corner. The reason why the spoke has been preserved in this field is the shelter belt of trees on its western perimeter. However, it is generally true that the fields which have been abandoned for the longest time tend to not have spokes, and this suggests that they are gradually obliterated with the passage of time. Field 5 exhibits a faint bright line in the L-band which could be classified as a spoke; however, this line does not appear in the P-band which is the case for all other spokes with that orientation.

C. Polarization Signatures: The polarization signatures displayed in this paper follow the conventions in [3]. The oblique-view block diagrams are arranged with a co-polarized signature on the left. Co-polarization refers to transmitting and receiving in the same polarization, e.g. HH polarization, while cross-polarization refers to orthogonal transmit and receive polarizations, e.g. HV polarization. In the top views, the ellipticity angles χ are plotted along the vertical axis from $+45°$, corresponding to right-handed circular, at the top to $-45°$ at the bottom. The orientation angle ψ is plotted horizontally from 0°, horizontal, at the left, through 90°, vertical, at the center, to 180° at the right. A horizontal line through the center of each of the top views represents linear polarizations, which will be the principal concern in what follows. The brighter the area is in the top view, the stronger the reflected signal at that polarization. The closest corner of the oblique views is the $\chi = -45°$, $\psi = 180°$ or lower left corner of the top views.

Figure 4 is a series of L-band polarization signatures taken in a vertical sequence along the eastern part of the image in background area. The background shows a fairly typical VV response as mentioned in part A, above. These four signatures show nothing unusual about this background, and the maximum of the co-polarization signatures occurs at $\chi = 0°$, $\psi = 90°$. The important result here is the fact that there is no systematic change in the polarization signatures simply due to changing incidence angle.

A series of polarization signatures from the fields under examination is shown in figure 5. They are arranged from field 1 at the top to field 8 at the bottom, which should also be an age sequence from the most recently abandoned field at the top to the field with the longest abandonment time at the bottom. The important piece of information from this sequence is the changing location of the peak of maximum co-polarized return, and table 1 lists the location of the peaks on these various fields. If fields 3, 4 and 5 are excluded from the sequence, we see a definite leftward shift in the maximum peak to $\psi = 55^{\circ}$ (table 1).

Even in this most recently abandoned field, field 1, the peak is shifted slightly away from $\chi = 0^{\circ}$, $\psi = 90^{\circ}$, so the first question to address is the cause of the initial slight shift to the left. From [4] we know that a dielectric cylinder located at an angle away from vertical will give a response with the maximum peak shifted away from vertical. In most natural settings the dielectric cylinders (plant stems) are more or less randomly oriented causing the left or right shifts of the peaks from the individual cylinders to add destructively and the vertical responses to sum constructively resulting in the typical VV response. Figure 3b is a photograph taken facing to the north on field 1. There is a clearly perceptible tendency for the taller stems to lean downwind to the east; this is probably responsible for the slight leftward shift observed in the polarization signatures from this field.

The more dramatic shifts to the left in the older fields seem to be caused by a more extreme wind related feature. Figure 6 is comprised of two photographs taken on field 8. The small dark bar in each picture is a metal ruler of 6.5 inches total length. As can clearly be seen in figure 6a, there is an extensive pattern of wind ripples on this field oriented approximately 170° from north with an amplitude of 1 to 2 inches. Figure 6b is a high angle picture of these ripples showing that they have a wavelength of approximately 12 inches and are composed of very coarse sand. A virtually identical situation occurs on field 5, and wind ripple patterns of a considerably less well-defined nature exist on fields 6 and 7. Figure 7 is a polarization signature generated using a model developed by van Zyl *et al.* [3], which simulates the important features of the observations quite well (including an excess of left-handed polarization which is shown in table 2). The modelled surface had a sinusoidal undulation oriented in the same manner as the wind ripples.

D. Diffuse Scattering: Diffuse scattering may be estimated in several ways from the polarization signatures. The most commonly used way is the pedestal height [3, 5] which is determined by taking the ratio of the minimum of the co-polarized signature to the maximum of the signature. In effect, this represents the degree to which the pixels in the area analyzed to produce the polarization signature vary from each other. Table 2 lists pedestal heights in both the C- and L-bands for the eight fields and a background area. A qualitative feel for the pedestal heights is to look on the co-polarized signature for the minimum response level; the rest of the signature sits on top of this minimum value much as a statue sits on top of its pedestal. In principle, a taller pedestal indicates a rougher surface. It is clear from Table 2, however, that there is no systematic increase or decrease even if fields 3, 4 and 5 are eliminated.

If a right-hand circularly polarized wave is reflected from a normal, smooth dielectric surface, the observed return will be received as a left-hand circularly polarized wave. The ratio of transmit right(left)-hand circular receive left(right)-hand circular, which we refer to as right(left)-hand expected, to transmit right(left)-hand circular receive right(left)-hand circular, which we refer to as right(left)-hand diffuse, effectively compares the directly reflected power to the diffusely scattered power. The primary difference between this and the pedestal height technique is that the pedestal height technique uses all polarizations in its determination and this ratio technique uses only one polarization at a time.

These ratios are also noted in table 2. Here, the exclusion of fields 3, 4 and 5 makes immediately apparent a trend of decreasing ratios of expected to diffuse scattering. This indicates that the fields are getting rougher with time. Field investigation indicates that this roughening is not due to increased vegetation on the fields; in fact, the oldest fields generally have the sparsest vegetation. It may be reasonable to conclude that a great deal of this roughening is due to the formation of the wind ripples and the deflation of the field's surface. It is worth pointing out that the bright southwestern "corner" of field 8, which was avoided in constructing the polarization signatures, is much rougher than any of the fields or even the general background according to the ratio test (table 2).

It is noted that with respect to the left-hand expected to left-hand diffuse ratio from the C-band data this trend is not very good. Field 2 seems very slightly smoother than field 1, and field 7 seems slightly smoother than field 6. However, for all of the other C- and L-band ratios this trend of roughening with age is quite clear. The very weak P-band response of the fields coupled with the fairly substantial interference of the off-image radar makes such ratio techniques very difficult to employ in the P-band.

E. HH Background: As was pointed out above, there is a background region which exhibits a rather strong return in the HH polarization. Fields 3, 4 and 5 which have been ignored in the sequences above are located in this area, as well as field 8. Figure 8 shows a sequence of three polarization signatures taken from west (at top) to east (at bottom) between fields 5 and 8. A shift in the location of the maximum response peak is noted in these signatures, but the interesting aspect of these shifts is that they are to the right. The first two have their maxima at $\psi = 115^o$ and the third has its maximum at $\psi = 105^o$, so while the general background of fields

3, 4, 5 and 8 show a peak shift, it is in the opposite direction of the shift observed in the fields. Figure 9a is a photograph taken of the area exhibiting the first polarization signature in figure 8, and figure 9b is of the area containing the bottom signature in figure 8. Clearly, these two areas look different on the ground, and figure 9b actually resembles a slightly less well vegetated version of the more normal (VV) background desert surface.

The existence of the unusually strong HH returns lends some justification to the rejection of fields 3, 4 and 5, and it also suggests that field 8 should not be included in the analysis either. However, if field 8 is eliminated from the sequences above, the remaining four fields still exhibit all of the systematic changes outlined above. Further, the fact that the desert closest to field 8 more closely resembles the normal background suggests that it is less dramatically affected by its background than fields 3, 4 and 5.

The next consideration is the cause of the HH region. The area photographed in figure 9a, showing the extensive dunes, appears slightly redder in the three-polarization image (see slide 20) than the area closest to field 8. The increasingly red areas further to the north are also areas of shifting sand and dunes. There is evidence that this area is a Late Pleistocene/Holocene sand bar deposit [6], which could account for the extensive amount of easily mobilizable sand. The dunes, in turn, probably account for the enhanced HH return as well as the rightward shift to ψ values of 105^o and 115^o in the background polarization signatures, but more work must be done on this subject. This could account for the occurrence of wind ripples on a young field (field 5), and the shelter belts of trees around fields 3 and 4 may have protected them from a similar fate.

III. Conclusions:

1. It is clear that systematic changes occur on the time scale of a few years to these abandoned fields which can be detected by the use of JPL AIRSAR.

2. "Scratching" by man produces easily observable responses at the radar wavelengths used by this system.

3. Man's scratches are obliterated in a few years and replaced by a new set of surface patterns produced by surficial processes (in this case, wind) which are also detectable with this system by the use of polarimetry.

4. Semi-periodic eolian features (wind ripples and dunes) can be "seen" with the polarimetric data even if the features are not resolvable in the image.

5. Roughening of surfaces in arid settings may have no connection to vegetation.

6. These methods should be applicable to other areas where farming has been or is being done in marginal semi-arid to arid areas. This could lead to effective monitoring of such areas on a global scale by the use of an orbiting quad-pol SAR system with occasional field work.

IV. References:

[1] G. T. Jefferson, "Brief history of Pleistocene Lake Manix," *Manix Lake and the Manix Fault,* Quarterly San Bernardino Co. Museum Assoc., vol. 29, pp. 7-14, 1982.

[2] J. J. van Zyl, "Calibration of polarimetric radar images using only image parameters and trihedral corner reflector responses," *IEEE Trans. on Geosci. Remote Sensing,* vol. 28, pp. 337-348, 1990.

[3] J. J. van Zyl, H. A. Zebker and C. Elachi, "Imaging radar polarization signatures: Theory and observation," *Radio Science,* vol. 22, pp. 529-543, 1987.

[4] J. J. van Zyl and F. T. Ulaby, "Scattering matrix representation for simple targets," *Radar Polarimetry for Geoscience Applications,* Artech House, Norwood, MA, F. T. Ulaby and C. Elachi, eds., pp. 17-52, 1990.

[5] D. L. Evans *et al.,*"Radar polarimetry: Analysis tools and applications," *IEEE Trans. on Geosci. Remote Sensing,* vol. 26, pp. 774-789, 1988.

[6] B. Murray, personal communication, 1991.

V. Acknowledgements:

We would like to thank Elizabeth Duxbury for extensive work in compiling data regarding the cultural history of the area. Dr. Bruce Murray and Stefanie Brachfeld provided useful insights in several discussions that we had with each of them. Thanks also to Dr. Dan McCleese for providing initial impetus for this project.

Field Number	Last Year Irrigated	Vegetation Cover	Spokes?	Wind Ripples?	ψ at L-band Maximum co-pol
1	1987	40%	yes	none	85°
2	1986	25%	yes	none	80°
3	1984	70%	no	none	75°
4	1984	30%	yes	none	70°
5	1984	5%	?	yes	60°
6	1982	25%	no	weak	80°
7	1980	10%	no	yes	70°
8	1973	5%	no	yes	55°

Table 1: Pertinent data about fields used in this study. For the location of the numbered fields see figure 2a.

Field Number	Pedestal Height		Circular expected/ Circular diffuse				Left-hand/ Right-hand
			Left-hand		Right-hand		
	C	L	C	L	C	L	L-band
1	.1882	.0902	1.0000	1.0000	1.0000	1.0000	1.0000
2	.1530	.1294	1.0046	.9145	.8725	.9440	1.0088
3	.2275	.1372	.8163	.7095	.7139	.7980	1.1043
4	.3451	.2275	.7668	.6219	.6693	.6553	1.0409
5	.2740	.1333	.8104	.6399	.6716	.7783	1.2197
6	.1490	.0980	.9153	.8131	.8228	.8573	1.0449
7	.1255	.1059	.9205	.7770	.8132	.8342	1.0569
8	.2706	.1568	.7870	.5895	.6676	.6943	1.1644
BG			.7088	.5937	.6304	.5659	.9623

Table 2: Data from the eight fields and a normal background area (BG). The letters immediately above each column represent the wavelength band data used in the column. Circular polarization ratios have been normalized to field 1 being equal to 1.0000. Increasing pedestal heights and decreasing circular expected to circular diffuse ratios should indicate increasing surface roughness at scales of the radar wavelength.

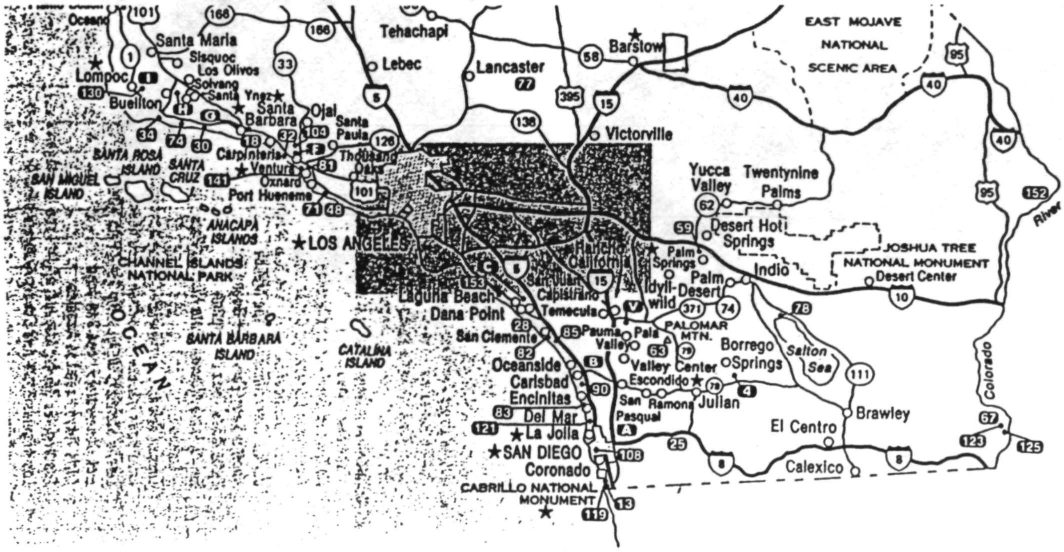

Figure 1: Location map showing general location of the study area.

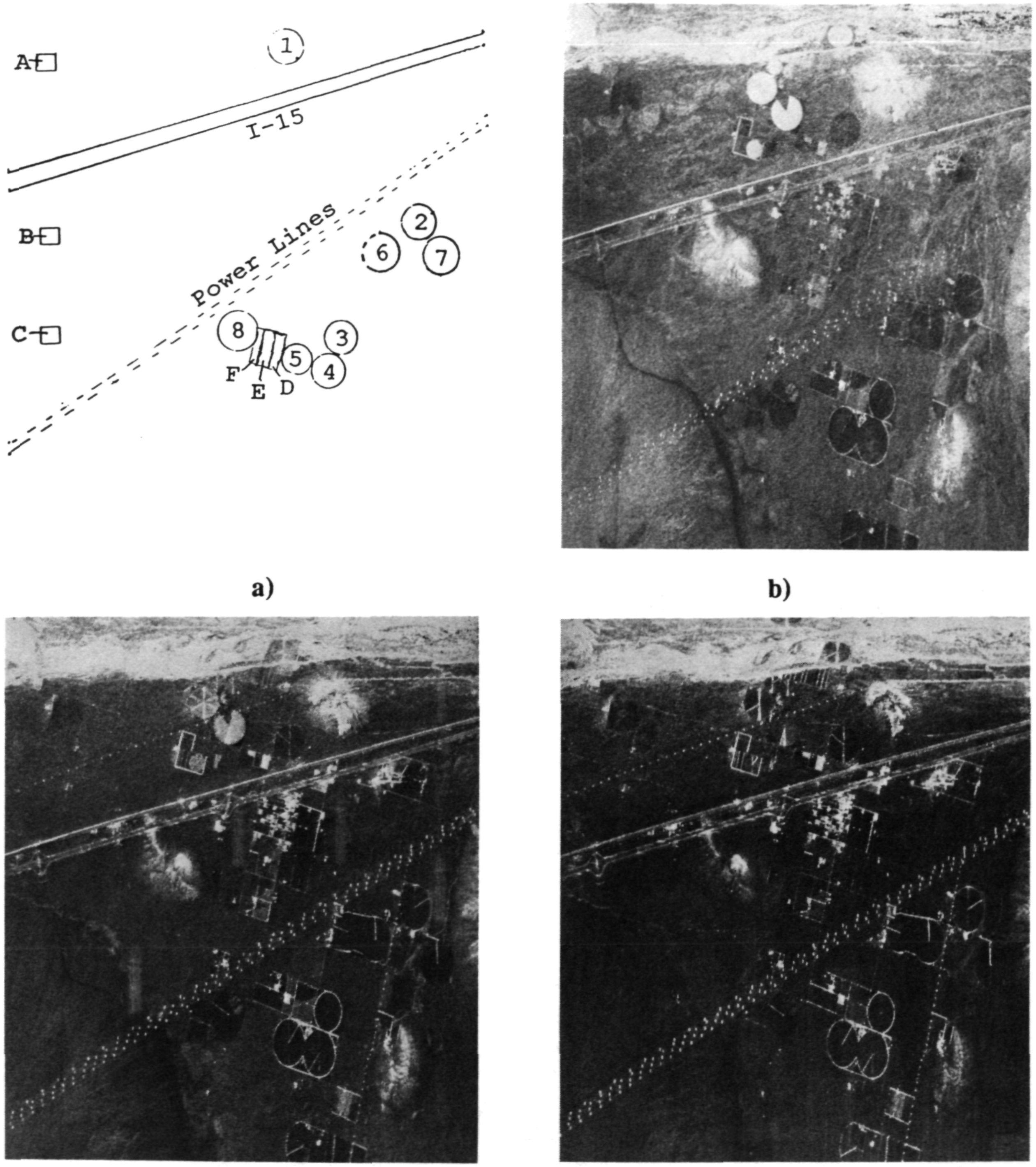

a)

b)

c)

d)

Figure 2: **a)** Index sketch map showing locations and numbers assigned to each field and locations and letters assigned to six background areas; **b)** C-band total power image; south is to the top of the images, and the top edge parallels the flight line; **c)** L-band total power image; note spokes in fields 1, 2 and 4; **d)** P-band total power image. For color composite of these images with C-band as blue, L-band as green and P-band as red, see slide no. 19.

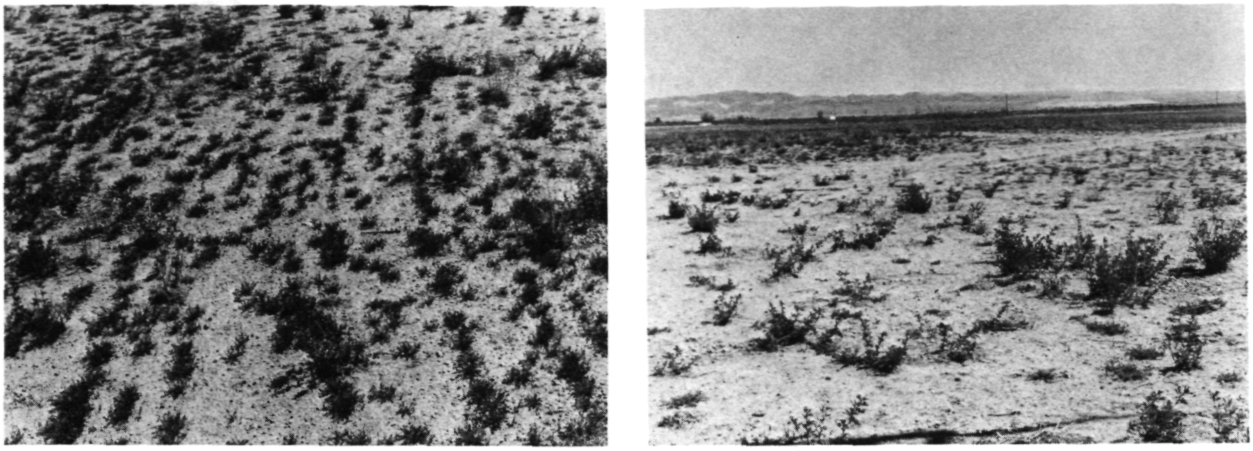

a) **b)**

Figure 3: **a)** Photograph of field 1 showing circular rows of desert plants; **b)** photograph of field 1 facing north; note eastward tilt of plants.

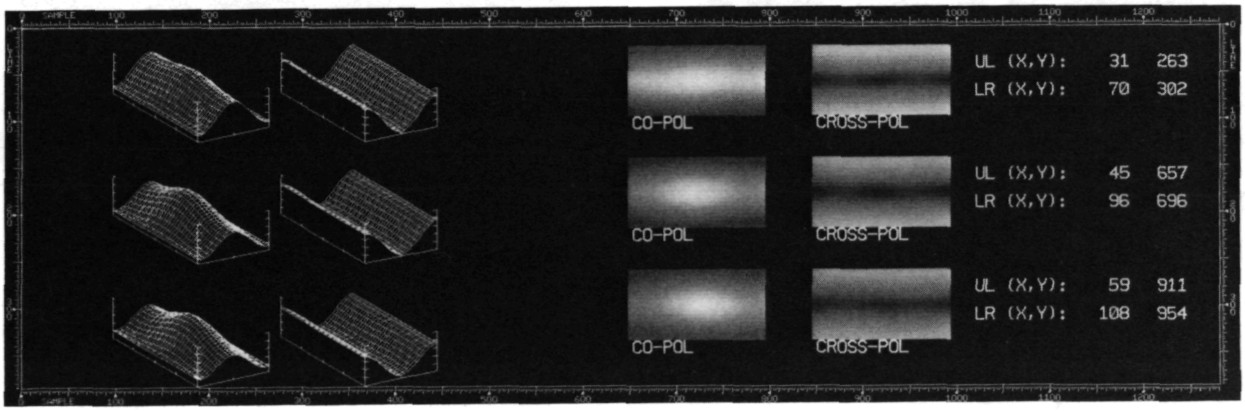

UL (X,Y): 31 263
LR (X,Y): 70 302

UL (X,Y): 45 657
LR (X,Y): 96 696

UL (X,Y): 59 911
LR (X,Y): 108 954

Figure 4: L-band polarization signatures of background at different incidence angles from 40° (background area A) at the top to 55° (background area C) at the bottom. Note central peak of all co-polarization signatures. (See text for explanation of polarization signature layout.)

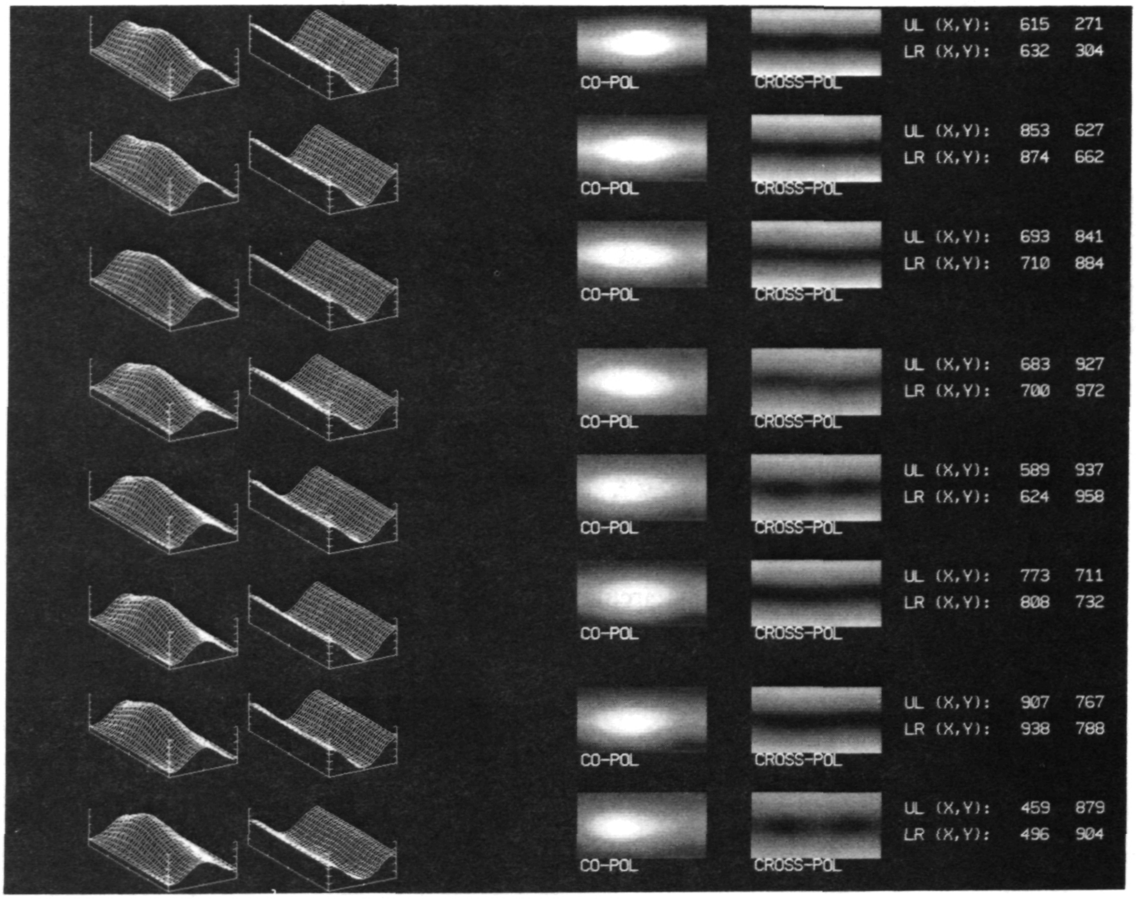

Figure 5: L-band polarization signatures of fields arranged from field 1 at top to field 8 at bottom. Note leftward peak shift in co-polarized signature.

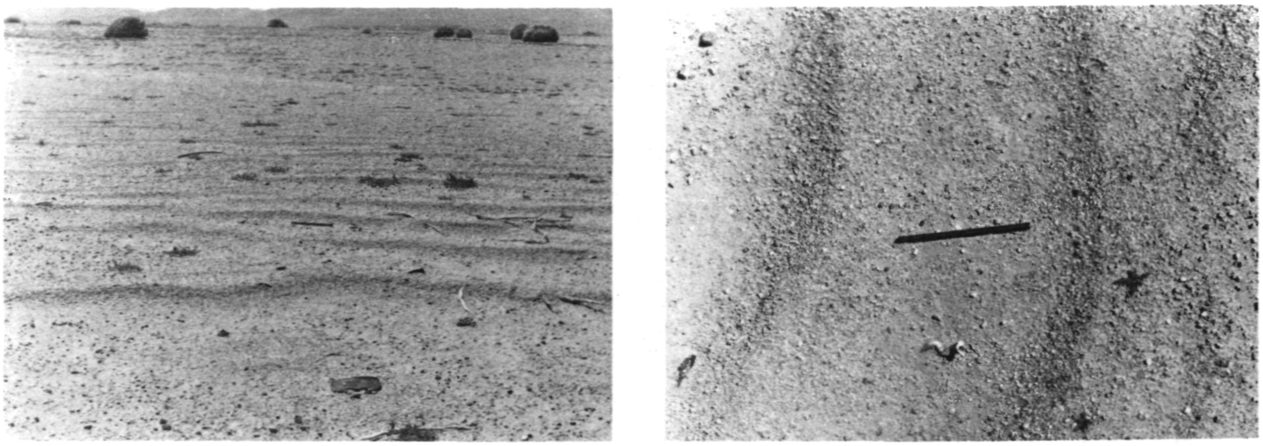

a)

b)

Figure 6: a) Photograph of wind ripples on field 8. Small bar is 6.5 inches long. **b)** High-angle photograph of wind ripples. Note coarse size of constituent grains and distance between peaks.

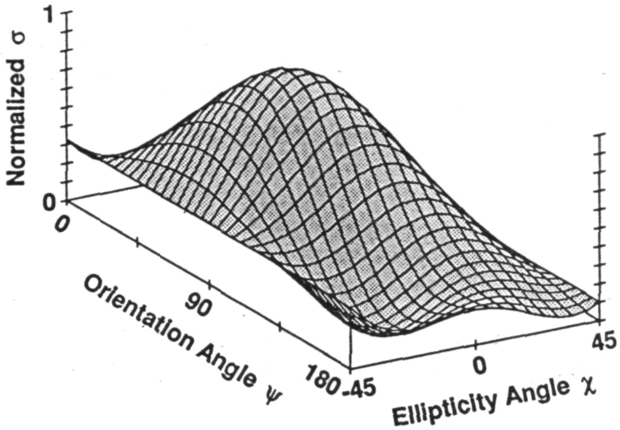

Figure 7: Co-polarized signal from model surface with near-sinusoidal topography oriented in the same manner with respect to the flight line as the wind ripples on fields 5 and 8. Note leftward peak shift and excess left-hand circular polarization. (dielectric constant 3, incidence angle 30^{o})

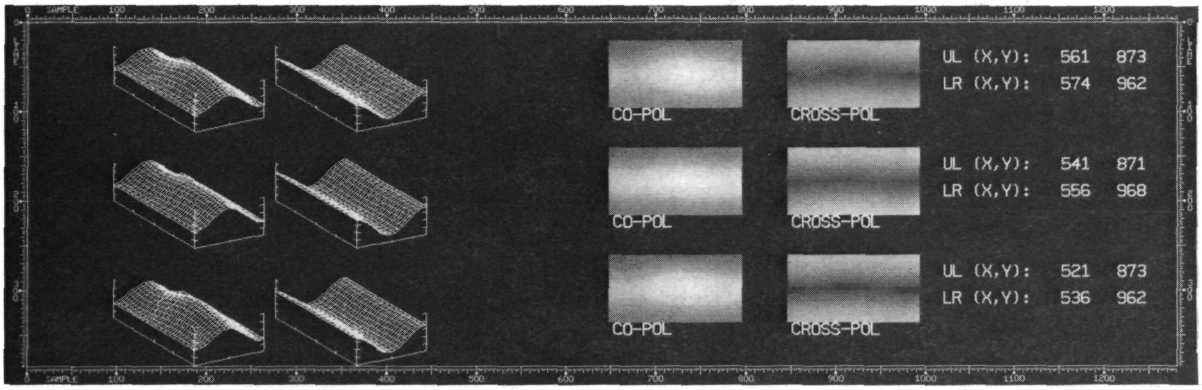

Figure 8: L-band polarization signatures of background areas D, E and F. Note rightward peak shift.

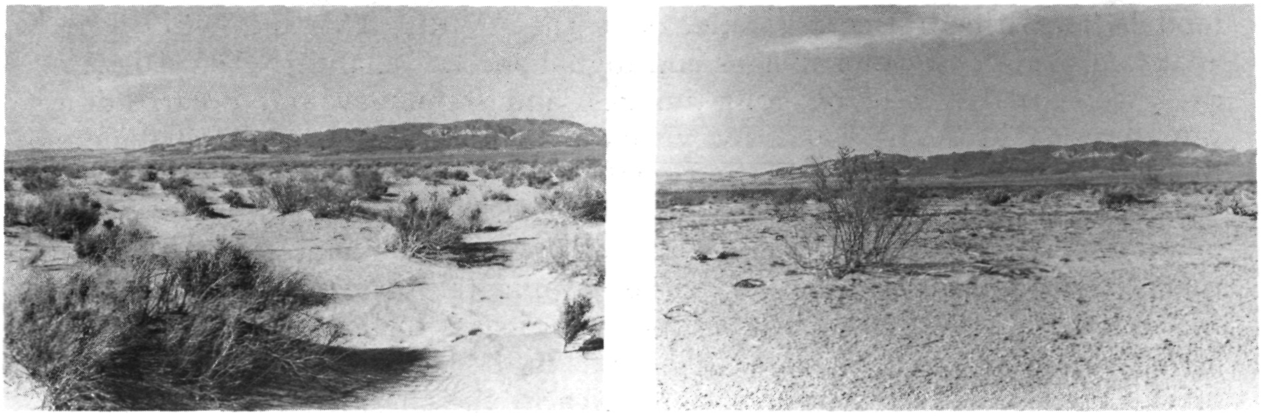

a) b)

Figure 9: **a)** Photograph of background area D. **b)** Photograph of background area F.

N92-28026

GEOLOGIC MAPPING IN DEATH VALLEY, CALIFORNIA/NEVADA USING NASA/JPL AIRBORNE SYSTEMS (AVIRIS, TIMS, AND AIRSAR)

Fred A. Kruse[1,2], John B. Dietz[1,], and Kathryn S. Kierein Young[1,2]

[1]Center for the Study of Earth from Space (CSES), CIRES
[2]Department of Geological Sciences
University of Colorado, Boulder, CO 80309

EXTENDED ABSTRACT

A multi-sensor aircraft campaign called the "Geologic Remote Sensing Field Experiment" (GRSFE) conducted during 1989 resulted in acquisition of high quality multispectral images in the visible, near infrared, shortwave infrared, thermal infrared, and microwave regions of the electromagnetic spectrum. The airborne data sets include the Airborne Visible/Infrared Imaging Spectrometer (AVIRIS) (0.4 - 2.5 µm, 224 bands), the Thermal Infrared Multispectral Scanner (TIMS) (8-12 µm, 6 bands) and the airborne Synthetic Aperture Radar (AIRSAR) (P, L, and C band, quad polarization, multiple incidence angles). Ancillary data include Landsat Thematic Mapper (TM, 7 bands), laboratory and field spectral measurements, and traditional geologic mapping.

The GRSFE data for a site in the northern Death Valley, (California and Nevada) region, USA were calibrated to physical units and geometrically registered to a map base. AVIRIS data were calibrated to reflectance using ground targets and the "empirical line" method. TIMS data were calibrated to radiance using the onboard blackbody measurements and converted to emissivity using the modelled emittance method (assuming an emissivity of 0.93 in band 6). AIRSAR phase, cross-talk, co-channel imbalance, and absolute radiometry were calibrated using data characteristics, theoretical models, and trihedral corner reflectors. The AVIRIS, TM, and TIMS were analyzed using both color images and digital spectral analysis. The AIRSAR data were analyzed using color images, and frequency and polarization signatures. The AVIRIS and TM visible and infrared multispectral remote sensing observations provided information about the surficial composition (mineralogy) of the rocks and soils. AVIRIS allowed identification and mapping of the minerals calcite, dolomite, sericite, hematite, and goethite based on their spectral signatures. Selected mineral mixtures were identified and mapped by utilizing discrete absorption bands in the visible portion of the spectrum for the iron oxides and bands in the shortwave infrared for the other minerals. TIMS spectral signatures in the thermal infrared region between 8 and 12 µm and emissivity ratio images provided compositional (lithological) information not contained in AVIRIS data (primarily silica

content information). Variation of the AIRSAR radar backscatter as a function of wavelength allowed mapping of varied surface morphology (relative surface roughness).

A variety of rock types, regional and localized lithological variation, and the effects of processes such as weathering, erosion, soil development, and faulting were detected and mapped using the optical remote sensing data. The Radar data were used to characterize both local and regional faulting and other geologic structures, particularly in unconsolidated alluvium. The integrated optical and microwave data sets provided complementary information that allowed identification and mapping of new structures, control of both lithology and alteration by structure, and associations of surface morphology and composition. This case study establishes that the use of combined optical and microwave image data for deriving physically based, quantitative measurements of the Earth's surface results in improved geologic mapping. The results to date are an improved understanding of the nature and distribution of structures, lithology, weathering, and alteration in the northern Death Valley Region. The research is presently being expanded to cover much of Death Valley from Artist's Drive northward. New geologic information derived from the quantitative remote sensing studies will be used to develop models that explain the interaction of complex depositional and erosional processes controlling the configuration of the modern land surface in this region.**

** This is a summary of results published during 1991 at two symposia. The complete references are listed below.

Kruse, F. A., and Dietz, J. B., 1991, Integration of optical and microwave images for geologic mapping and resource exploration: in Proceedings, International Symposium on Remote Sensing of Environment, Thematic Conference on Remote Sensing for Exploration Geology, 8th, 29 April - 2 May 1991, Denver, Colorado, Environmental Research Institute of Michigan, Ann Arbor, p. 535-548.

Kruse, F. A., and Dietz, J. B., 1991, Integration of diverse remote sensing data sets for geologic mapping and resource exploration: SPIE Symposium on Remote Sensing for Geology and Geophysics, 1-5 April 1991, Orlando, Florida, (in press).

N92-28027

Airborne SAR Determination of Relative Ages of Walker Valley Moraines, Eastern Sierra Nevada

A. Fox, B. Isacks, A. Bloom, E. Fielding, D. McMurry
Department of Geological Sciences, Snee Hall, Cornell University, Ithaca, New York 14853-1504

A regional study of the distribution and elevations of Pleistocene moraines in the Andes requires a method of determining relative age from space. One of our primary objectives is to establish the relative chronology of major climatic events responsible for glaciation in the Andes and other regions that are difficult to access on the ground and where suitable material for absolute age determination is lacking. The sensitivity of radar to surface roughness makes it possible to develop a remotely-based relative dating technique for landforms for which surface age and roughness can be correlated. We are developing such a technique with airborne SAR imagery of the eastern Sierra Nevada where independent evidence is available for the ages and physical characteristics of moraines. The Sierra Nevada moraines are similar in form and environmental setting to Andean moraines that we have targeted for study during the pending SIR-C mission.

SAR imagery is used to differentiate the ages of five moraine sequences of Walker Valley in the eastern Sierra Nevada. These sequences were previously determined to be significantly different in age on the basis of relative geomorphic position, degree of surface weathering, and cosmogenic chlorine-36 dating. A predictable decrease in moraine surface roughness occurs with increasing age because natural mechanical and chemical weathering processes reduce mean boulder size, frequency and local surface relief through time.

Relative height measurements were collected at 15 cm intervals along topographic profiles 15 m long on the crests of the moraines comprising the five glacial sequences. A one-dimensional Fourier power spectrum was calculated for each topographic profile in order to estimate relative surface roughnesses at P, L, and C radar wavelengths. Surface roughness measurements correlate best in relative magnitude with the radar backscatter recorded as image pixel DN values for HH polarization at the P-band wavelength of 68 cm. The shorter wavelength radar band images (L and C) highlight the sagebrush covering the moraines and their radar backscatter measurements do not correlate well with the roughness measured on the moraine surface beneath the vegetation. Pixel-to-pixel differences in radar backscatter measured along the same moraine crest result from speckle and from variations in surface roughness and mean surface slope. With the limited control on local slope differences measured in the field and from a 30 m resolution digital elevation model, P-band SAR imagery can differentiate Tioga and Tenaya moraines from the Younger Tahoe, Older Tahoe, and Mono Basin moraine sequences.

N92-28028

MAESTRO1 data set calibration: the JRC approach

C. Lavalle, G. De Grandi, H. De Groof, A.J. Sieber

Institute for Remote Sensing Applications
Commission of the European Communities
J.R.C. Ispra

ABSTRACT

Calibration is a fundamental task for analysis. Therefore the Microwave Team of the JRC Ispra has put considerable effort investigating and checking the different calibration techniques, using the data collected during the MAESTRO1 campaign. In this paper we report on this activity. The paper is structured as follows: at first we give an overview of the algorithms used for phase and radiometric calibration; then we describe the software tools that have been developed to support the calibration data processing; finally we present and discuss the results obtained from the calibration in the test sites of Freiburg and Flevoland.

1. INTRODUCTION

The Institute for Remote Sensing Applications (IRSA) of the Commission of the European Communities Joint Research Center is responsible for Pilots Projects concerning forestry and agricultural investigations (namely the IFI and TREES projects). Therefore several airborne campaigns (i.e. Maestro 1 in 1989, MAC-EUROPE in 1991, EARSEC program in 1991) have been organized over European test sites to prepare the operational procedure to be adopted in those projects.

Since extended target discrimination and recognition is the objective of this investigation, it is clear that one fundamental task to fulfill is the achievement of a good calibrated data set. In particular, efforts are directed to the study of the possibility to cross-calibrate images coming from different sensors, either airborne or satellite-borne. In this context, the Microwave Team of the JRC Ispra has put considerable effort into investigating and checking the different calibration techniques by using the data collected during the MAESTRO1 campaign.

In this paper we report on this activity. The paper is structured as follows: at first we give an overview of the algorithms used for phase and radiometric calibration; then we describe the software tools that have been developed to support the calibration data processing; finally we present and discuss the results obtained from the calibration in the test sites of Freiburg and Flevoland.

2. CALIBRATION ALGORITHMS

2.1 Phase Calibration.

Phase calibration is the most important step to achieve polarimetrically meaningful data. The implemented procedure follows the method described by Zebker et al. (1990).

The algorithm estimates the true scattering matrix for a resolution element from the measured scattering matrix, where the phase factors are affected by path differences in the radar system and processor.

Two equations are required to solve for ϕ_t and ϕ_r, where ϕ_t is the phase difference between the transmit H and V channels, and ϕ_r is the phase difference between the receive H and V channels. An homogeneous extended target for which the HH-VV phase difference is expected to be zero is used for the estimate of $\phi_t+\phi_r$. Since system noise in each channel is uncorrelated, we expect the mean HV-VH phase to depend only on the path length. Therefore the mean HV-VH phase difference over the whole image is used to estimate $\phi_t - \phi_r$.

2.2. Cross Talk.

Cross talk removal has been implemented according to the algorithm described in Van Zyl (1990) and Freeman(1990) .

Imperfections in the radar antennas result in impure polarization states for the individual polarization combinations, measured directly by the hardware. This source of error is described by the following system model: $\bar{Y} = Ae^{i\phi} \bar{S}_R \bar{S} \bar{S}_T$, where $\bar{Y}$ is the measured scattering matrix; $\bar{S}$ is the desired scattering matrix; $\bar{S}_R$ represents the receiving system; $\bar{S}_T$ represents the transmitting system; A is an absolute amplification factor and ϕ is an absolute phase factor. The cross-talk removal algorithm is based on two assumptions: reciprocity $\bar{S}_R = \bar{\tilde{S}}_T$; no correlation due to the imaged targets between like and cross-polarized returns (i.e. HH and HV). Therefore correlation is due to the radar and can be removed from the data.

Using an iterative method, an estimate of $\delta 1$ and $\frac{\delta 2}{f}$ (the crosstalk parameters) can be made (where $\delta 1 = S_{T12}$, $\delta 2 = S_{T21}$ and $f = S_{T22}$). Inversion of the system model equation gives the estimate of the true scattering matrix.

2.3. Co-channel imbalance.

Imbalance between the HH and VV channel can be filtered out by evaluating the main diagonal term in the transmitter matrix. The known phase and amplitude relations among the elements of the scattering matrix for a trihedral corner reflector are compared to the correspondent measured values and the difference is used to correct the image.

2.4. Radiometric calibration

Our objective in the radiometric calibration of power data is to obtain an estimate of the normalized scattering coefficient σ^0 on a pixel basis for the imaged scene. The methodology involves computing the calibration factor by evaluating the returned power from a set of known targets.

Each pixel of the original image is then scaled by :

$$F = \sigma_{meas} \; A \; / \; \sigma_{th}$$

where

A = slant range pixel length x azimuth pixel length
σ_{meas} = measured target cross section
σ_{th} = theoretical target cross section.

σ_{meas} is calculated by using the integral power contained in a 16 x 16 pixels window centered around the point target and then subtracting the background power computed in a low scattering surrounding area.

At this point two assumptions are made :

1. the image is corrected for the antenna range-gain (actually a theoretical antenna pattern is used to scale the image; to take into account the real variation of the pattern in range, that corresponds to the situation when the antenna is mounted on the platform, one should filter out the theoretical correction and then compute from the data the true G(θ) pattern, where θ is the incidence angle).
2. system gain, multiplicative noise, transmitted power and platform motion parameters are constant during the operational time of the sensor.

2.5. Impulse Response Function analysis.

As described in de Grandi et al.(1991), point target analysis can be performed on a 16 x 16 pixel window centered around the reflector. Successive interpolation using the sin(x)/x method allows the calculation of the following quantities :

- peak power
- peak position (useful to estimate the spatial offset among different channels)
- 3-dB peak width in slant range and azimuth
- peak to sidelobe ratios in both the directions
- integrated peak to sidelobe energy ratio
- range and azimuth profiles.

It is to be noted that examining the profile, one is able to discriminate eventual ambiguities (i.e. double peaks or peaks broadening) due to wrong sampling rate used for the range and/or azimuth compression.

Results of this analysis for our sites are given in de Grandi et al.(1991). An example of the analysis is reported in Fig. 1.

3. SOFTWARE TOOLS

In this section we describe the software tools developed by the JRC MWT in the SUN OS environment, to support the calibration data processing.

The tools are an end product which is visible to the user; this product is built using a number of components. Indeed the calibration software can be architecturally divided into three layers: procedures that implement the calibration algorithms; drivers, that activate the procedures in ways that are suitable for a specific application; the user's interface. The components of the procedure layer can be associated with different drivers and user interfaces, to tailor the tool to a particular sensor (for instance AIRSAR or ERS1) or to build different operational environments (batch or interactive processing).

We will focus here on two tools: CALTOOL an interactive tool for the JPL polarimetric SAR data calibration; LAUNCHER a general purpose front end for batch processing.

3.1. CALTOOL

CALTOOL is an interactive tool for the calibration of the JPL Stokes matrix polarimetric products. It is written in the SUNVIEW windowing environment. CALTOOL has been conceived as an analysis tool, to investigate issues related to the calibration algorithms, and as a front end to the calibration batch processing. Usually the calibration algorithms can be broken down into a parameter extraction phase and the actual calibration of the data set; this latter phase is generally quite computing intensive, and is better suited for batch processing. Therefore the role of CALTOOL is to allow the user to examine the original data set, analyze some parameters (for instance the impulse response function), and prepare in a file the correction factors for further processing. Of course the entire calibration chain can also be performed within the tool, and this is usually done to experiment with a limited number of data sets.

In the following we will describe the functions and the user interface of CALTOOL.

The functions for calibration processing are:

- phase calibration
- cross talk removal
- cochannel imbalance
- impulse response function analysis
- radiometric calibration
- gain calculation

The algorithms relative to these functions have been described in section 2.

Moreover a number of functions are implemented, which are intended as a support to the calibration activity. These functions are:

- image synthesis and display
- image processing

- polarimetric signature calculation
- result organizer

The image synthesis and display (with the ancillary image processor) is useful to select point targets, or to select areas in the image where a set of parameters should be evaluated, to assess for instance the parameter dependence from particular features.

The signature calculation is intended as a diagnostic tool, to check the influence of the calibration on the polarimetric behavior.

The result organizer allows the user to save and restore synthesized images, and to have an iconic vision of the saved objects.

The user interface is s based on the SunView models, namely graphic objects like buttons, sliders, icons that are acted upon interactively with a pointing device (mouse). The model for data presentation is inherited by other tools developed by the JRC MWT, namely POLTOOL and SMTOOL (de Grandi, (1990)); the common design allows us to reuse proficiently software and to offer to the user a consistent interface over the span of the tools; the model consists of a set of overlapping widows, where objects are drawn (see Fig. 2). A main canvas is always present, where the full image is shown. On the main canvas areas of interest can be defined in several modes: a square box, scalable in fixed steps; a rectangle that can be rubber banded to any dimension; a polygon. Each area is mapped into an object, which is visually characterized by a color. The computational kernel can then be applied to the object, and suitable presentations of the results spawned in different subwindows.

3.2. LAUNCHERS

The calibration of a full polarimetric data set (3 frequencies) is a computationally intensive procedure; this type of processing is much more amenable to batch processing, rather than to an interactive tool. The LAUNCHER is a general purpose environment designed to cope with this kind of problem. It is based on a client server paradigm, and on a simple service description language interpreter.

The client server paradigm means that the atomic level processing (operator applied to a single area and a single data set) is carried out by server processes; the user controls the processing by a client process, that accepts a textual description of the multidimensional processing, serializes the requests, and dispatches commands to the servers. This approach offers advantages with respect to the shell interpreter solution, because the entire network resource allowance can be exploited, controlling the distribution of server processes.

The interpreter is composed of a lexical analyzer, a parser and an interface to the server that uses RPC calls. The lexical analyzer is implemented using LEX; LEX is a program generator based on regular expressions; a set of regular expressions specifying the lexical rules and the corresponding actions is converted into a C program. The parser is implemented using YACC; YACC generates a program that scans an input language, and according to some specifications of the grammar, invokes actions (procedures). YACC relies in turn on the program generated by LEX for the lexical analysis. Very simple grammar rules have been defined for the launcher description language. These rules can be easily modified, changing the YACC specification file; new procedures must be eventually written if new actions are introduced, but then the program generation is completely automatic; this paves the way to an easy upgrade of the launcher environment for future needs.

The user visibility of the tool consists of the following: a description of the parameters of interest is entered in a text file, together with a description of the data sets to be calibrated and the corresponding result files. The LAUNCHER is then activated in the background, and will proceed unattended to scan the list of services to implement and to activate the suitable procedures with the proper parameters.

4. SELECTED RESULTS

Some results of the analysis performed on the Freiburg and Flevoland test sites are presented in this section.

4.1. Cross-talk

In Fig. 3, 4 cross talk parameters δ_1 and δ_2 are shown for the Freiburg site (L-band) on two different areas: in Fig. 3 the parameters are computed for an urban area containing typical man-made high reflecting artifacts, like metal roofs, cars etc.; Fig. 4 shows the parameters for a forested area, at the same incidence angle range.

The overall behavior of the parameters is similar in the two areas but the values from the urban area show an offset of at least 5dB bigger than the other, likely due to the nature of the scene. After cross talk removal the graphs (Fig. 5, 6) appear shifted downward, although the trend is the same.

No relevant changes can be observed in the phases of the parameters. This feature is found also at C and P bands.

The following considerations can be made:

1. We have observed a dependence of the cross talk parameters on the target, therefore care must be taken in the estimation of these parameters. For example, in our implementation we take the mean value of the parameters over the whole azimuth line.
2. The amplitude of the parameters is below -30dB (except for high reflecting sites) also before removal is performed. If a $\pm\ 1dB$ radiometrical accuracy is required, this value can be considered acceptable and then cross-talk removal could be avoided (at least on a uniform area such as a forest and agricultural fields). Anyway one can check the crosstalk parameters on part of the image and then decide whether to apply the cross talk correction to the whole image or not.
3. Parameters computed on the same scene, but from different flight lines, present the same behavior in amplitude but quite a different behavior in phase, reflecting the influence of the different path of the received signals therefore parameters computed on one image cannot be used to filter out cross talk of another image.

4.2. Channel imbalance.

The results obtained correcting the images for the co-channel imbalance are strictly dependent on the frequency used. For C-band data the offset in amplitude between the HH and VV channel, as measured from trihedral corner reflectors, shows an average improvement of 3%. The offsets in phase are practically not changed by the algorithm. The values (both amplitude and phase) are anyway well within the goals (10 degrees in phase and $\pm\ 0.4dB$ in amplitude), also without imbalance correction (as a direct consequence of the symmetrization procedure and of the phase calibration).

For L-band, there is a 5% improvement in amplitude, but phase imbalance is about 18^o, also after the correction. A possible explanation can be the different response of the reflector at L-band (it has to be pointed out that only one corner has been used at this frequency).

4.3. Radiometric calibration

The accuracy of our absolute calibration was limited by the reduced number of available corner reflectors: three calibrators at C-band and one at L-band. We corrected the images for the bias, assuming that the antenna pattern correction was performed correctly.

Table I shows the calibration factors at different frequencies.

Table I - Radiometric Calibration

Band	ANG	RCS	SIG	SNR	FACT(dB)	FACT	ERR
C	41.09	29.30	55.15	29.98	44.91	30984.78	0.0634
C	42.85	29.30	53.76	26.79	43.52	22512.88	0.0915
C	44.51	41.40	57.02	35.95	34.68	2938.01	0.0319
L	44.51	28.80	35.57	23.14	25.83	383.18	0.1393

Radiometric Calibration parameters. ANG = target incidence angle, RCS = theoretical target radar cross *section, SIG = measured target cross section, SNR = signal to noise ratio, FACT(dB) = calibration factor in decibels, FACT = calibration factor, ERR = Error due to signal to noise level.*

4.4. Extended target analysis.

As suggested in Hawkins(1990) and Moore et al.(1988), the antenna elevation pattern can be determined using "suitably" uniform regions, that is with scattering coefficient not strictly dependent on incidence angle. Uniformity can be reached also by providing averages on data, and this is the case of Stokes format data.

Results of a statistical analysis performed on 128 x 128 pixels (1550mt x 850 mt) areas on the fully calibrated images are shown in table II. The table shows the normalized backscattering coefficients and the coefficients of variation (c.v.) as measured from 128 x 128 pixels size areas. The presented σ_0 and c.v. values are the averages from three areas centered at incidence angles shifted of, respectively, +5, 0, -5 degrees with respect to the indicated angle.

The areas were selected along the range on the forested region. The coefficient of variation $(\frac{sd}{mean})$ for L-band data reveals that the assumption of homogeneity is quite valid for the scene; moreover the backscattering coefficients have values spread within a range of $\pm 0.5dB$, which are acceptable for the assumed accuracy.

At C-band the σ^0 values are still not varying with incidence angle, but the coefficient of variation doesn't allow any conclusion on the assumption of uniformity of each single area.

Again the basic assumption concerns the antenna correction, performed using a theoretical pattern.

Table II - Extended Target Analysis

Incidence angle	sigma0		coeff. of var.	
	l-band	c-band	l-band	c-band
35	-3.8	-18.9	0.33	0.34
44	-3.2	-18.2	0.32	0.32
50	-3.5	-18.2	0.33	0.34
53	-4.0	-18.5	0.33	0.46

5. CONCLUSIONS

The analysis carried out on the data sets acquired by the NASA/JPL DC-8 Polarimetric SAR had three main objectives :

- Make quality assessment and calibration considerations on data coming from the sensor that currently represents the status of the art for polarimetric applications.
- Demonstrate the potential of the tools developed by the MWT at JRC, also with regard to the reliability of the obtained results.
- Investigate scattering behaviors of the forest in the Freiburg region, in view of the utilization of this test site for future projects.

As to the first point, our conclusions concerning the sensor stability and the possibility to fully calibrate the imaged scenes with the available algorithms, are highly positive. Further investigation is being carried out on the antenna pattern; this will entail the removal of the filtering applied by JPL on the processed images.

The results of the calibration processing, obtained using the in-house developed software, are in good agreement with results found in the literature. Due to the flexible software architecture, these tools seem to be quite useful both for an investigation activity and for an operational phase.

The most interesting considerations stem from the uniformity assumption on the Freiburg forest. The examined data confirm this hypothesis and make the site a candidate for satellite calibration, as the rain forest of the Amazon (used for Seasat scatterometer) and the tropical forest in French Guyana for ERS-1.

Future objectives of the MWT calibration activity will include the deployment of more active and passive calibrators in the test sites of interest, and the systematic collection of ground truth data, also in view of some modeling effort. These actions are already planned and operational for the Freiburg area in view of the MAC-EUROPE campaign and ERS-1 launch during 1991.

6. REFERENCES

[1] F.T. Ulaby, C. Elachi editors, *Radar Polarimetry for Geoscience Applications,* Artech House, 1990.

[2] H.A. Zebker, Y. Lou, *Phase Calibration of Imaging Radar Polarimeter Stokes Matrix,* IEEE Trans. Geosci. Re. Sens., Vol GE-28, pp. 246-252, 1990.

[3] J. van Zyl, *A Technique to Calibrate Polarimetric Radar Images Using Only Image Parameters and Trihedral Corner Reflectors,* IEEE Trans. Geosci. Re. Sens., Vol. GE-28, 1990.

[4] A. Freeman, *An Exact Solution to the Problem of Calibrating Stokes Matrix Format SAR Data,* Proc. IGARSS 90,Univ. of Maryland, MD, May 1990.

[5] G.F. de Grandi, H. de Groof, C. Lavalle, G.G. Lemoine, A.J. Sieber, *Data Quality Assessment and Calibration of the Maestro-1 Freiburg data set,* To be presented at IGARSS 91, Univ. of Techn. Helsinki, June 1991.

[6] G. De Grandi , *An Overview of the Software Tools for Radar Multipolarization Data Analysis and Presentation Developed in the SUN OS Environment by the JRC Ispra Microwave Team,* SUG European Conference, Den Haage, April 1990.

[7] R.K. Hawkins, *Determination of Antenna Elevation Pattern For Airborne SAR Using the Rough Target Approach,* IEEE Trans. Geosci. Re. Sens., Vol. GE-28, 1990.

[8] R.K. Moore, M. Hemmat *Determination of the Vertical Pattern of the SIR-B Antenna,* Int. J. Remote Sensing, Vol. 9,No. 5, 1988.

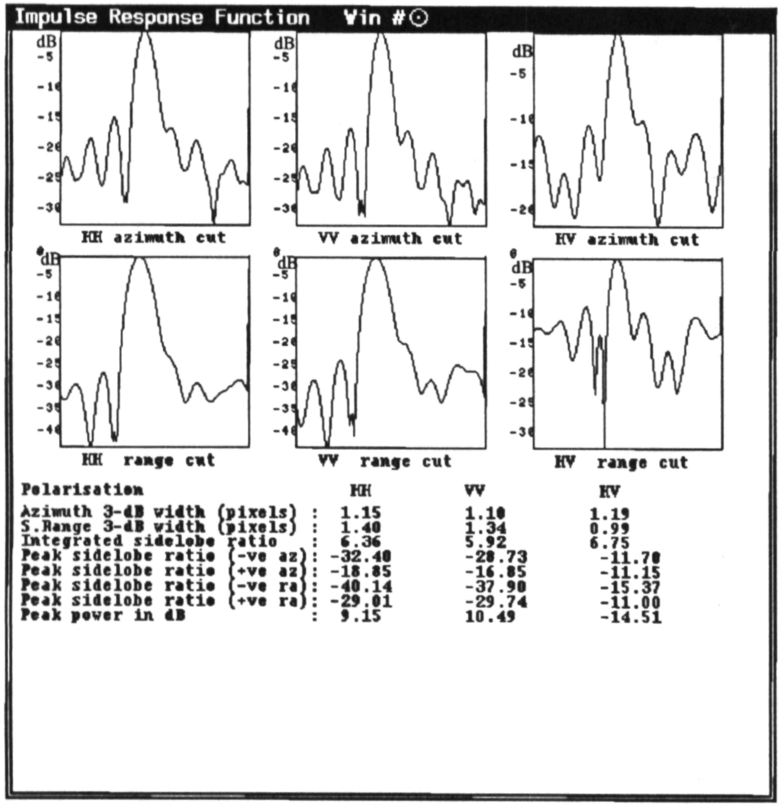

```
Polarisation                          HH        VV        HV
Azimuth 3-dB width (pixels) :       1.15      1.10      1.19
S.Range 3-dB width (pixels) :       1.40      1.34      0.99
Integrated sidelobe ratio   :       6.36      5.92      6.75
Peak sidelobe ratio (-ve az):     -32.40    -28.73    -11.70
Peak sidelobe ratio (+ve az):     -18.85    -16.85    -11.15
Peak sidelobe ratio (-ve ra):     -40.14    -37.90    -15.37
Peak sidelobe ratio (+ve ra):     -29.01    -29.74    -11.00
Peak power in dB            :       9.15     10.49    -14.51
```

Figure 1 : Impulse Response Function Analysis results as output from CALTOOL. Range and azimuth cuts are shown for the HH,VV and HV channels together with the relevant parameters.

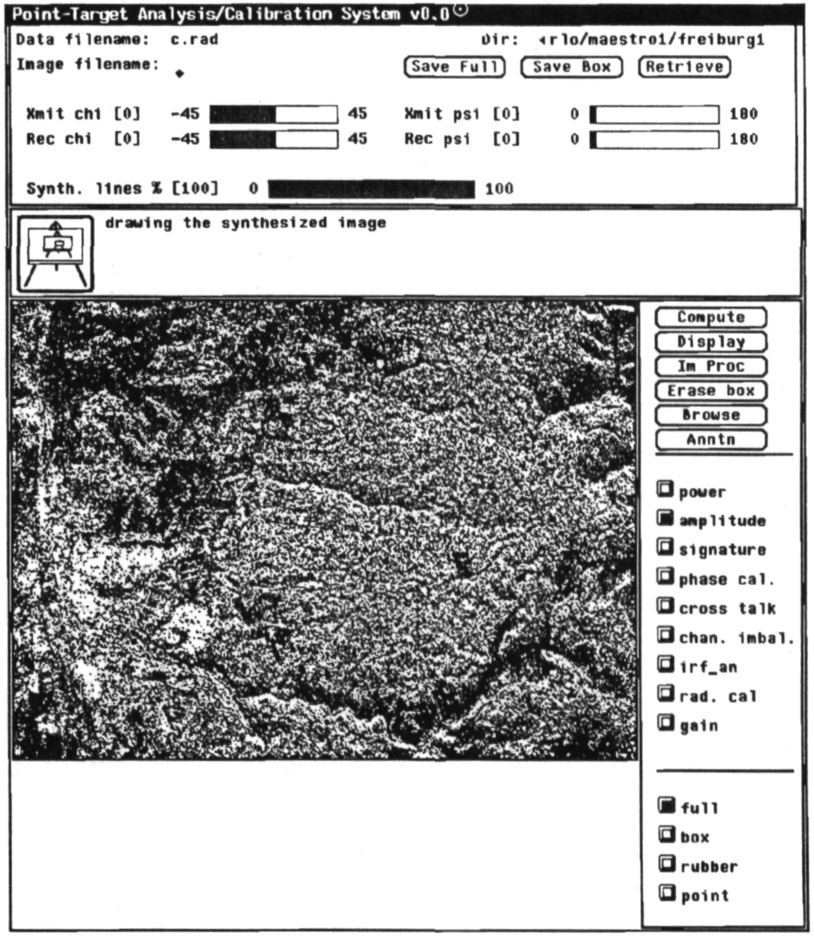

Data filename: c.rad Dir: ◂rlo/maestro1/freiburg1

Image filename:

Xmit chi [0] -45 45

Rec chi [0] -45 45

Xmit psi [0] 0 180

Rec psi [0] 0 180

Synth. lines % [100] 0 100

drawing the synthesized image

Figure 2 : CALTOOL layout

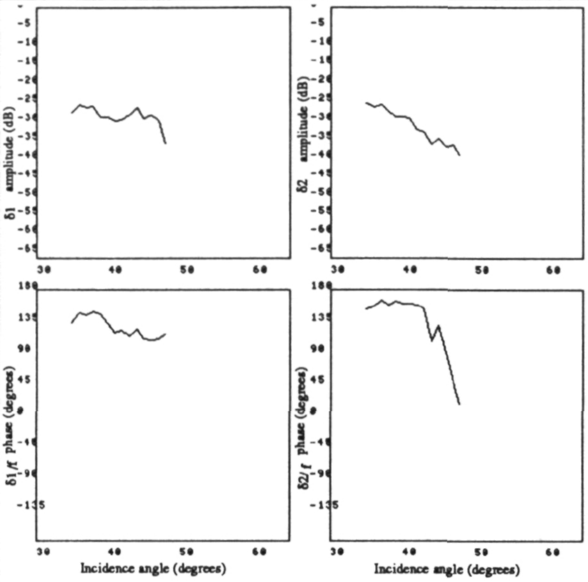

Fig. 3 : Cross talk parameters at L-band computed for an urban area.
The top graphs show parameters amplitude vs. incidence angle.
The bottom graphs show parameters phase vs. incidence angle.

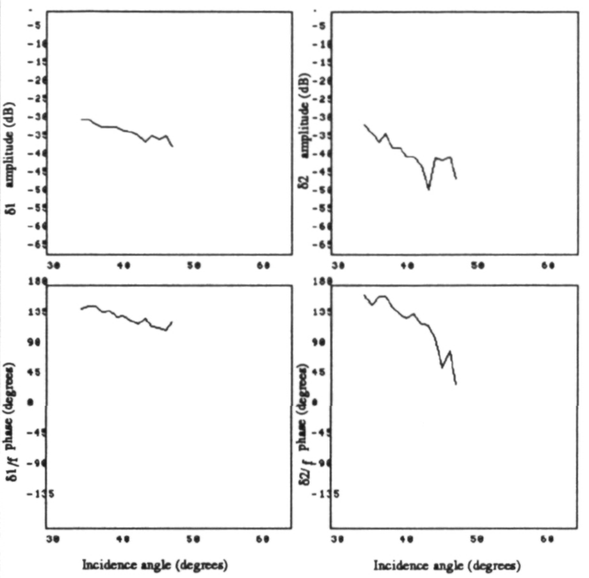

Fig. 4 : Cross talk parameters at L-band computed for a forested area.
The top graphs show parameters amplitude vs. incidence angle.
The bottom graphs show parameters phase vs. incidence angle.

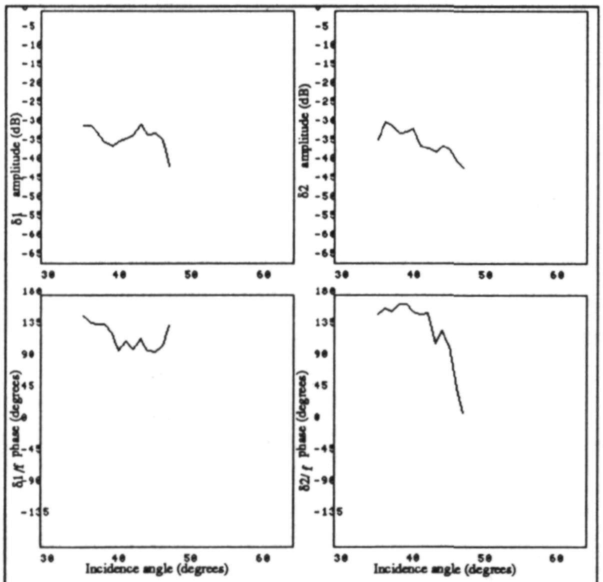

Fig. 5 : As fig. 3, after cross-talk removal.
The top graphs show parameters amplitude vs. incidence angle.
The bottom graphs show parameters phase vs. incidence angle.

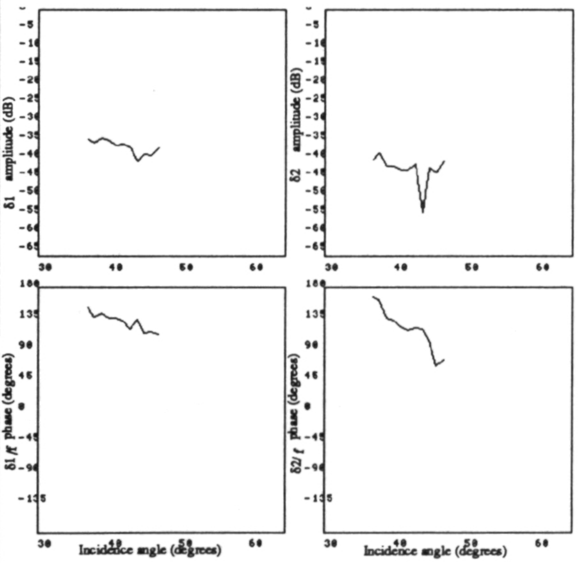

Fig. 6 : As fig. 4 , after cross-talk removal.
The top graphs show parameters amplitude vs. incidence angle.
The bottom graphs show parameters phase vs. incidence angle.

N92-28029

SAR Calibration and Principal Component Analysis

S. Quegan
University of Sheffield
Sheffield, UK

L. V. Dutra
INPE
Sao Paulo, Brazil

Abstract

Principal components analysis of ideal, complex quadpolarised SAR data tells us how the information is encoded in the eigenstructure of the data from homogeneous, distributed targets. Comparison with real data indicates distortion of the correlation matrices by system effects. The implications for measurement of the terms in the true correlation matrix are displayed. These are related to how accurately we can make inferences about the products of principal components analysis.

1. Introduction: The Principal Component Transformation

When dealing with any high-dimensional data set, such as that provided by the JPL DC–8 quadpolarised SAR, a central problem is to identify and reduce redundancy between channels, with a view to better identifying the information-bearing components of the data. This is important both in terms of data handling and display, and in clarifying the physical properties of the scattering process. For quadpolarised SAR data, it presents a particularly interesting problem, for at least four reasons:

1. There are a variety of data representations, e.g., as a scattering matrix (complex), as a Stokes vector, as intensity data;
2. There may be information carried by the phase;
3. There are theoretical predictions concerning correlation and independence of some channels; and
4. System effects cloud the interpretation of the observed measurements.

One possible approach to this problem is by means of the principal components transformation (PCT). This operates by linearly transforming the data to a coordinate system described by orthonormal vectors $(\phi_i)_{i=1}^{N}$, in which the representation of a vector

$$s = \sum_{i=1}^{N} C_i \phi_i \tag{1}$$

has coordinates $(C_1, ..., C_N)$ which are uncorrelated. The dimension of the underlying set of measurements is N. Assuming that the vectors s are drawn from a stationary random process, the vectors ϕ_i are found to be the eigenvectors of the correlation matrix

$$C = E(s\ s^{+}) \ ,$$

where + denotes conjugate transpose and E denotes expectation. Hence

$$C\phi_i = \lambda_i \phi_i \tag{2}$$

where λ_i is the eigenvalue associated with ϕ_i. This can be written

$$C = P\Lambda\, P^+ \tag{3}$$

where P is the unitary matrix whose ith column is given by ϕ_i, and Λ is the diagonal matrix

$$\Lambda_{ij} = \lambda_i \delta_{ij} \ .$$

The eigenvalues are all real and non-negative, and $\lambda_i = E(|C_i|^2)$. In addition, if the data vector $s = (s[1], s[2], ..., s[N])$ has components that are mean zero and for which component j has variance

$$\sigma_j^2 = E[|s(j)|^2] \ , \tag{4}$$

then $\sum_{i=1}^{N} \lambda_i = \sum_{j=1}^{N} \sigma_j^2$. This means that ordering the eigenvalues as $\lambda_1 \geqslant \lambda_2 \geqslant \ldots \geqslant \lambda_N \geqslant 0$ gives an ordering in the uncertainty in the coefficients C_i.

The PCT acts on the data s by

$$s \rightarrow P^+ s \tag{5}$$

to produce uncorrelated coefficients C_i. Note that decorrelation only occurs if the target is homogeneous. If it is heterogeneous, the PCT will act to produce decorrelated coefficients in the dominant target type (assuming its correlation matrix is not too distorted), but not in the minor types. The PCT may be target-specific, in which case it offers a possible route to discrimination and classification.

From this very terse description we can recognise two properties of the PCT:

1. If the eigenvalues exhibit a sharp cutoff from large to small values, this reveals an intrinsic dimensionality in the data. The small eigenvalues correspond to small uncertainty and hence little information content. This offers a means of data compression.
2. The above remark must be qualified, since it equates information with uncertainty and hence with energy. This is likely to present problems in treating phase as an information source.

2. The Scattering and Correlation Matrices

The scattering matrix for a single frequency is

$$S = \begin{pmatrix} S_{11} & S_{12} \\ S_{21} & S_{22} \end{pmatrix} \ , \tag{6}$$

giving rise to a vector

$$\begin{aligned} s &= (S_{11}, S_{22}, S_{12}, S_{21})^t \\ &= (s[1], s[2], s[3], s[4])^t \ . \end{aligned}$$

For distributed homogeneous targets we expect

$$E(S_{ij}\, S_{ji}^*) = E(|S_{ij}|^2) \ ,$$

$$E(S_{ii}\, S_{ij}^*) = 0 \ , \qquad i \neq j.$$

This gives rise to a correlation matrix

$$C_s = E(s\ s^+) = \begin{bmatrix} \sigma_1^2 & \varrho & 0 & 0 \\ \varrho^* & \sigma_2^2 & 0 & 0 \\ 0 & 0 & \sigma_3^2 & \sigma_3^2 \\ 0 & 0 & \sigma_3^2 & \sigma_3^2 \end{bmatrix} \tag{7}$$

where $\varrho = E(S_{11}\ S_{22}^*)$. Hence C_s carries five potential information sources: $\sigma_1^2, \sigma_2^2, \sigma_3^2$, $|\varrho|$, and $\mathrm{Arg}(\varrho)$.

Note that $\varrho = E(r_1\ r_2)\ E(e^{i\phi})$ if we write $S_{ii} = r_i\ e^{i\phi_i}$, assume that the amplitude and phase of S_{ii} are independent, and put $\phi = \phi_1 - \phi_2$. Hence phase enters the correlation matrix through the function $E(e^{i\phi})$.

A useful minor result is that if the probability density function of ϕ, $P(\phi)$, has a line of symmetry about ϕ_0 (mod 2π), then

$$\mathrm{Arg}(\varrho) = \mathrm{Arg}[E(e^{i\phi})] = \phi_0\ . \tag{8}$$

However,

$$E(\phi) = \phi_o - \pi \int_{-\pi}^{2\phi_0 - \pi} P(\phi) d\phi\ .$$

This can be significantly different from ϕ_0, though ϕ_0 is (in our experience) the better choice of representative value. (If $\phi_0 < 0$, the expression for $E(\phi)$ needs a slight modification; also, there is an ambiguity of $\pm\ \pi$ in the value of ϕ_0 given by $E(e^{i\phi})$). A practical difficulty arises in using the correlation matrix to derive ϕ_0 if the correlation coefficients become small, since then the measurement of phase is likely to be unreliable, and direct use of the phase difference histogram may be necessary.

In the ideal case, given by equation (7), two eigenvalues are given by

$$\lambda_{1,2} = \frac{1}{2}\left[\sigma_1^2 + \sigma_2^2 \pm \sqrt{(\sigma_1^2 - \sigma_2^2)^2 + 4|\varrho|^2}\right] \tag{9}$$

with eigenvectors

$$\phi_i = \kappa_i \left(1, \frac{\lambda_i - \sigma_1^2}{\varrho}, 0, 0\right)^t, \qquad i = 1, 2\ ,$$

$$= \kappa_i \left(1, \frac{\sigma_2^2 - \sigma_1^2 \pm \sqrt{(\sigma_2^2 - \sigma_1^2)^2 + 4|\varrho|^2}}{2\varrho}, 0, 0\right)^t, \tag{10}$$

where κ_i is a normalisation constant to ensure that $\| \phi_i \| = 1$. Notice that

$$\mathrm{Arg}(\varrho) = \mathrm{Arg}(\phi_1[1]/\phi_1[2])$$

and that

$$\mathrm{Arg}(\phi_2[1]/\phi_2[2]) = \mathrm{Arg}(\phi_1[1]/\phi_1[2]) \pm \pi\ ,$$

i.e., all the phase information goes into the eigenvectors, not the eigenvalues. This can be understood in terms of the PCT rotating the second component (in the complex plane), to align it parallel or anti-parallel to the first component before performing a weighted average of the two. In the transformed data, all phase information is lost.

The third and fourth eigenvalues and eigenvectors are given by

$$\begin{aligned} \lambda_3 &= 2\sigma_3^2 \quad ; \quad \phi_3 = \left(0, 0, \frac{1}{\sqrt{2}}, \frac{1}{\sqrt{2}}\right)^t \\ \lambda_4 &= 0 \quad ; \quad \phi_4 = \left(0, 0, \frac{1}{\sqrt{2}}, \frac{-1}{\sqrt{2}}\right)^t . \end{aligned} \tag{11}$$

The relative size of λ_2 and λ_3 depends on $|\varrho|$. For uncorrelated HH and VV channels, $\varrho = 0$, $\lambda_2 = \sigma_1^2$ (or σ_2^2), and we would expect $\lambda_2 > \lambda_3$. If the HH and VV channels are fully correlated, $|\varrho|^2 = \sigma_1^2 \, \sigma_2^2$, $\lambda_2 = 0$, and $\lambda_2 < \lambda_3$.

When two frequencies are used, we expect them to yield uncorrelated observations, so that the overall correlation matrix will be of the form

$$\begin{pmatrix} C_1 & 0 \\ 0 & C_2 \end{pmatrix} ,$$

where C_i is a matrix of the same form as (7).

3. Observed Correlation Matrices and Eigenstructures

In practice, observed correlation matrices do not have the ideal form given by equation (7). Table 1 is an example of L-band observations taken from an apparently homogeneous agricultural area. The first column gives the ordered eigenvalues, while the next 4 × 4 block is the correlation matrix. The upper triangle has been omitted because this matrix is Hermitian. The entries in the matrix are given in terms of their amplitude and phase. The last three columns give the first three eigenvectors, also in terms of amplitude and phase.

The correlation matrix has some of the expected features, with the magnitudes of the bottom-right block being approximately equal and the diagonal terms in the upper-left block being an order of magnitude larger. However, the off-diagonal blocks are non-zero and, in fact, are of comparable magnitude to the bottom-right block. Also, a phase term (42°) appears in the off-diagonal elements of the bottom-right block. The eigenvalue structure is close to that expected, with the fourth eigenvalue being small. The eigenvectors also have the expected structure. The first two are dominated by the contributions from the HH and VV channels. The phase difference in the first two components is 18° and −163°, which gives the correct relationship with Arg ϱ. The third eigenvector has equal contributions from HV and VH, which dominate the contributions from the HH and VV channels.

Table 2 is C-band data for a water body, set out in the same format. Here the off-diagonal blocks are near 0, but the off-diagonal terms in the bottom-right block are also near 0, contrary to expectation. The eigenvalue structure no longer clearly contains a small term. The phase and amplitude relations in the first two eigenvectors are as expected. The weighting of the third and fourth components of the other two eigenvectors is different from theory (but notice that the phase relations tend to line up with the complex components, as discussed above).

Table 3 is L- and C-band data for an agricultural area (Table 1 corresponds to its top-left block). The surprise in this table is the small but not insignificant correlation between the C-band HH channels and the two copolarised L-band channels. The intrinsic dimensionality of the data as evidenced by the eigenvalues is 4 or 5, and the eigenvectors are dominated, as expected, by the like-polarised terms (C-band contributes the first two eigenvectors, then L-band).

4. System Effects

The discrepancies between the theoretical and observed correlation and eigenstructures can be attributed to a number of possible sources:

(a) sampling statistics;
(b) noise;
(c) an erroneous model for the target, including lack of homogeneity;
(d) distortions introduced by the system.

Here we discuss only (d).

The simplest model for system effects is the widely quoted linear model (e.g., van Zyl, 1990), in which the observed data are given by

$$y = Ms \, ,$$

where M includes all phase, cross-talk, and channel imbalance effects on transmission and reception. The observed correlation matrix is then

$$C_y = E(y \, y^+) = M \, C_s \, M^+ = M \, P\Lambda \, P^+ M^+ \; . \tag{12}$$

Principal components analysis decomposes C_y as

$$C_y = Q \; \Lambda_y \; Q^+ \; . \tag{13}$$

The assumptions underlying calibration using extended targets are (van Zyl, 1990):

$$\begin{aligned} &E(S_{ii} \; S_{ij}^*) = 0 \qquad\qquad i \neq j \\ &S_{12} = S_{21} \\ &M_{ii} \approx 1 \quad \text{and} \quad M_{ij} << 1 \text{ if } i \neq j \; . \end{aligned}$$

Using these relations, calibration attempts to recover s from y by a linear transform. Effectively this involves finding M^{-1}.

These assumptions are clearly related to what the PCT does, and hence the PCT may be expected to be related to the calibration procedure. This relation is clear if M is orthogonal. Then the PCT of y is given by

$$Q^+ y = Q^+ M s \; .$$

But we see from (12) that $Q = MP$ (up to a possible reordering of eigenvalues), so that

$$Q^+ y = P^+ s \; , \tag{14}$$

which is the same as applying the PCT to the undistorted data. In particular, phase distortion has no effect on the PCT.

More generally, M is not orthogonal and hence changes the angles between the axes. Hence the PCT cannot invert M, and we need to look harder at how calibration affects the PCT.

5. Calibration

What is the most we can find out about the correlation matrix without prior knowledge or calibration devices (the situation faced over the Reedham site in the 1989 JPL Maestro campaign)? The linear distortion model in scattering matrix form becomes

$$S \rightarrow RST \ .$$

The left side gives s; the right side gives $y = Ms$. The ensuing correlation matrix C_y can be related to C_s in terms of two unknown parameters,

$$A = |r_{22}\, t_{22}|^{-2} \qquad > 0, \quad \text{real}$$

and

$$k = r_{11}/r_{22} \ ,$$

(k is complex, and we expect $|k| \sim 1$), together with two measurable parameters, z_1 (real) and z_3 (complex), by

$$\sigma_1^2 = A\ C_{11} \frac{|z_3|^2}{z_1^2} \ \frac{1}{|k|^4} \tag{15a}$$

$$\sigma_2^2 = A\ C_{22} \tag{15b}$$

$$\sigma_3^2 = A\ \frac{|z_3|^2}{z_1} \ \frac{1}{|k|^2} \tag{15c}$$

$$\varrho = A\ C_{12} \ \frac{z_3}{z_1} \ \frac{1}{k^2} \ , \tag{15d}$$

where

$$z_1 = C_{33} - u\ C_{13} - v\ C_{23} \tag{16a}$$

$$z_3 = C_{43} - u^*\ C_{41} - v^*\ C_{42} \tag{16b}$$

and

$$u = \frac{r_{21}}{r_{11}} = \frac{C_{22}\ C_{31} - C_{21}\ C_{32}}{C_{11}\ C_{22} - |C_{21}|^2} \tag{16c}$$

$$v = \frac{t_{21}}{t_{22}} = \frac{C_{11}\ C_{32} - C_{31}\ C_{12}}{C_{11}\ C_{22} - |C_{21}|^2} \ . \tag{16d}$$

Here C_{ij} refers to the (directly measurable) elements of C_y. A is simply a scaling term for a single frequency, but becomes important if we wish to use the PCT for multi-frequency data. Note that even small deviations of $|k| = |r_{11}/r_{22}|$ from unity have significant effects on our ability to make accurate estimates of the relative sizes of the terms in the true correlation matrix. If $|k| = 0.9$, the value of σ_1^2 will be inflated by more than 50%, and the values of σ_3^2 and $|\varrho|$ by more than 20%. The phase of ϱ is clearly dependent on Arg (k).

6. System Effects and the PCT

It is important to establish the consequences of the distortions discussed in Section 5 for our ability to make correct inferences about the eigenstructure of the true correlation matrix, and hence about the PCT. A detailed analysis is not presented here; we make only a few pertinent observations.

Referring to equation (9), we see that the expression inside the square root term can be written

$$\sigma_1^4 + \sigma_2^4 - 2\frac{A^2}{|k|^4}\,\frac{|k_3|^2}{z_1^2}(C_{11}\,C_{22} - 2|C_{12}|^2)\ .$$

Since the term $C_{11}\,C_{22} - 2|C_{12}|^2$ is directly measurable, we can make correct inferences on the relative importance of the correlation term $|\varrho|$.

The sizes and ordering of the eigenvalues are dependent on the value of $|k|$. If we are able to assume that $|k|$ does deviate too far from 1, we may still be able to ascertain the relative importance of the eigenvalues in the true correlation matrix.

The scaling constant A linearly scales each eigenvalue, but has no effect on the eigenvectors. Hence, for single-frequency data, A has no effect on our inferences from the PCT. For multi-frequency data, however, the relative size of A between different frequencies may affect the ordering of eigenvalues and, hence, our inferences on the relative importance of different channels.

The phase information carried by the eigenvectors is corrupted by Arg (k). This prevents us from making meaningful statements about the absolute value of phase differences for specific target types. However, if k is constant across a scene, then it is possible to draw perfectly valid conclusions about the variation of phase difference between target types.

7. Concluding Remarks

In this paper we have displayed some of the connections between the use of PCT and data calibration. This work is obviously incomplete at the moment. We have not presented an analysis of how the actual eigenvalues formed by uncalibrated PCT relate to the ideal eigenvalues. The relations set out in Section 5 have been used only to make a number of general observations on the uncertainties in the products of the true PCT, though they can be used to make detailed analysis of the relative importance of terms in the correlation matrix and in the eigenstructure. The discussion of why PCT fails to calibrate for system effects other than those giving rise to orthogonal matrices (Section 4) suggests a possible approach to calibration based on deskewing the data. The connections to principal components analysis using amplitude-only data have been analyzed, but are not presented here. Principal components analysis based on the Stokes' vectors has not yet been considered. These are topics of current work.

References

van Zyl, J. J. (1990): "A technique to calibrate polarimetric radar images using only image parameters and trihedral corner reflectors," *IEEE Trans.* **GE–28**, 337–348.

Table 1. **L-band observations of an agricultural region from the Reedham test site. Column 1 gives the relative size of the eigenvalues as a percentage. The next 4 $\times$ 4 block is the correlation matrix (amplitude and phase). The last three columns are the first three eigenvectors whose components are ordered as for the correlation matrix, i.e., HH, VV, HV, VH.**

λ(%)	0	1	2	3	ϕ_1	ϕ_2	ϕ_3
73.9	5.6				.71 60	.69 -155	.16 36
20.8	3.0 -18	5.5			.69 42	.72 8	.07 58
6.2	0.7 -110	0.6 -101	0.5		.11 -54	.05 134	.7 115
0.1	0.7 -152	0.6 -140	0.5 -42	0.5	.11 -94	.05 83	.7 73

Table 2. **Observations as for Table 1, but at C-band and for a water body. All four eigenvectors are given.**

λ(%)	0	1	2	3	ϕ_1	ϕ_2	ϕ_3	ϕ_4
79.5	0.8				0.54 129	0.83 -50	0.13 115	0.02 30
9.5	0.9 -94	1.6			0.84 35	0.53 36	0.12 -175	0.02 101
6.6	0.02 114	0.05 -166	0.14		0.03 -127	0.11 -160	0.49 -179	0.86 88
4.4	0.03 50	0.05 128	0.03 -77	0.17	0.03 166	0.13 124	0.85 103	0.5 -169

Table 3. **The L- and C-band combined data for the area used to create Table 1. In the 8 × 8 correlation matrix the only significant cross-frequency terms are those involving the C-band HH and the L-band copolarised terms. Only the first three eigenvectors are shown.**

λ(%)		0	1	2	3	4	5	6	7	ϕ_1	ϕ_2	ϕ_3
55.90	HH_L	5.625 0								0.004 20	0.016 34	.704 98
17.12	VV_L	3.043 -18.1	5.458 0							0.005 78	0.019 42	0.678 80
11.49	HV_L	0.676 -110.0	0.560 -101.0	0.486 0						0.001 -39	0.003 -70	0.108 -16
10.86	VH_L	0.699 -151.9	0.562 -140.4	0.474 -42.2	0.485 0					0.002 -81	0.003 -117	0.111 -56
3.27	HH_c	0.116 -77.4	0.226 -146.9	0.066 -21.6	0.074 22.3	34.7 0				0.858 -57	0.465 -118	0.039 168
0.981	VV_c					13.46 -91.3	20.02 0			0.512 -148	0.748 -31	0.060 -94
0.344	HV_c		<1%			0.432 -16.0	1.632 149.9	4.577 0		0.029 -19	0.323 128	0.083 -92
0.015	VH_c					0.443 -106.1	1.657 78.134	4.579 -73.1	5.125 0	0027 -94	0.344 55	0.086 -165

N92-28030

Results of the 1989 SAR Calibration Experiment at Oberpfaffenhofen

M. Zink

DLR - German Aerospace Research Establishment
Institute for Radio Frequency Technology
Oberpfaffenhofen / FRG

Abstract

Results are presented from the 1989 airborne SAR calibration campaign at the DLR test site in Oberpfaffenhofen. Passive corner reflectors were used to derive the receiver and transmitter distortion matrices and the absolute calibration factor of the multispectral polarimetric DC-8 SAR from the complex high resolution data. A basic requirement for cross-calibration of data from different tracks is the stability of the SAR system. The polarimetric properties of the uncalibrated data were used to describe this stability. Quality criteria for a successful polarimetric calibration were provided by the channel balance and cross-talk parameters.

1 Introduction

In August 1989 a calibration campaign took place at the DLR test site in Oberpfaffenhofen which includes the DORNIER airfield [1,2]. The airborne sensors used were the DLR E-SAR and the NASA/JPL DC-8 SAR. We deployed 46 precisely manufactured corner reflectors (42 trihedrals and 4 dihedrals). Our colleagues from the Institute for Navigation at the University of Stuttgart successfully tested a prototype of a C-band polarimetric active radar calibrator (PARC). Each aircraft performed flights at incidence angles of 30^o, 45^o and 55^o, three tracks parallel to and three tracks perpendicular to the DORNIER runway.

Since we used passive trihedral corner reflectors up to a leg length of 1.0 m, the analysis presented in this paper is dedicated to the C-band data of the DC-8 SAR. We intend to employ active radar calibrators to calibrate data from future spaceborne and airborne SAR sensors acquired at lower frequencies (e.g. L-band).

In the polarimetric calibration approach using corner reflectors, a problem arises from the very narrow beamwidth of the dihedrals in the plane of their seams. Even if the reflectors are precisely aligned to the radar, adequate dihedral returns are only obtained from some tracks because of unavoidable flight pass deviations and the drift of the platform. As a consequence, there is a need for polarimetric cross-track calibration. A successful cross-calibration of data from different tracks requires a stable SAR system. To demonstrate this stability and the improvement achieved by polarimetric calibration we considered two essential indicators: the channel-imbalance and the cross-talk behaviour derived from trihedral corner reflectors and other point reference targets and the image background.

About thirty colleagues realigned each corner reflector on ground after each track. Because of a misunderstanding between the DC-8 crew and the ground team, tracks 4 and 6 perpendicular to the runway at incidence angles of 55^o and 30^o were interchanged. It is not possible to correct a misalignment of 25^o; so we dropped tracks 4 and 6 from our analysis.

2 Calibration Procedure

To introduce the task of calibrating a polarimetric imaging radar we establish a suitable equation describing the quad-polarized measurement $\mathcal{M}$ as follows

$$\mathcal{M} = \alpha \mathcal{R}^t \mathcal{S} \mathcal{T} + \mathcal{N} . \tag{1}$$

$\mathcal{S}$ is the target scattering matrix and the complex scalar quantity α represents the radar system gains and losses, the attenuation due to the round trip propagation and the corresponding phase delay. The receiver and transmitter distortion matrices $\mathcal{R}$ and $\mathcal{T}$ describe the polarization characteristics of the radar and do not depend on target properties. The superscript "t" indicates the transpose of a matrix. For the ideal case, implying no losses, no gains, and no polarization impurities in either the receiver or the transmitter, the $\mathcal{R}$ and $\mathcal{T}$ matrices are equal to the identity matrix. The matrix $\mathcal{N}$ represents the noise voltage present in each radar channel which can be neglected because of the sufficient signal to noise ratio in the DC-8 airborne case.

In mathematical terms, the estimation of α, $\mathcal{R}$, and $\mathcal{T}$ is equivalent to the solution of a system of three matrix equations. We developed a new polarimetric calibration procedure based on the numerical solution of a system of nonlinear equations. The ideal identity matrices were used as start values for the iterative algorithm. The advantage of this approach is that no further assumptions are necessary and a greater number of calibration targets with arbitrary scattering matrix can be taken into account. In addition, it is possible to consider alignment errors (e.g. a rotation between the sensor H-V coordinate system and the corresponding system on the ground). As for all procedures utilizing point targets, we obtain only one solution for the $\mathcal{R}$ and $\mathcal{T}$ matrices which implies that the distortions are the same for the whole scene. This is particularly not true for the cross-talk, which is mainly determined by the properties of the antenna and is therefore incidence angle or range dependent.

For polarimetric investigations we are only concerned with the relative phase between terms in $\mathcal{S}$. Therefore there is no further need to deal with the absolute phase of α. Applying adequate radiometric corrections [1,2] results in an elimination of any range dependence in the amplitude of α. So a mean $|\alpha|$ quantity can be calculated by averaging the $|\alpha|$-values found from several corner reflectors using an integration approach [2].

3 System Stability

Future spaceborne SAR missions illuminate calibration test sites once per day or once per week. Data from other tracks have then to be calibrated using the correction parameters found from the image of the calibration test site. The calibration of airborne data could also be simplified by doing external calibration in certain time intervals. The performance of such cross-calibration depends mainly on the stability of the radar system. The full polarimetric DC-8 SAR represents a complex sensor with the capability to measure the whole scattering matrix for each resolution cell in the imaged scene. Such increased radar complexity requires an increased effort to calibrate the system. On the other hand, more parameters can be derived even from the uncalibrated complex high resolution data to demonstrate the stability of the system.

The channel imbalance and the cross-talk, two essential indicators of polarimetric performance, provide information about this stability. The spread in the properties of electrical devices used to build a multichannel radar is responsible for different amplitude and phase characteristics in different channels. This channel imbalance can be derived from any discrepancy between the like-polarized responses from trihedrals or other point targets with corresponding scattering matrix or between the cross-polarized signals from natural targets (backscattering and reciprocity assumed). Because of a lack of polarization isolation in polarimetric radars, an unwanted amount of H-polarized energy always couples into the V-polarized channel and vice versa. This leakage effect is called cross-talk and can be estimated, for example, from the ratio of the cross- and like-polarized corner reflector responses.

Fig. 1 shows the channel imbalance of the like-polarized channels computed from the trihedral corner reflector responses. The amplitude ratio in dB and the relative phase difference in degrees are plotted against the corresponding off-nadir angle for all considered tracks. The amplitudes of the uncalibrated system are well balanced but the phase difference is about 150^o offset from the expected theoretical 0^o. The system cross-talk is mainly determined by the properties of the antenna and is range or incidence angle dependent (Fig. 2).

Coherent averaging of the pixel contributions in each image line leads to similar statements concerning the properties of the image background. In Fig. 3 the relative phase of HH/VV and HV/HH is plotted versus off-nadir angles. Because of the stability of the system there was no need to distinguish data from different tracks (track 1, 2 and 5 in the off-nadir angle range from 10^o to 53^o and track 3 from 45^o to 62^o). After [3] the HH and VV scattering matrix elements should be in phase in situations where specular reflections occur. These situations include reflection from smoother surfaces near normal incidence angles and specular reflection from very rough surfaces where scattering is dominated by reflection of facets oriented orthogonally to the incident wave. The HH/VV phase difference in Fig. 3 is about 150^o, as for the trihedrals, and flat across the swath. Dihedral like structures in urban areas (incidence angles greater than 30^o) lead to deviations from this value. It has been shown in [4] that as long as planar random media can be considered to be azimuthally symmetric, the like- and cross-polarized scattering matrix elements will be uncorrelated. The HV/HH relative phase in Fig. 3 depicts a strong correlation between the two channels and the same functional characteristics for all tracks. Too high cross-talk levels are responsible for this correlation.

For backscattered signals due to natural targets, reciprocity assumed, the cross-polarized terms HV and VH should be equal. The amplitudes in Fig. 4 are as well balanced as the like-polarized amplitudes from the trihedral corner reflectors. The corresponding phase difference (Fig. 4) is in the order of 30^o and very stable within a scene. The only deviations from these values coincide with the positions of the PARC for the different tracks.

Table 1 summarizes the channel imbalance and cross-talk parameters derived from the uncalibrated data. Corresponding parameters for the PARC and dihedral corner reflectors are in good agreement with those derived from trihedral corner reflectors and the image background. The consistency of the parameters in Table 1 indicates a fairly stable DC-8 SAR system as far as polarimetric properties are concerned.

4 Calibration Results

For the polarimetric calibration of the DC-8 complex high resolution data, we used the procedure described in Section 2 utilizing only trihedral and dihedral corner reflectors. The very narrow beamwidth of the dihedrals in the plane of their seams requires accurate alignment towards the radar and exact tracking of the predetermined flight pass. In addition, the weather should be calm to keep the platform drift angle as small as possible. Because of the very accurate flights accomplished by the JPL AIRSAR crew and the fine weather during those flights we acquired useful dihedral data from tracks 1, 2 and 3. In the image from track 5 we found no dihedral response; the platform drift angle was -6.1°. Therefore we could not apply the calibration procedure to this data and had to perform cross-track calibration using correction parameters from track 2.

The calibration parameters for the first three tracks are listed in Table 2. The transmitter and receiver distortion matrices, represented as amplitudes in dB and phases in degrees, are stable except for the small VH terms. The mean of the absolute radiometric calibration factors in Table 2 is about 5.5 dB for all tracks. The standard deviations are in the order of 0.8 dB. These results indicate the stability of the DC-8 system during the campaign.

If we consider longer time intervals between two flights to be cross-calibrated, it becomes necessary to monitor the sensor, to ensure the cross-calibration performance [5]. Any variation of the transmitted signal (in amplitude and phase) and of the receiver gain should be monitored and recorded before and after or, if possible, during the data take. To avoid any additional errors, special care has to be taken in the radiometric corrections performed on the image data. Platform position data are required to calculate the target range and incidence angle. Because of its great influence the inflight antenna pattern should be measured using ground calibration receivers. Such measurements are planned with the future spaceborne SAR missions [6].

After calibrating the data using the corresponding calibration parameters from Table 2, we found the channel imbalance and cross-talk parameters depicted in Figs. 5 and 6. The amplitudes of the HH and VV trihedral responses were well balanced before calibration (see Fig. 1) and therefore no obvious calibration improvement can be achieved. However, we attained a considerable improvement for the relative phases and calibrated phase differences close to the expected theoretical 0°. As indicated in Fig. 6 an isolation improvement in the order of 5 to 10 dB is achieved by our calibration procedure. This leads to a cross-talk reduction beyond the desirable -30 dB ratio adequate for polarimetric analysis [7].

The HH/VV phase difference calculated from the background clutter is reduced and slightly oscillating around 0° (Fig. 7). Deviations from this value appear as in Fig. 3. The relative phase between HV and HH in Fig. 7 indicates one problem of the applied polarimetric calibration procedure. As mentioned previously the cross-talk is a function of the incidence angle. Contrary to calibration procedures utilizing clutter statistics for cross-talk removal [8], our algorithm applies the same correction parameters (Table 2) to the whole image. Therefore a considerable cross-talk reduction and, as a consequence, a decorrelation of like- and cross-polarized channels is only achieved in that incidence angle range where the calibration targets were deployed. The average background HV/VH amplitude ratios (Fig. 8) are less than 1 dB and the corresponding phase differences (Fig. 8) are improved to the desired delta peak at 0°. The uncalibrated HV/VH relative phases in Fig. 4 depict slight differences between the data from different tracks (see also Table 1). Those difference between tracks 2 and 5 appear in the same manner in Fig. 8 because we applied the correction parameter from track 2 to the data from track 5.

The polarimetric calibration results are compiled in Table 3 including parameters derived from the PARC and dihedral corner reflectors. The data reveal the good performance of the DC-8 SAR system in the C-band quad-polarized mode and the efficiency of our polarimetric calibration procedure. The data from track 5 reveal remarkable well performed polarimetric corrections.

Table 4 includes RCS values of point targets and backscattering coefficients of selected areas in the image of track 2 seen from both the DC-8 SAR and the E-SAR. The ratio of the standard deviation and the mean image power, s/μ, for the distributed targets is also listed. The DC-8 data are single look ($s/\mu = 1.0$), whereas E-SAR data are four look ($s/\mu = 0.5$). The consistency of the measured data is satisfactory. The s/μ ratio met the theoretical value in most cases. The explanation for the increased E-SAR σ^o values could be the changed weather conditions: light rain in the morning during the E-SAR flights, warm and sunny in the afternoon during the DC-8 flights. Simultaneously acquired scatterometer data could fully clarify such discrepancies.

5 Conclusions

Adequate radiometric corrections require the inflight antenna pattern and accurate flight pass and platform attitude data. Measurements of the inflight antenna pattern are planned with the 1991 DC-8/E-SAR campaign at Oberpfaffenhofen and the future spaceborne SAR missions. The polarimetric calibration results using our numerical procedure to find the transmitter and receiver distortions are satisfactory. Only the cross-talk correction has to be improved. The cross-talk should be estimated and removed line by line using clutter statistics. Alternatively, trihedral corner reflectors could be deployed across the swath to determine the cross-talk as a function of range. As we use the integration approach for absolute radiometric calibration, the calibration targets should be positioned on a uniform background which at least extends over the target response being integrated. We have gained a lot of experience from our first calibration experiment and are looking forward to calibrating future spaceborne and airborne SAR sensors.

References

[1] M. Zink, F. Heel, and H. Kietzmann, "The Oberpfaffenhofen SAR Calibration Experiment of 1989," *to be published in Journal of Electromagnetic Waves and Applications.*

[2] M. Zink, "Cross-Calibration Between Airborne SAR Sensors," *DLR-Forschungsbericht 91-10*, 1991.

[3] J. J. van Zyl, H. A. Zebker, and C. Elachi, "Imaging Radar Polarization Signatures: Theory and Observation," *Radio Science*, Vol. 22, No. 4, July 1987, pp. 529-543.

[4] M. Borgeaud, R. T. Shin, and J. A. Kong, "Theoretical models for polarimetric radar clutter," *Journal of Electromagnetic Waves and Applications*, Vol. 1, No. 1, 1987, pp. 73-89.

[5] H. Blötscher, H. Kietzmann, and P. Seifert, "Internal X-SAR Calibration," presented at *CEOS SAR Calibration Workshop*, (Frascati, Italy), Sept. 1989.

[6] F. Heel, H. Kietzmann, J. Nithack, and M. Reich, "X-SAR/SIR-C Radiometric Calibration Experiments," Accepted X-SAR/SIR-C Experiment Proposal, Oberpfaffenhofen, DFVLR, 1987.

[7] A. Freeman, J. C. Curlander, P. Dubois, and J. D. Klein, "Shuttle Imaging Radar-C Calibration Workshop Report," *JPL Technical Report 88-003*, (Pasadena CA, USA), Nov. 1988.

[8] J. J. van Zyl, "Calibration of Polarimetric Radar Images Using Only Image Parameters and Trihedral Corner Reflector Responses," *IEEE Trans. on Geoscience and Remote Sensing*, Vol. 28, No. 3, May 1990, pp. 337-348.

	Track 1	Track 2	Track 3	Track 5	Source
	30^o	45^o	55^o	45^o	
HH/VV ampl. [dB]	-0.4 (±0.7)	0.5 (±0.7)	0.01 (±0.7)	0.3 (±0.6)	Trihedrals
	-0.2	0.0	0.3	0.3	45^o PARC
	-1.1	0.4	0.4	-	0^o Dihedral
HH/VV phase [deg]	150.0 (±3.4)	145.5 (±2.4)	143.3 (±4.0)	140.8 (±2.7)	Trihedrals
	-25.8	-34.4	-37.1	-43.6	45^o PARC
	-32.5	-35.4	-39.7	-	0^o Dihedral
	139.1	130.1	124.3	129.8	Clutter
HV/HH ampl. [dB]	-24.8 (±3.8)	-25.9 (±2.6)	-20.4 (±0.8)	-27.5 (±2.6)	Trihedrals
VH/HH ampl. [dB]	-24.1 (±4.7)	-25.4 (±2.8)	-19.7 (±0.9)	-27.5 (±2.5)	Trihedrals
HV/VH ampl. [dB]	-3.3	-1.8	-1.9	0.4	45^o PARC
	-0.1	-0.3	0.0	-0.5	45^o Dihedral
	0.4	0.5	0.8	0.5	Clutter
HV/VH phase [deg]	-147.9	-145.0	-145.4	-138.6	45^o PARC
	27.0	28.9	32.6	31.5	45^o Dihedral
	25.5	28.5	32.5	32.7	Clutter

Table 1: Polarimetric parameters derived from uncalibrated data.

	α	$\mathcal{T}$	$\mathcal{R}$
	[dB]	[dB] ∠ [deg]	[dB] ∠ [deg]
Track 1	5.1 ± 0.8	$\begin{pmatrix} 0.0 \angle 0.0 & -11.7 \angle -136.6 \\ -9.8 \angle 163.2 & 0.2 \angle -88.2 \end{pmatrix}$	$\begin{pmatrix} 0.0 \angle 0.0 & -12.1 \angle -94.6 \\ -9.6 \angle 163.0 & 0.1 \angle -61.9 \end{pmatrix}$
Track 2	5.7 ± 0.7	$\begin{pmatrix} 0.0 \angle 0.0 & -11.1 \angle -116.7 \\ -14.7 \angle 122.0 & 0.0 \angle -87.3 \end{pmatrix}$	$\begin{pmatrix} 0.0 \angle 0.0 & -11.6 \angle -86.2 \\ -14.7 \angle 124.1 & -0.1 \angle -58.0 \end{pmatrix}$
Track 3	5.9 ± 0.9	$\begin{pmatrix} 0.0 \angle 0.0 & -10.7 \angle -123.1 \\ -17.8 \angle -62.6 & 0.2 \angle -86.9 \end{pmatrix}$	$\begin{pmatrix} 0.0 \angle 0.0 & -10.8 \angle -83.8 \\ -17.8 \angle -70.0 & -0.1 \angle -54.9 \end{pmatrix}$

Table 2: Absolute calibration factors, transmitter and receiver distortion matrices from data of tracks 1, 2 and 3.

	Track 1	Track 2	Track 3	Track 5	Source
	30°	45°	55°	45°	
HH/VV ampl. [dB]	-0.1 (±0.8) -0.4 -0.5	0.4 (±0.7) -0.1 -0.6	0.2 (±0.7) 0.4 0.5	0.2 (±0.6) 0.3 -	Trihedrals 45° PARC 0° Dihedral
HH/VV phase [deg]	0.07 (±3.4) -176.7 -177.3 -4.5	0.0 (±2.4) 180.0 179.9 -2.8	1.2 (±4.0) -179.0 -179.1 -5.2	-4.8 (±2.5) 170.9 - 0.8	Trihedrals 45° PARC 0° Dihedral Clutter
HV/HH ampl. [dB]	-28.1 (±4.0)	-32.2 (±4.1)	-34.5 (±4.7)	-32.6 (±2.5)	Trihedrals
VH/HH ampl. [dB]	-28.1 (±3.6)	-31.1 (±4.3)	-33.4 (±3.3)	-31.8 (±3.6)	Trihedrals
HV/VH ampl. [dB]	-0.6 0.0 0.6	-0.1 0.0 0.8	-0.3 0.9 1.2	2.1 -0.3 0.8	45° PARC 45° Dihedral Clutter
HV/VH phase [deg]	177.3 -0.6 -0.5	178.3 -0.5 -0.3	179.2 0.6 0.9	-175.6 3.4 3.8	45° PARC 45° Dihedral Clutter

Table 3: Polarimetric parameters derived from calibrated data.

	DC-8				E-SAR		theor.
σ [dBm^2]	HH		VV		VV		
Trihedral (1.0m)	32.5		32.0		30.7		31.2
Trihedral (0.9m)	29.3±0.5		29.2±0.4		29.2±1.3		29.3
45^o PARC	51.0		51.2		52.4		52.0
	σ^o [dB]	s/μ	σ^o [dB]	s/μ	σ^o [dB]	s/μ	
Runway	-19.5	1.31	-18.5	1.22	-17.6	0.52	
Grass	-13.4	1.05	-14.3	1.08	-12.8	0.56	
Field	-9.2	1.00	-11.4	0.98	-10.5	0.64	
Forest	-9.8	1.24	-8.9	1.15	-5.5	0.83	
Urban	3.2	4.75	-0.5	5.27	0.0	6.26	

Table 4: Radiometric comparison of calibrated DC-8 and E-SAR data from Track 2.

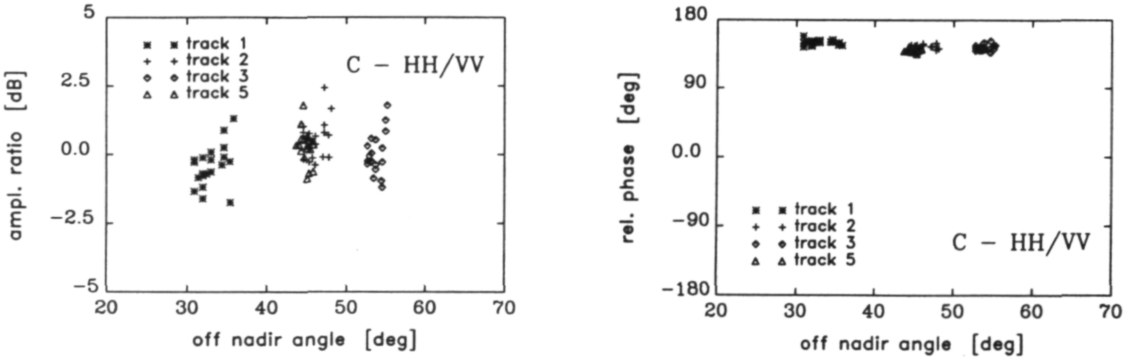

Figure 1: Trihedral corner reflector channel imbalance, uncalibrated HH/VV amplitude ratio and phase difference.

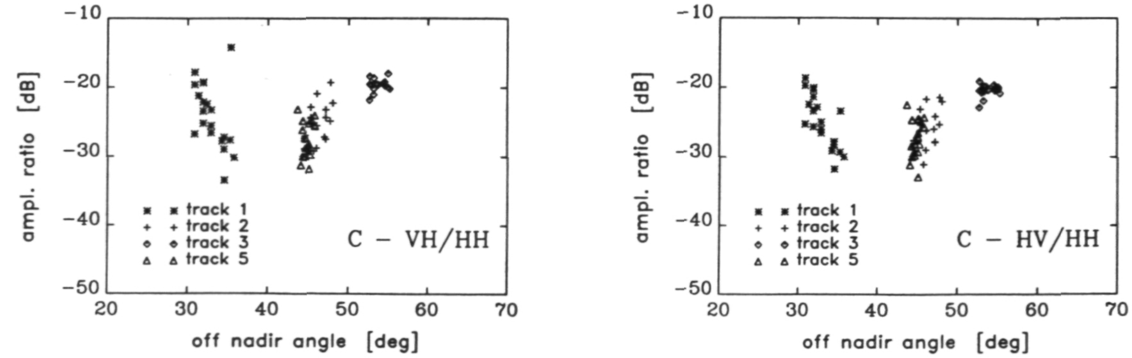

Figure 2: Trihedral corner reflector cross-talk, uncalibrated HV/HH and VH/HH amplitude ratio.

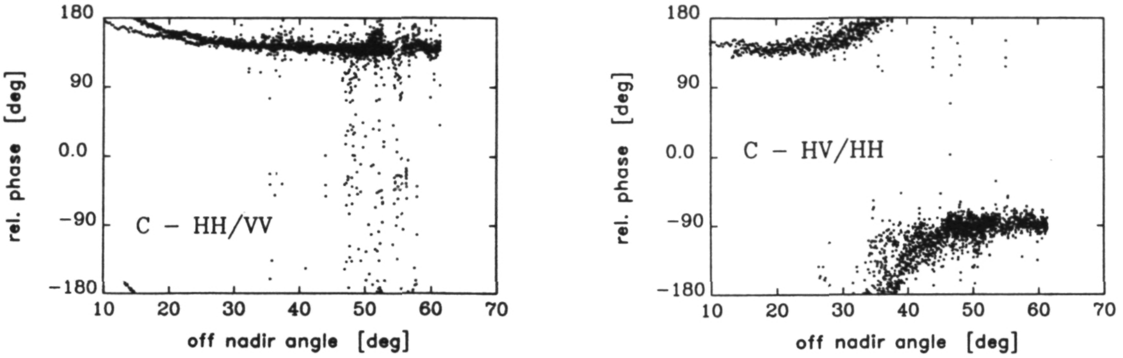

Figure 3: Image background, uncalibrated HH/VV and HV/HH phase difference.

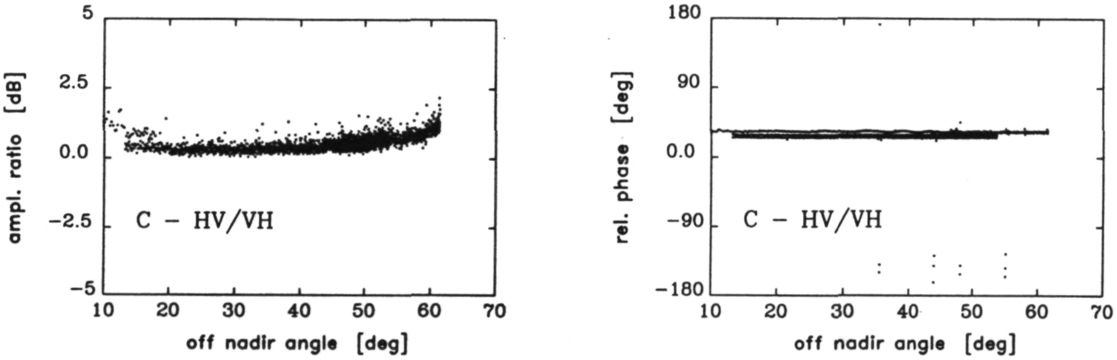

Figure 4: Image background, uncalibrated HV/VH amplitude ratio and phase difference.

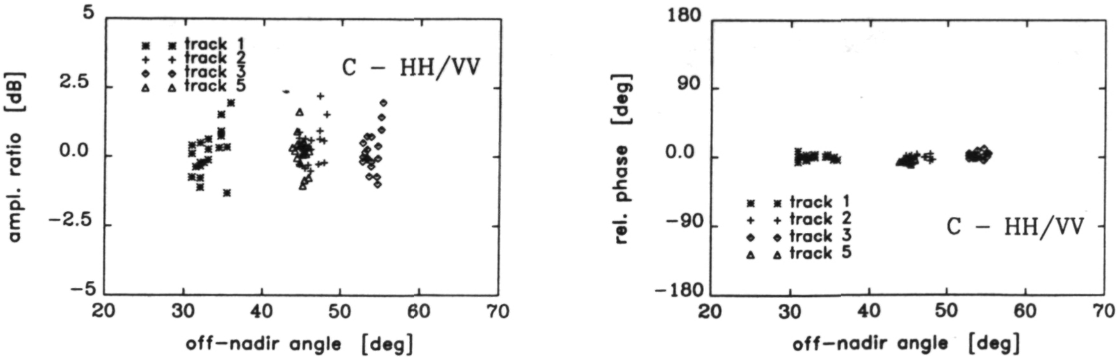

Figure 5: Trihedral corner reflector channel imbalance, calibrated HH/VV amplitude ratio and phase difference.

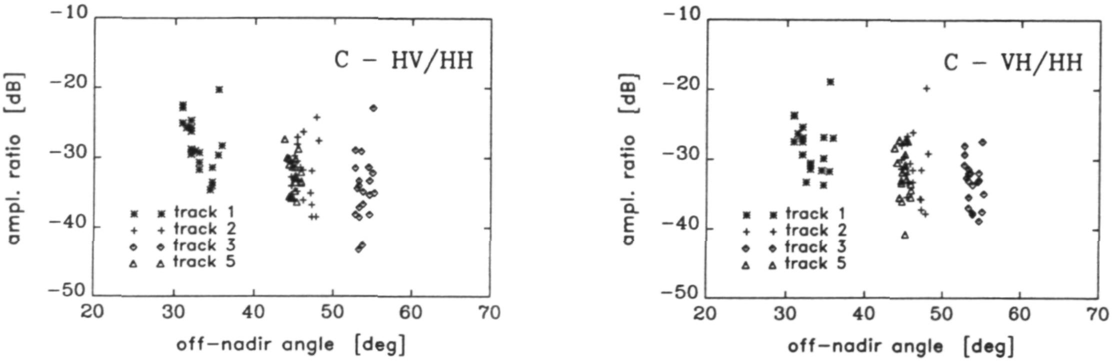

Figure 6: Trihedral corner reflector cross-talk, calibrated HV/HH and VH/HH amplitude ratio.

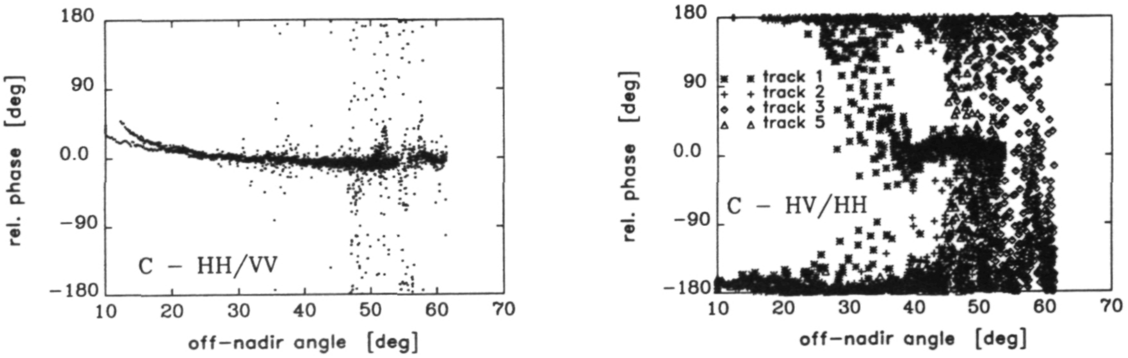

Figure 7: Image background, calibrated HH/VV and HV/HH phase difference.

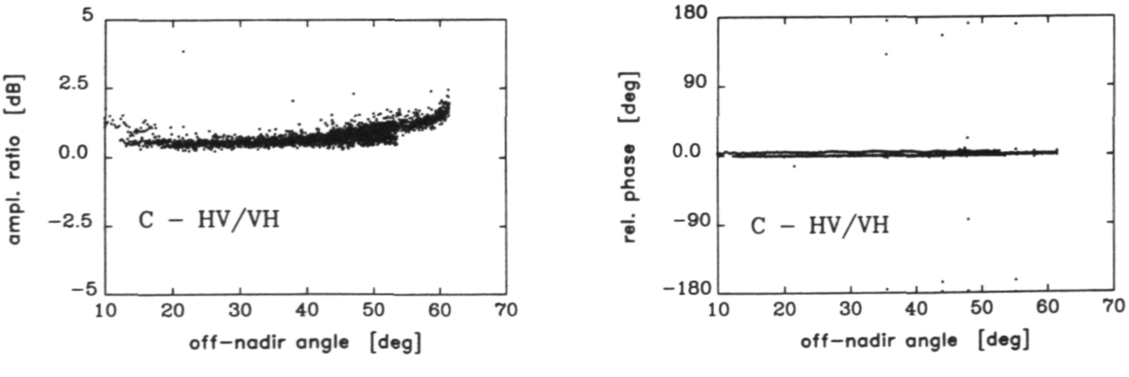

Figure 8: Image background, calibrated HV/VH amplitude ratio and phase difference.

N92-28031

EXTERNAL CALIBRATION OF POLARIMETRIC RADARS USING POINT AND DISTRIBUTED TARGETS

S. H. Yueh, J. A. Kong, and R. T. Shin

Department of Electrical Engineering and Computer Science
and Research Laboratory of Electronics
Massachusetts Institute of Technology
Cambridge, Massachusetts

ABSTRACT. Polarimetric calibration algorithms using combinations of point targets and reciprocal distributed targets are developed. From the reciprocity relations of distributed targets, an equivalent point target response is derived. Then the problem of polarimetric calibration using two point targets and one distributed target reduces to that using three point targets, which has been solved before. For calibration using one point target and one reciprocal distributed target, two cases are analyzed with the point target being a trihedral reflector or a polarimetric active radar calibrator (PARC). For both cases, the general solutions of the system distortion matrices are written as a product of a particular solution and a matrix with one free parameter. For the trihedral-reflector case, this free parameter is determined by assuming azimuthal symmetry for the distributed target. For the PARC case, knowledge of one ratio of two covariance matrix elements of the distributed target is required to solve for the free parameter. Numerical results are simulated to demonstrate the usefulness of the algorithms developed in this paper.

I. Introduction

In this paper the measured scattering matrix corresponding to a target with scattering matrix S is assumed to be [1]

$$X = cRST \tag{1}$$

The matrices T and R account for the channel imbalance and cross-polarization coupling of the transmitting and receiving ports, respectively. Propagation delay and loss between the radar and the target is accounted for by parameter c. The objective of polarimetric calibration is to solve for the R and T matrices using responses from targets with known polarization scattering parameters.

For general polarimetric systems, six parameters need to be estimated for relative polarimetric calibration: three for each of the transmitting and receiving ports including one for channel imbalance and two for cross-talk. To calibrate a general polarimetric system, algorithms using three point targets (in-scene reflectors) have been developed in [1-5] and a calibration algorithm using one distributed target and two point targets was presented in [6,7].

For polarimetric radars with a specific form, the number of calibration targets can be reduced. For example, a commonly adopted model is the reciprocal radar (R being the transpose of T). In this case, a calibration technique using natural distributed targets with azimuthal symmetry and trihedral corner reflectors was developed [8].

In this paper, we will investigate algorithms for calibrating a general polarimetric system using combinations of point and distributed targets.

II. Equivalent Point Target Response Using Reciprocity

In this section, we derive an equivalent point target from the response of reciprocal distributed targets, utilizing the model of polarimetric radars defined by Equation (1). Let us define a mapping between the scattering matrix X and a column vector $\mathcal{X}$ as

$$X = \begin{bmatrix} X_{11} & X_{12} \\ X_{21} & X_{22} \end{bmatrix} \longleftrightarrow \mathcal{X} = [\,X_{11} \quad X_{12} \quad X_{21} \quad X_{22}\,]^t \tag{2}$$

where the superscript t signifies transpose. Likewise, we can map the matrix S into the column vector $\mathcal{S}$. Thereafter, Equation (1) can be converted into a matrix equation

$$\mathcal{X} = A\mathcal{S} \tag{3}$$

where A is the direct product of R and T^t

$$A = R \otimes T^t \tag{4}$$

For the case that S is the response from a distributed target, it is more appropriate to describe the distributed target by its covariance matrix, C_s. From Equation (3), the measured covariance matrices C_x of $\mathcal{X}$ is related to C_s by

$$C_x = AC_sA^+ \tag{5}$$

where '+' signifies conjugate transpose.

By assuming the distributed target is reciprocal ($S_{12} = S_{21}$) and its covariance matrix C_s has rank 3, Klein and Freeman [6,7] derived the following equation

$$\mathcal{Q}_x = c' A^{+^{-1}} \mathcal{Q}_s \tag{6}$$

where $\mathcal{Q}_x$ and $\mathcal{Q}_s$ are, respectively, the eigenvectors of C_x and C_s with zero eigenvalue. In addition, $S_{12} = S_{21}$ means that columns 2 and 3 of C_s are equal. Hence,

$$\mathcal{Q}_s = [0 \quad -1 \quad 1 \quad 0]^t \tag{7}$$

Note that c' is an appropriate scaling constant, taking into account the arbitrary absolute magnitudes of eigenvectors.

Equation (6) is an important observation made by Klein and Freeman [6,7] using the reciprocity relations satisfied by the distributed targets. Subsequently, they carried out the matrix inversion and multiplication in Equation (6) and obtained three nonlinear equations for matrix elements of R and T [Ref. 6, Eqs. (19)-(21)]. Further supplementing these three equations with the response from two point targets, they solved for the normalized matrix elements of R and T explicitly.

A. Equivalent Point Target Response

In this paper, we recast Equation (6) into another form to allow for a general application. After realizing that the mapping from Equation (1) to Equation (3) is one to one in nature, we can convert Equation (6) into the following form

$$Q_x^{+^{-1}} = \frac{1}{c'^*} R Q_s^{+^{-1}} T \tag{8}$$

where Q_s and Q_x are 2 by 2 matrices corresponding to vectors $\mathcal{Q}_s$ and $\mathcal{Q}_x$, respectively, through the mapping defined by Equation (2). '$*$' denotes complex conjugate. Comparing Equation (8) with Equation (1), we can identify that $Q_x^{+^{-1}}$ is the response from a point target with scattering matrix $Q_s^{+^{-1}}$.

B. Reciprocation of Polarimetric Radar

As we know that a polarimetric radar is in general not reciprocal ($R \neq T^t$), therefore the measured scattering matrix X is not symmetric when S is symmetric. As to be shown in the following, Equation (8) can be utilized to symmetrize the measured scattering matrix.

From Equation (8), it can be shown that

$$T = R^t \left(Q_x^+ Q_s^t \right)^{-1} \tag{9}$$

For convenience, all the proportional constants like c' will not be written out explicitly from now on. Then substituting Equations (9) into (1), it is easy to show that

$$Y \overset{\text{def}}{=} X Q_x^+ Q_s^t = R S R^t \tag{10}$$

Note that if S is symmetric, so is Y. After comparing Equations (10) with (1), we can readily interpret Y as the response observed by a reciprocal polarimetric radar with T being the transpose of R.

If X is the backscatter from a reciprocal distributed target, then we can derive from C_x a reciprocated covariance matrix C_y of Y which is given by

$$C_y = A_y C_x A_y^+ \tag{11}$$

where

$$A_y = I \otimes \left(Q_s Q_x^* \right) \tag{12}$$

The results of this section show that the target reciprocity can be utilized to derive an equivalent target response and makes a polarimetric radar reciprocal.

III. Calibration Using Two Point Targets and One Reciprocal Distributed Target

This section discusses how to use two general point targets and one reciprocal distributed target for polarimetric calibration. Note that a general class of problems where these two point targets are two reciprocal reflectors have been solved explicitly by Klein and Freeman and verified with the Jet Propulsion Laboratory polarimetric sensors [7]. Here, we will show how the equivalent target can be used to solve the problem.

As shown in the previous section, we obtain an equivalent target from the reciprocity. Hence, by combining this equivalent target with another two point targets, the problem of calibration using two point targets and one distributed target is converted to that using three point targets, which has already been solved [3].

IV. One Trihedral Reflector and One Reciprocal Distributed Target

This section discusses how to calibrate a polarimetric radar using the responses from a trihedral reflector and one distributed target. Note that van Zyl [8] has already provided a scheme for calibrating a reciprocal polarimetric radar ($T = R^t$) using one trihedral reflector and one distributed target with azimuthal symmetry. Also in the previous section we have shown that a general polarimetric radar ($R \neq T^t$) can be made symmetric by using the reciprocity, indicating that van Zyl's approach can be directly applied. However, we will take a different approach in solving the problem so that partial calibration can be carried out without assuming the azimuthal symmetry for distributed targets.

Suppose that the measured response from a trihedral is given by

$$X_c = RT \tag{13}$$

Hence,

$$Y_c = X_c Q_x^+ Q_s^t = R R^t \tag{14}$$

and T can be expressed as

$$T = R^{-1}X_c \tag{15}$$

The general solution of R can be written as the product of a particular solution R_p and a matrix M

$$R = R_p M^{-1} \tag{16}$$

where the particular solution R_p has the following form:

$$R_p = \begin{bmatrix} R_{p11} & 0 \\ R_{p21} & R_{p22} \end{bmatrix} \tag{17}$$

and

$$M = \begin{bmatrix} \cos\theta & \sin\theta \\ -\sin\theta & \cos\theta \end{bmatrix} \tag{18}$$

Note that θ is allowed to be complex. After substituting Equation (16) into Equation (14), we can solve for the following quantities from the resulting equation

$$\frac{R_{p21}}{R_{p11}} = \frac{Y_{c12}}{Y_{c11}} = \frac{Y_{c21}}{Y_{c11}} \tag{19a}$$

$$\frac{R_{p22}}{R_{p11}} = \pm\sqrt{\frac{Y_{c22}}{Y_{c11}} - \left(\frac{R_{p21}}{R_{p11}}\right)^2} \tag{19b}$$

Then from Equation (15), we obtain the particular solution of T_p ($= R_p^{-1}X_c$) and the general solution of T ($= MT_p$). Hence, the general forms of R and T have been deduced and only one parameter α ($= \tan\theta$) remains to be determined. In the following, we assume the azimuthal symmetry for the distributed target to determine α. Azimuthal symmetry of the distributed target implies that

$$C_{s12} = C_{s13} = C_{s24} = C_{s34} = 0 \tag{20}$$

By substituting the general form of R and T into Equation (1), it can be shown that

$$X_p = R_p^{-1} X T_p^{-1} = M^{-1} S M \tag{21}$$

Note that $M^{-1} = M^t$. Therefore, matrix X_p is symmetric.

Representing X_p by a vector $\mathcal{X}_p$ according to Equation (2), we can define the covariance matrix $C_p = E[\mathcal{X}_p \mathcal{X}_p^+]$ which is related to C_x and C_s by

$$C_p = A_p C_x A_p^+ \tag{22a}$$

$$= A_m C_s A_m^+ \tag{22b}$$

where

$$A_p = R_p^{-1} \otimes T_p^{-1^t} \tag{23a}$$

$$A_m = M^{-1} \otimes M^t \tag{23b}$$

Multiplying both sides of Equation (21) by M, then calculating the ensemble average of the products of matrix elements, and using the fact that $C_{p12} = C_{p13}$ and $C_{p34} = C_{p24}$, we obtain the following equations for α

$$\alpha(C_{p32} + C_{s22} - C_{p22} - C_{s32}) + \alpha^*(C_{p14} - C_{s11} + C_{p44} - C_{s41}) = -(C_{p12} + C_{p42}) \tag{24}$$

$$\alpha(C_{p33}+C_{s23}-C_{p23}-C_{s33})+\alpha^*(-C_{p11}+C_{s14}-C_{p41}+C_{s44})=-(C_{p13}+C_{p43}) \quad (25)$$

Note that α can be obtained by utilizing the solution of the following equation

$$a\alpha + b\alpha^* = c \quad (26)$$

which has the following solution

$$\alpha = \frac{ca^* - c^*b}{|a|^2-|b|^2}, \quad \text{provided } |a| \neq |b|. \quad (27)$$

The criterion $|a| \neq |b|$ can be satisfied for a large class of distributed targets as observed from Equations (24) and (25).

If we start with a polarimetric radar having good channel isolation (small α), we can use the following iterative scheme to determine the value of α:

Step 1. Initialize α as zero.

Step 2. Evaluate A_m from Equation (23b) with the current value of α and calculate $C'_s = A_m^{-1} C_p A_m^{-1+}$ from Equation (22b) as the current estimate of C_s.

Step 3. Solve α from either Equations (24) or (25) by using the current value of C'_s.

Step 4. Repeat Steps 2 and 3 until C'_{s12}, C'_{s13}, C'_{s24}, and C'_{s34} are smaller than a selected threshold, which in our case is set to be 10^{-6} times C'_{s11}.

Once α is solved, the solution for R and T is complete except for their absolute magnitudes.

V. One Polarimetric Active Radar Calibrator and One Reciprocal Distributed Target

This section discusses how to use a PARC and a distributed target for calibration. Suppose that there is a PARC with the following scattering matrix [2],

$$S_c = \begin{bmatrix} 0 & 1 \\ 0 & 0 \end{bmatrix} \quad (28)$$

Subsequently, substituting Equation (28) into (10) results in a equation for the transformed scattering matrix Y_c. Then it is straightforward to show that the general solution of R has the following form

$$R = R_\mu M_\mu^{-1} \quad (29)$$

where the particular solution R_μ is

$$R_\mu = R_{11} \begin{bmatrix} 1 & Y_{c11}/Y_{c12} \\ Y_{c22}/Y_{c12} & 1 \end{bmatrix} \quad (30)$$

and

$$M_\mu = \begin{bmatrix} 1 & 0 \\ 0 & 1/\beta \end{bmatrix}. \quad (31)$$

Here β is a free parameter. In addition, the particular solution of T is obtained from Equation (8) and is given by

$$T_\mu = Q_s^t R_\mu^{-1} Q_x^{-1+} \quad (32)$$

It can be shown that the general solution of T can be written as

$$T = \frac{1}{\beta} M_\mu^{-1} T_\mu \quad (33)$$

Substituting Equations (29) and (33) into Equation (1) results in

$$M_\mu^{-1} S M_\mu^{-1} = R_\mu^{-1} X T_\mu^{-1} \tag{34}$$

Let $X_\mu = R_\mu^{-1} X T_\mu^{-1}$ and vectorize it as $\mathcal{X}_\mu$ by Equation (2). We can relate the covariance matrix $C_\mu = E[\mathcal{X}_\mu \mathcal{X}_\mu^+]$ to C_x by

$$C_\mu = A_\mu C_x A_\mu^+ \tag{35}$$

where

$$A_\mu = R_\mu^{-1} \otimes T_\mu^{-1^t} \tag{36}$$

Multiplying X_μ by R_μ from the left-hand side of (34) and carrying out the ensemble average of products of matrix elements, we can obtain the following equations

$$\beta = \left(\frac{C_{s11}}{C_{s12}}\frac{C_{\mu12}}{C_{\mu11}}\right)^* = \left(\frac{C_{s11}}{C_{s13}}\frac{C_{\mu13}}{C_{\mu11}}\right)^* \tag{37a}$$

$$= \frac{C_{s12}}{C_{s22}}\frac{C_{\mu22}}{C_{\mu12}} = \frac{C_{s13}}{C_{s23}}\frac{C_{\mu23}}{C_{\mu13}} \tag{37b}$$

$$= \left(\frac{C_{s22}}{C_{s24}}\frac{C_{\mu24}}{C_{\mu22}}\right)^* = \left(\frac{C_{s23}}{C_{s34}}\frac{C_{\mu34}}{C_{\mu23}}\right)^* \tag{37c}$$

and

$$\beta = \pm\sqrt{\left(\frac{C_{s11}}{C_{s14}}\frac{C_{\mu14}}{C_{\mu11}}\right)^*} = \pm\sqrt{\frac{C_{s14}}{C_{s44}}\frac{C_{\mu44}}{C_{\mu14}}} \tag{38}$$

Here we can see that in order to solve the parameter β, it is necessary to know one of the ratios of matrix elements of C_s beforehand. Also notice that Equation (37) is not applicable to distributed targets with azimuthal symmetry which will result in the case of zero divided by zero.

VI. Numerical Simulation and Discussion

In this section numerical simulation of algorithms discussed in the previous two sections will be presented. The polarization transfer matrices of the polarimetric radar are assumed to be

$$R = \begin{bmatrix} 1 & 0.0426\angle -169.5^\circ \\ 0.0532\angle 113.6^\circ & 1.0638\angle -86.3^\circ \end{bmatrix} \tag{39}$$

$$T = \begin{bmatrix} 1 & 0.1042\angle -77.8^\circ \\ 0.0625\angle 30^\circ & 1.0417\angle -57.9^\circ \end{bmatrix} \tag{40}$$

This set of system matrices corresponds to the distortion matrices of the Jet Propulsion Laboratory L-band radar estimated by a three-point-target approach [9]. Note that the cross-talk errors are smaller than −20 dB and the channel imbalances are around 0.5 dB. The most severe errors are the differences in phases between channels, which will significantly distort the co-polarization signature [10] of trihedral reflectors and make it look like that of a dihedral reflector.

In this paper, we denote channels 1 and 2 as horizontal (h) and vertical (v) polarizations, respectively. Therefore, the parameters of a covariance matrix C_s are defined as

$$C_s = \sigma_{hh} \begin{bmatrix} 1 & \sqrt{\epsilon_{hv}}\rho_{hhhv} & \sqrt{\epsilon_{vh}}\rho_{hhvh} & \sqrt{\gamma}\rho_{hhvv} \\ \sqrt{\epsilon_{hv}}\rho^*_{hhhv} & \epsilon_{hv} & \sqrt{\epsilon_{hv}\epsilon_{vh}}\rho_{hvvh} & \sqrt{\epsilon_{hv}\gamma}\rho_{hvvv} \\ \sqrt{\epsilon_{vh}}\rho^*_{hhvh} & \sqrt{\epsilon_{hv}\epsilon_{vh}}\rho^*_{hvvh} & \epsilon_{vh} & \sqrt{\epsilon_{vh}\gamma}\rho_{vhvv} \\ \sqrt{\gamma}\rho^*_{hhvv} & \sqrt{\epsilon_{hv}\gamma}\rho^*_{hvvv} & \sqrt{\epsilon_{vh}\gamma}\rho^*_{vhvv} & \gamma \end{bmatrix} \tag{41}$$

Here, $\rho_{\alpha\beta\gamma\delta}$ represents the correlation coefficient of '$\alpha\beta$' and '$\gamma\delta$' polarizations. For distributed targets with azimuthal symmetry, $\rho_{hhhv} = \rho_{hhvh} = \rho_{hvvv} = \rho_{vhvv} = 0$.

Listed in column 1, Table 1 are the covariance parameters of the distributed target to be used for the simulation of calibration algorithms, and its co-polarization signature is shown in Figure 1(a). Due to the channel imbalance and cross-talk for the radar defined by Equations (39) and (40), the observed co-polarization signature would be that shown in Figure 1(b). After the reciprocity is applied, the co-polarization signature corresponding to the reciprocated covariance matrix C_y is illustrated in Figure 1(c), which becomes symmetric with respect to the 90-degree orientation angle.

A. One Trihedral Reflector and One Reciprocal Distributed Target

Considered below is the trihedral-reflector approach (see Section III). Two solutions were obtained. One produces the correct R and T and the other is related to the correct one by

$$R' = R \begin{bmatrix} 1 & 0 \\ 0 & -1 \end{bmatrix}, \quad T' = \begin{bmatrix} 1 & 0 \\ 0 & -1 \end{bmatrix} T. \tag{42}$$

Using these two solutions to calibrate the radar, the calibrated covariance parameters of the distributed target are the same as those given in column 2 of Table 1. This is due to the fact the sign difference does not affect the responses from trihedral reflectors and azimuthally symmetric distributed targets.

Particular solutions for the case considered are given by

$$R_{p1} = \begin{bmatrix} 1 & 0 \\ 0.098\angle 109.24^\circ & 1.06\angle -86.40^\circ \end{bmatrix}, \quad T_{p1} = \begin{bmatrix} 1 & 0.0698\angle -96.51^\circ \\ 0.1038\angle 22.21^\circ & 1.0482\angle -57.84^\circ \end{bmatrix}$$

and

$$R_{p2} = \begin{bmatrix} 1 & 0 \\ 0.098\angle 109.24^\circ & 1.06\angle 93.6^\circ \end{bmatrix}, \quad T_{p2} = \begin{bmatrix} 1 & 0.0698\angle -96.51^\circ \\ 0.1038\angle -157.79^\circ & 1.0482\angle 122.16^\circ \end{bmatrix}$$

Note that the first solution is very close to the correct system parameters, in particular, the channel imbalance. If the system is calibrated by the particular solution, the calibrated distributed target parameters are given in columns 4 and 5 of Table 1, and the corresponding polarization signatures are shown in Figures 1(d) and 1(e), respectively, which are not visibly distinguishable from the correct signature shown in Figure 1(a).

B. One Polarimetric Active Radar Calibrator and One Reciprocal Distributed Target

The PARC approach outlined in Section IV is considered next. The particular solution is given by

$$R_\mu = \begin{bmatrix} 1 & 0.400\angle -83.2^\circ \\ 0.0532\angle 113.6^\circ & 1.0 \end{bmatrix}, \quad T_\mu = \begin{bmatrix} 1 & 0.1042\angle -77.8^\circ \\ 0.0588\angle 116.3^\circ & 0.9792\angle 28.4^\circ \end{bmatrix}$$

We can see that $R_{\mu 21}$ and $T_{\mu 12}$ match correctly with R_{21} and T_{12} [see (29) and (33)]. Calibration by the particular solution alone yields the parameters of C_μ which are shown in Table 2. Note that all the correlation coefficients are well calibrated except the phase of ρ_{hhvv}. Hence, if we have a system with an ideal phase balance between h and v channels, then all the correlation coefficients can be well calibrated by the particular solution, R_μ and T_μ.

Further assuming that two of the distributed target parameters γ and ρ_{hhvv} are known, we can apply Equation (38) for the calculation of β and to obtain two solutions. One correctly produces the system parameters, whereas the other is related to it by Equation (42). By calibrating the system using these two solutions, the calibrated covariance matrix parameters are given in column 2, Table 2, which correctly match the original parameters. It should be noted that if correlation coefficients, ρ_{hhhv}, ρ_{hhvh}, ρ_{hvvv}, and ρ_{vhvv} are not zeros, then the correlation parameters after calibration by the wrong solution will carry an opposite sign.

C. Comparison of Trihedral Reflector and PARC Approaches

The results of the above two sub-sections indicate that when the particular solution is applied for calibration, the trihedral-reflector approach is quite robust in calibrating the channel imbalance and weak at detecting the cross-polarization couplings. In contrast, the PARC approach is poor at removing the channel imbalance and useful in estimating the cross-talk. In other words, the trihedral-reflector approach is useful when the system has relatively small cross-talk, and the PARC approach is useful when the system has good channel balance, if no further assumption about the distributed targets is made.

We should also note that the alignment of point target is less critical in the trihedral-reflector approach than the PARC approach, since the PARCs needs to be carefully oriented in order to avoid artificial cross-talks. However, the PARC approach can provide a larger signal to noise ratio than the trihedral-reflector approach.

REFERENCES

[1] R. M. Barnes, "Antenna Polarization Calibration Using In-scene Reflectors," Proceedings of the Tenth DARPA/Tri-Service Millimeter Wave Symposium, U. S. Army Harry Diamond Lab., Adelphi, MD, April 8-10, 1986.

[2] A. Freeman, Y. Shen, and C. Werner, "Polarimetric SAR Calibration Experiment Using Active Radar Calibrators," *IEEE Trans. Geosci. Remote Sensing,* Vol. 28, No. 2, pp. 224-240, 1990.

[3] S. H. Yueh, J. A. Kong, and R. T. Shin, "Calibration of Polarimetric Radars Using In-Scene Reflectors," *Progress In Electromagnetics Research*, Elsevier, New York, Vol. 3, Chapter 9, 1990.

[4] S. H. Yueh, J. A. Kong, R. M. Barnes, and R. T. Shin, "Calibration of Polarimetric Radars Using In-scene Reflectors," *J. Electromagnetic Waves and Appl.,* Vol. 4, No. 1, 27–49, 1990.

[5] M. W. Whitt and F. Ulaby, "A Polarimetric Radar Calibration Technique with Insensitivity to Target Orientation," *Radio Science,* Vol. 25, No. 6, pp. 1137-1143, 1990.

[6] J. D. Klein, "Polarimetric SAR Calibration Using Two Targets and Reciprocity," *Proc. IGRASS '90 Symposium*, pp. 1105-1108, Washington, D.C., May 20-24, 1990.

[7] J. D. Klein and A. Freeman, "Quadpolarization SAR Calibration Using Target Reciprocity," *J. Electromagnetic Waves and Appl.*, in press, 1991.

[8] J. J. van Zyl, "Calibration of Polarimetric Radar Images Using Only Image Parameters and Trihedral Corner Reflectors Responses," *IEEE Trans. Geoscience and Remote Sensing,* Vol. 28, No. 3, 337-348, 1990.

[9] M. Zink, F. Heel, and H. Kietzmann, "Airborne SAR Calibration," submitted for publication in *J. Electromagnetic Waves and Appl.,* 1990.

[10] J. J. van Zyl, H. A. Zebker and C. Elachi, "Imaging Radar Polarization Signature:

Theory and Observation," *Radio Science,* Vol. 22, No. 4, pp. 529-543, 1987.

Acknowledgments

This work was supported by the NASA Contract NAGW-1272, the ARMY Corp of Engineers Contract DACA39-87-K-0022, the NASA Grant NAG5-270, and the ONR Contract N00014-83-K-0258.

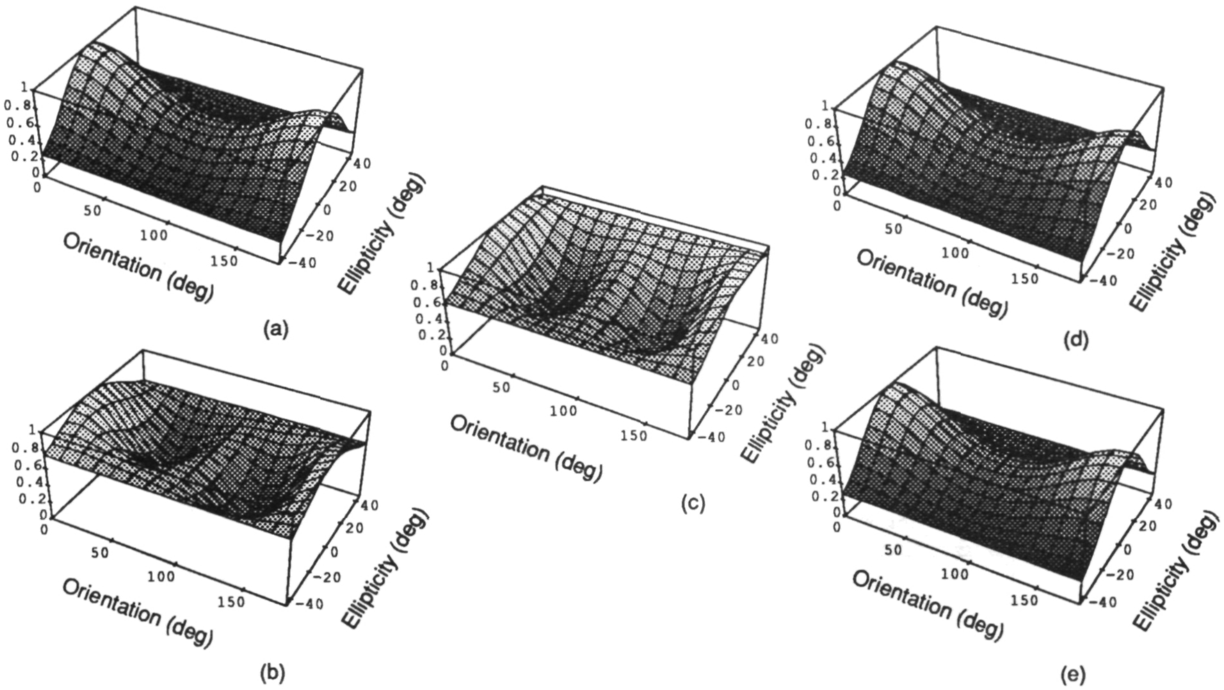

Figure 1. Co-polarization signatures of a distributed target with azimuthal symmetry: (a) original, (b) distorted (C_x), (c) reciprocated (C_y), (d) calibrated by the particular solution, R_{p1} and T_{p1}, and (e) calibrated by the particular solution, R_{p2} and T_{p2}.

Covariance Matrix Parameters	Original and Fully Calibrated	Observed (distorted)	Calibrated by R_{p1} and T_{p1}	Calibrated by R_{p2} and T_{p2}
ϵ_{hv}	0.1	0.1162	0.1006	0.1006
ϵ_{vh}	0.1	0.1150	0.1006	0.1006
γ	0.5	0.6104	0.5011	0.5011
ρ_{hhvv}	0.6	$0.594\angle 144^\circ$	$0.601\angle -0.044^\circ$	$0.601\angle -0.044^\circ$
ρ_{hhhv}	0	$0.266\angle 84.97^\circ$	$0.053\angle -20.9^\circ$	$0.053\angle 159.1^\circ$
ρ_{hhvh}	0	$0.074\angle -108.7^\circ$	$0.053\angle -20.9^\circ$	$0.053\angle 159.1^\circ$
ρ_{hvvh}	1	$0.93\angle 29.45^\circ$	1.0	1.0
ρ_{hvvv}	0	$0.116\angle 57.03^\circ$	$0.0251\angle -22.35^\circ$	$0.0251\angle 157.7^\circ$
ρ_{vhvv}	0	$0.08\angle 106.42^\circ$	$0.0251\angle -22.35^\circ$	$0.0251\angle 157.7^\circ$

Table 1. Original, observed, and calibrated covariance matrix parameters by using the responses from a trihedral reflector and azimuthal symmetric distributed targets.

Covariance Matrix Parameters	Original and Fully Calibrated	Observed (distorted)	Calibrated by R_μ and T_μ
ϵ_{hv}	0.1	0.1162	0.1132
ϵ_{vh}	0.1	0.1150	0.1132
γ	0.5	0.6104	0.6404
ρ_{hhvv}	0.6	$0.594\angle 144^\circ$	$0.6\angle 172.6^\circ$
ρ_{hhhv}	0	$0.266\angle 84.97^\circ$	0
ρ_{hhvh}	0	$0.074\angle -108.7^\circ$	0
ρ_{hvvh}	1	$0.93\angle 29.45^\circ$	1.0
ρ_{hvvv}	0	$0.116\angle 57.03^\circ$	0
ρ_{vhvv}	0	$0.08\angle 106.42^\circ$	0

Table 2. Original, observed, and calibrated covariance matrix parameters by using the responses from a PARC and azimuthal symmetric distributed targets with known γ and ρ_{hhvv}.

CALIBRATION OF A POLARIMETRIC IMAGING SAR

K. Sarabandi, L.E. Pierce, and F.T. Ulaby
Radiation Laboratory
Department of Electrical Engineering and Computer Science
The University of Michigan – Ann Arbor

Abstract

Calibration of polarimetric imaging SARs using point calibration targets is discussed. The four-port network calibration technique [5] is used to describe the radar error model. The polarimetric ambiguity function of the SAR is then found using a single point target, namely a trihedral corner reflector. Based on this, an estimate for the backscattering coefficient of the terrain is found by a deconvolution process.

A radar image taken by the JPL aircraft SAR is used for verification of the deconvolution calibration method. The calibrated responses of point targets in the image are compared both with theory and the POLCAL technique [8]. Also, responses of a distributed target are compared using the deconvolution and POLCAL techniques.

1 Introduction

Calibration techniques available in the literature can be categorized into two major groups: 1) calibration techniques for imaging radars, and 2) calibration techniques for point-target measurement systems, which may also be appropriate for imaging radars. In the first group, the scattering properties of clutter are usually employed to simplify the calibration problem such as in Sheen and Kasischke [1989], van Zyl [1990], and Klein [1989]. Among the point-target calibration techniques, are Whitt, et al. [1990], Barnes [1986], and Sarabandi, et al. [1990] which uses a sphere and any other depolarizing calibration target. However, the isolated antenna assumption can lead to significant errors when the ratio of cross- to like-polarized terms is small and/or cross-talk contamination is large. To remove this drawback, the single target calibration technique (STCT) has recently been developed [Sarabandi and Ulaby, 1990].

The main thrust of this paper is to show how the point target calibration techniques can be applied to imaging SARs. In particular, the STCT will be employed here since it only requires one calibration target. This method is then compared with the POLCAL technique [8] which has been developed specifically for imaging radars.

2 A New Approach for Calibration of Imaging SARs

In this new method the polarimetric ambiguity function of the SAR processor as well as the distortion matrices of the radar system are found from a trihedral corner reflector response. First a summary of the single target calibration technique (STCT) is given and then a theoretical model which relates the point target response to distributed targets will be developed. The model in conjunction with the STCT is then used to obtain a deconvolution matrix for estimation of the backscattering coefficient.

2.1 Single Target Calibration Technique

In this technique the antenna system and two orthogonal directions in free space are modeled as a four-port passive device. The measured scattering matrix of a target with real scattering matrix **s** is approximated by

$$\mathbf{U} = \begin{bmatrix} R_v & CR_v \\ CR_h & R_h \end{bmatrix} \mathbf{s} \begin{bmatrix} T_v & CT_h \\ CT_v & T_h \end{bmatrix}. \tag{1}$$

The complex quantities R_p, T_q are the receive and transmit channel distortions with $p, q = v, h$ and C is the antenna cross-talk factor. Once the distortion parameters of the radar system are found through the measurement of a trihedral corner reflector, $\mathbf{U}_t$, with radar cross section σ_t whose scattering matrix is diagonal, the actual scattering matrix of the target can be obtained from

$$\mathbf{s} = \frac{1}{R_v T_v (1+C^2)^2} \begin{bmatrix} 1 & -C\frac{R_v}{R_h} \\ -C & \frac{R_v}{R_h} \end{bmatrix} \mathbf{U} \begin{bmatrix} 1 & -C \\ -C\frac{T_v}{T_h} & \frac{T_v}{T_h} \end{bmatrix}. \tag{2}$$

with

$$C = \pm \frac{1}{\sqrt{a}} (1 - \sqrt{1-a}) \tag{3}$$

where the branch cut for $\sqrt{1-a}$ is chosen such that $\mathrm{Re}[\sqrt{1-a}] > 0$, and

$$a \triangleq \frac{u^t_{vh} u^t_{hv}}{u^t_{vv} u^t_{hh}}, \qquad R_v T_v = \frac{u^t_{vv}}{(1+C^2)\sqrt{\sigma_t/4\pi}}, \tag{4}$$

$$\frac{R_v}{R_h} = \frac{1+C^2}{2C} \cdot \frac{u^t_{vh}}{u^t_{hh}}, \qquad \frac{T_v}{T_h} = \frac{2C}{1+C^2} \cdot \frac{u^t_{vv}}{u^t_{vh}}. \tag{5}$$

The single target calibration technique (STCT) has been tested both under laboratory and field conditions using L-, C-, and X-band scatterometer systems and it has been shown that a calibration accuracy of 0.5 dB in amplitude and 5 degrees in phase can be achieved.

2.2 Difficulties in Calibration of SARs Using Point Targets

To understand the steps involved in calibration of imaging SARs using point calibration targets, the generation of a high resolution image from raw data must be examined. The received raw data in each of the channels of a polarimetric SAR can be described by

$$U_{pq}(t) = \int_A S^0_{pq}(x', y') \, f\left(t - \frac{2R}{c}\right) dx'dy' \quad p, q = v, h \tag{6}$$

where A is the illumination area by the physical antenna, $S^0_{pq}(x', y')$ is the reflectivity of the terrain being mapped ($\sigma^0_{pq}(x, y) = 4\pi \mid S^0_{pq}(x, y) \mid^2$), and p and q are the polarization state of the receiver and transmitter respectively. Function $f(t)$ is a particular wave form radiated by the transmitter and can usually be represented by

$$f(t) = g(t) \, e^{i\omega_0 t} \tag{7}$$

where $g(t)$ is a slowly varying function and ω_0 is the angular frequency of the radar system. In equation (6) R is the distance from the antenna to the scattering point (x', y') on the ground.

One way to retrieve the backscattering coefficient $\sigma^0_{pq}(x, y)$ from the received signal $U_{pq}(t)$ is to pass the signal through a matched filter having an impulse response $f^*\left(t - \frac{2R}{c}\right)$ [Cutiona, 1970], that is

$$U'_{pq}(x, y) = \int_t \int_A \sigma^0_{pq}(x', y')\, f\left(t - \frac{2R'}{c}\right) f^*\left(t - \frac{2R}{c}\right) dx'dy'dt \tag{8}$$

By performing the integration with respect to time, the quantity

$$\psi(x, y; x', y') = \int_t f\left(t - \frac{2R'}{c}\right) f^*\left(f - \frac{2R}{c}\right) dt \tag{9}$$

known as the ambiguity function can be obtained. Therefore (8) can be written as

$$U'_{pq}(x, y) = \int_A \sigma^0_{pq}(x', y')\, \psi(x, y; x', y')\, dx'dy' \,. \tag{10}$$

If the ambiguity function is a Dirac delta function, i.e. $\psi(x, y; x', y') = \delta(x - x', y - y')$, the backscattering coefficient can be directly obtained from (10).

By substituting (7) into (9) and assuming that $g(t)$ is a linearly frequency-modulated pulse of duration τ $\left(g(t) = e^{i\frac{\pi \Delta f}{\tau} t^2}\right)$ and that the integration time in (9) is over $N + 1$ pulses of the transmitter we have

$$\psi(x, y; x', y') = \sum_{-\frac{N}{2}}^{\frac{N}{2}} e^{-2iw_0(R-R')/c} \int_{-\tau/2}^{\tau/2} e^{i\frac{\pi \Delta f}{\tau}\left[\left(t - \frac{2R'}{c}\right)^2 - \left(t - \frac{2R}{c}\right)^2\right]} dt \tag{11}$$

Using (11) in (10) does not resolve $\sigma^0_{pq}(x, y)$ completely. To obtain a better estimate a deconvolution process must be attempted. This requires that the calibration technique be able to estimate the ambiguity function.

2.3 Calibration Procedure and Estimation of Backscattering Coefficient

The error model for a polarimetric SAR must include the uncertainties such as the antenna cross talk and channel imbalances as well as the uncertainties in the ambiguity function. Suppose the radar system is linear. The polarimetric response of the terrain with polarimetric reflectivity $\mathbf{S}^0(x, y)$ is given by

$$\mathbf{U}(x, y) = \mathbf{R}\left[\int_A \mathbf{S}^0(x', y')\, \psi(x, y; x', y') dx'dy'\right] \mathbf{T} \,. \tag{12}$$

In (12) the amplitude and phase of the propagation factor $\left(\frac{e^{2ik_0R}}{R^2}\right)$ has been excluded and $\mathbf{R}$ and $\mathbf{T}$ are, respectively, the receive and transmit distortion matrices. Assume

$\psi(x,y;x',y') = \psi(x-x',y-y')$. Since radar images are discretized into a finite number of pixels, the discretized form of (12) must be considered, where the integral is approximated by a double summation, thus

$$\mathbf{U}(m,n) = \mathbf{R}\left[\sum_i \sum_j \mathbf{S}^0(i,j)\psi(m-i,n-j)\,\Delta x \Delta y\right]\mathbf{T} \tag{13}$$

By changing the index of the summations such that the maximum of the ambiguity function occurs at $(0,0)$, and lumping together the ambiguity function and distortion matrices, equation (13) becomes

$$\mathbf{U}(m,n) = \Delta x \Delta y \sum_{i=\frac{-N}{2}}^{\frac{N}{2}} \sum_{j=\frac{-M}{2}}^{\frac{M}{2}} \mathbf{AR}_{ij}\; \mathbf{S}^0(m-i,n-j)\;\; \mathbf{AT}_{ij} \tag{14}$$

where $\mathbf{AR}_{ij}$ and $\mathbf{AT}_{ij}$ are the receive and transmit ambiguity-distortion matrices respectively.

If a trihedral with radar cross section σ_T located at (x_0, y_0) is used as a calibration target, its reflectivity function is expressed by

$$\mathbf{S}^0_T(x,y) = \sqrt{\frac{\sigma_T}{4\pi}}\;\; \mathbf{I}\;\; \delta(x-x_0)\,\delta(y-y_0) \tag{15}$$

where $\mathbf{I}$ is a 2×2 identity matrix. Substituting (15) into (12) results in the polarimetric response of the SAR to the trihedral. When the discretized form of this response is combined with the resultant ambiguity function and distortion matrices, the response becomes

$$\mathbf{U}_T(k+i,l+j) = \sqrt{\frac{\sigma_T}{4\pi}}\;\; \mathbf{AR}_{ij}\;\; \mathbf{I}\;\; \mathbf{AT}_{ij} \tag{16}$$

with

$$i \in \left\{-\frac{N}{2},\cdots,\frac{N}{2}\right\} \text{ and } j \in \left\{-\frac{M}{2},\cdots,\frac{M}{2}\right\},$$

where $i = m-k$ and $j = n-l$ for a trihedral at the klth pixel. Figure (1) shows the measured amplitude of the polarimetric response of the JPL aircraft SAR to an 8-foot trihedral.

An approximate form of (14) can be obtained by assuming that over the pixels where the ambiguity function is non-zero the reflectivity of the terrain is constant and is equal to that of the center pixel, giving

$$\mathbf{U}(m,n) = \Delta x \Delta y \sum_{i=\frac{-N}{2}}^{\frac{N}{2}} \sum_{j=\frac{-M}{2}}^{\frac{M}{2}} \mathbf{AR}_{ij}\; \hat{\mathbf{S}}^0(m,n)\; \mathbf{AT}_{ij} \tag{17}$$

If the four-vector form of $\mathbf{U}(m,n)$ and $\hat{\mathbf{S}}^0(m,n)$ are, respectively, denoted by

$$\boldsymbol{\mathcal{U}}(m,n) = \begin{bmatrix} U_{vv}(m,n) \\ U_{vh}(m,n) \\ U_{hv}(m,n) \\ U_{hh}(m,n) \end{bmatrix}, \quad \hat{\boldsymbol{\mathcal{S}}}^0(m,n) = \begin{bmatrix} \hat{S}^0_{vv}(m,n) \\ \hat{S}^0_{vh}(m,n) \\ \hat{S}^0_{hv}(m,n) \\ \hat{S}^0_{hh}(m,n) \end{bmatrix}$$

then (17) becomes

$$\mathcal{U}(m,n) = \left[\sum_{i=\frac{-N}{2}}^{\frac{N}{2}} \sum_{j=\frac{-M}{2}}^{\frac{M}{2}} \mathbf{D}_{ij} \right] \hat{\mathcal{S}}^{0}(m,n) \triangleq \mathbf{D}\hat{\mathcal{S}}^{0}(m,n) \ . \tag{18}$$

where $\mathbf{D}$ is the deconvolution matrix which is independent of pixel coordinates m and n. Therefore the calibrated estimate of the reflectivity matrix is given by

$$\hat{\mathcal{S}}^{0}(m,n) = \mathbf{D}^{-1}\,\mathcal{U}(m,n) \ .$$

3 JPL POLCAL Technique

POLCAL [van Zyl et al., 1990] is a combination of phase calibration by Zebker and Lou [1990] and a calibration algorithm by van Zyl [1990] based on properties of distributed targets. In this technique the radar error model and corrections are done in three steps. The first step is phase calibration where the radar distortion matrices are assumed to be diagonal with only phase differences. That is, the measured scattering matrix is assumed to be

$$\mathbf{U} = \begin{bmatrix} s_{vv} & s_{vh}e^{i\phi_r} \\ s_{hv}e^{i\phi_t} & s_{hh}e^{i(\phi_r+\phi_t)} \end{bmatrix} .$$

where s_{pq} are the theoretical values for the scattering matrix elements. Reciprocity mandates that $s_{hv} = s_{vh}$ and therefore the quantity $u_{hv}u_{vh}^{*}$ must have zero phase. The phase difference $\phi_t - \phi_r$ is averaged over the entire image, then subtracted from u_{hv}, to form a matrix $\mathbf{Z}$ whose off-diagonal elements have almost identical phases. Next this matrix is symmetrized by averaging the off-diagonal elements and then stored in the matrix $\mathbf{Y}$. The data is then coded and stored in the form of the Stokes scattering operator, with groups of four adjacent pixels in a row being summed. The quantity $\phi_r + \phi_t$ is obtained from a trihedral response by calculating $Y_{hh}Y_{vv}^{*}$.

The next steps include cross-talk removal and adjusting for co-channel gain balance. Here the radar error model of the phase calibrated symmetrized response ($\mathbf{Y}'$) is represented by reciprocal transmit and receive distortion matrices, i.e.

$$\mathbf{Y}' = A \begin{bmatrix} 1 & \delta_2 \\ \delta_1 & f \end{bmatrix} \mathbf{s} \begin{bmatrix} 1 & \delta_1 \\ \delta_2 & f \end{bmatrix} . \tag{19}$$

where $\mathbf{s}$ is the actual scattering matrix of the target, δ_1 and δ_2 represent the antenna cross-talk, and f is the co-channel imbalance. Using the above equations δ_1 and δ_2/f are found iteratively. The amplitude of the co-channel imbalance f is obtained by calculating the ratio of the total power of VV to HH of a corner reflector response over 16×16 surrounding pixels. However, it is left unjustified why the HH and VV responses should be added noncoherently.

4 Results and Comparison

This section presents the results of applying the three different calibration techniques described in sections 2.1, 2.3, and 3 to the same scene. Each technique was applied twice, each time with a different calibration target, which helped in determining the reproducibility of the calibration.

4.1 Data Formats and Test Scene

The results given in this section were obtained by processing the same JPL AirSAR scene as provided by JPL in two different formats. The format used by the techniques described in section 2 is the so-called "hires" format, which provides the four scattering matrix elements as single-precision (4-byte) complex numbers. The format used by the POLCAL technique is radically different. The symmetrization, quantization from 4 bytes to 1, and summing from 1-look to 4-look, as described in section 3, have been carried out to produce the so-called "compressed" format.

Figure 2 shows the total power image of the particular scene used during this study. Figure 3 shows the uncalibrated HH polarized raw data in the vicinity of the three trihedrals. Note that the trihedrals are identical but that the responses are not, which is of great concern when calibration depends on identical responses to identical targets. Also, a distributed target, as outlined in Fig. 2, was used for comparisons despite the lack of any known values for its cross sections.

4.2 Assessment of STCT

Figure 4 shows the calibrated polarization signatures for the trihedral that was **not** used as calibration target, in each of the two cases. The results are excellent: the levels are within 1 dB of theory, with the co-channel imbalance no more than 0.5 dB. Also, the cross-to-like isolation has improved from 20 dB before calibration to about 40 dB.

Figure 5 shows the calibrated signatures of two different PARCs: VV and 45°. The VV PARC signature is as expected with a 23 dB isolation between VV and HH. The 45° PARC signature has the peak very nearly centered on $\chi = 0, \Psi = 45°$, as expected. Because of this favorable comparison with the expected results one can conclude that this technique is applicable to the JPL AirSAR imaging radar data.

4.3 Assesment of POLCAL

Because the calibration trihedral is used only to determine the co-channel imbalance and absolute level, this calibration technique gives noticeably different results when compared to those in section 4.2. Figure 6 shows the single-pixel signatures of various trihedrals after calibration with POLCAL. Here the co-channel imbalance is between 0.5 dB and 1 dB, slightly worse than for STCT. The cross-to-like isolation is generally 23 dB, 17 dB worse than for STCT, while one has an isolation of 175 dB, apparently a fluke since it appears only once.

To compare the absolute levels, the signatures are computed by summing over the same region that is used to sum the powers of the calibration target. These results are shown in Fig. 7. Generally the signatures do not as closely resemble a trihedral as did those when using just a single pixel (Fig. 6). The absolute levels, however, are within 1 dB of the expected levels.

Figure 8 shows the same two PARCs as before, however they look quite different using the POLCAL calibration scheme. The VV PARC has a 15 dB isolation, 8 dB worse than STCT, while the cross-pol signature is significantly distorted due to the symmetrization step: the 45° PARC now has **two** cross-pol peaks, at ±45°.

4.4 Comparison using a distributed target

First, a comparison of the two formats, uncalibrated, is in order. Figure 9 shows that the hires data has a VV power of about 3.75 dB less than HH, while the compressed data has them 4.75 dB apart. There are similar differences after calibration as well.

The deconvolution calibration scheme described in Sec. 2.3 was used, with the summation on $\mathbf{D}_{ij}$ done over all pixels in the vicinity of the calibration target that had a cross-pol magnitude about 20 dB above the noise. The results are shown in Fig. 10. The signatures are very similar, the only difference being in their absolute levels – a difference of at most 0.75 dB. Hence, the differences in the measured ambiguity function for the different calibration targets do not significantly affect the calibration of distributed targets. Figure 11 shows the results of the POLCAL calibration and looks very similar to the results in Fig. 10. The difference between the two calibration schemes is only on the order of 1 dB.

5 Conclusions

A new method for calibration of polarimetric imaging SARs using point targets has been developed. The technique requires a single calibration target, namely a trihedral, to find the ambiguity-distortion matrix (polarimetric ambiguity) function of the SAR system.

The validity of the technique is examined by calibrating a scene which includes a variety of point targets with known scattering matrices. It is found that the error model provided by STCT is an appropriate one and enhances the measured polarization of the point targets. The deconvolution technique compares favorably with the POLCAL technique for absolute radiometric calibration of distributed targets. This new technique is preferred to POLCAL only if the radar system has large distortions.

Acknowledgement

This project was conducted under JPL contract #JPL-C-958749. The authors appreciate the help of the JPL Radar Science group in providing the POLCAL software and the AirSAR image data used here.

References

[1] Barnes, R.M., "Polarimetric calibration using in-scene reflectors," Rep. TT.65, MIT, Lincoln Laboratory, Lexington, MA, Sept. 1986.

[2] Cutrona, L. J., "Synthetic aperture radar," Radar Handbook, (Ed. M. Skolnik), McGraw-Hill, 1970.

[3] Klein, J. D.,"Calibration of quadpolarization SAR data using backscattering statistics," Proc. 1989 Intern. Geosci. Remote Sens. Symp., Vancouver, Canada, July 1989.

[4] Sarabandi, K., F.T. Ulaby, and M.A. Tassoudji, "Calibration of polarimetric radar systems with good polarization isolation," *IEEE Trans. Geosci. and Remote Sens.,* vol. 28, no. 1, Jan. 1990.

[5] Sarabandi, K., and F.T. Ulaby, "A Convenient technique for polarimetric calibration of single-antenna radar systems," *IEEE Trans. Geosci. and Remote Sens.,* vol. 28, no. 6, Nov. 1990.

[6] Sheen, D.R. and E.S. Kasischke,"Comparison of SAR polarimetric calibration technique using clutter," Proc. 1989 Intern. Geosci. Remote Sens. Symp., Vancouver, Canada, July 1989.

[7] Ulaby, F.T., and Elachi C., eds. Radar Polarimetry for Geoscience Applications, Artech, 1990.

[8] van Zyl, J. J., " Calibration of polarimetric radar images using only image parameters and trihedral corner reflector responses," *IEEE Trans. Geosci. and Remote Sens.,* vol. 28, no. 3, May 1990.

[9] van Zyl, J. J., C.F. Burnette, H. A. Zebker, A. Freeman, and J. Holt, "POLCAL User's Manual," Jet Propulsion Laboratory, D-7715, Aug. 1990.

[10] Whitt, M.W., F.T. Ulaby, P. Polatin, and V.V. Liepa, "A general polarimetric radar calibration technique," *IEEE Trans. Antennas Propagat.*, vol. 39, no. 1, Jan. 1991.

[11] Zebker, H. A., and Y. Lou, "Phase calibration of imaging radar polarimeter Stokes matrices," *IEEE Trans. Geosci. and Remote Sens.,* vol. 28, no. 2, March 1990.

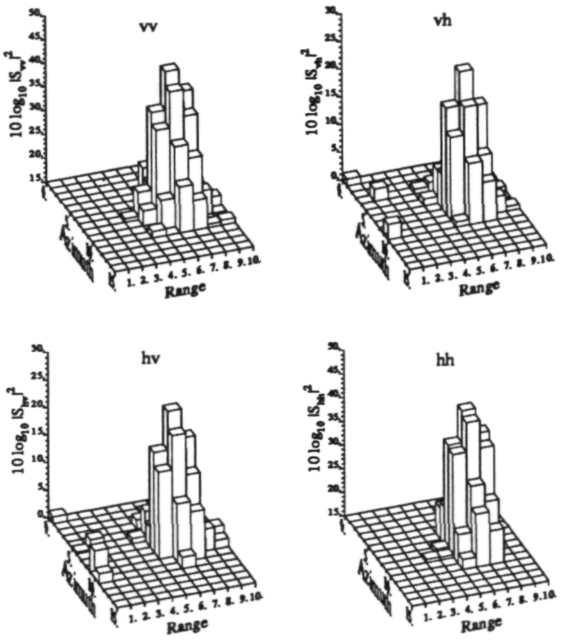

Figure 1: Measured Ambiguity-Distortion Matrix values in dB for a single trihedral. A small region surrounding the brightest pixel is shown.

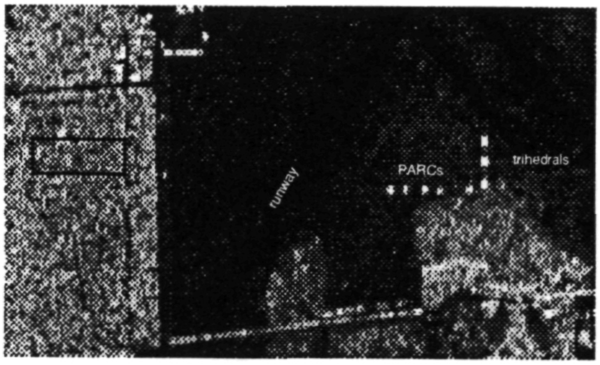

Figure 2: Total Power image of calibration targets and surrounding area. Shown are all three trihedrals, the five PARCs, and the distributed target area to the left.

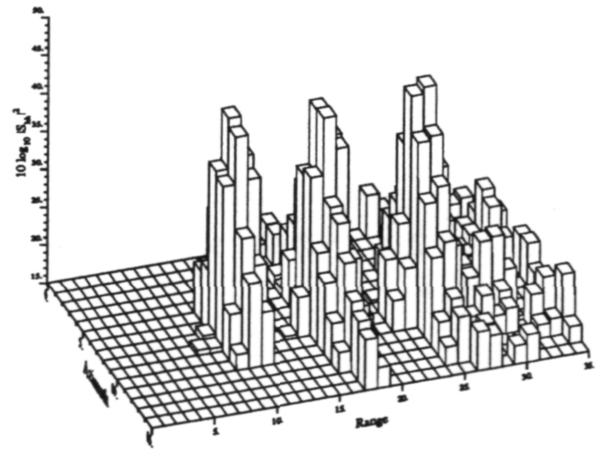

Figure 3: Measured HH-polarized values in dB for all three trihedrals. A small region surrounding them is shown. Note that the response is significantly different for the identical trihedrals.

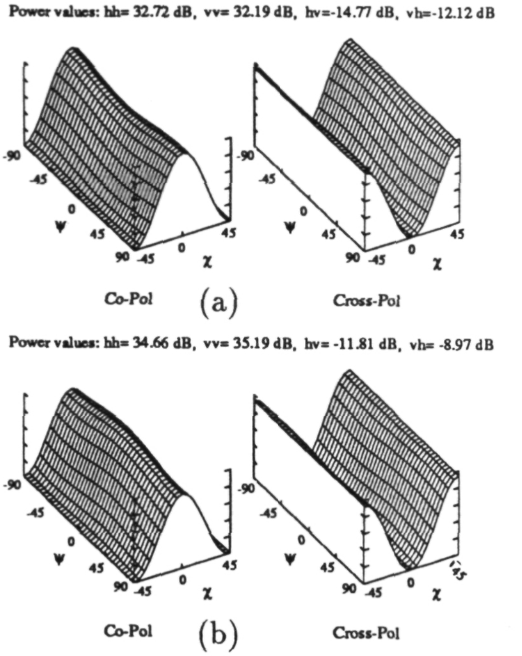

Figure 4: Validation results for STCT. (a) shows trihedral #2 when the calibration target was trihedral #1. (b) shows trihedral #1 when the calibration target was trihedral #2.

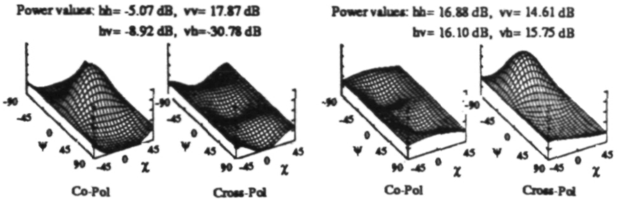

VV PARC (a) 45° PARC

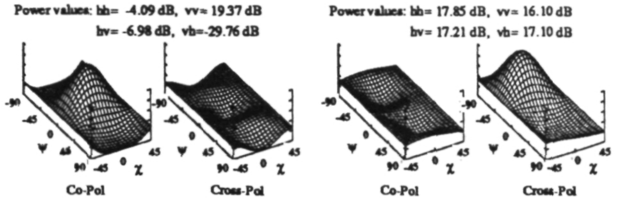

VV PARC (b) 45° PARC

Figure 5: Validation results for STCT. (a) shows the VV and 45° PARCs when the calibration target was trihedral #1. (b) shows the VV and 45° PARCs when the calibration target was trihedral #2.

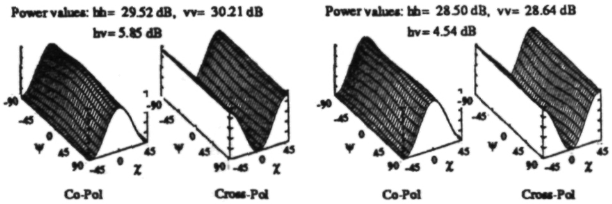

trihedral #1 (a) trihedral #2

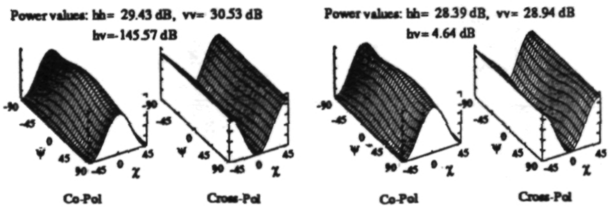

trihedral #1 (b) trihedral #2

Figure 6: Validation results for POLCAL, displaying only 1 pixel. (a) shows both trihedrals when the calibration target was trihedral #1. (b) shows both trihedrals when the calibration target was trihedral #2.

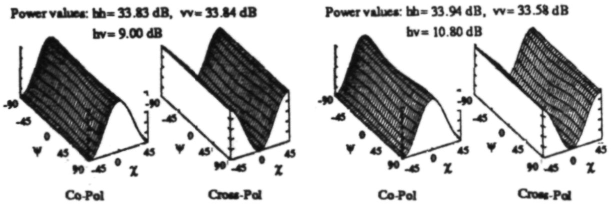

trihedral #1 (a) trihedral #2

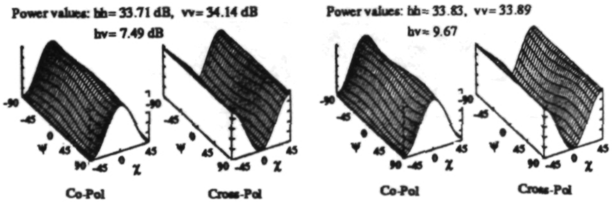

trihedral #1 (b) trihedral #2

Figure 7: Validation results for POLCAL, displaying sum over adjacent area. (a) shows both trihedrals when the calibration target was trihedral #1. (b) shows both trihedrals when the calibration target was trihedral #2.

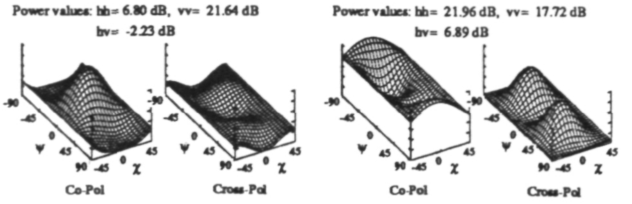

VV PARC (a) 45° PARC

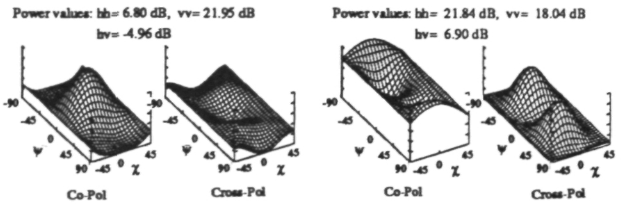

VV PARC (b) 45° PARC

Figure 8: Validation results for POLCAL, displaying only 1 pixel. (a) shows the VV and 45° PARCs when the calibration target was trihedral #1. (b) shows the VV and 45° PARCs when the calibration target was trihedral #2.

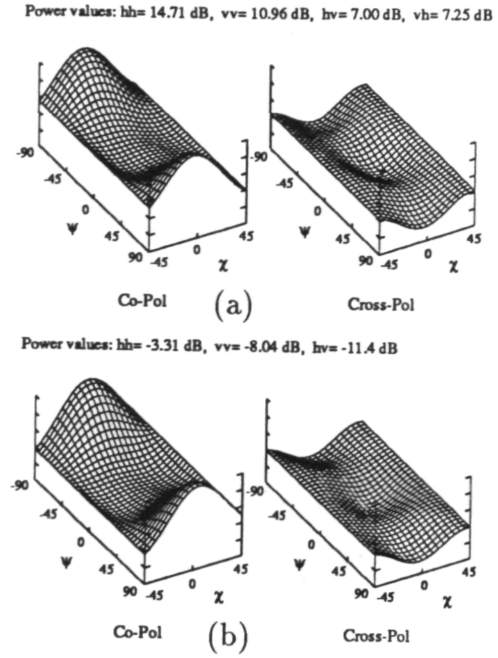

Figure 9: Uncalibrated Signature of distributed target region. (a) shows the hires format, (b) shows the compressed format.

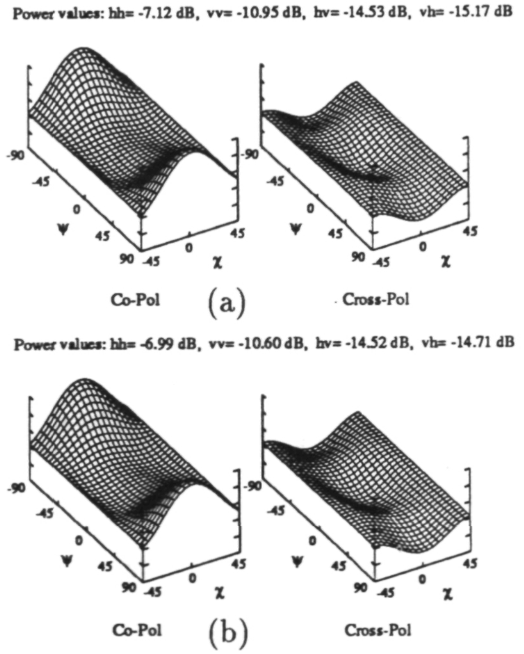

Figure 10: Signature of distributed target region, Deconvolution calibration. (a) shows the response with trihedral #1 as the calibration target. (a) shows the response with trihedral #2 as the calibration target.

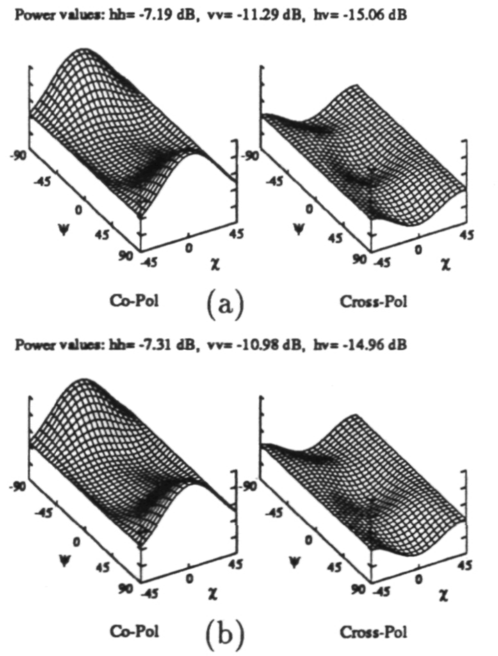

Figure 11: Signature of distributed target region, POLCAL calibration. (a) shows the response with trihedral #1 as the calibration target. (a) shows the response with trihedral #2 as the calibration target.

N92-28033

Information Content of Polarimetric SAR Data

Ian G. Cumming[1], David L. Small[2], and Jakob J. van Zyl[3]

---

[1] MacDonald Dettwiler and Associates, 13800 Commerce Parkway, Richmond, BC, V6V 2J3 Canada
[2] Dept. of Electrical Engineering, University of British Columbia, 2356 Main Mall, Vancouver, BC, V6T 1Z4 Canada
[3] Jet Propulsion Laboratory, California Institute of Technology, 4800 Oak Grove Drive, Pasadena, CA, 91109 USA

Abstract

The information content of the compressed Stokes' matrix data from the AIRSAR is examined in two ways — by measuring how each feature separates classes of terrain in an image, and by measuring how well a classifier performs with and without each feature. In this way, the features may then be ranked in order of information content (or in order of utility to the classifier). Suggestions are made regarding those variables that can be omitted in a data compression scheme or in a future simplified radar system.

Keywords: SAR, Polarimetric radar, Classification, Information content, Data reduction, Radar system simplification.

I. Introduction

This report continues work initiated in 1988 and first reported at IGARSS'89[1], on the utility of features in polarimetric radar data. The objective is to determine which of the many variables measured by a quad-pol radar are important to such applications as the classification of terrain types.

In comparison to the 1988/89 work, this study considers scenes acquired by the current AIRSAR polarimetric radar, in addition to data from the earlier radar built in 1985. This has meant that we have been able to examine extra points such as:

- multiple frequencies (P-, L-, and C-bands)
- more scenes with different terrain classes
- classes chosen by different methods
- a more robust classifier

The aim has been to understand which polarimetric features contain information useful for classification, and apply that knowledge to improve classification and reduce the volume of radar data used in storage, data links, and processing. It was thought that better classifications might be obtained by removing those features that were predominantly noise, and that knowledge of which features had the best information content would be helpful in designing simplified polarimetric radar systems with classification performance comparable to that of fully polarimetric radars.

Data Source

Eleven polarimetric radar scenes were studied. Each was processed to a SAR image at JPL; as much calibration as possible was performed; the scattering matrix data was translated into Stokes' matrix form; 4-look averaging was done; the data was compressed [2] and written to magnetic tape (see Figure 1). Analysis therefore began with 4-look Stokes' matrix data.

The Stokes' matrix data were converted into the form of scattering matrix cross products during the analysis, since this form is directly related to the radar's four complex polarimetric radar channels (HH, HV, VH, VV). As the cross-product variables have a more direct physical interpretation, they were used as the features to a classifier, rather than the Stokes' matrix elements. The cross products lend themselves to ready interpretation of

---

This work was supported by the Province of British Columbia Science Council G.R.E.A.T. Award Program and the Canadian Natural Sciences and Engineering Research Council

ǁ Presented at the 1991 JPL Airborne Geoscience Workshop

their scattering behaviour: For example, it is well known that the phase angle between the HH and VV channels is a direct function of the number of bounces in the reflection process [3].

The cross products were normalized with respect to the total power (*span*) image to reduce incidence angle brightness effects and make the polarimetric properties of the radar more apparent. The result is a more orthogonal feature set.

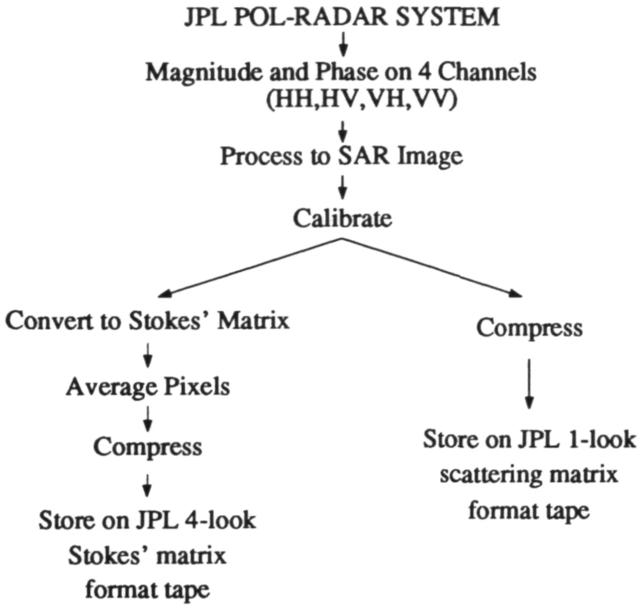

Figure 1 JPL Polarimetric Radar Processing

Polarimetric Radar Features

The polarimetric feature set $\vec{F}$ was selected to be the *span* plus the nine normalized cross products:

$$\vec{F} = \begin{pmatrix} F_0 \\ F_1 \\ F_2 \\ F_3 \\ F_4 \\ F_5 \\ F_6 \\ F_7 \\ F_8 \\ F_9 \end{pmatrix} = \begin{pmatrix} span \\ HH\,HH^* \\ VV\,VV^* \\ HV\,HV^* \\ \Re\{HH\,VV^*\} \\ \Im\{HH\,VV^*\} \\ \Re\{HV\,VV^*\} \\ \Im\{HV\,VV^*\} \\ \Re\{HH\,HV^*\} \\ \Im\{HH\,HV^*\} \end{pmatrix} \qquad (1)$$

The cross products are the product of the complex return from one channel with the complex conjugate of the return from another channel. The cross products themselves are generally complex, unless the two channels are the same, in which case their cross product is a scalar.

The feature vector is derived from the Stokes' matrix A as follows:

$$\vec{F} = \begin{pmatrix} a_{11} \\ [2(a_{11}+a_{12})-(a_{33}+a_{44})]/a_{11} \\ [2(a_{11}-a_{12})-(a_{33}+a_{44})]/a_{11} \\ (a_{33}+a_{44})/a_{11} \\ (a_{33}-a_{44})/a_{11} \\ -2a_{34}/a_{11} \\ (a_{13}-a_{23})/a_{11} \\ (a_{24}-a_{14})/a_{11} \\ (a_{13}+a_{23})/a_{11} \\ -(a_{24}+a_{14})/a_{11} \end{pmatrix} \qquad (2)$$

Note that *HH HH**, *HV HV**, and *VV VV** measure polarimetric power *ratios*, rather than absolute backscatter at these polarizations. F_4 to F_9 are also normalized.

In order to improve classification performance, a spatial function of these features was used: the average of the features over a 2×2 window.

II. Class Separation by Feature

Training areas were selected within the eleven scenes studied based on ground truth, class choices from other studies of the same scene [4][5], and van Zyl's unsupervised classifier [6]. The van Zyl classifier groups pixels into even-bounce, diffuse, or odd-bounce (EDO) scattering classes. Subjective grouping based on an *HH* brightness image was used when other means were not available and the van Zyl EDO classes did not all exist in the scene.

The mean and standard deviation of each feature in equation (1) were collected within each training area. A graphical representation of these statistics for a scene from Bonanza Creek, Alaska is shown in Figure 2. Each bar is centered on the feature's mean with a length encompassing ± 1 sigma (the feature's standard deviation). If the class bars are well separated for a certain feature, then that feature is a useful discriminator between

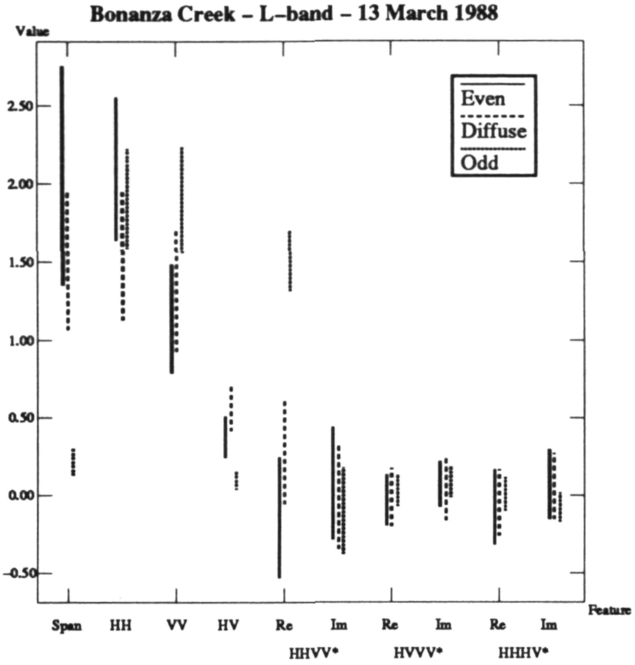

Figure 2 Feature Distribution in Bonanza Creek, Alaska (13 March 1988) L-band scene

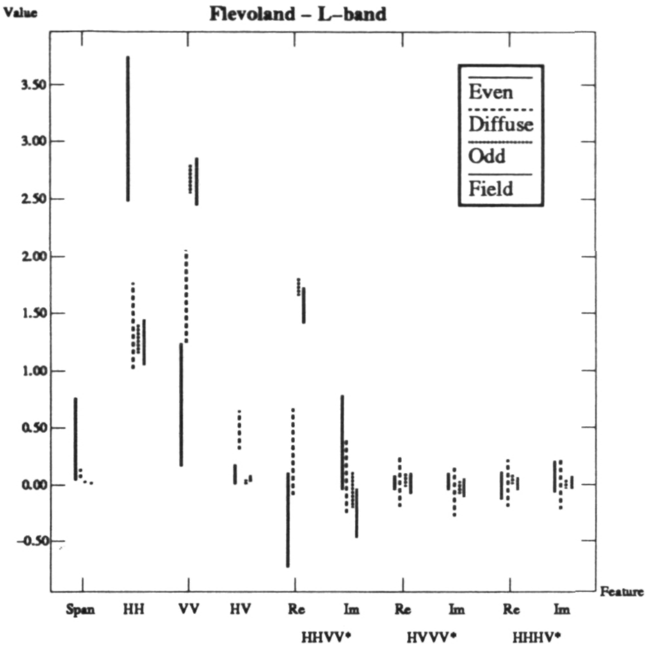

Figure 3 Feature Distribution in Flevoland, NL (16 August 1989) L-band scene

those classes. For instance, it can be seen from Figure 2 that the *span*, $\Re\{HH\ VV^*\}$, and *HV* features discriminate well between odd-bounce and diffuse scatterers.

In Figure 2, when the class bars have a distinct range of values (are separate), then the feature is a useful discriminator. The concept is formalized in the *class separability* [7][8], defined as the ratio of the difference in the feature's mean values to the sum of its standard deviations. For feature vectors $\vec{A}$ and $\vec{B}$ prototyping two terrain classes, the class separation is defined as:

$$Sep(A_i, B_i) = \frac{|\bar{A}_i - \bar{B}_i|}{\breve{A}_i + \breve{B}_i} \tag{3}$$

where $\breve{A}_i$ and $\breve{B}_i$ are the standard deviations of feature i in classes *A* and *B*, respectively. A class separation above approximately 0.9 indicates that the feature is useful for discrimination; above 2, the feature provides close to perfect discrimination on its own. Class separations lower than about 0.9 indicate that the feature adds little discriminatory information, and could be predominantly noise.

How Features Separate Classes

From Figures 2 and 3 it is apparent that some features provide good class separation while others do not. The average class separation, over all class pairs within each scene, of the ten features is shown in Figure 4. There is a marked difference between the separation provided by the first five features and that provided by the last five. The *span*, $\Re\{HH\ VV^*\}$, $HV\,HV^*$, $VV\,VV^*$, and $HH\,HH^*$ features provide good separation information, while the other features appear to be zero mean random variables carrying little class-specific information. This finding holds true over a large number of scenes and class types.

III. Classification Trials

Although class separation measures are useful for determining the ability of single features to discriminate between classes, they ignore the correlation between features. This section introduces a measure of the information that each feature adds.

Assuming the full feature-set classification to be correct, counting the number of pixels that change classification between that "reference" run and one using an incomplete feature set will give

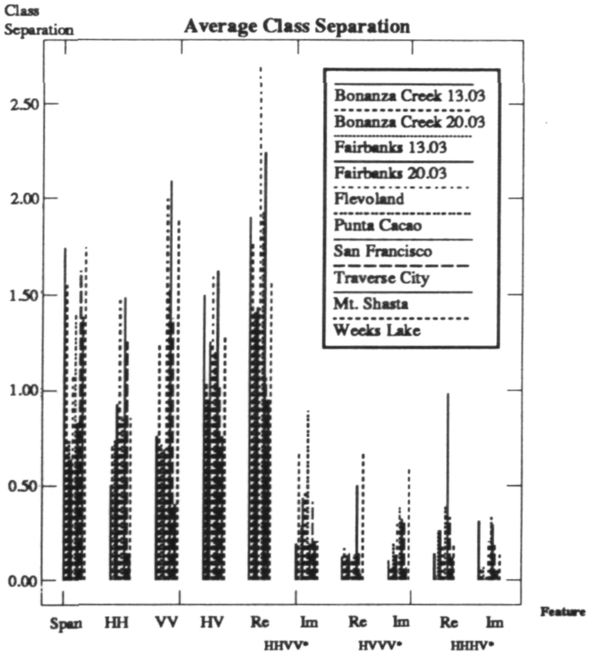

Figure 4 Average Class Separations for L-band Scenes

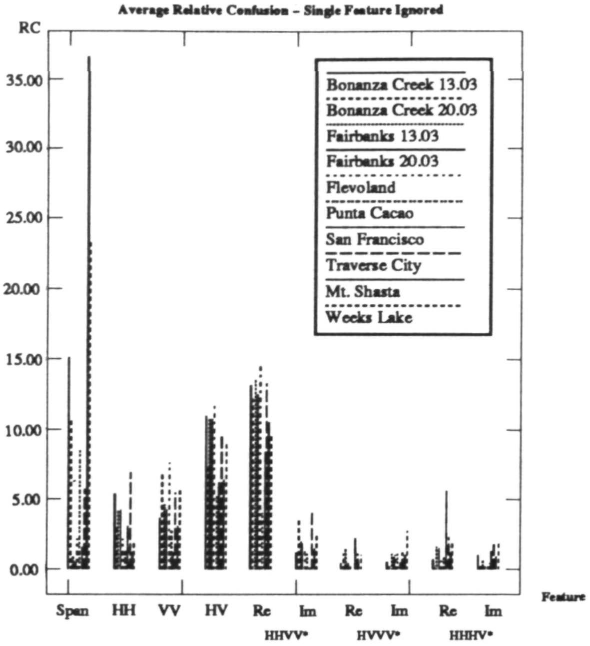

Figure 5 Average Relative Confusion for Single Feature Ignored (Reference is L-band Full Feature Set Classification)

an indication of the importance (for classification purposes) of the features absent from the incomplete feature set. The *relative confusion* (*RC*) is defined as the percentage of pixels that changes classification between image classifications A and B, where A uses an incomplete feature set, and B a full feature set. A supervised minimum distance classifier was used.

The utility of each feature was estimated by calculating the relative confusion (*RC*) when each feature was dropped singly (ten classification runs of nine features each). The results are shown for all scenes in Figure 5.

The *span*, $\Re\{HH\ VV^*\}$, and $HV\,HV^*$ are clearly the most influential features, with the $HH\,HH^*$ and $VV\,VV^*$ features being somewhat influential, and the last five features having close to no effect on the classification results.

Visual inspection of classification images (e.g., red=clear-cut, green=forest, blue=water) produced, omitting one (or often more) of the last five members of the feature set, revealed that systematic changes in pixel classification occurred rarely (notably after dropping $\Re\{HH\ HV^*\}$ from the feature set in the San Francisco scene).

Figure 7 shows a set of image classifications illustrating that many features may be ignored while still producing acceptable classifications. In this case, the classification changes appear to be essentially random until the *VV* feature is dropped, at which time systematic changes begin to appear (in this case, as more water pixels at the expense of clear-cut classifications).

IV. Ranking of Features

Based on the relative confusion experiments and the overall class separation results, the ten features were "ranked" in a feature utility order. As the classification trials revealed the impact of each feature on classification accuracy, features were ranked based on the *relative confusion* caused when the feature was removed from a full-feature classification, close ties being broken by the *class separation* result. For consistency, only L-band data were used, as they were available with all scenes, and had the best calibration. Although only a limited number of multifrequency scenes were analysed, the tentative conclusions are that the generalizations expressed here with respect to feature utility are not strongly frequency depen-

Rank	*Feature*	*Mean RC*	*Mean Class Separation*
1	*span*	12.7	1.28
2	$\Re\{HH\ VV^*\}$	11.3	1.57
3	*HV*	8.9	1.15
4	*VV*	5.4	1.21
5	*HH*	4.2	.86
6	$\Im\{HH\ VV^*\}$	2.8	.38
7	$\Re\{HH\ HV^*\}$	1.7	.27
8	$\Re\{HV\ VV^*\}$	1.4	.20
9	$\Im\{HV\ VV^*\}$	1.2	.23
10	$\Im\{HH\ HV^*\}$	1.0	.16

Table 1 Basis for Feature Utility Ranking

dent. A ranking of the ten feature vector elements based on the above criterion is shown in Table 1.

The feature utility ranking is important insofar as it (a) illustrates the order in which features may be dropped (during data compression), and (b) calls attention to those information-laden features that will be useful in constructing improved classifiers. The polarimetric data should be well calibrated for the ranking to be valid. For example, if the data is not phase calibrated, some information will migrate from the $\Re\{HH\ VV^*\}$ feature to the $\Im\{HH\ VV^*\}$ feature.

Different scene-types produce slightly different rankings, as can be seen in Table 2. The table shows that for a variety of scene-types, the discriminatory information resides mainly in the {*span*, $\Re\{HH\ VV^*\}$, $HV\ HV^*$, $VV\ VV^*$, $HH\ HH^*$} feature subset. A data-encoding scheme could eliminate the features involving the product of a co-pol term and a cross-pol term (the four bottom ranked features) with little loss of classification accuracy.

V. Simplified Radar Systems

Investigation of partially polarimetric radars that acquire most of the useful set of features might therefore be warranted. This section explores three such schemes.

Fully polarimetric radars pay a price in complexity and data storage/processing requirements for the extra radar channels that they make available. Fully polarimetric radars return four channels (*HH*, *HV*, *VH*, *VV*), while conventional single-channel radars return only one.

Dual-channel radars are intermediate between conventional single-channel and fully polarimetric radars. Only one of the two most distinctive features ($\Re\{HH\ VV^*\}$ and $HV\ HV^*$) can be included in a two-channel radar simultaneously, as three channels are required to obtain both.

A co-polarized radar is the simplest radar that can acquire the $\Re\{HH\ VV^*\}$ feature, and the single transmit radar is the simplest one that includes the $HV\ HV^*$ feature. The following

Rank	*All*	*EDO*	*non-EDO*	*Forest*	*Agricultural (Flevoland)*	*Comments*
1	*span*	$\Re\{HH\ VV^*\}$	*span*	*span*	$\Re\{HH\ VV^*\}$	Most distinctive
2	$\Re\{HH\ VV^*\}$	*HV*	$\Re\{HH\ VV^*\}$	$\Re\{HH\ VV^*\}$	*HV*	
3	*HV*	*span*	*HV*	*HV*	*VV*	Provide some useful separation
4	*VV*	*VV*	*VV*	*VV*	*span*	
5	*HH*	*HH*	*HH*	*HH*	*HH*	
6	$\Im\{HH\ VV^*\}$	$\Im\{HH\ VV^*\}$	$\Im\{HH\ VV^*\}$	$\Im\{HH\ VV^*\}$	$\Im\{HH\ VV^*\}$	Mainly noise
7	$\Re\{HH\ HV^*\}$	$\Re\{HH\ HV^*\}$	$\Re\{HV\ VV^*\}$	$\Re\{HH\ HV^*\}$	$\Im\{HV\ VV^*\}$	
8	$\Re\{HV\ VV^*\}$	$\Im\{HV\ VV^*\}$	$\Im\{HV\ VV^*\}$	$\Im\{HV\ VV^*\}$	$\Re\{HH\ HV^*\}$	
9	$\Im\{HV\ VV^*\}$	$\Re\{HV\ VV^*\}$	$\Re\{HH\ HV^*\}$	$\Im\{HH\ HV^*\}$	$\Re\{HV\ VV^*\}$	
10	$\Im\{HH\ HV^*\}$	$\Im\{HH\ HV^*\}$	$\Im\{HH\ HV^*\}$	$\Re\{HV\ VV^*\}$	$\Im\{HH\ HV^*\}$	

Table 2 Feature Utility Rankings for various scene types

sections study these dual-channel radars, together with a simple three-channel amplitude-only radar.

CO-POL Radar A CO-POL radar has only the *HH* and *VV* channels. Only one receiver is required, and less transmitted power is needed for a given SNR, as the comparatively weak *HV* channel is omitted. The data transmission, processing, and storage requirements are halved compared to the fully polarimetric radar.

In comparison to a fully polarimetric SAR (see equation (1)), a CO-POL radar returns the following features:

$$\vec{F}_{CO-POL} = \begin{pmatrix} span' \\ HH\ HH^* \\ VV\ VV^* \\ \Re\{HH\ VV^*\} \\ \Im\{HH\ VV^*\} \end{pmatrix} \tag{4}$$

Note that the definition of *span* is modified in this case to half the sum of the unnormalized *HH* and *VV* amplitude channels, recognizing that the *HV* channel is not available. The polarization phase difference is preserved, as it is computed from the $\Re\{HH\ VV^*\}$ and $\Im\{HH\ VV^*\}$ features.

Amplitude Radar An amplitude (AMPL) radar measures the amplitude of the *HH*, *HV*, *VH*, and *VV* channels, but not their phase. No interchannel phase calibration, and less storage are its principal advantages. Such a radar collects the following features:

$$\vec{F}_{AMPL} = \begin{pmatrix} span \\ HH\ HH^* \\ VV\ VV^* \\ HV\ HV^* \end{pmatrix} \tag{5}$$

Note that the important *HV HV** feature is present, but that the $\Re\{HH\ VV^*\}$ feature is missing.

Single Transmit Radar Single transmit radars transmit on only a single polarization, but receive on two polarizations. They require no high-speed, high-power waveguide switch, less transmit power and less complex timing control than a fully polarimetric radar. Two receivers are needed, but there is no receive-path waveguide switch, and the receive data does not need to be de-multiplexed. Transmission, processing, and archive storage requirements are halved.

A horizontal transmit radar returns the following features:

$$\vec{F}_{H-TX} = \begin{pmatrix} span'' \\ HH\ HH^* \\ HV\ HV^* \\ \Re\{HH\ HV^*\} \\ \Im\{HH\ HV^*\} \end{pmatrix} \tag{6}$$

while a vertical transmit radar returns:

$$\vec{F}_{V-TX} = \begin{pmatrix} span''' \\ VV\ VV^* \\ HV\ HV^* \\ \Re\{HV\ VV^*\} \\ \Im\{HV\ VV^*\} \end{pmatrix} \tag{7}$$

The definition of *span* in both equations is modified to use only those of the *HH*, *HV*, *VH*, and *VV* features that are available. Compared to the CO-POL radar, the $HV\ HV^*$ feature is available, but the co-polarized phase ($\Re\{HH\ VV^*\}$ and $\Im\{HH\ VV^*\}$) and one of the $VV\ \ VV^*$ and $HH\ \ HH^*$ features are not.

Comparison The potential performance of simplified pol-radar systems was evaluated by checking their relative confusion in classifier trials, comparing them with the full pol-radar. Co-polarized, amplitude-only, and single-transmit, radars were emulated. The radar's relative confusion performances (in comparison to a fully polarimetric radar) may be compared in Figure 6. For the Flevoland scene, classifications resulting from each of the simplified radar feature subsets are visually juxtaposed in Figure 8. Structural changes to the classification results are not apparent.

The CO-POL radar performed best; its classifications were generally closest to those using the full feature set. Of the simplified radars, it alone returns the $\Re\{HH\ VV^*\}$ and $\Im\{HH\ VV^*\}$ features, and hence provides the useful polarization phase difference (PPD) [6], [9], [10], [11] for analysis.

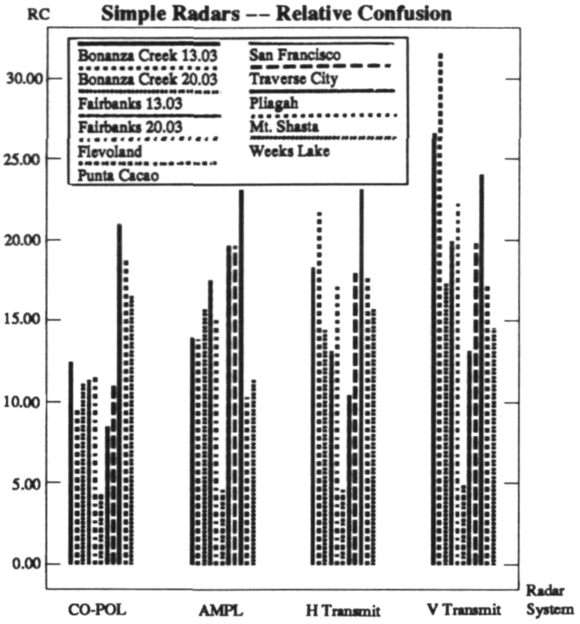

Figure 6 Relative Confusion of Simple Radars in L-band Scenes

VI. Discussion

To a certain extent the results on feature utility are biased by the classes chosen in the classification experiment. For example, if the classes are chosen by their distinctive brightness in the scene, then *span* is bound to be a feature that provides good class discrimination.

We have tried to avoid this bias by selecting classes by a variety of different methods. In addition to using van Zyl's unsupervised classifier [6] to select terrain classes in about half of the scenes, we have used subjective means and other peoples' analysis to select classes in the remaining ones.

Van Zyl's unsupervised classifier uses distinctive properties of the polarimetric data to distinguish terrain classes. Specifically, the orientation angle and the handedness of the scattered wave, in comparison to the transmitted wave, are used to classify individual pixels without consideration of other scene properties or spatial pattern recognition. As the polarimetric phase difference and the cross-pol returns are keys to this method of classification, it is not surprising that the variables $\Re\{HH\ VV^*\}$ and $HV\,HV^*$ rank highly in the utility of features in the polarimetric data.

On the other hand, it is clear from the physics of the radar that these two variables are among the most distinctive among the variables measured by the quad-pol radar as compared to a single-channel radar. This reflects the polarimetric radar's ability to measure relative strength and path length of reflection of EM waves of different polarizations, and how a scatterer changes the polarization of the EM wave (depolarization) in the reflection process.

For this reason, we feel confident in proposing the stated ranking of polarimetric features, despite the bias discussed above. This ranking will vary in detail with radar frequency, scene content and radar image analysis method, but the general ranking (i.e., the high, medium, and low importance groups of Table 2) should apply to most polarimetric radar scenes.

VII. Conclusions

Motivated by the desire to reduce the data transmission, recording, and processing requirements attendant with polarimetric data, we have analysed the information content of polarimetric SAR features and found that there is a sharp distinction between those features that carry information useful for classification and those that do not. Classification performance is good (and may be improved) when only 50–70% of the image set is used. Data reduction is possible, particularly if classification is the main use of the data. Of the simplified partially polarimetric SAR systems explored, the CO-POL radar (with only the *HH* and *VV* channels) was found to give the best classification performance, often nearly equal to that of a fully polarimetric radar.

References

[1] Ian G. Cumming and Jakob J. van Zyl. Feature Utility in Polarimetric Radar Classification. In *IGARSS'89*, pages 1841–1846, June 1989.

[2] P.C. Dubois and L. Norikane. Data Volume Reduction for Imaging Radar Polarimetry. In *IGARSS'87*, 1987.

[3] Jakob J. van Zyl, Howard A. Zebker, and Charles Elachi. Imaging Radar Polarization Signatures: Theory

and Observation. *Radio Science*, 22(4):529–543, July 1987.

[4] Fawwaz T. Ulaby and Charles Elachi, editors. *Radar Polarimetry for Geoscience Applications*. Artech House, 1990.

[5] Jobea Way, Jack Paris, Eric Kasischke, Charles Slaughter, Leslie Viereck, Norman Christensen, Myron C. Dobson, Fawwaz Ulaby, John Richards, Anthony Milne, Alois Sieber, Francis J. Ahern, David Simonett, Roger Hoffer, Mar Imhoff, and James Weber. The Effect of Changing Environmental Conditions on Microwave Signatures of Forest Ecosystems: Preliminary Results of the March 1988 Alaskan Aircraft SAR Experiment. *International Journal of Remote Sensing*, 11(7):1119–1144, July 1990.

[6] Jakob J. van Zyl. Unsupervised Classification of Scattering Behavior Using Radar Polarimetry Data. *IEEE Transactions on Geoscience and Remote Sensing*, 27(1):36–45, January 1989.

[7] Stephen L. Durden, Jeffrey D. Klein, and Howard A. Zebker. Polarimetric Radar Measurements of a Forested Area Near Mt. Shasta. *IEEE Transactions on Geoscience and Remote Sensing*, 29(3):444–450, May 1991.

[8] Shih-Tseng Wu and Steven A. Sader. Multipolarization SAR Data for Surface Feature Delineation and Forest Vegetation Characterization. *IEEE Transactions on Geoscience and Remote Sensing*, GE-25(1):67–76, January 1987.

[9] W-M. Boerner, B-Y. Foo, and H.J. Eom. Interpretation of the Polarimetric Co-polarization Phase Term in Radar Images Obtained with the JPL Airborne *L*-band SAR System. *IEEE Transactions on Geoscience and Remote Sensing*, GE-25(1):77–81, January 1987.

[10] Hyo J. Eom and Wolfgang-M. Boerner. Statistical Properties of the Phase Difference Between Two Orthogonally Polarized SAR Signals. *IEEE Transactions on Geoscience and Remote Sensing*, 29(1):182–184, January 1991.

[11] F. T. Ulaby, D. Held, M.C. Dobson, K.C. McDonald, and T.B.A. Senior. Relating Polarization Phase Difference of SAR Signals to Scene Properties. *IEEE Transactions on Geoscience and Remote Sensing*, GE-25(1):683–701, January 1987.

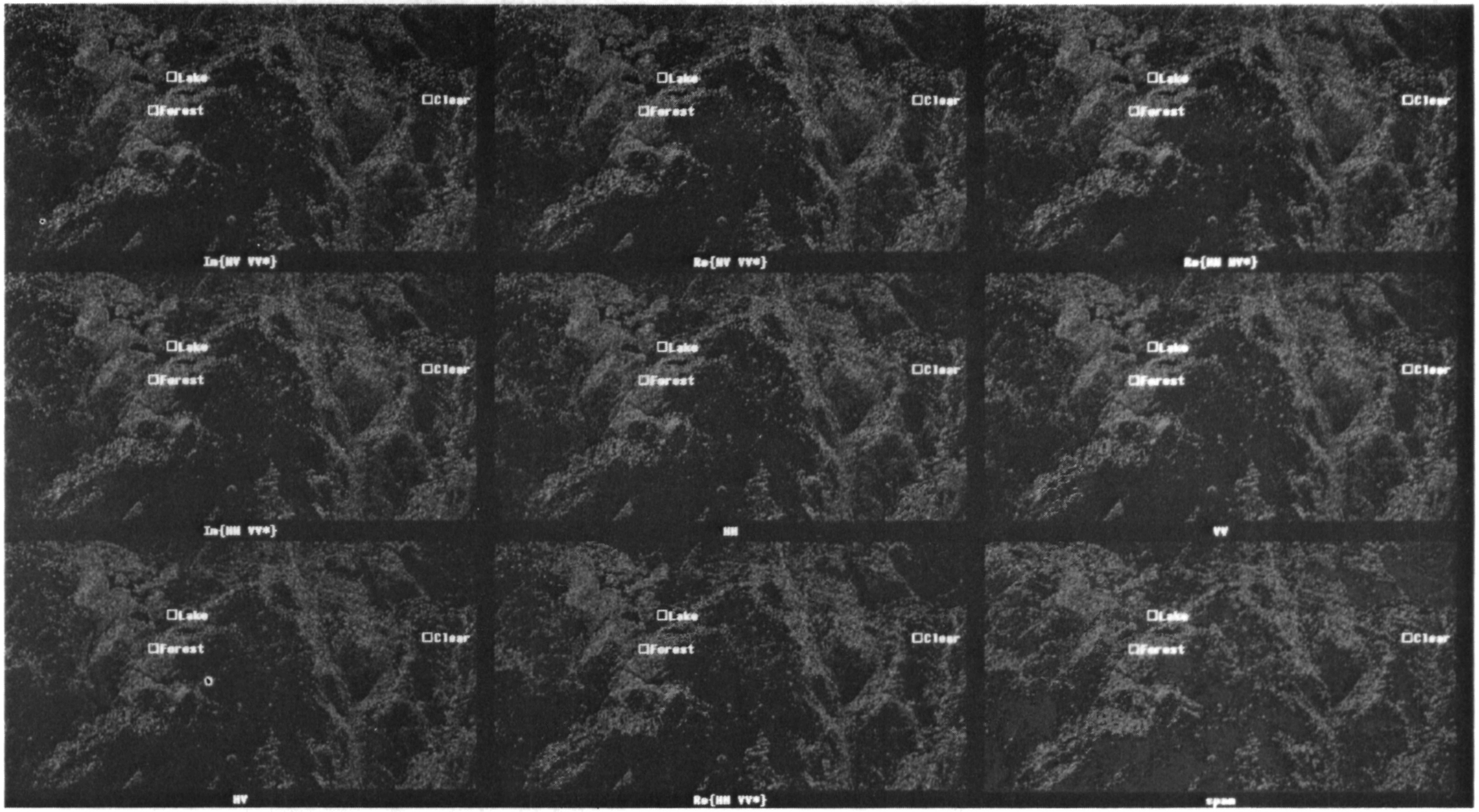

Figure 7 Sequence of Features Dropped (9 images) in Weeks Lake, BC, Canada Scene (23 March 1988). Features were dropped in reverse-rank order of Table 1. The last feature not dropped labels each image. (red=clear-cut, green=forest, blue=lake)
(See color slide no. 21.)

ORIGINAL PAGE
BLACK AND WHITE PHOTOGRAPH

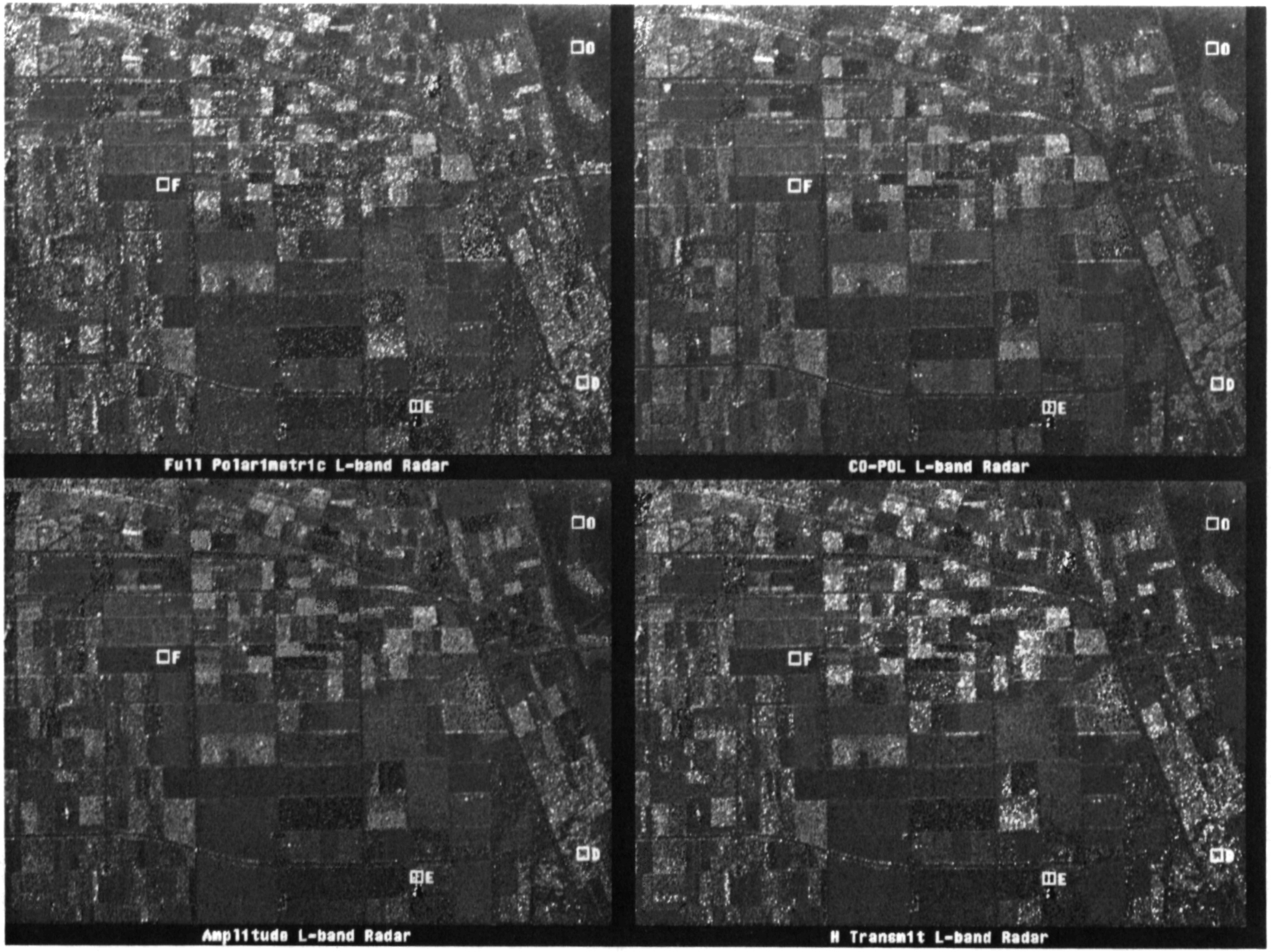

Figure 8 Visual Classification Comparison of Simplified Radar Systems — Flevoland, NL Scene (16 August 1989) — (red=even-bounce, green=diffuse/forest, blue=water, yellow=field)

(See color slide no. 22.)

N92-28034

The AIRSAR Image Browse System

A. Pang, L. Nguyen and R. Kwok
Jet Propulsion Laboratory
California Institute of Technology
Pasadena, California

Abstract. The volume of data acquired by synthetic aperture radar (SAR) missions motivates the development of a technique that will provide investigators with timely access to image data, and the capability to visually inspect images to determine various characteristics of the data collected, as well as the extent of the data coverage. A system has been designed for accessing and browsing an on-line archive of NASA aircraft SAR (AIRSAR) imagery and is being developed as an extension to the SAR Data Catalog System (SDCS). The AIRSAR browse system consists of three elements: 1) an on-line, compressed imagery archive; 2) a user interface for selecting and accessing the on-line images; and 3) a software application program for reconstructing and displaying the images. Details of these elements are described. The goals are to maximize the utilization of the AIRSAR data set, and to demonstrate the image browse concept for SAR data so that baseline catalog systems supporting SIR-C and future SAR missions will feature this capability.

I. Introduction

The early versions of the NASA spaceborne and airborne SAR distribution systems did not handle the large data volumes and diverse user groups very well. Typical problems encountered by data users included delays in data delivery and the lack of readily accessible data inventories. The development of the SAR Data Catalog System (SDCS) in the mid-1980's was intended to bridge the gap between the SAR data processing and archive facilities at JPL and the end data users [1]. The goals of the SDCS were to provide the science community with access to information about the SAR missions and data, and to facilitate the dissemination of SAR data.

NASA's ongoing AIRSAR campaigns provide scientists with a continuous source of SAR data. The AIRSAR system has the capability to image sites frequently and on multiple passes under different conditions. The result is a large, diverse data set, which is plenishing the archive at a rate of approximately 15 terabits/year. This increase in data volume, however, introduces the complexity of selecting optimum data sets for science investigations. No longer is the ability to peruse a catalog of the data sufficient since the determination of the most favorable data sets, typically, requires the comparison of several data sets side-by-side. Scientists using the AIRSAR data, therefore, need the aid of an image browse system which will not only allow them to determine the availability of data, but also to inspect and assess the characteristics of the data. Additionally, after the image selection is complete, the system should provide scientists with a mechanism to make requests for the actual data products.

The functionalities of this system encapsulate the goals of the SAR Data Catalog System. The natural progression in prototyping such a system, therefore, is to extend the capabilities of the SDCS to include features for examining an on-line imagery archive.

II. Image Browse System

At present, the SAR Data Catalog System inventories mission and image information for the SEASAT SAR, the Shuttle Imaging Radar B (SIR-B), and AIRSAR data sets. The features of the SDCS include determining mission coverage, searching the image inventory, and placing requests for data products on-line. These are described in [2]. Figure 1 is a block diagram showing the SDCS with the inclusion of the AIRSAR image browse system. The host computer system is a MicroVAX III with two SUMO optical disk drives, a magnetic disk drive and an array processor. One of the optical disks is used as the on-line image archive, while the magnetic disk stores user files. The array processor is used to optimize the throughput of the image compression software.

The three components of the AIRSAR image browse system are the on-line, compressed imagery archive, the user interface via the SDCS, and an application program for the Macintosh personal computer distributed to AIRSAR data users for reconstructing and displaying the compressed browse imagery. Each of these will be discussed below.

A. On-line Archive

The on-line browse image archive consists of a collection of compressed AIRSAR power images and their corresponding codebooks. Since the standard AIRSAR image product is stored in the compressed Stokes Matrix format, the first step in the generation of the on-line imagery archive is to extract and magnitude detect the total power image using the equation:

$$A_{Tot} = \sqrt{S_{HH}^2 + S_{VV}^2 + 2S_{HV}^2}$$

where S_{HH}, S_{VV}, S_{HV} are the complex image pixel values for the HH, VV and HV channels, respectively. The power images are then compressed using the vector quantization (VQ) algorithm. This compression technique was chosen because it provides high compression ratio and good reconstructed image quality [3]. A compression ratio approaching 16:1 can be achieved for the AIRSAR images. An additional advantage of this algorithm is that the decoding procedure requires only a simple table lookup.

Each AIRSAR browse image is comprised of a 64 KB compressed image and a 4 KB codebook. As the compressed, browse images and their codebooks are placed on-line in the read-write optical disk platter, the location of these files, along with parameters describing the characteristics of the compressed images, are entered into the SDCS database to facilitate searching for the browse images. Over 3000 AIRSAR browse images can be stored on-line in a single 300 MB optical disk platter.

Plans are to keep all newly processed AIRSAR images in the on-line browse archive. The capacity of the optical disk platter allows for two years worth of AIRSAR browse images to be placed on-line at one time. Thirty new AIRSAR images will be loaded into the archive weekly. Since the image compression function is computationally intensive, the archive loading will be performed during the second work shift to minimize the impact on users working on the system.

The browse image archive is searchable by any appropriate combination of spatial and temporal parameters, as well as experiment and site names. Detailed information about a particular image can be retrieved from the larger SDCS image metadata inventory and displayed on the user's computer terminal.

When browse images have been selected, they are copied from the on-line archive into the user's disk area. Users are informed of the location of the image files and are responsible for initiating the file transfers to their local computer system where the compressed image data can be reconstructed and viewed.

B. User-interface

An objective of the SDCS was that it be easy to use, especially by investigators who would use it infrequently. This design philosophy is followed by the AIRSAR browse system. The basic user-interface of the SAR Data Catalog System and the AIRSAR browse system is a system of menus, from which the user makes selections. The advantage of this design is that users need little or no a priori knowledge of a query language or details about the system or its data sets to begin using it.

Once information regarding the browse images has been retrieved from the database, it is formatted and displayed in tables. These tables can be saved into output files for later reference.

C. Image Reconstruction and Display

An application program, MacCmpView, has been developed for the Macintosh II, IIx, and IIcx (with 8-bit video and a minimum of 3 MB of memory) to reconstruct and display the compressed browse images. MacCmpView is available free of charge to all AIRSAR data users. The MacCmpView distribution package includes a user's guide and a 3.5 inch floppy disk containing the executable code and sample data files.

The user-interface of this software package conforms to the user-interface of typical Macintosh applications. The options in MacCmpView are activated by making appropriate menu item selections.

To reconstruct the browse image, a user would select the "decode" option. After specifying the codebook and compressed data file to use, MacCmpView begins the VQ table look-up decompression process. A detected AIRSAR image (1024 pixels x 750 image lines) can be reconstructed in about 2.2 minutes. Decoded images are written to output files on disk. This process can be repeated any number of times.

Browse images are displayed in MacCmpView by "opening" the decompressed image files from the "file" option. An image window is displayed on the screen within 4 seconds. Multiple images can be displayed simultaneously (see Figure 2). In addition, there are options for zooming in on targets of interest, displaying images in pseudo-color, adding textual annotation to the image, and printing the image on a printer that can interpret PostScript commands (see Figure 3).

III. Conclusion

The prototype AIRSAR image browse system demonstrates the feasibility of a low-cost, sophisticated tool useful for screening SAR imagery. This result is important for future SAR missions which plan to collect and process large volumes of data several orders of magnitude larger than the AIRSAR mission. The implementation described in this paper greatly simplifies the process of selecting data sets for science investigations and allows for maximum accessibility to the processed SAR imagery. The concept and design of the AIRSAR image browse system can be adapted to incorporate other image data sets which are often used in conjunction with SAR data analysis and interpretation. The MacCmpView program can be enhanced to include features for viewing image data from different sensors and instruments.

References

[1] Pang, A., Holmes, A., "The SAR Data Catalog System: An Interface Between the Scientist and the Data System," Proceedings of the Digital Equipment Computer Users Society, Dallas, TX, 1986.

[2] Nguyen, L., Pang, A., Richardson, A., SAR Data Catalog System User's Guide, JPL D-7657, May 15, 1990 (JPL internal document).

[3] Chang, C.Y., Kwok, R., Curlander, J.C., Data Compression of Synthetic Aperture Radar Imagery, JPL D-5210, February 1988 (JPL internal document).

Acknowledgements

The authors would like to acknowledge L. Norikane for her help in the development of the MacCmpView application, and C. Y. Chang for the use of the VQ compression and decompression software that he developed.

This paper presents the results of work carried out at the Jet Propulsion Laboratory, California Institute of Technology, under contract with the National Aeronautics and Space Administration.

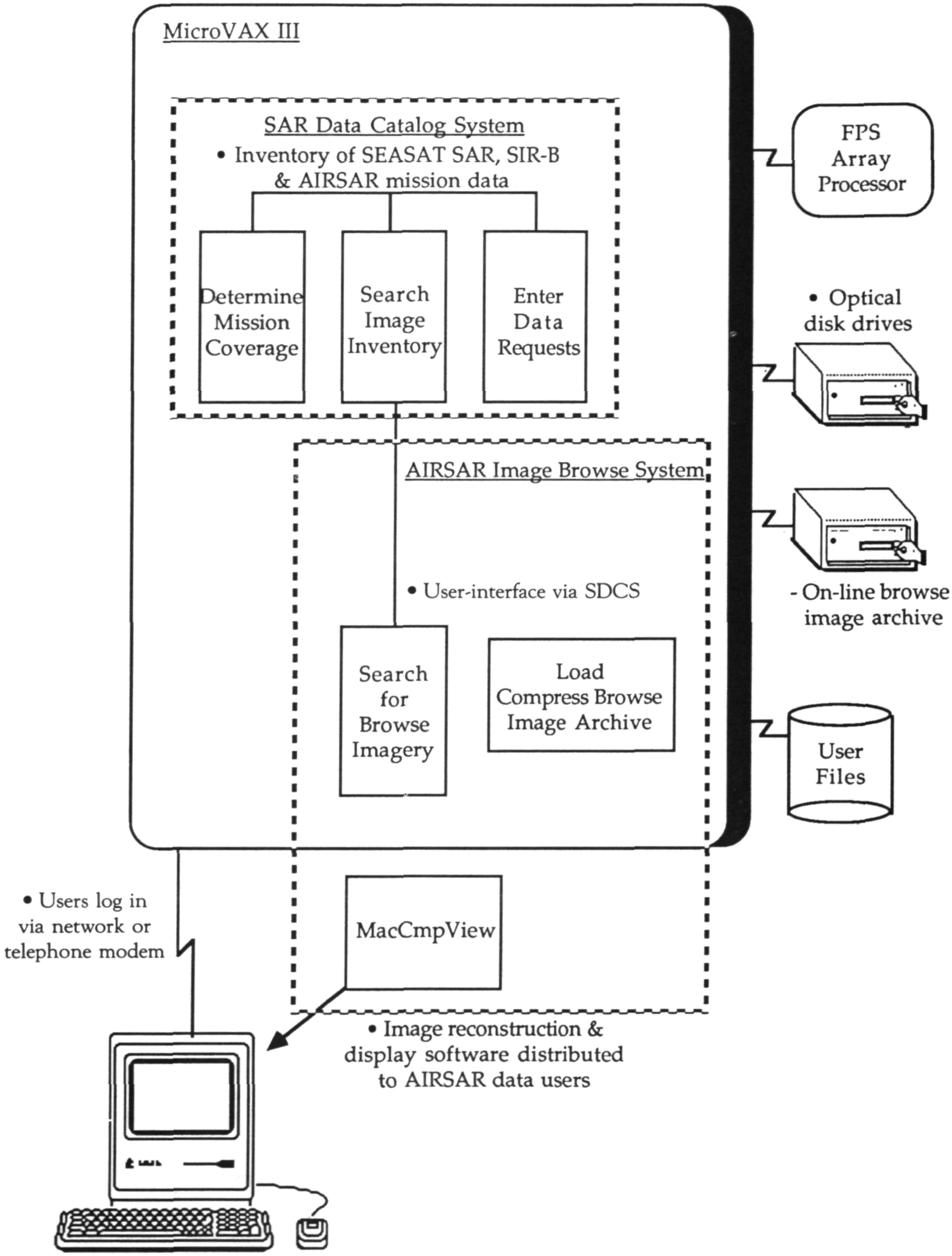

Figure 1: Block diagram showing SDCS with AIRSAR image browse system.

ORIGINAL PAGE
BLACK AND WHITE PHOTOGRAPH

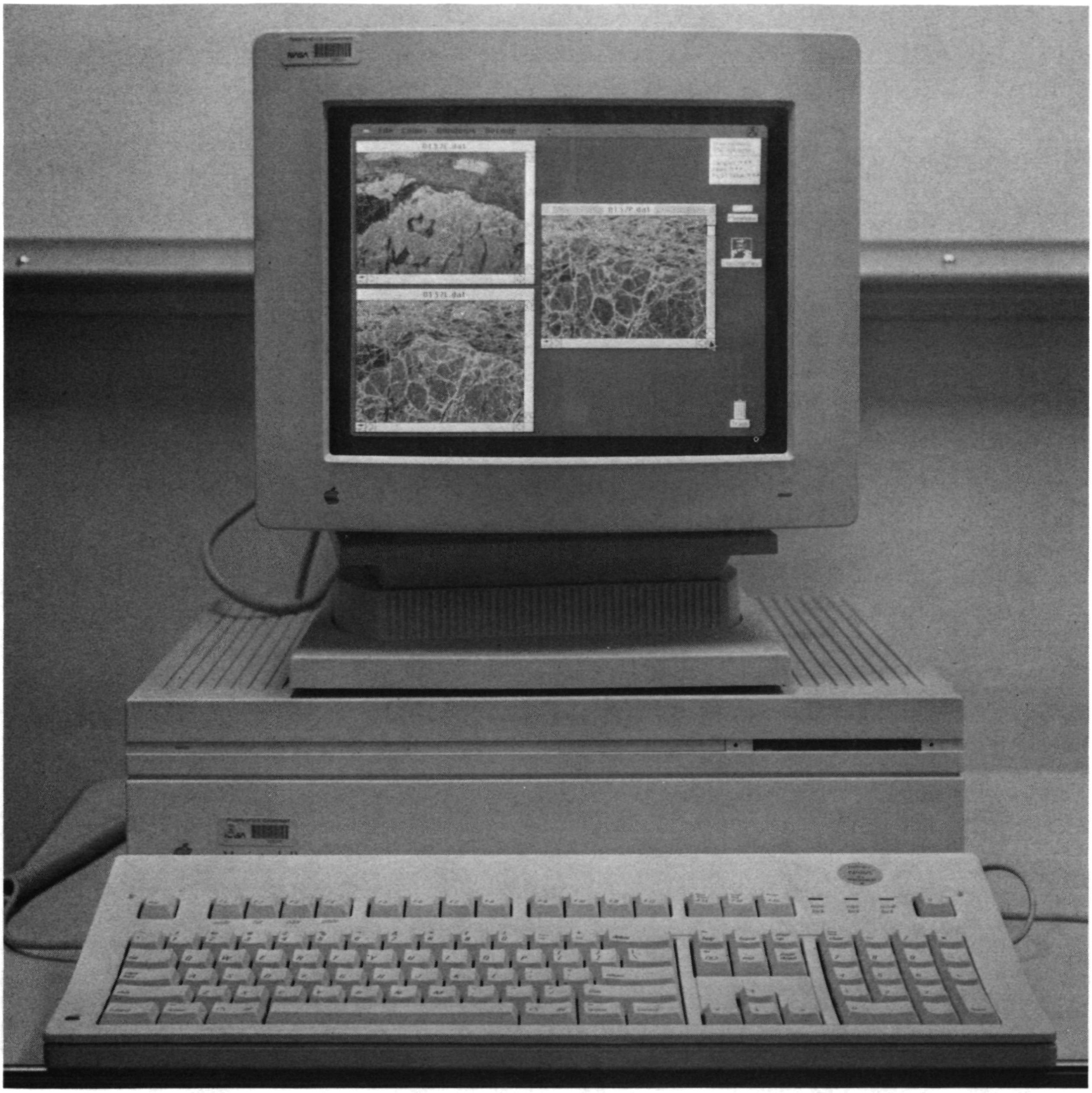

Figure 2: MacCmpView browse image reconstruction and display program.

ORIGINAL PAGE
BLACK AND WHITE PHOTOGRAPH

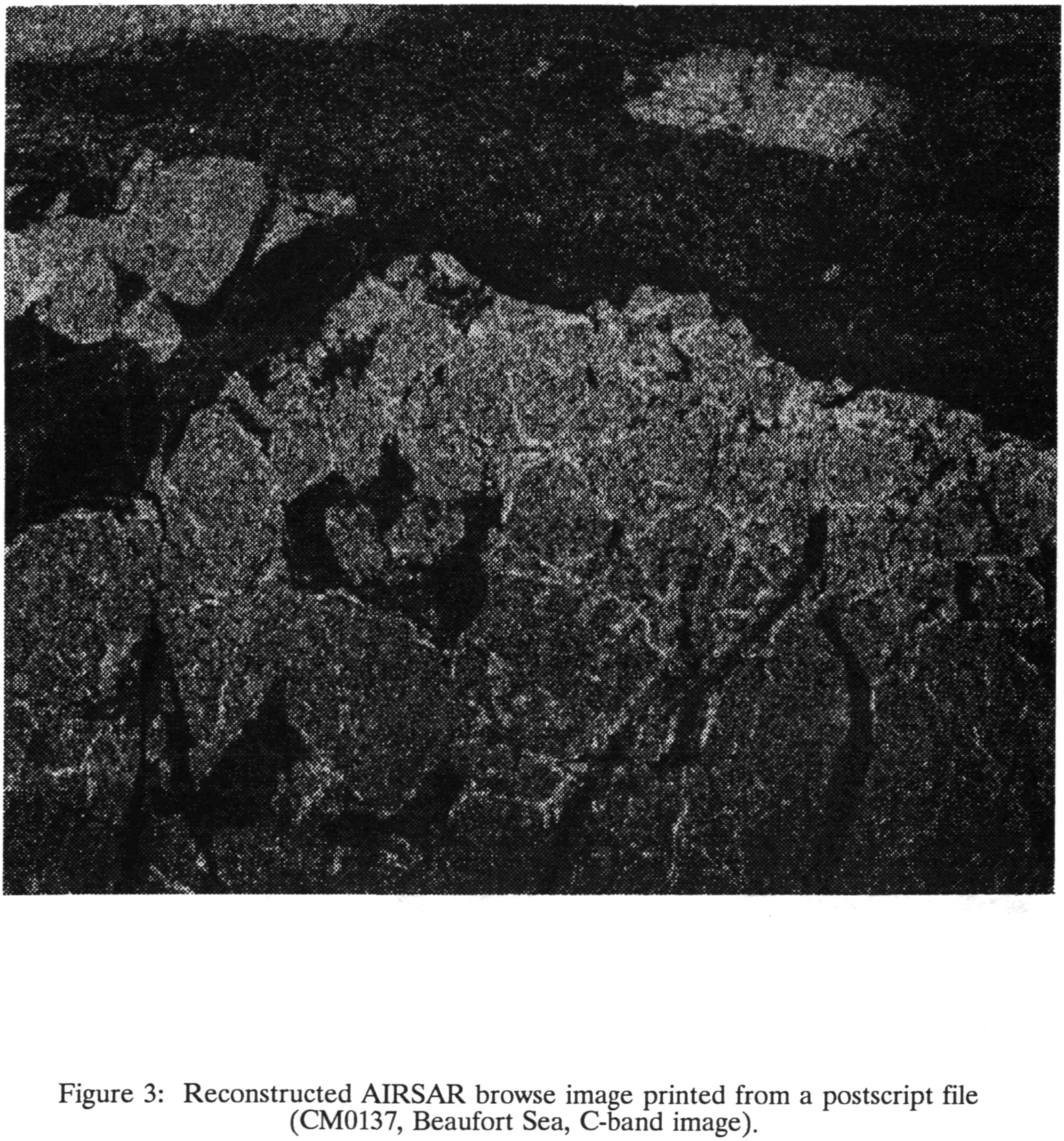

Figure 3: Reconstructed AIRSAR browse image printed from a postscript file (CM0137, Beaufort Sea, C-band image).

N92-28035

Geometric Rectification and Geocoding of JPL 's AIRSAR data over hilly terrain.

H. De Groof, G. De Grandi, A. J. Sieber
Commission of the European Communities
Joint Research Center - Ispra , Italy
Institute of Remote Sensing Applications - Advanced Technologies

Abstract: A post-processing system has been developed to georeference and geocode airborne SAR data collected by the JPL-AIRSAR system over hilly terrain during the 1990 MAESTRO1 campaign. Georectification relates image coordinates and object coordinates while the geocoding involves resampling. The georectification method uses a hybrid method based upon a number of navigational parameters and minimal two ground-control points which are referenced in both image and map space. The calculation of the intersection of the SAR signal wavefront and a digital elevation model allowed, within certain error bounds, acquisition of the object-to-image and image-to-object relationships.

I. Introduction

During the summer of 1990 JPL's AIRSAR collected polarimetric SAR data over a number of European sites in the framework of the MAESTRO1 campaign. The Joint Research Center's (JRC) site was located in the Blackforest in the Federal Republic of Germany. The Blackforest is a hilly to mountainous area covered by one of Western-Europe's most extended coniferous forests. JRC's prime interest in the area is the study of the interaction mechanisms between the forest canopies and the multi-frequency polarimetric SAR signal. Therefore a wide variety of physical characteristics of the forest canopy was collected on the ground at different levels of intensity over a number of forest stands in the area. This information was then stored in both the EURACS (European Radar Cross Section database) and as thematic layers in a geographical information system (GIS). In order to relate these forest characteristics and thematic layers to the AIRSAR data a geometric registration system needed to be implemented. Our scope was to attach to every pixel in the SAR data its geographic location. This process of georectification falls within the scientific field of radargrammetry, a science which goes back to the 1960's.

The 1960's and 1970's could be described as the age of airborne radargrammetry (ref 8) while the spaceborne implementations obtained extensive attention in the 1980's (ref 2,3,5,6,7). At this stage it has to be recognized already that from the conceptual point of view the problem hasn't changed since the 1960's.

II. General Problem Definition

For a radargrammetric formulation we need to define the sensor position vector, $S(t) = [s_x(t), s_y(t), s_z(t)]$ and the antenna angular attitude described by roll angle, $\rho(t)$, pitch angle, $\xi(t)$ and yaw angle, $\Upsilon(t)$. All quantities being a function of the time interval, t_0 to t_n over which the radar data were collected. The attitude of a SAR antenna is merely defined by its velocity vector, $V(t) = [v_x(t), v_y(t), v_z(t)]$.

The following reasoning applies to one time vent, t_m and its notation will therefore be dropped. The definition of the object coordinate system with unit vectors O1,O2,O3 and the sensor coordinate system with unit vectors U1, U2, U3 allows definition of the position vector S of a point p in object space as (Figure 1)

$$S = p_x O1 + p_y O2 + p_z O3 \tag{1}$$

and in sensor space with a position vector R as

$$R = u_p U1 + + v_p U2 + w_p U3 \tag{2}$$

Hence,

$$P = S + R \tag{3}$$

Given a squint angle, τ and a look-angle, θ (Figure 2) we can write

$$\begin{aligned} u_p &= R \sin \tau \\ v_p &= R (\sin^2 \theta - \sin^2 \tau)^{0.5} \\ w_p &= -R \cos \theta \end{aligned} \tag{4}$$

The product of the vector $T = [u_p, v_p, w_p]$ with the rotation matrix, A rotates the sensor system U1,U2,U3 into the object system O1,O2,O3:

$$P = S + A . T \tag{5}$$

where

$$A = \begin{bmatrix} U1_x & U1_y & U1_z \\ U2_x & U2_y & U2_z \\ U3_x & U3_y & U3_z \end{bmatrix} \tag{6}$$

The elements of A can contain the attitude angles, ξ, Υ and ρ or, in the case of a SAR system the velocity vector, V.

$$\begin{aligned} U1 &= [U1_x, U1_y, U1_z] = V / | V | \\ U2 &= [U2_x, U2_y, U2_z] = (V \times V) / | V \times V | \\ U3 &= [U3_x, U3_y, U3_z] = (U1 \times U2) / | U1 \times U2 | \end{aligned} \tag{7}$$

It is clear that the sensor roll angle, ρ does not enter the transformation matrix A. Roll has no geometric effect on the SAR image.

If both the velocity vector V and the rotation matrix A are known (by measuring the antenna's accelerations for example) we can solve a system with 3 equations (5) and four unknowns, being p_x, p_y, p_z and the look-angle, θ. If we eliminate the look-angle θ we reduce the problem to solving the following 2 equations with 3 unknowns:

$$R = | P - S | \tag{8}$$

$$U1 (P - S) = \sin \tau \, | U1 | \, | P - S | = \sin \tau \, . \, R \tag{9}$$

Consequently the radar projection case of a point can be resumed as the intersection of a range sphere, defined by equation 8 with the cone of equation 16.

The range sphere relates to the echo-time measurement which is inherent to a radar system. The geometric concept of a squint angle,τ in the SAR imaging process corresponds to the physical concept of Doppler frequency. The cone of equation 9 corresponds to lines of iso-doppler.

Equation (9) can therefore be written as

$$f_D = 2. / \lambda R \, . \, (U1 \, . \, (S - P)) \tag{10}$$

where

λ = wavelength

f_D = Doppler frequency

Equations 8 and 9 or 10 are most commonly used as the start point for every algorithm, whether airborne or spaceborne applications are concerned. Adding an object velocity vector and an object elevation wouldn’t change any of these basic concepts.

III.Georeferencing AIRSAR data

A. The Status of the Ancillary AIRSAR data Relevant for Georeferencing

Section II made clear that in order to construct a rigorous parametric model of the AIRSAR’s viewing process the following parameters need to be known:

The positioning vector of the antenna, S in object space at every sample position along the flight track.

The velocity vector, V of the antenna.

If we would tackle the problem from the Doppler point of view we would ideally need the Doppler frequency used in the correlation process for every SAR data sample.

The header associated with the AIRSAR data contains only a very limited set of parameters which could be of potential use in georeferencing the parametric model. Moreover, they are not associated with every along-track sample position. The sensor's position vector and velocity vector is unknown. The altitude of the platform is specified without a geometric basis or reference plane. We therefore retained only the azimuth pixel spacing, APS, the slant-range pixel spacing, SPS and the distance to the first slant-range pixel, FSP as an input in our georeferencing system.

B. Additional Requirements for the Georeferencing process

When we relate the timing, range and Doppler frequency parameters to the Earth's position we essentially determine the intersection of the range sphere with the Earth's surface if we assume the data have been processed at zero Doppler (a squint angle, $\tau = 0$). It is clear from Figure 2 that local elevation results in an intersection point which is different from the one on the reference surface. The mapping of the slant-range to the reference surface will have to correct for the displacement effect and the scaling errors. Therefore the availability of a digital elevation model,DEM is a prerequisite for the georeferencing of the AIRSAR data over the Blackforest.

The DEM available to us has a gridsize of 30 by 30 meters.

C. The Georeferencing Algorithm

Our first step was to construct the antenna's position vector in the object space.

The following two basic hypotheses regarding the processing of the AIRSAR data were formulated. The data have been processed at zero doppler. The azimuth sample spacing is constant along the flight-track.

Since it is our ultimate goal to refer the image azimuth-range coordinates to a map based information system we will further refer to the object space as map space.

1. Reconstruction of the Flight-track

The direction of the Velocity vector is required at every sample interval along-track.

Therefore ground control points, GCP were selected in both map and image space.

The control points were then grouped two by two where we tried to minimize the azimuth distance between the two points as much as possible. The angle δ between the geographical

North of the map and the vector connecting both points can easily be computed by :

$$\delta = \mathrm{atan}\ (\ (gcp2\_mx - gcp1\_mx)^2 / (gcp2\_my - gcp1\_mx)^2) \tag{11}$$

(_mx are map coordinates)

the distance between the two control points, G in map space by :

$$G = ((gcp2\_mx - gcp1\_mx)^2 + (gcp2\_my - gcp1\_mx)^2)^{0.5} \tag{12}$$

the along-track distance, K between the two GCP's :

$$K = |\ (gcp1\_ix - gcp2\_ix\ )\ .\ APS\ | \tag{13}$$

(_ ix are image coordinates.)

where APS corresponds to the along-track pixel spacing found in the image data header.

The track angle, κ from the North is then derived by

$$\kappa = \delta - \mathrm{acos}\ (\ K / G) + \pi / 2 \tag{14}$$

The track angle, κ is then stored for as many positions along track as we registered GCP pairs. Depending upon the trend of κ along-track first or second degree functions have been fitted resulting in a value for κ at every along-track position.

2. Determination of the Altitude of the Antenna above the Reference Plane

A second essential parameter is the altitude of the sensor along-track.

This has been achieved by simple trigonometric calculations and using the range information in the slant-range image. We used the same GCP pairs as used in section C.1.

The distance from the sensor to the GCP's,SR1 and SR2 is found from

$$SR1 = FSP + gcp1\_ix * SPS \tag{15}$$

$$SR2 = FSP + gcp2\_ix * SPS$$

where FSP is the distance to the first slant-range pixel and SPS, the slant-range pixel spacing as found in the JPL header.

The across-track distance between the two GCP's , RD when they are aligned perpendicular to the flight-tack is given by

$$RD = (\ K^2 - G^2)^{0.5.} \tag{16}$$

let

$$\Omega = \mathrm{atan}(dh / RD) \tag{17}$$

and

$$B = dh / \sin(\Omega) \tag{18}$$

where dh = h2 - h1 , the elevations of the GCP's.

Then the sensor's altitude, H is given by:

$$H = \sin (\pi - \operatorname{acos} ((SR1^2 + B^2 - SR2^2) / (2 \ SR1 . B)) + \Omega) + h1 \qquad (19)$$

where h1 equals the elevation of the GCP closest to the flight-track.

The sensor altitude, H is then stored for as many positions along-track as we registered GCP pairs. Depending upon the trend of H along-track first or second degree functions have been fitted resulting in a value for H at every along-track position.

3. Determination of the Map coordinates of the Sensor's Flight-track

The sensor's elevation, H(t) and track angle, $\kappa(t)$ for a given number of along-track positions corresponding to events t and a number of GCP's map and image coordinates allows the computation of the map coordinates of the first slant-range image coordinates at events t.

For every GCP the position in the DEM can be computed and the elevation interpolated. By following a profile in the DEM whose direction corresponds with the track angle + $n\pi$, the intersection of the range projection sphere with the DEM and the corresponding projected slant-range pixel size can be computed (see Figure 2).

Let the equation of a segment of the DEM in a coordinate system with origin at the sensor's position be given by

$$y = mx + t \qquad (20)$$

the range sphere's projection circle by

$$x^2 + y^2 = r^2 \qquad (21)$$

where r corresponds to the slant-range distance to a point at a position $y = (H - h)$ and x corresponds to the ground range of the GCP point, $x = (sr1^2 - H^2)$.

The ground-range coordinate xi of the intersection along the ground range profile is then given by

$$xi = (- mt \ / (m^2 + 1)) + f ((1 / m^2 + 1) ((r^2 m^2 + r^2 - t^2)^{0.5})) \qquad (22)$$

where f = +1 or -1.

For every intersection, xi the map coordinates are derived. The slant-range, r and ground-range position, x are updated until the coordinates of the first slant range pixel of the SAR image at event t are found. Since the elevation of every intersection is found as well, the relief corrected coordinate of the sensor's flight track can be found.

This procedure is repeated for all available GCP's. Again a function is fitted to the map coordinates of the sensors ground track as a function of along-track position.

4. Mapping the Slant-Range Coordinates to the Object Coordinate System

The ground track and sensor elevation are known for every along-track position from section C.2 and C.3. The slant range to the first pixel is known from the JPL header.

The same procedure described in C.3 is then used to retrieve the map coordinates for every slant-range image pixel starting from the near-range to the far-range for every along-track sample event. In addition to the elevation, the local incidence angle, δ the projected slant-range pixel size,PR2 the along-track aspect angle and a shadow map are stored (figure 2 and slide 23).

D. Results of the Georeferencing

It has to be recognized that the results are highly determined by the accuracy with which the sensor's position vector can be reconstructed. If we reject any contribution to the geometrical errors caused by possible shortcomings in the SAR instrument as drifts in the radar frequency, timing errors, or linear phase offsets and assume optimal processing at zero doppler, we still face a wide range of potential errors which might influence the final accuracy of our geo-referencing efforts. Although it is acceptable to represent the Earth's surface by a high-precision topographical map (and digital elevation model) in the case of the limited spatial coverage of the AIRSAR images errors will be introduced by these assumptions.

Therefore the results obtained are very much case dependent. The results of a typical geo-referencing process are presented in table 1.

The results of table 1 have been obtained after fitting a linear function to the ground-track. Fitting a higher order polynomial or piece-wise approximations might improve the results.

An error measure for an entire scene does not make sense since our objective is to assign to every pixel its corresponding map position. A visual evaluation of the georeferencing accuracy is obtained by mapping thematic layers from our GIS database to the slant-range image as is illustrated in slide 24.

GCP	error in Easting(m)	error in Northing(m)
1	65.09	-20.04
2	-11.05	-37.94
3	-16.60	48.25
4	-15.10	-53.74
5	-18.40	16.68
6	-13.89	-10.70
7	-16.77	-15.54
8	-9.35	-10.17
9	-5.02	-31.49
10	-10.61	-14.52
11	-14.38	-19.18
12	-3.62	-7.63
13	-8.87	35.18
14	-10.07	5.41
15	-13.82	-22.46
16	-17.50	-20.01

Table 1. Errors in map coordinates for a number of GCP

E. The Geocoding Step

The geocoding process is aimed at producing a radar-orthophotomap in a desired map projection system. It therefore requires a resampling step. The effect on the spatial and radiometric properties of resampling, even on non-polarimetric SAR data , has not yet been fully understood (Ref. 6). In the case of polarimetric SAR data the problems become even more complex. At this stage of research we decided to assign to a pixel in the radar orthophotomap its corresponding nearest neighbor in the slant-range image. We are fully aware of eventual violations of sampling theorem and spatial distortions which might result from this operation. Yet, it has to be kept in mind that we do not support any analysis on these products.We rather convert our ground observations to the slant-range projection, as illustrated in slide 24.

F. Conclusions

Ten years ago radar data sets were generated and georeferenced with techniques and algorithms very similar to the one presented in this paper. The authors noted at that time that the geometric accuracy did not seem to be of great concern, since the interpretation of image detail was the focus. Yet they were optimistic that future radar systems would provide digital, image-referenced navigational and attitude data. The MAESTRO1 data sets still lack this information.

The results obtained by implementing the previously described processing system might be sufficient for some applications, but for others they definitely are not. It is our belief that the generation of products such as absolute map position or pixel, local incidence angle, and others will greatly help us to improve our knowledge of the backscatter mechanisms. The user community would therefore greatly benefit from more extensive sensor positional information.

G. References

1. Guidon, B., P.M. Teillet, and D.G. Goodenough, Relief Effects and the Use of Digital Terrain Models in SAR Image Processing, Canada, 1980.

2. Naraghi, M., W. Stromberg, and M. Daily, Geometric Rectification of Radar Imagery Using Digital Elevation Models, *Photogrammetric Engineering and Remote Sensing,* Vol. 49, No. 2, Pasadena, CA, 1983.

3. Curlander, J., Utilization of Spaceborne SAR Data for Mapping, *IEEE Transactions on Geoscience and Remote Sensing,* Vol. GE-22, No. 2, 1984.

4. Blacknell, D., A. Freeman, G.W. White, and J.W. Wood, *IEEE Transactions on Geoscience and Remote Sensing,* Vol. GE-25, No. 6, 1987.

5. Curlander, J., R. Kwok, and S. Pang, A Postprocessing System for Automated Rectification and Registration of Spaceborne SAR Imagery, *Int. J. Remote Sensing,* Vol. 8, No. 4, 1987.

6. Sowter, A., D.J. Smith, J.E. Laycock, H. Raggam, D. Strobl, and G. Triebnig, An Error Budget for ERS-1 SAR Imagery, ESA Study Contract Report No. 7689/88/HGE-I, 1990.

7. Nuesh, D.R., E.H. Meier, D.K. Baettler, K. Graf, and F. Holecz, Merging Spaceborne Image Data of Optical and Microwave Sensors.

8. Leberl, F.W., Photogrammetric Aspects of Remote Sensing with Imaging Radar, *Remote Sensing Reviews,* Vol. 1, No. 1, London, 1983.

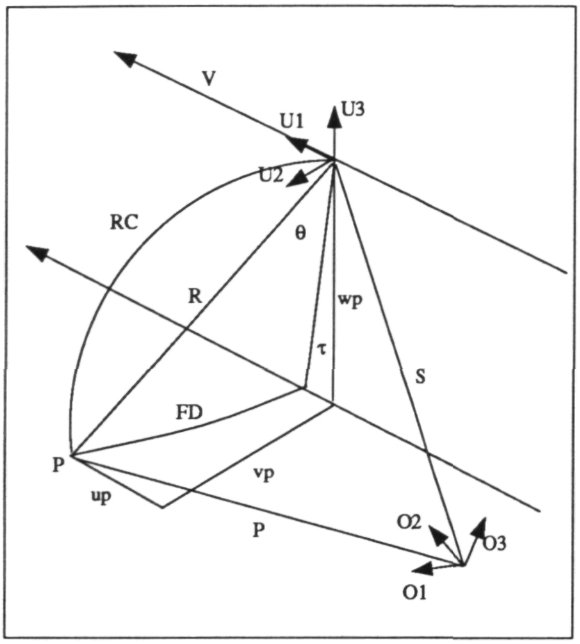

Figure 1. Defining Object and Image Space

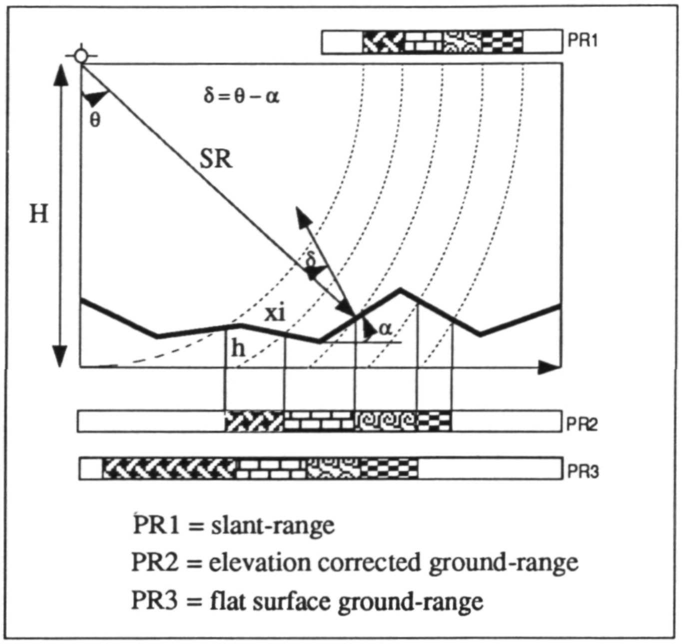

PR1 = slant-range
PR2 = elevation corrected ground-range
PR3 = flat surface ground-range

Figure 2. Relations between range projection circle and terrain elevations

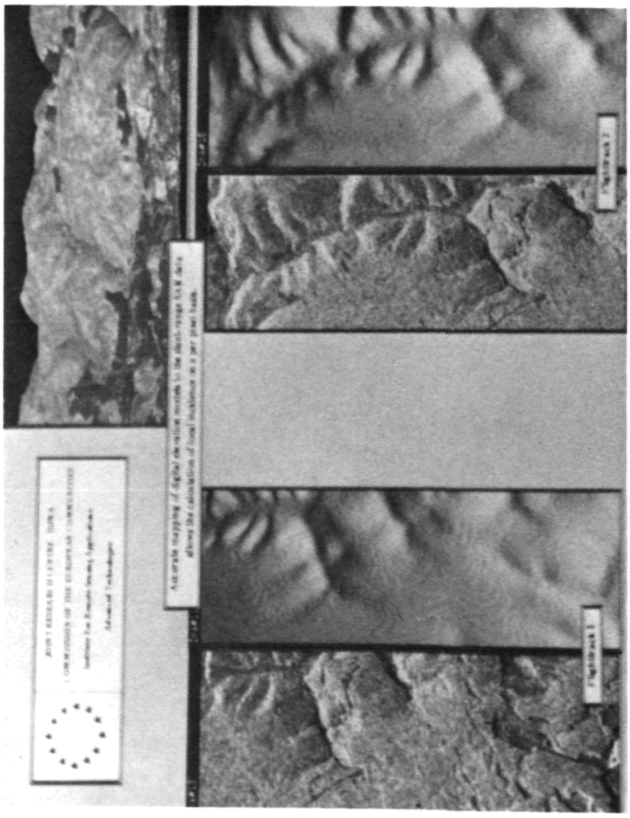

Slide 1 (see color slide no. 23)

Slide 2 (see color slide no. 24)

N92-28036

Approaches to Vegetation Mapping and Ecophysiological Hypothesis Testing Using Combined Information from TIMS, AVIRIS, and AIRSAR

R. Oren
Duke University

G. Vane, R. Zimmermann, V. Carrere,
V. Realmuto, and H. Zebker
Jet Propulsion Laboratory
California Institute of Technology

P. Schoeneberger
N. Carolina State U.

M. Schoeneberger
U.S. Forest Service

Abstract. The Tropical Rainforest Ecology Experiment (TREE) had two primary objectives: (1) to design a method for mapping vegetation in tropical regions using remote sensing and determine whether the result improves on available vegetation maps, and (2) to test a specific hypothesis on plant/water relations. Both objectives were thought achievable with the combined information from the Thermal Infrared Multispectral Scanner (TIMS), Airborne Visible/Infrared Imaging Spectrometer (AVIRIS), and Airborne Synthetic Aperture Radar (AIRSAR). Implicitly, two additional objectives were (3) to ascertain that the range within each variable potentially measurable with the three instruments is large enough in the study site, relative to the sensitivity of the instruments, so that differences between ecological groups may be detectable, and (4) to determine the ability of the three systems to quantify different variables and sensitivities. We found that the ranges in values of foliar nitrogen concentration, water availability, stand structure and species composition, and plant/water relations were large, even within the upland broadleaf vegetation type. The range was larger when other vegetation types were considered. Unfortunately, cloud cover and navigation errors compromised the utility of the TIMS and AVIRIS data. Nevertheless, the AIRSAR data alone appear to have improved on the available vegetation map for the study area. An example from an area converted to a farm is given to demonstrate how the combined information from AIRSAR, TIMS, and AVIRIS can uniquely identify distinct classes of land use. The example alludes to the potential utility of the three instruments for identifying vegetation at an ecological scale finer than vegetation types.

Introduction

Vegetation maps of inaccessible areas in the tropics tend to divide vegetation into broad types such as broadleaf deciduous or deciduous semi-evergreen seasonal forest, high or low marsh forest, cohune palm forest, and others. These maps are based mostly on aerial photography and on the relationship between topography and soils and vegetation obtained with limited validation on the ground. Within each vegetation type which appears homogeneous from a bird's-eye view, there are groups of vegetation, each unique in one or more characteristics. These characteristics include size-species distribution, vertical canopy structure, demand for nutrients, water and tissue concentration of nutrients, and water content. The function of ecosystems, both as a home for numerous animal species and in terms of matter and energy cycles, depends on the number, size, and arrangement of these groups.

The main objective of the Tropical Rainforest Ecology Experiment (TREE) was to improve on the existing vegetation maps available for northwestern Belize, by producing a map in which each vegetation type is further divided into ecological groups. We intended to do so by combining data on ecologically relevant variables obtained with three remote-sensing instruments: TIMS, AVIRIS, and AIRSAR. These variables include surface (mostly canopy) temperature with TIMS; nitrogen, lignin, and chlorophyll concentrations and leaf-area index (LAI) or normalized difference vegetation index (NDVI) with AVIRIS; and several stand structural characteristics, forest floor flooding status, and plant/water relation conditions (water content or potential) with AIRSAR. With either a statistical technique (e.g., canonical correlation) or a geographical information system (GIS), each pixel was to be classified based on a set of predetermined ranges in each variable. All pixels classified similarly based on all variables would be considered an ecological group of a unique characteristic.

The secondary objective of TREE was to test the hypothesis that tropical tree species respond to drought in one of three ways: (1) by shedding foliage, (2) by reducing transpiration through stomatal regulation, or (3) by continuing to transpire in direct relation to the atmospheric vapor pressure deficit, which would result in a reduction in tissue water content and/or potential. AVIRIS estimation of lower NDVI should detect groups that contain a large proportion of trees responding by shedding leaves. TIMS estimation of higher canopy temperature, resulting from lower transpirational cooling, would detect groups dominated by species responding by increasing stomatal resistance to water flux. AIRSAR estimation of lower water content or potential would identify groups dominated by species without control over water loss. Such groupings might result from either differences in the stage of stand development since the last disturbance and the type of disturbance, or from variations in soil/water relations (e.g., annual trends in water availability, height of water table, or persistence of perched water table).

Study Area

The Rio Bravo Resource Management and Conservation Area encompasses more than 1000 km^2 in northwestern Belize (Fig. 1). It is mostly wild, tropical forest, uninhabited and little disturbed. Near its southern border, the Rio Bravo contains a farm with lightly to greatly disturbed areas, e.g., coffee plantations under intact canopy, citrus and banana plantations, corn and sorghum fields (which were at an early germination stage at the time of the overpasses), recently clear-cut forest with trees still on the ground, and abundant fields at various stages of regeneration.

The climate in northern Belize places it in the "subtropical moist" life zone (Holdridge et al., 1971). The Rio Bravo lies between 17° and 18° N latitude, geographically in the transition between the tropics and the subtropics (Brokaw and Mallory, 1989). The annual precipitation, which averages 150 cm, is typically distributed unevenly between the wet season (≈25 cm/month, June through January) and the dry season (<10 cm/month, February through April or May).

Elevation at the Rio Bravo ranges from 50 to 220 m above sea level. In upland areas to the west are calcareous soils from Eocene limestone rock; in depressions are thick wetland deposits of calcareous clay or loam; and on the northeast is a band of siliceous soils deposited as sediments from the Mayan Mountains on a former shoreline. The effect of different processes of soil formation resulted in 11 upland calcareous soil types which support forest (Brokaw and Mallory, 1989). These soils vary greatly in moisture-holding capacity; some are excessively dry. The lower, wetland soils are of two very different types: deep clays and peaty loams. Deep clays occur in wooded, shallow depressions, termed "bajos" or "akalches." Bajos are thought to be infertile. Bajo soils are often submerged during the wet season, but create a condition of "edaphic drought" (Lundell, 1937) for vegetation during the dry season. Peaty loams occur mostly under a broad strip of marsh east of the Booth's River Escarpment. These soils are submerged during the wet season and remain mostly wet even during the dry season. Highly infertile siliceous soils in the northeast part of the Rio Bravo support savanna vegetation. During periods of heavy rain the upper layer becomes saturated, but it is exceedingly arid during the dry season (Brokaw and Mallory, 1989).

Five major vegetation types, with several variants of each, are found in the Rio Bravo. The vegetation types are upland broadleaf forest covering about 63% of the area, swamp forest including bajo vegetation (20%), palm forest (8%), marsh (7%), and savanna (2%). The vegetation types vary greatly in species composition, tree density and size (both diameter and height) distribution, nutritional requirements, and phenology. Topography, soil type, water regime, and historical land use (during both the Maya civilization and the 20th century) interact to affect the distribution of the vegetation types and their variants (Brokaw and Mallory, 1989).

Methods

Ecological ground measurements were made to generate data necessary to interpret remote-sensing information and to characterize the canopy. The ground measurements were designed to evaluate the capabilities of the remote-sensing instruments. As a minimum we expected the instruments to be able to separate among broadly defined vegetation types. As a maximum we hoped they would succeed in separating among ecological groups within each vegetation type. In addition, the ground measurements were to be used to test hypotheses regarding the response of various species to drought.

We established eight plots: five plots in a mature upland broadleaf forest, one in a regenerating upland broadleaf forest, one in a bajo, and one in another swamp forest of a greater flooding duration than the bajo. The second swamp forest contained larger diameter trees at a lower density. The five plots in the upland broadleaf forest type represented a gradient in moisture regime, in the density of palm in the upper canopy, and in the general appearance of the stands. However, from aerial photography these upland forest plots are difficult to differentiate. Plots had dimensions of at least 120 × 200 m, permitting averaging of about eight pixels of TIMS (ground pixel size 50 m from an altitude of 20 km), 60 pixels of AVIRIS (20 m from an altitude of 8 km), and 240 pixels of AIRSAR (10 m from an altitude of 8 km). Twice these numbers of pixels can be obtained within the larger plots.

Ecological variables measured included:

(1) Nitrogen concentration of upper canopy foliage, harvested in May 1990 with a shotgun and dried at 70°C for 48 hours, was determined with a Carlo Erba C/N Analyzer (see Oren et al., 1988, for a full description of the procedure).

(2) Saturated hydraulic conductivity of the soil (K_{sat}) was measured in March and again in May 1990 with a compact constant-head permeameter (Ammozegar, 1989).

(3) Transpiration sap flux was measured in six to nine trees in each of the five upland broadleaf forest plots from March 1990 to March 1991 with heat flux density measurement sensors (Granier, 1985). These sensors measure the temperature gradient between a heated, constant-energy-output heat source and the tree trunk temperature. Sap flux density is calculated based on the measured gradient. This method requires the estimation of the total hydroactive xylem area, which was done by taking tree core samples next to each sensor at the end of the study.

(4) Temperature and relative humidity measurements were also made in the upper canopy of the five upland broadleaf forest plots, in parallel with the heat-flux measurements. The measurements were made with a temperature/relative-humidity sensor (Delta-T Devices). Measurements were averaged and logged as the heat-flux measurements.

The TIMS and AVIRIS were flown on the NASA ER-2 on March 15, 1990. The TIMS is a six-channel airborne instrument that measures radiation in the 8-to-12-μm region of the electromagnetic spectrum (Kahle and Goetz, 1983). The instrument has a 2.5-mrad field of view (FOV), which from the 20-km operational altitude of the ER-2 produces digital imagery with a ground pixel size of 50 m and a swath width of about 30 km. TIMS carries two internal heat sources which are monitored with every scan line. The measurements of these references are used to reduce the digital numbers recorded by the instrument to units of radiance. AVIRIS is an imaging spectrometer that gathers high-spectral- and spatial-resolution images from 0.4 to 2.5 μm in 10-nm-wide contiguous spectral bands (Vane, 1987). From the NASA ER-2, the ground pixel size is 20 m and the swath width is 10.5 km. The images are 614 pixels across and are gathered in 224 spectral bands. Raw AVIRIS data are calibrated to spectral radiance using laboratory- and/or field-derived calibration files.

Because of the anomalously cloudy conditions in March 1990, during the period when clear skies typical of the local dry season normally occur, it was decided to have the ER-2 fly over the study site six successive times on March 15 to increase the likelihood of at least one clear view of each plot and the calibration targets. At the time of the overflights, cloud cover was 1/8 to 4/8 cumulus with no cirrus. Most of the vegetation sites of interest were imaged, but a navigational error on the aircraft resulted in failure to acquire any data over one of the AVIRIS calibration sites. The combination of cloud cover and navigational error caused the TIMS calibration site to be viewed on only three of the six flight lines. A second ER-2 flight was planned for the next and final day of the campaign, March 16, when cloud cover was less, but a power failure on the aircraft forced the mission to be aborted.

Ground measurements at the time of the ER-2 overflight included the following:

(1) Reagan sun photometer measurements from sunrise until mid-afternoon, interrupted intermittently by clouds. The purpose of these measurements was to characterize the atmosphere in terms of optical depth and total column abundance of atmospheric water vapor and ozone, required to correct AVIRIS data to reflectance.

(2) Airsonde measurements of water vapor content and atmospheric temperature and pressure, for correcting both TIMS and AVIRIS data.

(3) Portable Instantaneous Display and Analysis Spectrometer (PIDAS) (Goetz, 1987) measurements of calibration targets to be used to make an atmospheric correction for AVIRIS. Two targets were characterized, a bright and a dark target. The dark target was missed by the aircraft because of the navigational error.

(4) The temperature of Laguna Verde, a deep lake, was measured with a calibrated radiant thermometer in order to calibrate TIMS data. This target was missed by the aircraft on three of the six passes.

(5) PIDAS measurements of leaves were made for correlation with AVIRIS reflectance spectra acquired over the canopies at the test sites.

We attempted to reduce the TIMS data to ground temperature by using the LOWTRAN 6 radiative transfer code to model the radiance of the atmosphere. The brightness temperature measurements of Laguna Verde were used to evaluate the final accuracy of our model. The atmospheric temperature and humidity profiles obtained with the airsonde were entered into the LOWTRAN code and were manually modified until a uniform emissivity spectrum was recovered over a selected portion of the forest canopy. In the final analysis, we determined that the humidity and temperature of the atmosphere were too variable to be characterized by a single airsonde sampling.

The AVIRIS data were calibrated to radiance using the JPL laboratory calibration. The radiance values derived from the data in this manner represent the combined radiance of the atmosphere and the Earth's surface. In order to characterize plant biochemistry, it is necessary to convert the radiance data to surface reflectance. This can be done in one of the following two ways:

(1) Use a radiative transfer code such as LOWTRAN 7 and sun photometer measurements of atmospheric depth, or

(2) Use a regression technique which requires an independent measurement of the reflectance of a bright and a dark target in the scene, as we did with PIDAS.

Because clouds interrupted the sun photometer measurements of optical depth, technique (1) above could not be used, and because the aircraft missed the dark calibration target, technique (2) could not be used. Therefore, we decided to use the radiance data themselves and the so-called "greenness index," or normalized difference vegetation index (NDVI) to look for differences in the vegetation cover in the vicinity of the Gallon Jug Ranch. The NDVI has been used for many years to map green vegetation with satellite data. It takes advantage of the high contrast between the red and infrared response characteristics of vegetation compared to soils. Fig. 2 illustrates the differences in spectral reflectance of vegetation and soil over the solar reflected portion of the spectrum.

The NDVI corresponds to the ratio

$$(\text{Infrared} - \text{Red})/(\text{Infrared} + \text{Red})$$

From the AVIRIS data we used spectral band 42, centered at 761.6 nm, for the infrared, and spectral band 29, centered at 675.4 nm, for the red. The resulting ratio image was then density sliced using a look-up table to produce a color image in which dark blue represents a low concentration of green vegetation and red represents a high concentration. Such an image is presented and described later in this paper.

AIRSAR was flown on March 15 aboard the NASA DC-8, which flew a series of parallel east-west flight lines to acquire data for a 50-by-50-km mosaic image of Rio Bravo, Belize, and nearby portions of Guatemala and Mexico. AIRSAR is a three-frequency multipolarization imaging radar that transmits and receives multipolarized radar signals at wavelengths of 5.6, 23, and 67 cm (C-band, L-band, and P-band, respectively) (van Zyl, 1991). Polarization synthesis techniques permit viewing the resulting images illuminated with arbitrary polarization. Installed on the NASA DC-8 aircraft, AIRSAR produces images approximately 12 km across and up to 100 km long, with a ground pixel size of 10 m. The digital data are recorded aboard the aircraft on high-density tape and subsequently converted into images at the JPL AIRSAR ground processor in Pasadena.

Several days prior to the AIRSAR flight, corner reflectors were installed at several locations in the Rio Bravo area. Some were placed in open areas to calibrate the sensor. Others were placed in the canopies at the various test sites to attempt to quantify the penetration, particularly of P-band, through the canopy. The response of each of the reflectors is determined in a postprocessing step. The measurements from the reflectors positioned in the open areas are used to correct the amplitude response of the instrument. The responses from the reflectors placed in the canopies will be used to estimate the wavelength dependence of attenuation through the canopy, which we will attempt to relate to the light attenuation function of the forest.

Two separate data processors were used in the analysis of the AIRSAR data. First, the fully polarimetric frame processor, which produces 12 channels (three frequencies and four polarizations each) of four-look data, was used to process 10-by-10-km regions over Gallon Jug, Chan Chich, and the Booth River. These data permit the complete polarimetric analysis required for scattering mechanism identification and accurate modeling. The second processor is a strip processor which develops 10-by-100-km images for a limited number of channels, typically three. An example from this processor, including one channel each from the P-,L-, and C-band radars, is discussed later.

Results and Discussion

(a) Ecology

There was a large range in foliar nitrogen concentration among the plots in the upland broadleaf forest type. Plot means ranged from 1.66% to 2.62% of dry weight. The foliar nitrogen concentration in the swamp forest type was 1.41% in the bajo and 2.21% in the taller, more flooded forest. Thus, variations were large within each vegetation type, and the range in nitrogen concentration became larger when ecological groups of both types were considered. Wessman et al. (1988) and Peterson et al. (1988) have demonstrated that, in principle, instruments similar to AVIRIS can be used to assess such differences in canopy chemistry.

Saturated hydraulic conductivity in the A horizon of soils in March 1990 ranged from 2 to 445 mm/hr among the plots in the upland broadleaf forest type. The lowest conductivity, 0.3 mm/hr, was found in the bajo plot. In May, after the soil dried and fissured, conductivity increased to between 103 and 777 mm/hr in the upland broadleaf forest type. The conductivity of the A horizon in the bajo increased to 694 mm/hr. Based on these data, it is clear that large variations in conductivity existed among plots on the day of the flights. This, combined with differential seasonal changes in conductivity among the vegetation types and plots within each type, implies that the mixture of species occupying each plot is likely to be somewhat different, conforming to the difference in conditions. Preliminary results on species density distribution in the plots confirm this conclusion.

Measurements of tree transpiration, performed from March 1990 through March 1991, revealed that species of the upland broadleaf forest type responded to drought in one of the three hypothesized ways, or in a combination of these ways with one response dominating.

In Fig. 3, daily transpiration is displayed in relation to the average daily saturation vapor pressure deficit, the atmospheric driving force of transpiration, during four 10-

day periods representing a range in soil moisture from wet to dry. *Drypetes brownei* shows stomatal response in all periods, coupled perhaps with partial defoliation during the dry season. Figure 4 shows that *D. brownei* controls the rate of water loss by reducing canopy conductance at midday, while the driving force remains relatively constant. This results in a reduction in the transpiration rate, which should be reflected in a higher crown temperature relative to the trees that maintain high transpiration rate when subjected to the same set of microclimate conditions.

The ability of TIMS to detect differences in canopy temperature has already been demonstrated in tropical forests (Luvall et al., 1990). The relationship between canopy temperature and the transpiration rate is implicit in another study demonstrating that relatively higher temperatures were recorded for trees growing on ancient Mayan roads (T. Sever, pers. comm.); compacted substrata reduce the ability of trees to extract water for use in transpiration.

The response of *Brosimum alicastrum* in Fig. 3 indicates a relative lack of control over stomatal conductance. Thus, in general, transpiration rate increases with the driving force for transpiration. *B. alicastrum* demonstrates some form of control over transpiration, which becomes apparent only at very high transpiration rates during the dry season. The general lack of control over the rate of water loss by *B. alicastrum* is apparent in Fig. 4. It shows that, after a short period of very high canopy conductance in the morning, conductance is stabilized at an intermediate level and does not vary much during the rest of the day. Thus, the diurnal pattern of transpiration rate follows closely that of the saturation vapor pressure deficit.

Pithecellobium arboreum appears to respond less to the driving force as conditions become drier (Fig. 3). The absolute transpiration rates are also reduced as the seasons progress from wet to dry. This is indicative of progressive loss of foliage. Indeed, there are several species in the study area that shed foliage in various amounts. The relationship between red and near-infrared reflectance has been used for over a decade to assess the amount of foliage over the ground, and it could be used to detect whether an area with relatively low canopy density occurs within the forest (Kimes and Kirchner, 1981; Guyot and Baret, 1989).

The transpiration rate on an area basis during the middle of the dry season (March 1991) in the upland broadleaf forest plots ranged between 0.4 and 1.8 mm/day, compared to a range of 0.3 to 0.6 mm/day during the wet season (Nov/Dec 1990). Based on this fact and on the results displayed in Figs. 3 and 4, we conclude that, if a species responds to drought by one of the three mechanisms described above, it should be possible to identify it with remotely sensed data. However, the results also indicate that the only time to separate the groups is during a drought, when transpiration exceeds precipitation.

There are days and times during the day that are more conducive to greater separation among trees, based on water relations. In Fig. 5, the 24-hour trend in transpiration is displayed in relation to the saturation vapor pressure deficit.

Transpiration increases at a faster rate and decreases at a slower rate on both dates, but the difference is markedly larger on a relatively dry day (left). The larger difference on dry days reveals that the trees are unable to take up water from the soil at a rate that matches their transpiration rate, thus using their internal storage of water. This should lower both moisture content and water potential on such a day more than on a relatively moist day. It is also clear that the plants are under greatest stress during the early afternoon, just before the decline in transpiration begins.

We conclude that maximum difference in water relation occurs among tropical species during the early afternoon, on relatively dry days, during the middle or latter part of the dry season.

(b) Remote Sensing

We planned to fly the instruments from late morning to early afternoon in March, typically one of the driest months of the year. In Fig. 6, precipitation measured in Gallon Jug, at the center of the study area, is displayed for 1990 and the early part of 1991. Typical dry-season precipitation is evident during March 1991. It is clear that the conditions during March 1990 were not normal for the dry season. Because of our limited flexibility in rescheduling flights, remote-sensing data were obtained under conditions that can cause only small water relation differences among species.

The passage of clouds interrupted the ground measurements of optical depth. In addition, a problem with the inertial navigation system aboard the ER-2 caused the pilot to miss the calibration targets of both TIMS and AVIRIS. As a result, the utility of the TIMS and AVIRIS data was strongly compromised.

In contrast to TIMS and AVIRIS, the acquisition of AIRSAR data proceeded without any difficulty. Lack of sufficient funding, however, resulted in only partial analysis of the data; results presented here only hint at the information that can be generated with AIRSAR. For more details regarding the AIRSAR data analysis, refer to Durden et al. (1991, in these proceedings).

Although the TIMS and AVIRIS data were not optimal, the information derived from them, presented on a relative basis and together with one of the AIRSAR images, serves as an example of how the three systems can classify an area properly where none of the systems alone could have done so as well. We used a temperature map generated from TIMS data, an NDVI map generated from AVIRIS data, and a map composed of CHH, LHV, and PHH backscatter derived from four-look AIRSAR data. These three maps are presented, along with the vegetation map available for the same area, in Fig. 7.

Based on TIMS data, the area designated as (2) is the warmest, indicating very little vegetation or unvegetated dark soil. The area designated as (1) is slightly cooler, which indicates that it either has more vegetation, is covered with mulch, or is a lighter colored soil. However, AVIRIS data reveal that area (1) is unvegetated, and AIRSAR data indicate that the backscatter is from large, horizontal objects. Put together, this information indicates a recently clear-cut forest where trees are still on the ground, the dead foliage and branches are acting as mulch, and no regeneration has yet taken place. Area (2), based on little backscatter, implies a relatively smooth surface with very small objects. Including the information from TIMS and AVIRIS, this can mean only germinating vegetation in recently plowed, dark soil.

TIMS and AVIRIS indicate that area (3) is cooler and more vegetated than areas (1) and (2). AIRSAR does not separate areas (2) and (3) very clearly; thus area (3) contains relatively low-lying small vegetation. Within area (3), both TIMS and AVIRIS identify two major temperature and vegetation cover zones which do not overlap completely. For example, the higher temperature is associated with two levels of vegetation cover, one of which is similar to the vegetation cover in area (4). Area (4) is an upland broadleaf forest. AIRSAR clearly separates it from the other areas. It can be concluded that area (3) is covered by short vegetation (e.g., small seedlings, herbaceous vegetation, or grasses, less than 50 mm tall). The vegetation covers the ground completely, unlike area (2), and contains groups that transpire at a similar rate as the adjacent forest, with a similar or lower NDVI.

The examples above rely mostly on differences among manipulated areas. We intended to perform a similar analysis over the natural vegetation types in the Rio Bravo, but because most of the necessary variables were unsalvageable we turned to a simpler "ecological" system for demonstration. Even in such a simple system it is apparent that each sensor provides unique information that is necessary for proper classification of vegetation and land uses.

Finally, a 16-look AIRSAR mosaic composed of CHH, LHV, and PHH is shown in Fig. 8 next to the vegetation map (Wright et al., 1959) of the same region. Even with only three variables incorporated in the analysis, an improvement over the currently available vegetation map is evident. A 14.75-km transect across the Booth River basin confirmed in detail the interpretation of the AIRSAR image. The color and grain consistently match the vegetation patterns seen on the ground. The image permits identification of upland broadleaf forest (mesic and dry), cohune ridge, cohune swamp, riparian forest, bajo, mangrove, and all the variants and transitions among them.

A classification based on all of the nonredundant AIRSAR information, synthesized with GIS, could provide ecologists and ecosystem scientists with the necessary base to study ecosystem structure and function. The incorporation of TIMS and AVIRIS data will improve the classification of natural ecosystems and will add more information on manipulated systems—information that is required by socioecologists, socioeconomists, and policy makers.

Conclusions

In conclusion, much was achieved on TREE, but much could yet be done with the data collected, especially if they were supplemented with those data sets that were not acquired for reasons noted elsewhere. In terms of the ecological aspects of TREE, we have established for the first time a long-term quantitative assessment of transpiration rates in a tropical broadleaf upland forest. With respect to the remote-sensing component of TREE, we have produced the SAR mosaic of a tropical rainforest, which has significantly more species information in it than the best previous vegetation maps of the area. We have also shown the potential of TIMS and AVIRIS to provide information of importance to the tropical ecologist that cannot be obtained in any other way.

That we could not achieve more of our objectives is the result of two events: the unseasonably poor weather in March 1990, which compromised the acquisition of the optical remote-sensing data, and cancellation of funding for the second and third years of the project, which prevented us from acquiring in 1991 the remote-sensing data we failed to acquire adequately in 1990. While the data we did acquire from the three airborne sensors, coupled with the ecological data acquired on the ground, show clearly the utility of these sensor systems individually and collectively, much more could have been done with adequately corrected optical data uncorrupted by clouds and their effects.

Acknowledgments

The work described in this paper was carried out by the Jet Propulsion Laboratory, California Institute of Technology, and the School of Forestry and Environmental Studies, Duke University, and was sponsored by the National Geographic Society and the National Aeronautics and Space Administration. The authors would like to express their deep gratitude to Mr. Barry Bowen, owner of the Gallon Jug Ranch, and Mrs. Joy Grant, director of the Programme for Belize, for their enthusiastic support of our work in Belize, without which this project would not have been possible.

References

Ammozegar, A. (1989), "A compact constant-head permeameter for measuring saturated hydraulic conductivity of the vadose zone: comparison of the Glover solution with simultaneous-equations approach for measuring hydraulic conductivity," *J. Soil Sci. Soc. Am.,* 53:1356–1361.

Brokaw, N.V.L., and E.P. Mallory (1989), "Natural history of the Rio Bravo resource management and conservation area," Report for the Programme for Belize, Belize City.

Durden, S., A. Freeman, J. Klein, G. Vane, H. Zebker, R. Zimmermann, and R. Oren (1991), "Polarimetric radar measurements of a tropical rain forest," in these proceedings.

Goetz, A.F.H. (1987), "The Portable Instant Display and Analysis Spectrometer (PIDAS)," in *Proceedings of the Third Airborne Imaging Spectrometer Data Analysis Workshop* (G. Vane, ed.), pp. 8-17, JPL Publication No. 87-30, Jet Propulsion Laboratory, Pasadena, CA.

Granier, A. (1985), "Une nouvelle méthode pour la mesure du flux de sève brute dans le tronc des arbres," *Ann. Sci. For.,* 42:193–320.

Guyot, G., and F. Baret (1989), "La haute résolution spectrale; détermination des déformations spectrales entre le rouge et le proche-infrarouge," in *Télédétection et Gestion des Resources,* vol. 4, Bernies, Bonn, and Gagnon, eds., Association Québecoise de Télédétection.

Holdridge, L.R., W.C. Grenke, W.H. Hathaway, T. Liang, and J.A. Tosi (1971), *Forest Environments in Tropical Life Zones,* New York: Pergamon.

Kahle, A.B., and A.F.H. Goetz (1983), "Mineralogic information from a new airborne thermal infrared multispectral scanner," *Science,* 222:24–27.

Kimes, D.S., and J.A. Kirchner (1981), "Modelling the effects of various radiant transfers in mountainous terrain on sensor response," *IEEE Trans. Geoscience and Remote Sensing,* GE19-2:100—108.

Lundell, C.L. (1937), "The Vegetation of Peten," Carnegie Institute of Washington, Publication No. 478:1–244.

Luvall, J.C., D. Lieberman, L. Lieberman, G.S. Hartshon, and R. Peralta (1990), "Estimation of tropical forest canopy temperatures, thermal response numbers, and evapotranspiration using an aircraft-based thermal sensor," *Photogrammetric Engineering,* 56:1393–1401.

Oren, R., K.S. Werk, E-D Schulze, J. Meyer, B.U. Schneider, and P. Schramel (1988), "Performance of two *Picea abies* (L.) Karst stands at different stages of decline: VI. Nutrient concentrations," *Oecologia* (Berlin), 77:151–162.

Peterson, D.L., J.D. Aber, P.A. Matson, D.H. Card, N. Swanberg, C.A. Wessman, and M. Spanner (1988), "Remote sensing of forest canopy and leaf biochemical contents," *Remote Sensing Environ.,* 24:85–105.

Vane, G. (1987), "First results from the Airborne Visible/Infrared Imaging Spectrometer (AVIRIS)," in *Imaging Spectroscopy II* (G. Vane, ed.), 166–174, SPIE, Bellingham, WA.

van Zyl, J.J. (ed.) (1991), "The Airborne Synthetic Aperture Radar (AIRSAR) reference manual," in preparation, JPL Publication, Pasadena, CA.

Wessman, C.A., J.D. Aber, D.L. Peterson, and J.M. Mililo (1988), "Remote sensing of canopy chemistry and nitrogen cycling in temperate forest ecosystems," *Nature,* 335:154–156.

Wright, A.C.S., D.H. Romney, R.H. Arbuckle, and V.E. Vial (1959), "Land in British Honduras," Colonial Research Publication No. 24, Her Majesty's Stationery Office, London. Map from Wright is available from Edward Stanford, Ltd., 12–14 Long Acre, Covent Garden, London WC2E 9LP.

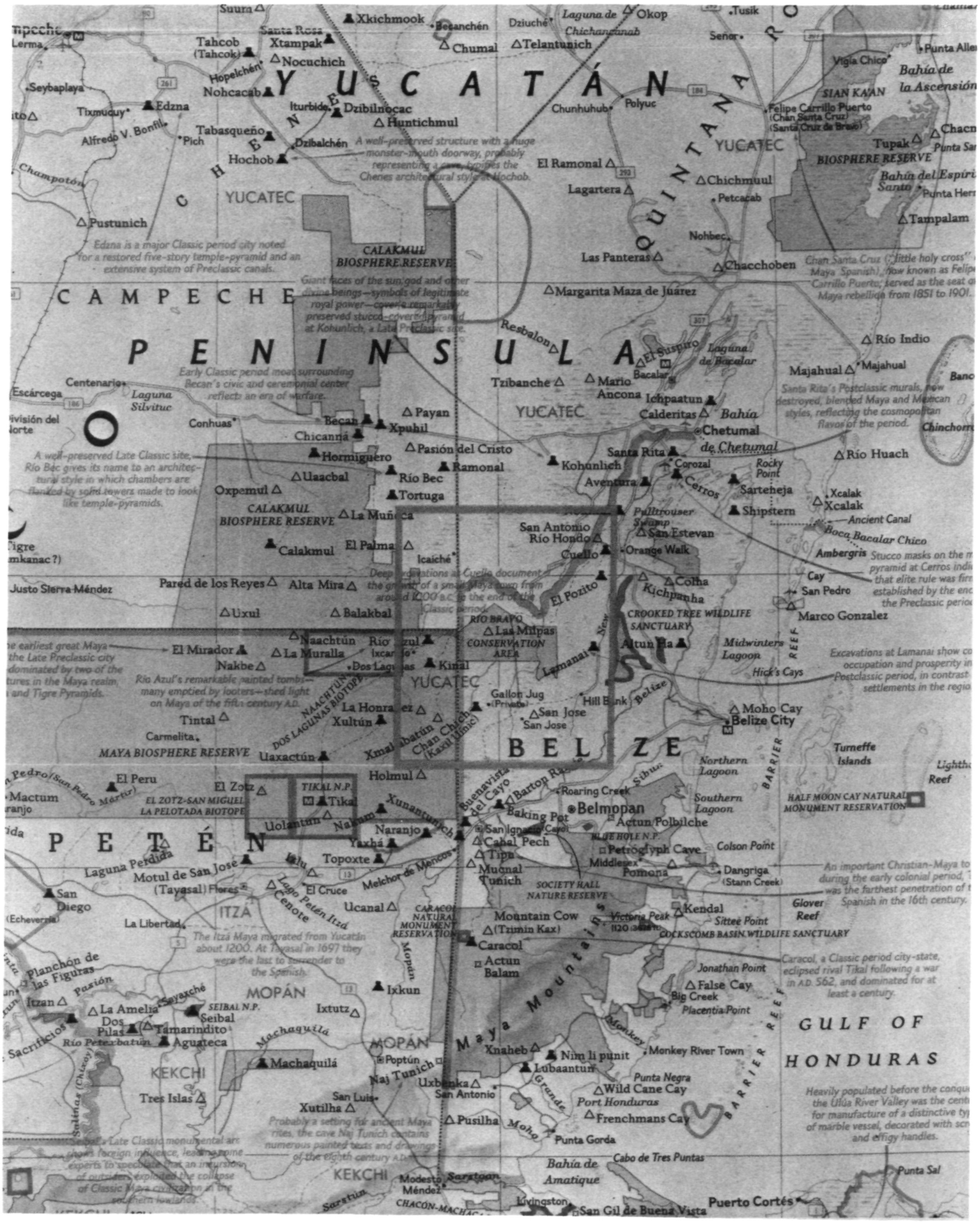

Fig. 1. A map of the study area showing the Rio Bravo Resource Management and Conservation Area and Gallon Jug Ranch in northern Belize, along with neighboring portions of Mexico and Guatemala. The box centered on Rio Bravo indicates the AIRSAR mosaic image area of Fig. 8. (Map courtesy of National Geographic magazine)

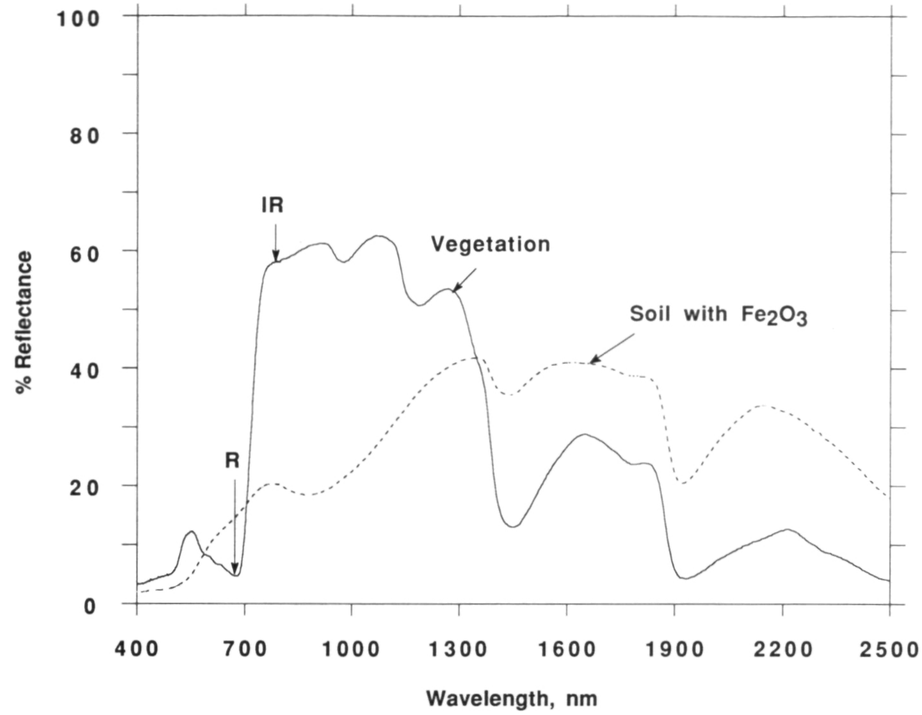

Fig. 2. Spectral reflectance curves for vegetation and iron-bearing soil showing the steep rise in reflectance from the red (about 700 nm) to the infrared (beginning at about 750 nm) for vegetation compared to soil. (Spectra acquired with a Beckman laboratory spectrophotometer)

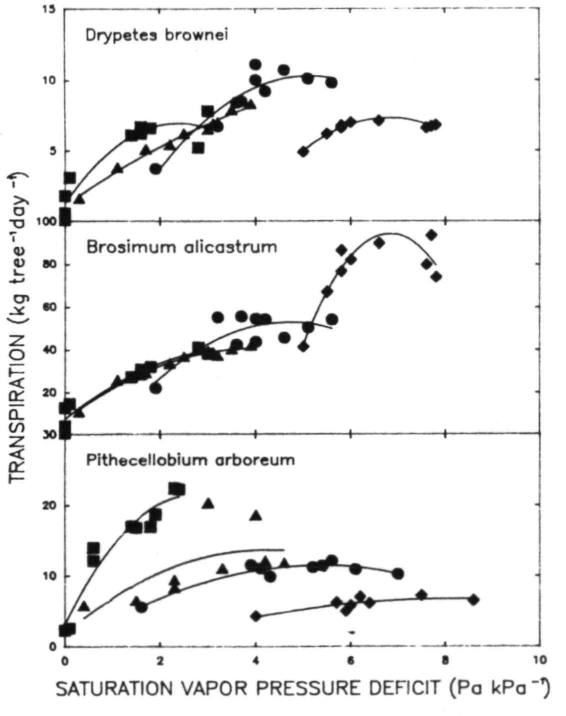

Fig. 3. Daily transpiration of three species in relation to the saturation vapor pressure deficit, displaying three types of responses to increasing demand for water and decreasing availability of water in the soil. Symbols indicate measurement periods: squares, Nov/Dec (very wet soils); triangles, Jul/Aug (wet soils); circles, May/Jun (dry soils); diamonds, Mar (very dry soils).

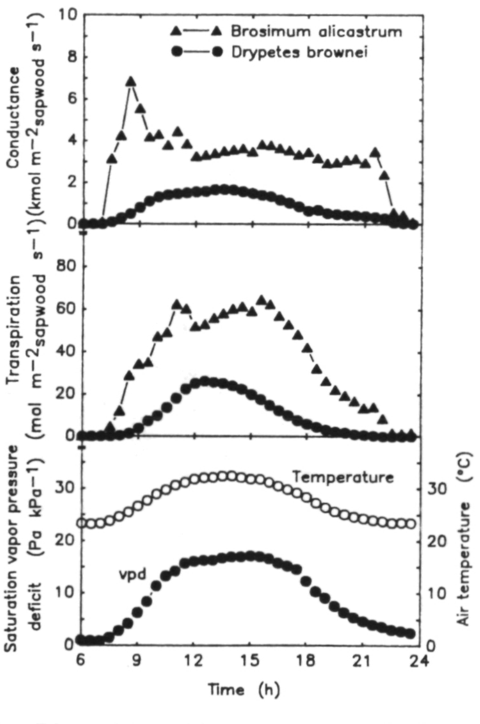

Fig. 4. Diurnal trend in canopy conductance and transpiration of two species, saturation vapor pressure deficit, and temperature within the canopy. The two species differ in their control over water loss (transpiration), as apparent from differences in their conductance.

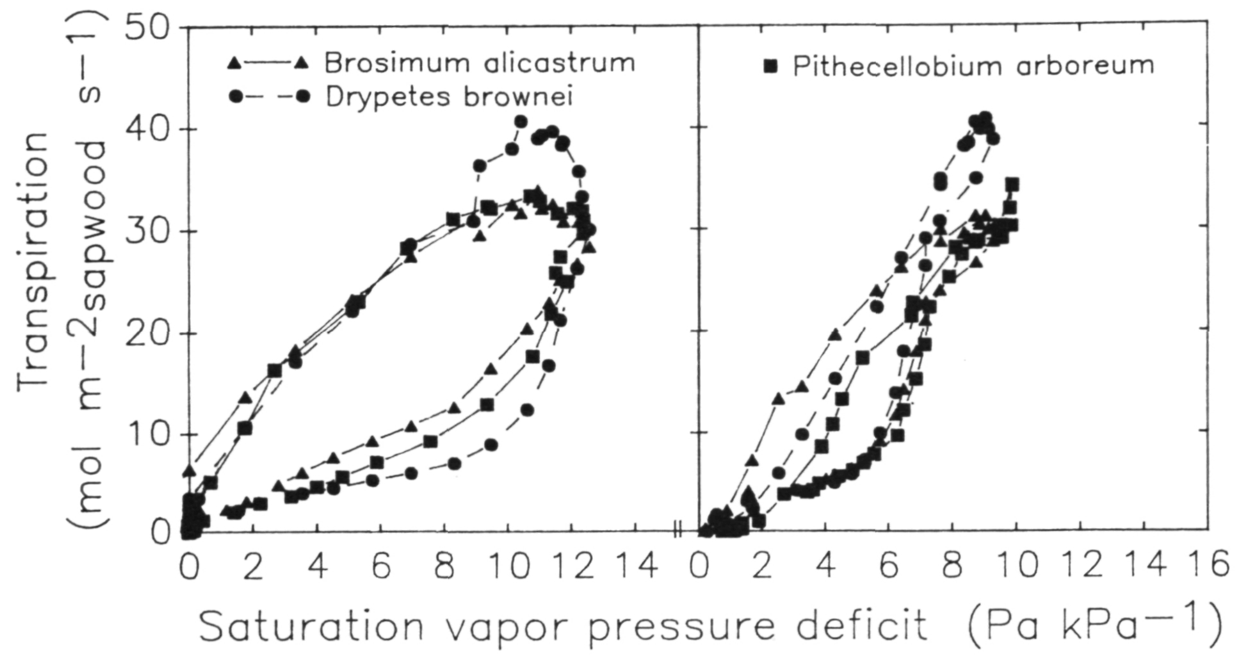

Fig. 5. Diurnal (24-hour) relationships between transpiration and saturation vapor pressure deficit for three species for a dry (left) and a humid (right) day. The hysteresis, more apparent on the dry day, represents the use for transpiration of water stored in the trees.

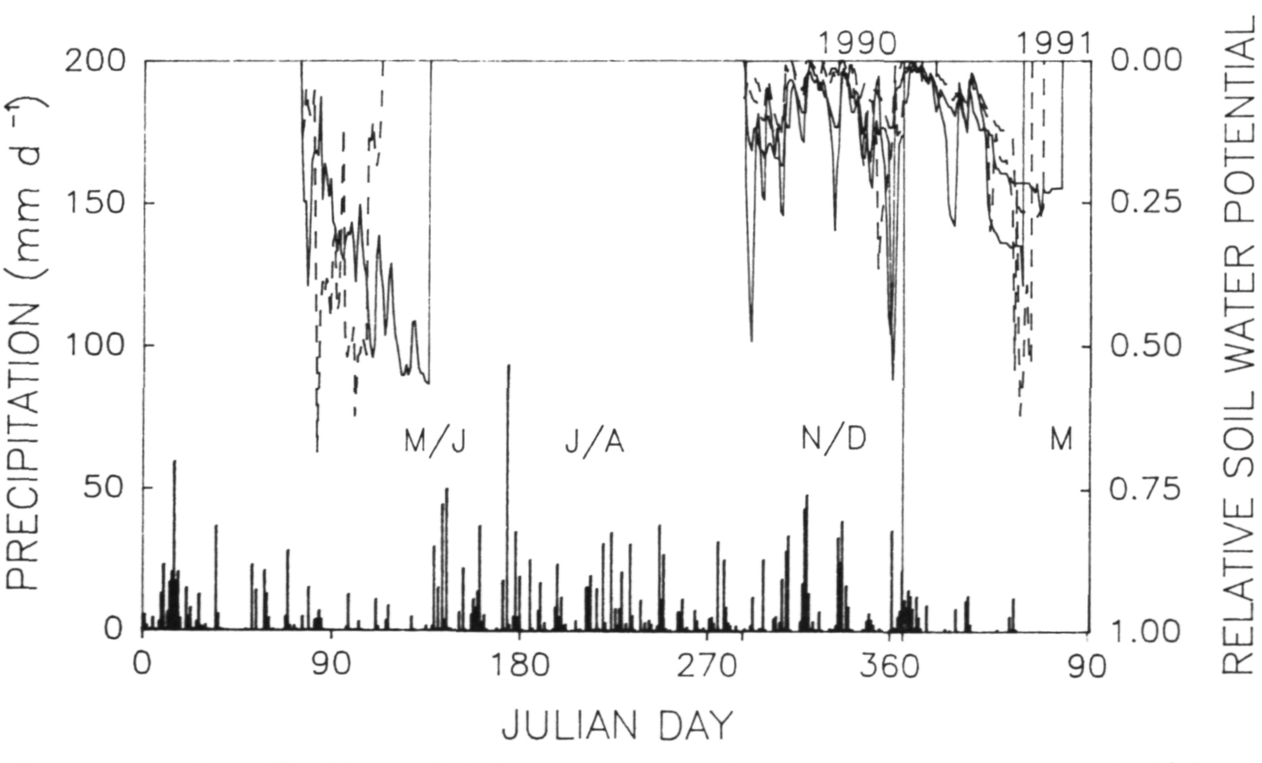

Fig. 6. Annual trend in daily precipitation and average soil water potential (on a relative basis) from January 1990 through March 1991. The months marked correspond to the four periods of transpiration measurements displayed in Fig. 2.

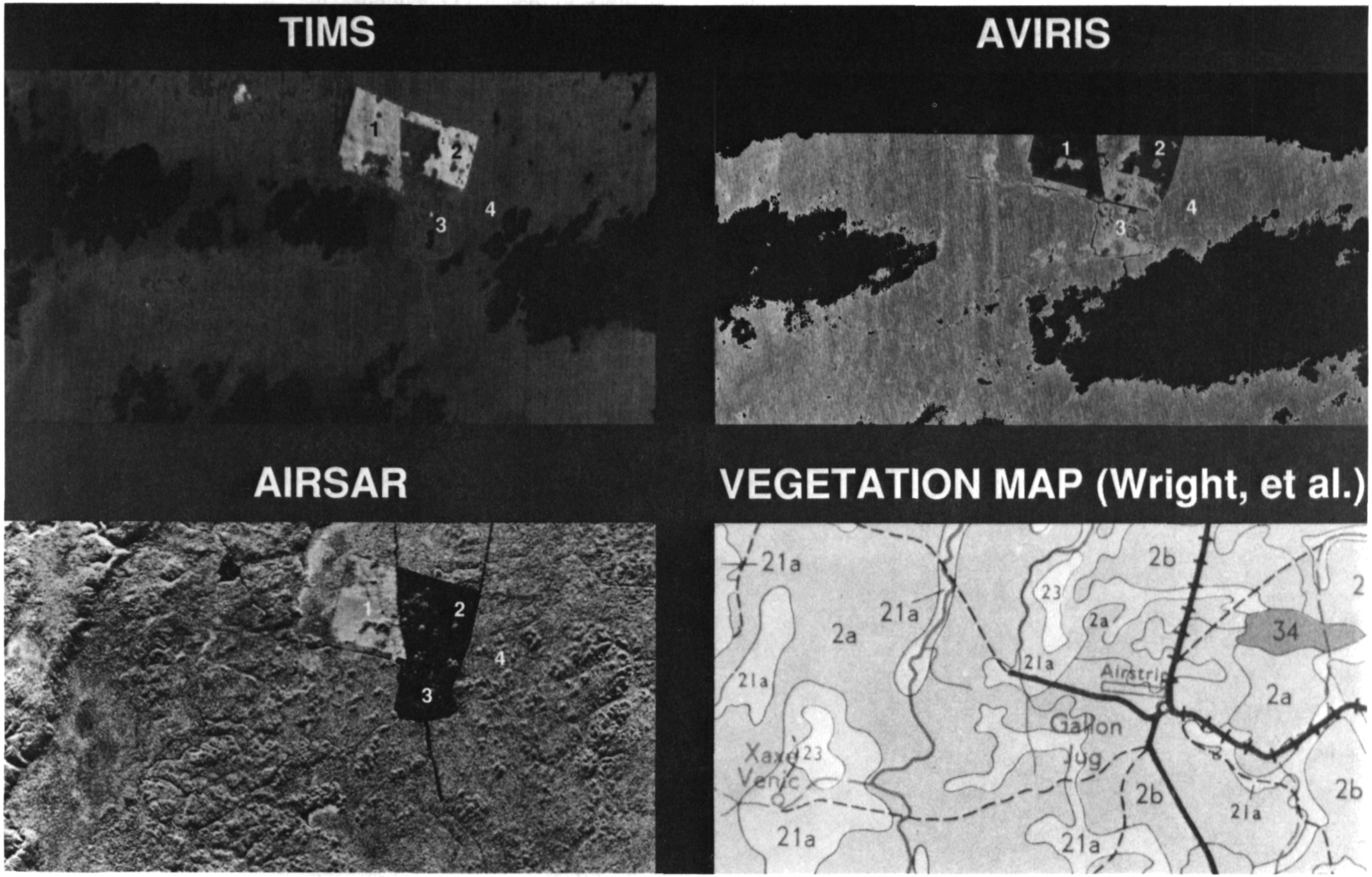

Fig. 7. TIMS (upper left), AVIRIS (upper right), AIRSAR (lower left) images, and a preexisting vegetation map (lower right) of the area surrounding Gallon Jug, northwestern Belize. The images were acquired on March 15, 1990. The vegetation map is from Wright et al. (1959). See text for explanation of the numbered areas. (See slide no. 25.)

ORIGINAL PAGE
BLACK AND WHITE PHOTOGRAPH

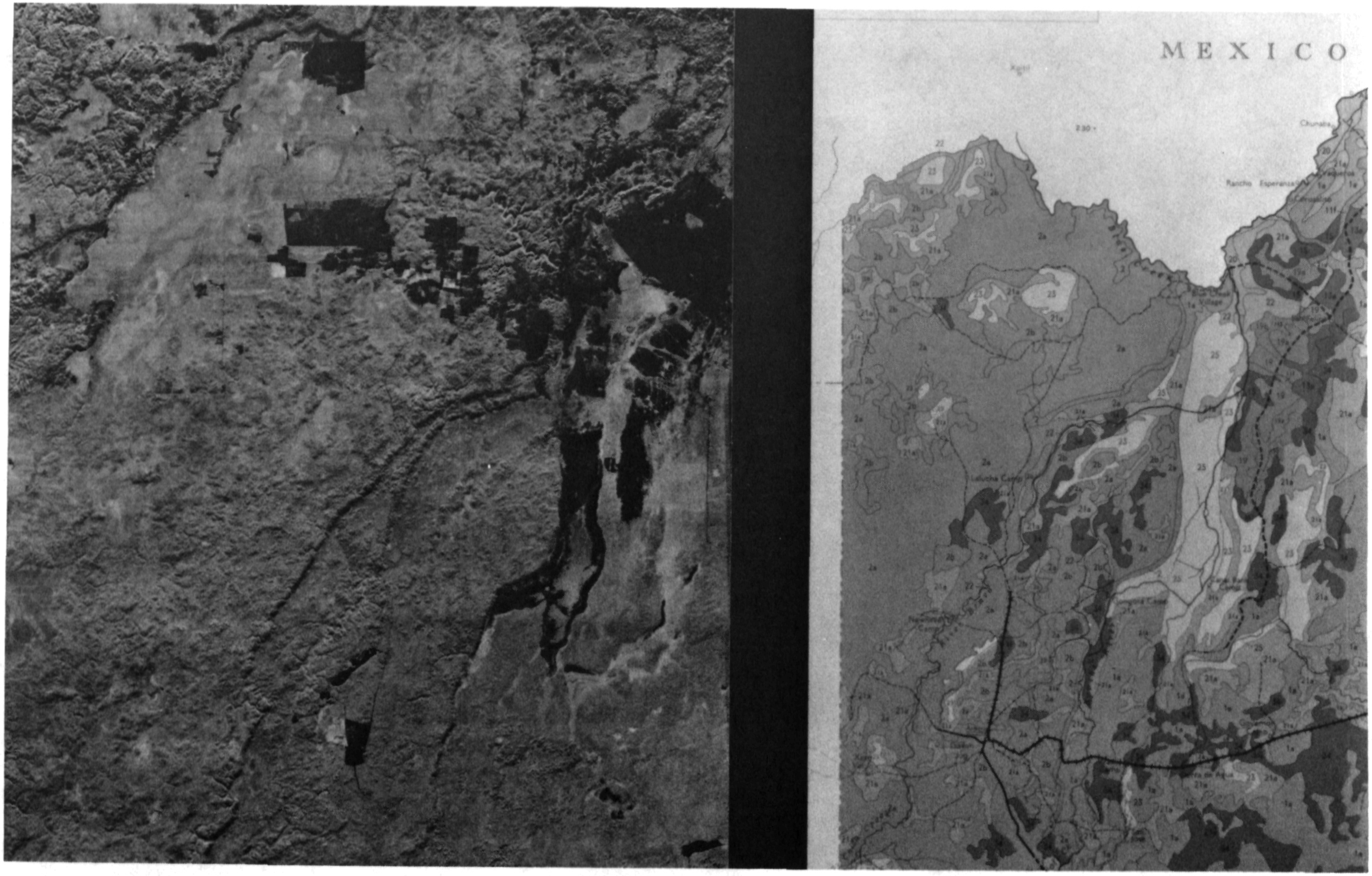

Fig. 8. AIRSAR (left) displays a much greater number of vegetation types and ecological groups within each type, relative to the existing vegetation map of northern Belize (right) from Wright et al. (1959). (See slide no. 26.)

N92-28037

POLARIMETRIC RADAR MEASUREMENTS OF A TROPICAL RAINFOREST

S. Durden, A. Freeman, J. Klein, G. Vane, H. Zebker, and R. Zimmermann
Jet Propulsion Laboratory
California Institute of Technology

R. Oren
Duke University

Abstract. In March 1990 the NASA/JPL DC-8 AIRSAR was flown over an area in northern Belize and the surrounding areas of Guatemala and Mexico. We have extracted the three-frequency polarimetric signatures of a variety of natural areas and have found that many appear to have a unique radar signature, if all polarizations and frequencies are examined.

Introduction

In March 1990 the NASA/JPL DC-8 AIRSAR was flown over an area in northern Belize and the neighboring countries of Guatemala and Mexico as part of the Tropical Rainforest Ecology Experiment (TREE). This was a joint experiment conducted by the National Geographic Society and NASA. The AIRSAR acquired data during numerous east-to-west passes over the area, and a 16-look mosaic of these data has been produced. In addition, lines were flown over an area in Belize which had been chosen for intensive field study. Three images covering these intensive study sites have been calibrated using corner reflectors deployed in clearings near the study sites. The intensive study sites were monitored for atmospheric conditions, transpiration, soil moisture, stand structure, and numerous other ecological parameters. A broad survey of the intensive study areas and other areas covered by the radar data has also been accomplished. In this paper we present characteristics of the natural vegetation as determined by ground measurements and then relate the characteristics of the different vegetation types to the radar signatures.

Vegetation

The area in northern Belize is dominated by old-growth upland tropical rainforest. There are also small areas that have been cleared of upland forest within the last five years and allowed to regrow. In addition, there are areas of almost pure palm forest, consisting of either cohune or botan palm trees. There are several types of wetland forests. Swamp forest has vegetation resembling the upland rainforest, but standing water is present during a large portion of the year. Another wetland forest is bajo. These areas have very poorly drained clay soils; the vegetation is short (a few meters) and densely packed and has sparse foliage. Yet another wetland forest type is mangrove swamp, consisting of mangrove trees growing out of standing water. Besides forest, there are sedge marsh and reed marsh. These are areas of herbaceous vegetation in standing water. The sedges are considerably taller than the reeds (200 cm versus 40 cm). In addition to these naturally occurring vegetation types, there are numerous agricultural areas consisting of cleared areas, bare soil, crops, and buildings or other man-made structures.

Data Analysis

As mentioned above, three images corresponding to the study sites were processed and calibrated. Calibration used 8-ft trihedral corner reflectors deployed in cleared areas. The calibration procedure consists of removal of effects caused by leakage between polarization channels, removal of imbalance between the channels (amplitude and phase), and absolute calibration [1,2]. The following polarization parameters were derived from the calibrated Stokes matrix data at each frequency:

- Total power (TP), HH, VV, and HV cross sections (per unit area)
- HH/VV and HV/HH cross-section ratios
- ρ: the magnitude of HH-VV correlation coefficient
- phase: the phase difference between HH and VV returns

We then formed a correlation matrix for these parameters to determine which were correlated and hence redundant. We found that the L-band parameters generally are highly correlated with P-band, although in some cases L-band provides unique information. In this paper we present primarily P- and C-band results and show L-band where appropriate.

Results

For the upland rainforest we have extracted cross sections across a radar image. Figure 1 plots these results for HH polarization at all three frequencies. As can be seen, the rainforest provides a very uniform target. We sorted cross sections for all natural vegetation types into ascending order. Figure 2 shows the results of sorting at P-band and sorting at C-band. In both cases, we have indicated the region spanned by the upland forest. If we examine the site type for each data point, we find that the horizontal axes at both frequencies correspond very roughly to biomass. What we see then for each case is a region of increasing cross section with biomass, followed by a plateau. This type of saturation of radar backscatter with biomass has been observed previously [3]. At both frequencies, especially C-band, we then see a secondary increase region. The sites corresponding to these data points may have much less biomass than the upland forest, but they have a brighter radar return. These areas all have some feature that adds a secondary scattering mechanism in addition to the volume scatter which dominates the upland forest. This would include, for example, double-bounce scattering from marshlands. Forest-scattering mechanisms and modeling are discussed in several papers (e.g., Durden et al. [4]).

We can study the importance of double-bounce scattering by examining the HH-VV phase difference and the HH-VV correlation coefficient ρ. Figure 3 shows the result of sorting the P-band phase into ascending order. In performing the sort, ρ was reordered to correspond to the phase. Note that ρ is generally small (around 0.2). It is large only for sites with near-zero phase difference or phase difference near 180°. In examining these sites we find that those with phase near zero are bare surfaces, while those with phase near 180° are typically wetland areas. Figure 4 shows this same procedure for the C-band phase and ρ. The correlation coefficient is typically larger (0.5) than at P-band. Note that, for phase near zero, ρ is larger than the typical value, as was true at P-band. However, for phase near 180°, ρ drops below 0.5, rather than increasing. Thus, at P-band the transition to wetland sites causes ρ to increase, while at C-band ρ decreases. In both cases the large phase differences are associated with wetland areas, or areas with thin canopy and smooth ground. For both frequencies the sites with large ρ and phase near zero are bare surfaces and would be dominated by surface scattering.

We can understand this phenomenon by using a very simple conceptual model of scattering. Assume that scattering from a vegetation layer is a combination of volume scattering from vegetation and double-bounce scattering from vegetation and ground. Let volume scattering be represented by scattering from very thin, randomly oriented cylinders.

$$|S_{hh}|^2 = |S_{vv}|^2 = 1,\ (S_{hh}S_{vv}^*) = 1/3$$

Let double-bounce scattering be represented by a dihedral corner reflector.

$$|S_{hh}|^2 = |S_{vv}|^2 = 1,\ (S_{hh}S_{vv}^*) = -1$$

Let the cross section for volume scattering be unity and for double-bounce scattering be x; then an incoherent sum yields

$$|S_{hh}|^2 = |S_{vv}|^2 = 1 + x,\ (S_{hh}S_{vv}^*) = 1/3 - x$$

We can calculate ρ as a function of the fraction x of double-bounce scattering relative to volume scattering. This is shown in Figure 5. When the double-bounce component is very small, ρ is 1/3 and the phase is zero. When the double-bounce cross section x becomes greater than 1/3 of the volume-scattering cross section, the phase is 180° and ρ is near zero. ρ increases beyond 1/3 only when the double-bounce cross section becomes greater than the volume-scattering cross section. Thus, the small correlation between HH and VV for canopy volume scattering allows the presence of the double-bounce mechanism to strongly affect the phase without actually dominating the return. This model shows that addition of the double-bounce component may increase or decrease ρ. This model leads us to believe that, for sites with phase close to zero and small ρ, volume scattering is much stronger than double-bounce scattering. For sites with phase approaching 180° and small ρ, double-bounce scattering is important but it *does not dominate.* The only site with large phase (–115°) *and* large ρ (0.72) is a reed marsh observed at

P-band. We believe that in this case double-bounce scattering dominates because of low P-band attenuation and low volume scattering. This same site viewed at C-band has a large phase (–136°), but ρ is only 0.44.

Next we examine the scattering characteristics of the various vegetation types, beginning with the upland forest. We find that the absolute cross sections (TP, VV, HH, HV) show little variation between sites; they vary within a 3-dB range. The upland forest absolute cross sections increase with frequency: PHH is –12 dB, LHH is –9 dB, and CHH is –6 dB. HH and VV returns are approximately equal at all frequencies. The HV/HH cross-section ratio is ≈ –6 dB, independent of frequency. These characteristics are indicative of volume scattering, with scatterers having nearly uniform random distribution. Note that the volume-scattering portion of the simple conceptual model used above predicts equal HH and VV and an HV/HH ratio of –4.8 dB. Areas of regrowth upland forest have P-band cross sections several dB lower than old growth. At higher frequencies the regrowth areas appear similar to the upland forest.

For palm forest we find two distinct cases. Some sites are dominated by palm but have a dense understory. The radar signatures for these areas appear the same as for the upland forest. If the understory is absent, however, double-bounce scattering is important. In this case, palm forest has a large PHH cross section (–10 dB), L- and C-band cross sections similar to upland forest, and a large P-band phase (–80°).

As mentioned in the vegetation section, there are several types of wetland forest. The swamp forest, which appears to have vegetation similar to the upland forest, has absolute cross sections 1 to 2 dB greater than those of the upland forest at P- and L-bands. The P-band phase is 25°, and L- and C-band phases are near zero. The mangrove swamp is characterized by a large P-band phase (–150°), an L- and C-band phase near zero, LHH 6 dB brighter than PHH, and CHH 10 dB brighter than PHH.

The bajo signature depends on whether standing water is present. If no standing water is present, absolute cross sections are 1 to 2 dB lower than for upland forest at P- and L-bands. If the bajo is flooded, cross sections are 1 to 2 dB *higher* than for upland forest at P- and L-bands. The P-band phase for a flooded bajo is in the range of –40° to –75°, implying that double-bounce scattering is important. L- and C-band phases are near zero for a flooded bajo.

Both reed and sedge marshes generally show large P-band phases, indicating that double bounce is important at P-band. At C-band the phase is large only for the reeds; sedges are too tall for penetration to the water surface. At P-band the sedges are brighter than upland forest, while the reeds are less bright. Reeds are less bright because they are shorter than the P-band wavelength. Sedges are brighter than upland forest because of double-bounce scattering. At C-band the situation is reversed: sedges are dimmer than upland forest, and reeds are brighter. This is caused by small penetration and hence small double-bounce return for sedges; reeds are short enough so that double bounce is important. These findings imply that radar data can be used to infer heights of marsh vegetation.

Conclusions

We were able to reach the following conclusions from our study: (1) cross sections due to volume scattering appear to increase with biomass until a plateau is reached, (2) cross sections are increased beyond the plateau only by the presence of additional scattering mechanisms, (3) vegetation with low biomass may have high cross sections due to double-bounce scattering, (4) polarization parameters are needed to detect the presence of nonvolume scattering, and (5) different vegetation types appear to have different radar signatures.

References

1. J. J. van Zyl, "Calibration of polarimetric radar images using only image parameters and trihedral corner reflector response," *IEEE Trans. Geosci. Remote Sensing*, vol. 28, pp. 337-348, 1990.

2. H. A. Zebker and Y. Lou, "Phase calibration of imaging radar polarimeter Stokes matrices," *IEEE Trans. Geosci. Remote Sensing*, vol. 28, pp. 246-252, 1990.

3. N. L. Christiansen, Jr., E. S. Kasischke, and M. C. Dobson, "SAR-derived estimates of aboveground biomass in forested landscapes," *Proc. IGARSS '90,* pp. 1209-1212.

4. S. L. Durden, J. J. van Zyl, and H. A. Zebker, "Modeling and observation of the radar polarization signature of forested areas," *IEEE Trans. Geosci. Remote Sensing*, vol. 27, pp. 290-301, 1989.

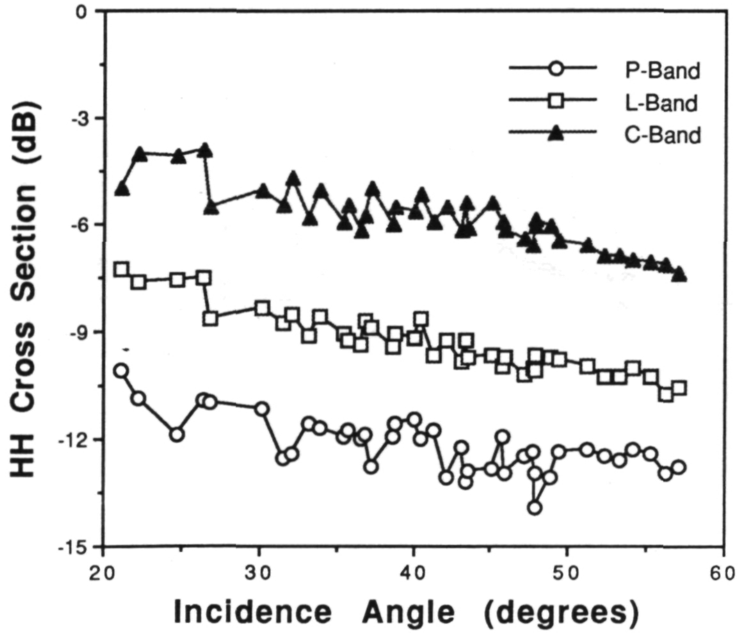

Figure 1. HH cross section versus incidence angle.

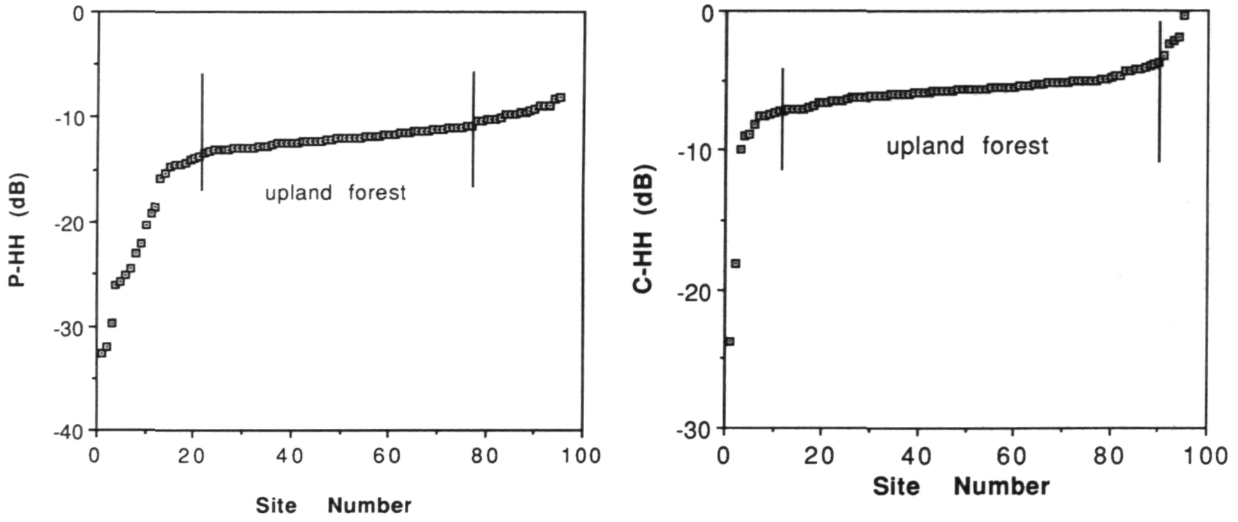

Figure 2. Cross sections sorted into ascending order. Site numbers for P-band and C-band do not correspond.

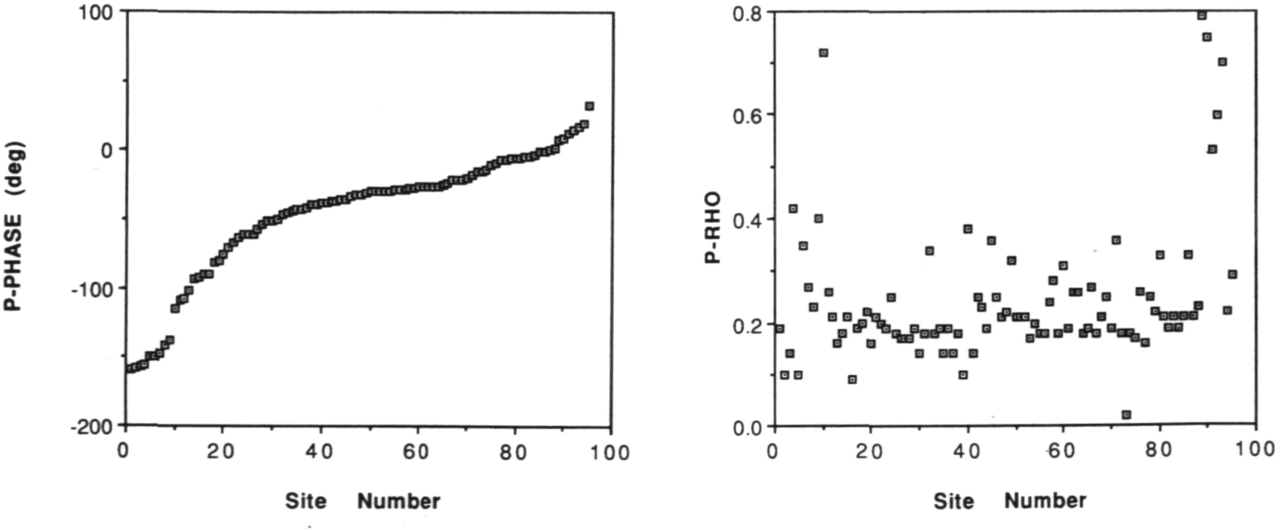

Figure 3. Sorted P-band phase and corresponding ρ.

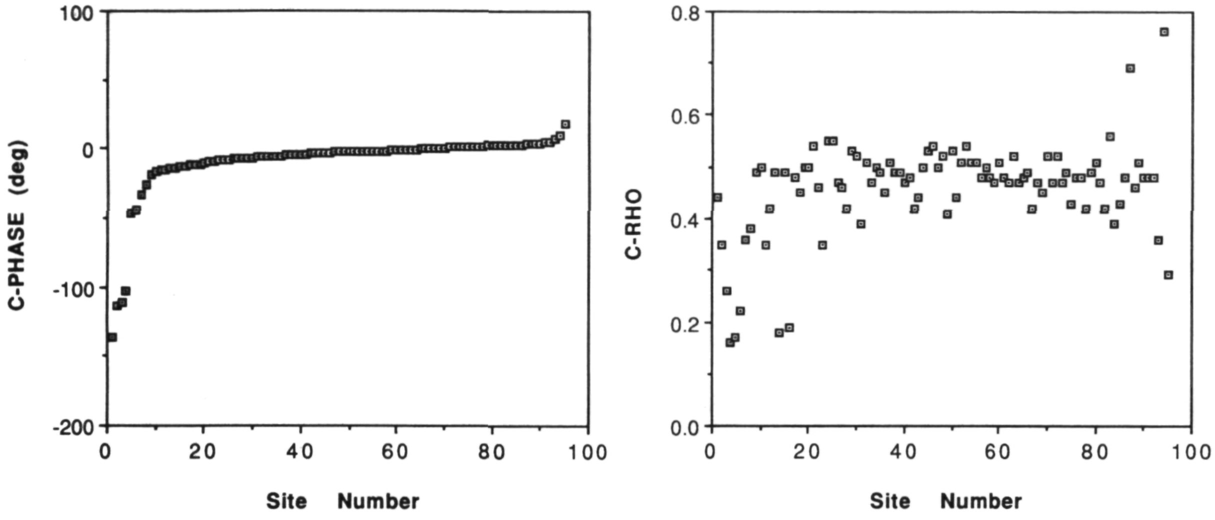

Figure 4. Sorted C-band phase and corresponding ρ.

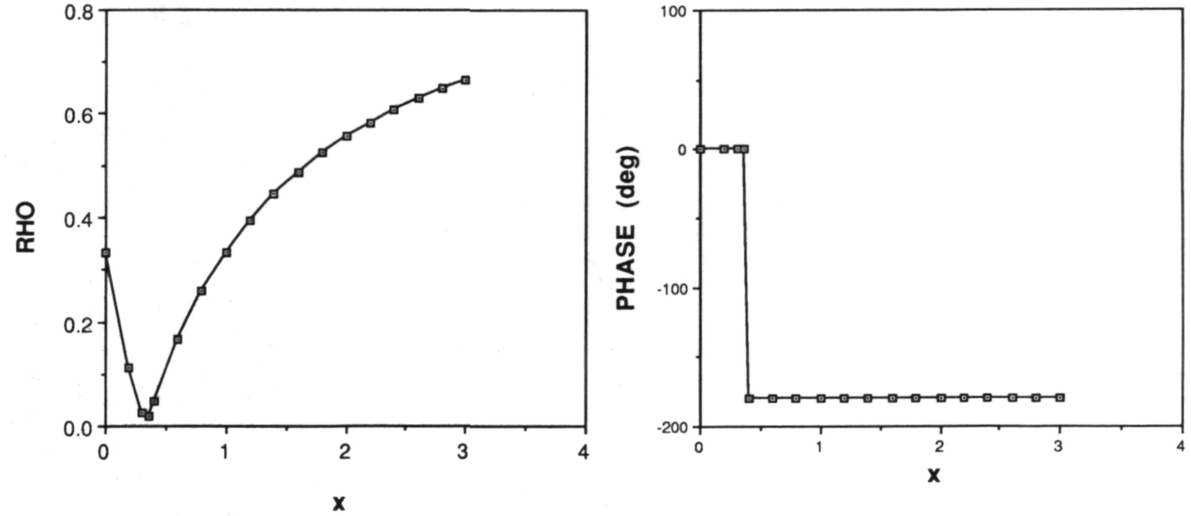

Figure 5. ρ and phase calculated using simple model.

N92-28038

The TOPSAR Interferometric Radar Topographic Mapping Instrument

Howard A. Zebker
Jet Propulsion Laboratory
California Institute of Technology
Pasadena, CA 91109

Abstract. We have augmented the NASA DC-8 AIRSAR instrument with a pair of C-band antennas displaced across the track to form an interferometer sensitive to topographic variations of the Earth's surface. The antennas were developed by Alenia Spazio under the sponsorship of the Italian Space Agency (ASI), and the AIRSAR instrument and modifications to it supporting TOPSAR were sponsored by NASA. A new data processor was developed at JPL for producing the topographic maps. As of May 1991, one engineering flight line over San Francisco, CA has been reduced to a cartographically rectified topographic map. Analysis of the results indicates that statistical errors are in the range of 2 to 4 m, while systematic effects due to aircraft motion are in the range of 6 to 12 m. Future aircraft motion compensation algorithms should reduce the systematic variations to near zero, while the statistical errors could likely be reduced to 2 m or less with some processor improvements.

Theoretical Considerations

Consider a set of two antennas A1 and A2, as shown in Figure 1. The topography is given by z(x), h is the aircraft altitude, B is the baseline distance, ρ is the range to a point on the ground, θ is the look angle, and α is the baseline deviation from the horizontal. Radar signals are transmitted from antenna A1, and the echoes are received at A1 and A2. The difference in the two path lengths is δ, which depends on the baseline distance, the baseline angle, the range, the look angle, and the height of a point z(x). This difference is directly related to the measured phase of the interferometer. A little algebra and geometry yield the following equations for height as a function of these parameters:

$$\delta = \phi\lambda \tag{1}$$

$$\beta = [(\rho+\delta)^2 - \rho^2 - B^2] / 2\rho B \tag{2}$$

$$z(x) = h - \rho \cos\alpha \sqrt{1-\beta^2} + (\rho \sin\alpha)\beta \tag{3}$$

where ϕ is the measured phase, λ is the wavelength, and β is an intermediate parameter.

Thus we measure the phase at each point in an image and apply equations based on knowledge of imaging geometry to produce the topographic height at each point.

Errors affect the results in two major ways. First, the phase measurements are of course noisy; the system signal-to-noise ratio imposes accuracy limitations. The noise may be reduced by increasing the signal-to-noise ratio or by averaging for larger resolution cells on the ground. The second major error source is in knowledge of the baseline angle. This value varies due to aircraft attitude and must be corrected in the final topographic maps.

Hardware Implementation

The existing radar was modified by the AIRSAR group to replace the C-band polarimetric antennas with the new pair of antennas developed by Alenia Spazio in Italy. In addition, since only two channels of data are required for the interferometer, rather than the four required by the polarimeter, the prf was doubled to approximately 600 Hz to gain transmitted power and reduce azimuth ambiguities. The L-band and P-band polarimeters were left unchanged so that those data can be acquired simultaneously with the TOPSAR data. Thus the altitude maps obtained at C-band can be used to geometrically rectify all three wavelength images. Note that only the C-band VV image is available in this mode, whereas all polarizations exist at L- and P-bands.

The antennas were mounted in special fairings built by Ames Research Center. The upper antenna is mounted near the aircraft passenger windows, and the cables are fed through bulkhead panels that replace two windows and serve as attachment points. The lower antenna is integrated into the power portion of the existing P-band antenna fairing, extending that fairing. The resulting baseline is 2.5 m at an angle of 67° with respect to the horizontal. This value is modified by aircraft attitude variations, and the appropriate correction is made in the processor.

Data Processing

Raw data were transferred to the computer using a new set of software developed by the AIRSAR group to accommodate the 600-Hz interferometer channels. A new set of code for processing was written and implemented on an Alliant general-purpose computer. The new code was required to process the 600-Hz data format at the full swath width. The complex images were transferred to a Sun workstation for interferogram generation and reduction to height maps, as well as for the geometric rectification and interpolation operations.

Sample Image

Figure 2 shows the first interferogram obtained from the TOPSAR aircraft interferometric topography mapper. These data were acquired during the engineering checkout flight on May 13, 1991, over the San Francisco peninsula. The figure consists of two images. The upper strip is the interferogram showing the phase response of the interferometer, corrected for the expected phase from a flat Earth; hence any residual phase is largely indicative of topography. In fact, the phase contours closely follow the topographic contours. The aircraft roll has been removed, although other artifacts of aircraft motion remain; they are not visible as distinct color shifts, but rather they affect absolute height accuracy.

The lower strip in Figure 2 shows the same data reduced to heights and geometrically rectified. The contour interval per color is 6 m. Thus one trip around the color wheel corresponds to 96 m for our 16-entry color table. The residual artifacts present in the ocean are related to uncompensated aircraft motions and also to nonideal phase responses of the antenna system. We plan to remove both of these sets of artifacts by future data processing.

We have also measured the residual statistical variations by examining the standard deviation of the signals from the presumably flat ocean. Although the signal-to-noise ratio over the ocean is not optimum, two boxes selected in the vicinity yielded 2.5-m and 4.5-m standard deviations from the mean altitude. Thus we are confident of our ability to reach roughly 1-m statistical errors with data acquired over brighter targets, or with a lower-noise data processor.

Summary

The TOPSAR addition to the NASA DC-8 AIRSAR instrument forms an interferometer sensitive to topographic variations of the Earth's surface. The antennas, developed by Alenia Spazio under the sponsorship of the Italian Space Agency (ASI), and the AIRSAR modifications supporting TOPSAR have been completed. A new data processor was developed at JPL. As of May 1991, one engineering flight line over San Francisco, CA has been reduced to a cartographically rectified topographic map. Analysis of the results indicates that statistical errors are in the range of 2 to 4 m, while systematic effects due to aircraft motion are in the range of 6 to 12 m. Aircraft compensation algorithms should reduce the systematic variations to near zero, and the statistical errors can probably be reduced to about 2 m.

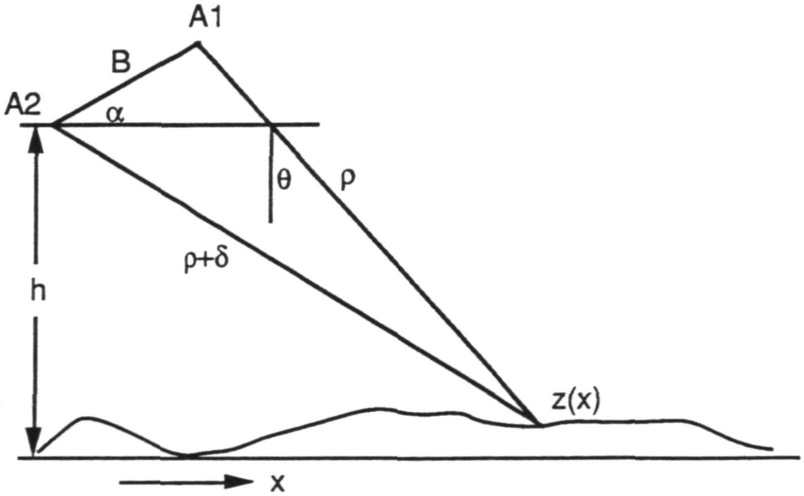

Figure 1. TOPSAR Geometry

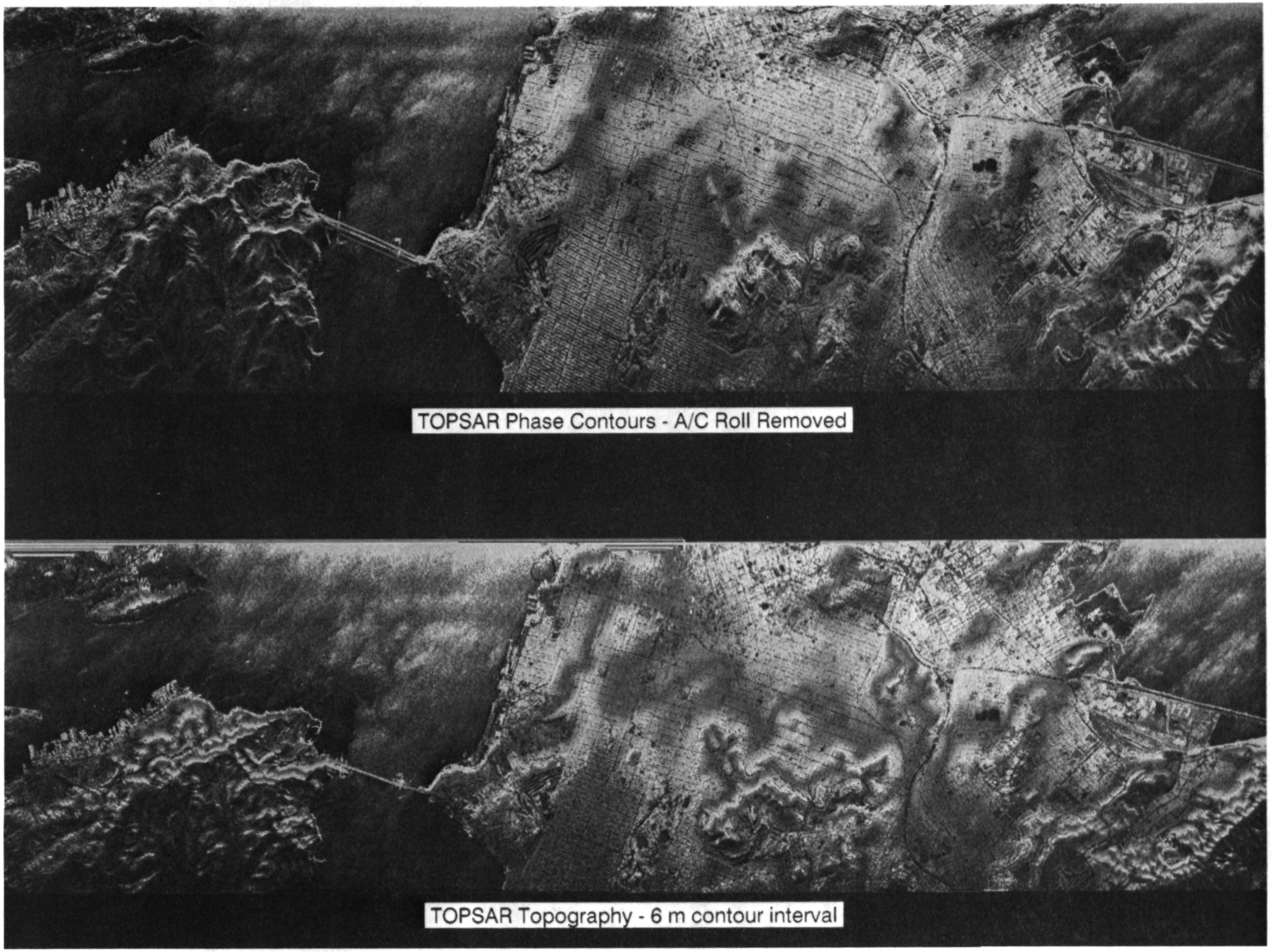

Figure 2. TOPSAR Interferogram Images of San Francisco Area (See Color Slide No. 27)

SLIDE CAPTIONS

Slide No.	Caption	Senior Author
1	Example of a C-band SAR phase difference image of mangrove stands on Boca Chica Key, Florida.	French
2	Examples of C- and L-band SAR phase difference images of flooded bald cypress stands in North Carolina.	French
3	AIRSAR total power image for April 1, 1990.	Dobson
4	AIRSAR total power image for July 8, 1990.	Dobson
5	Calibrated C-band HV-polarized image of the Flevoland scene.	Freeman
6	False colour SAR composite of C-W, C-HV, and C-HH narrow swath data from May 22.	Brown
7	A colour infra-red photograph of the study area showing the change from clay to sandy soil.	Brown
8	L-band multipolarization image.	Shi
9	Dielectric constant image.	Shi
10	TM image of study area.	Shi
11	Snow and glacier map.	Shi
12	Spring and summer images. Three-frequency overlay: P-band (red), L-band (green), and C-band (blue).	van Zyl
13	Three-polarization overlay of the C-band ratio image (summer/spring): HV (red), VV (green), and HH (blue). Note the brighter area in the center. The twenty areas used for analysis are marked.	van Zyl
14	The top scene corresponds to an area next to Corner Reflector 3, which displays only minor changes between the spring (left image) and summer (right image) in the backscatter coefficient. In both cases, the vegetation is greener in the summer.	van Zyl
15	South edge of the Gulf Stream.	Valenzuela
16	North edge of the Gulf Stream.	Valenzuela
17	16-look L-band along-track interferometer image produced from images formed by transmitting out the aft antenna and receiving through both the fore and aft antennas. The scene is of the outlet of the San Francisco Bay to the Pacific Ocean. North is to the right. The aircraft flight is from north to south (right to left) and above the image (looking east). The image is coded such that the pixel color represents phase change be-	Carande

	tween the fore and aft images, while pixel intensity is proportional to the fourth root of the 16-look power detected.	
18	16-look C-band along-track interferometer image produced from fore/fore and aft/aft complex images. This data was acquired simultaneously with the L-band data shown in figure 2.	Carande
19	Color composite of the study area with blue, green, and red representing C-, L-, and P-bands, respectively. South is toward the top, and the aircraft flight line is parallel to the south edge. Incidence angles range from 25° near the south edge to 60° near the north edge.	Ray
20	Color composite of L-band polarization with HH polarization as red, VV polarization as green, and VH polarization as blue.	Ray
21	Sequence of features dropped (9 images) in Weeks Lake, BC, Canada scene (23 March 1988). Features were dropped in reverse-rank order of Table 1. The last feature not dropped labels each image (red, clear-cut; green, forest; blue, lake).	Cumming
22	Visual classification comparison of simplified radar systems — Flevoland, NL scene (16 August 1989)—(red, even-bounce; green, diffuse/forest; blue, water; yellow, field).	Cumming
23	Results from mapping the slant-range coordinates to the object coordinate system.	De Groof
24	Slant-range projection: a visual evaluation of the georeferencing accuracy obtained by mapping thematic layers from the GIS database to the slant-range image.	De Groof
25	TIMS (upper left), AVIRIS (upper right), AIRSAR (lower left) images, and a preexisting vegetation map (lower right), of the area surrounding Gallon Jug, northwestern Belize. The images were acquired on March 15, 1990. See text for explanation of the numbered areas.	Oren
26	AIRSAR (left) displays a much greater number of vegetation types and ecological groups within each type, relative to the existing vegetation map of northern Belize (right).	Oren
27	TOPSAR interferogram images of San Francisco area.	Zebker

TECHNICAL REPORT STANDARD TITLE PAGE

1. Report No. JPL Pub. 91-30

2. Government Accession No.

3. Recipient's Catalog No.

4. Title and Subtitle
Proceedings of the Third Airborne Synthetic Aperture Radar (AIRSAR) Workshop; May 23 and 24, 1991

5. Report Date
August 1, 1991

6. Performing Organization Code

7. Author(s)
Jakob J. van Zyl, Editor

8. Performing Organization Report No.

9. Performing Organization Name and Address

JET PROPULSION LABORATORY
California Institute of Technology
4800 Oak Grove Drive
Pasadena, California 91109

10. Work Unit No.

11. Contract or Grant No.
NAS7-918

13. Type of Report and Period Covered

JPL Publication

12. Sponsoring Agency Name and Address

NATIONAL AERONAUTICS AND SPACE ADMINISTRATION
Washington, D.C. 20546

14. Sponsoring Agency Code
RE 221 BP 665-31-00-08-71

15. Supplementary Notes

16. Abstract

The third Airborne Synthetic Aperture Radar (AIRSAR) Workshop was held on May 23 and 24, 1991, at the Jet Propulsion Laboratory, Pasadena, California. Thirty oral presentations were made and 18 poster papers displayed during the workshop.

This publication contains papers from 25 of these presentations, which include analyses of AIRSAR operations and studies in SAR remote sensing, ecology, hydrology, soil science, geology, oceanography, volcanology, and SAR mapping and data handling. Results from these studies indicate the direction and emphases of future orbital radar-sensor missions that will be launched during the 1990s.

17. Key Words (Selected by Author(s))

Biology
Geosciences and Oceanography (General)
Earth Resources
Geology and Mineralogy

18. Distribution Statement

Unclassified -- Unlimited

19. Security Classif. (of this report)
Unclassified

20. Security Classif. (of this page)
Unclassified

21. No. of Pages
236

22. Price